Investigations on non-noble metal-based catalysts for water electrolysis

A Thesis Submitted for the Degree of

Doctor of Philosophy

By

Divya Bhutani

Chemistry and Physics of Materials Unit
Jawaharlal Nehru Centre for Advanced Scientific Research
(A Deemed University)
Bangalore - 560064 (INDIA)
March 2024

Dedicated to my soul within

(Bholenath), my parents

&

my siblings

DECLARATION

I hereby declare that the thesis entitled "***Investigations on non-noble metal-based catalysts for water electrolysis***" is an authentic record of research work carried out by me at the Chemistry and Physics of Materials Unit, Jawaharlal Nehru Centre for Advanced Scientific Research, Bangalore, India, under the supervision of **Prof. M. Eswaramoorthy** and that it has not been submitted elsewhere for the award of any degree or diploma.

In keeping with the general practice of reporting scientific observations, due acknowledgment has been made whenever the work described is based on the findings of other investigators. Any omission that might have occurred due to oversight or error in judgment is regretted.

Divya

Divya Bhutani

Jawaharlal Nehru Centre for Advanced Scientific Research

Prof. M. Eswaramoorthy
Chemistry and Physics of Materials Unit
Jawaharlal Nehru Centre for Advanced
Scientific Research (JNCASR)
Bangalore-560064,India
Phone : +91 80 2208 2870
Email: eswar@jncasr.ac.in

Date
12-03-2024

CERTIFICATE

I hereby certify that the work described in this thesis titled "***Investigations on non-noble metal-based catalysts for water electrolysis***" has been carried out by **Divya Bhutani** at the Chemistry and Physics of Materials Unit, Jawaharlal Nehru Centre for Advanced Scientific Research, Bangalore, India, under my supervision. It has not been submitted elsewhere for any degree or diploma award.

M. Eswaramoorthy
(Research Supervisor)

ACKNOWLEDGEMENTS

I am grateful to all the souls who helped me evolve during my Ph.D. Firstly, I would like to thank my research supervisor, **Prof. M. Eswaramoorthy***, for being supportive and giving me the freedom to think, act, and perform throughout this journey of my Ph.D. Performing research work under his supervision, guidance, and encouragement has been an immense pleasure. I heartfully thank him for introducing me to different fields of material chemistry and their physical significance and always providing a new view to see any problem. I appreciate the freedom of thought and actions he always built in me to visualize the struggles from beyond the perspective. His ever-ready critical questioning in analyzing and exploring the depth of any problem has provided me the courage to jump in freely with enthusiasm. He is one of the finest souls on this planet earth. It was amazing working with him. This entire journey of my Ph.D. has given me lessons, experiences, devotion, and knowledge towards science and this life and beyond.*

I want to express my sincere gratitude to **Prof. C. N. R. Rao, FRS** *for always being an inspiration. I am also grateful to Mrs. Indumati Rao for always being lovely, motivating and encouraging me and being a good friend. I wish you both good health.*

I thank the past and present chairpersons of CPMU for allowing me to use the various facilities of the centre.

I am thankful to Prof. A. Sundaresan and Prof. Kanishka Biswas from JNCASR, Prof. N. Ravishankar, Prof. S. Sampath, and Prof. Chinmoy Ranjan from IISc for their informative coursework.

My special thanks to my past and present lab family. I would like to thank Dr. Piyush, Dr. Amritroop, Dr. Dheeraj, Dr. Sisir, Dr. Sonu K.P., Himani, Dr. Sushumna, Dr. Anusha, Dr. Mehraj, Dr. Suchi, Dr. Soumita, Dr. Shivanna, Dr. Sudhakar, Arunava (always alive in my memories), Daizy, Dr. Momin, Surishi, Nijita, Abhishek, Swaraj, Ujjwal, Avinash, Elizabeth, and myself for all the support and lessons.

I would like to thank the visiting students who worked with me: Aditi, Bani, Rishir, Sathwik, Anita, Bibekananda, and all the POCE students.

It is a great pleasure to thank my collaborators: Prof. Umesh Waghmare (JNCASR), Shashank Chaturvedi (JNCASR), Prof. Chandrabhas Narayana (JNCASR), Dr. Divya Chalapathi (JNCASR), Prof. A. Sundaresan (JNCASR), Dr. Debendra Prasad Panda (JNCASR), Prof. Ranjani Viswanatha (JNCASR), Dr. Saptarshi Chakraborty (JNCASR), Prof. Swapan K. Pati (JNCASR), Dr. Supriti Dutta (JNCASR), Prof. Abhishek Singh (IISc), Pooja Gakhad (IISc), and Dr. Vinod C. Prabhakaran (NCL Pune) for fruitful collaborations.

I am thankful to Akshaysingh Shekhawat, Dheemahi, Dr. Bivas Saha, Rajeev Rai (IISc), Prof. Ravishankar (IISc), and Prof. Ranjan Datta for fruitful scientific discussions.

I am thankful to the following people for various technical assistance: Mrs. Usha (TEM); Mr. Kanan, Ms. Meenkashi, Mrs. Selvi, and Mr. Shreehari (FESEM); Mr. Vasu (UV, PL, IR, TGA); Mr. Sachin (XPS); Mr. Kanan, Mr. Arun and Mr. Rahul (TEM), Mr. Anil (XRD), Mrs. Durgasri (NMR), Mr. Nandkishore and Mr. Rajkumar, Mrs. Usha (CPMU office), and Mrs. Ramya (ICMS office).

I am thankful to the academic, administrative, Complab, library, hostel, mess, Dhanwantri, housekeeping, security, and canteen staff of JNCASR for their assistance.

I thank Prof. M. Eswaramoorthy and his family (Kaavya and Ma'am) for their hospitality and affection.

Financial assistance from UGC and JNCASR is gratefully acknowledged.

I am grateful to my earlier guides and mentors: Prof. Gera, Prof. Kohli, Prof. Geetanjali, Prof. Dutta, Dr. Pretty, Dr. Anita, and Dr. Neelima.

I am grateful to all my past friends: Manpreet, Deepak, Saurav, Nidhi, Payal, Anubhav, Vipin, Puhia, Shashank, Nirdosh, Nirmal, and my singing gang.

I am grateful to my loving 'Sab changa c' family for the nourishing NVSH days and after.

I feel grateful to my JNC friends: Akshay, Ankit, Sachin, Saif, Rohit, Vinita, Surishi, Shalu, Himani, Himanshu, Tanumoy, Shashank, Sinay, Saptarshi, Sumukh, *Mayank, Kamlesh, Bhupesh, Akhilesh, Uttam, Anjana, Bhawna, Prabhat, Rinya, Doha (Morocco), Tuse (Nigeria), skit-group, volunteering groups.*

My heartfelt gratitude to my Akshay for being there for me in every possible way throughout this chapter of our life. No words.

My love for my babies from the human kingdom, Ishu, Rishu, and Avi, and from the animal kingdom, Akku (hamster) and Chutku (kitten), with whom I have bundled memories of being in motherhood. You all stay in my heart; Mum loves you all.

My humble gratitude to the angelic grandparents blessing me from heaven: My grandfathers (Nanu and Dadu), grandmother (Nani), and Bey Ji (great-grandmother).

My gratitude to my big brothers, who always encourage me to live my life to the fullest; Sanchit and Aadi Jeeju.

I am grateful to the lovely old ladies: my bhui and my jhai g (grandmother).

Love for my selected old soul, my Pappa, and young soul, my mumma, for being my pillars.

Divine love for my all-time saviors and everything: Ishu (my brother) and Bhalu (Deepika, my sister).

I feel great love for and from my soul within, Bholenath, for always leading me to the way of evolution "from zero to zero and the life within".

Divya Bhutani

PREFACE

This thesis is divided into two parts. **Part 1** deals with the synthesis and application of metal phosphides and magnetic iron nanostructures toward alkaline water splitting. **Part 2** describes catalytic water splitting using benzyl alcohol and glucose oxidation reactions in place of oxygen evolution reaction along with glucose sensing application.

Chapter 1.1. introduces conventional water electrolysis. Hydrogen is a green fuel and a promising alternative to fossil fuels, with the highest energy density and zero carbon emission. The electrochemical route of hydrogen generation favors the commercial steam reforming process and can impact environmental sustainability. The overall efficiency and viability of electrochemical hydrogen production are affected mainly by the sluggish kinetics and electrochemistry of the counter-oxygen evolution reaction (OER). Various strategies have been employed to improve the performance of non-noble metal-based catalysts towards OER. The major challenge for commercial applications originates from the instability of the materials to attain high current densities and high stabilities in extreme conditions.

Chapter 1.2. describes the generation of hetero-interfaces by simple mixing of FeP and CoP nanoparticles and their enhanced performance for OER. The catalyst showed good activity in terms of low overpotential (η_{10} of 220 mV), high current density (1.37 A cm^{-2}), stability (200 h for 200 mA cm^{-2}), and high mass activity (18897 A g^{-1}). The post-reaction analysis and theoretical studies conclude that the effective charge transfer between Co and Fe sites with an effective decrease in the free energy of the oxygenated surface and barrierless kinetics lead to this enhanced performance as compared to the individual FeP and CoP catalysts.

Chapter 1.3. deals with studying the influence of a magnetic field on water electrolysis. Achieving commercial-level current densities and stabilities at ampere-level currents is the major challenge in electrolysis. Magnetic fields are known to improve the kinetics of OER by considering the spin contributions of magnetic electrocatalysts. Herein, the one-time application of a magnetic field improves the performance of magnetic Fe nanostructures towards OER. The catalyst showed lower overpotentials and imparted very high current densities of 5.5 A cm^{-2} in 1 M KOH electrolyte at 230 mV overpotential. The remarkable stability for more than 4200 h to achieve a current density of 1 A cm^{-2} and 700 % increase in magneto current make this catalyst very effective in electrochemical applications. The post-reaction analysis reveals the in-situ generation of Fe@$NiFe_2O_4$ core-shell morphology by catalyst-support interactions. Testing the catalyst shows ability to withstand high current densities of 17 A cm^{-2} (at 6.0 V) and -12 A cm^{-2} (at -3.3 V) towards oxygen and hydrogen evolution, respectively. Also, in harsh conditions of utilizing 10 M KOH, overpotentials sharply decreased to achieve a current density of 1 A cm^{-2} from 180 mV in 1 M KOH to 110 mV in 10 M KOH electrolyte.

Chapter 2.1. discusses the hybrid water electrolysis in replacing the energy-intensive OER with thermodynamically favorable reactions. Coupling the hydrogen evolution reaction (HER) with the oxidation of organic molecules helps not only to decrease the overpotentials, but also generate value-added products (VAPs) on their oxidation.

Chapter 2.2. investigates the electrooxidation of benzyl alcohol (BA) to valuable carbonyl products like benzaldehyde and benzoic acids, which have significant usage in food, pharmaceutical, and dye industries. Benzoic acid is produced from the conventional toluene oxidation route, involving the use of highly concentrated corrosive acids and reaction at high temperature and pressure with energy-intensive separation procedures. In the electrochemical oxidation of benzyl alcohol to produce benzoic acid, various non-noble metal (Ni, Cu and Co)-based systems have been employed in place of noble metal catalysts (Pt, Au, and Ru) to realise their commercial potential. However, achieving high current densities of > 400 mA cm^{-2} and high-purity benzoic acid is still a challenge. Considering the role of Cr as a pore-forming agent with its hydrophilicity and electropositive nature, chromium-treated Ni foam (CTNF) was used as a catalyst for the electrochemical production of PhCOOH. The CTNF catalyst showed 100 % BA conversion with 98% selectivity for benzoic acid. The surface studies reveal the inherent improvement of active sites in presence of chromium. The in-situ Raman analysis highlights the chemical oxidation of BA to PhCOOH through reversible electrochemical conversion of Ni^{2+} and Ni^{3+} species.

Chapter 2.3. demonstrates the electrochemical oxidation of glucose over CuO@NF(C) catalysts resulting in high current densities. CuO with specular morphology prepared on a nickel foam shows enhanced performance for electrochemical glucose oxidation with 93% conversion. In-situ Raman analysis suggests that Ni sites are the active sites for the chemical oxidation of glucose to aldaric acids. Further, there is an immense need to replace conventional enzymatic glucose sensors with non-enzymatic sensors because of their reliability, response, durability, and cost-effectiveness. When used as a glucose sensor, CuO@NF(C) catalyst showed a high sensitivity of 4.0 E9 μA mM^{-1} cm^2, a low detection limit of 5 nM, a very low response time of 0.5 s, and good stability.

Table of Contents

PART 1

Chapter 1.1. **An introduction to water electrolysis**

Chapter 1.2. **Heterostructures from hetero-mixtures: metal phosphides for oxygen evolution reaction (OER)**

Chapter 1.3. **Magnetically activated iron nanostructures for water splitting**

Chapter- 1.1 An introduction to water electrolysis

Summary:

This chapter provides an overview of different methods for hydrogen production and the influencing factors. Emphasizing the electrochemical route of hydrogen production, it outlines the challenges linked with the kinetically sluggish and energy-demanding anodic oxidation reaction. Key metrics are discussed when accessing the performance. Additionally, current catalysts are briefly surveyed, considering various constraints on their utilization and the potential substitution of noble metals with non-noble metal analogs.

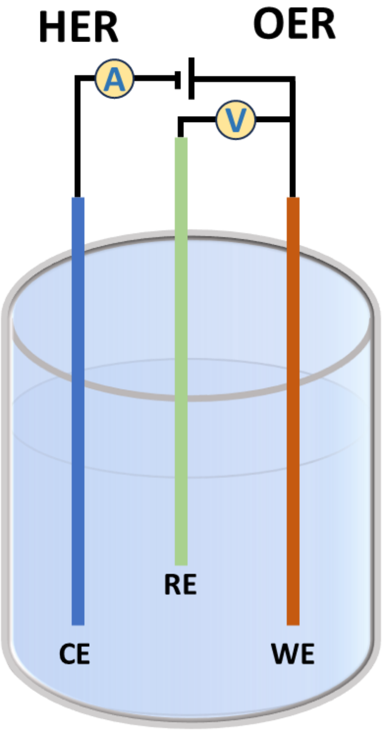

1.1.1. Need for a green fuel: Generation of hydrogen:

Growing energy demands have resulted in excessive utilization of fossil fuels, contributing to the accumulation of high concentrations of greenhouse gases and consequently increasing global warming. In order to mitigate this environmental impact, low-carbon or zero-carbon emitting fuels are preferred. Hydrogen is a promising option with a remarkable gravimetric energy density of 120 MJ kg^{-1}, three times higher than gasoline and petroleum.(*1*) The global economy can be substantially enhanced with sustainable hydrogen production as it is the only fuel with zero carbon emissions. Global hydrogen production follows diverse paths: approximately 48 % from natural gas, 30 % from oil, 18% from refineries and petrochemical industries, and merely 4 % from the electrochemical route **(*Figure 1.1.1.*).** Hydrogen produced through these methods has applications across various sectors. Notably, global hydrogen consumption can be allocated to 65 % in the production of ammonia and other chemicals, 25 % in petroleum refining, and the remaining in other sectors **(*Figure 1.1.1.*)**.(*2*)

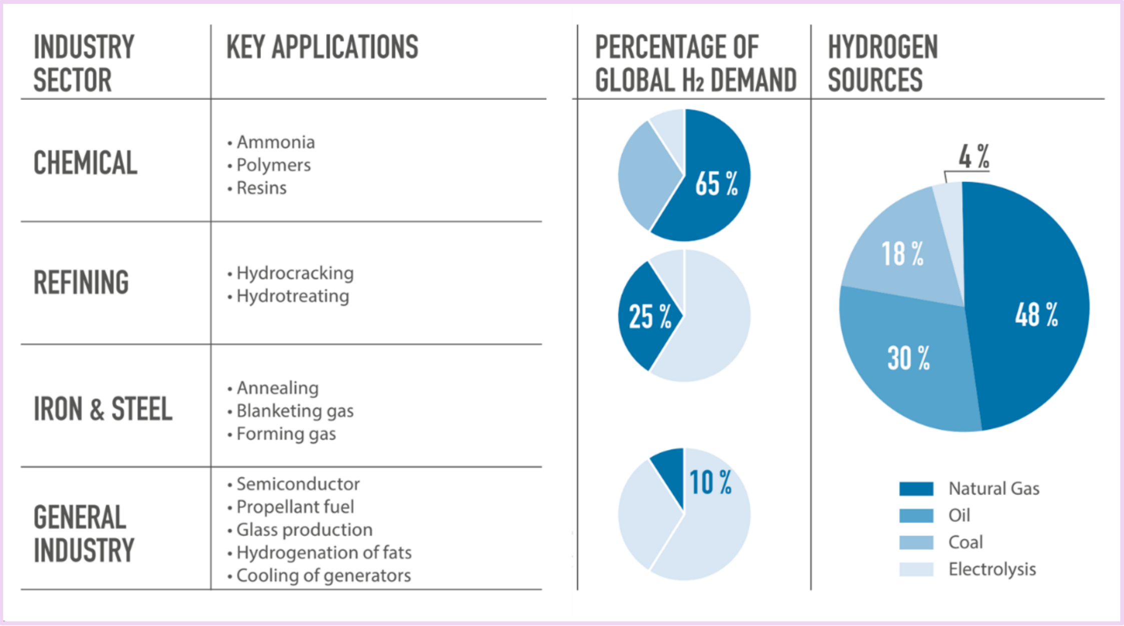

Figure 1.1. 1. Global hydrogen production and consumption in various sectors. Reproduced with permission from Ref. (2).

In recent years, there has been a surge in the rapid installation of electrochemical plants worldwide. The electrolyzer market demand is expected to reach 15-30 Mt by 2030, with manufacturing capacity reaching 200 % p.a. Current state and outlook for green hydrogen market is provided in ***Figure 1.1.2.***.(*3*)

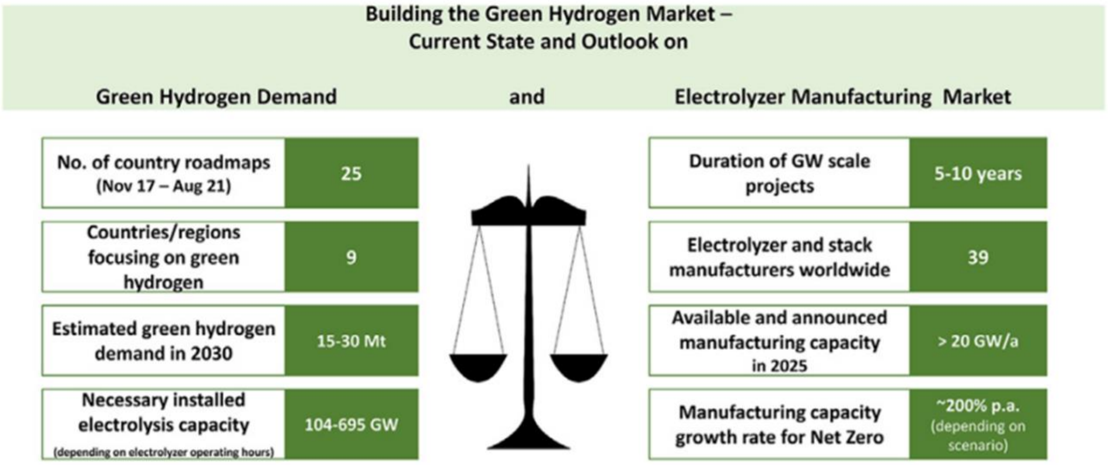

Figure 1.1. 2. Outlook of green hydrogen market with expected manufacturing capacity of different electrolyzers by 2025. Reproduced with permission from Ref. (3).

Different approaches have been employed considering this critical area of hydrogen production.(*4*) Various methods for the production of hydrogen(*5*, *6*) can be classified as follows:

a. **Thermochemical:** This process harnesses energy from diverse sources like natural gas, coal, and biomass, resulting in hydrogen release from the molecular structure of the resources.

The thermochemical process can be subdivided into four categories:(*7*)

(i) **Natural gas or steam reforming:** This involves the conversion of natural gases to H_2 and a mixture of gases at high temperature and pressure ***(Figure 1.1.3.)***. The commercial steam reforming process is the predominant method of hydrogen production. In this process, methane sourced from natural gas reacts with steam at high temperature (700- 1000 °C) under elevated pressure (3-25 bar), yielding hydrogen and CO as the products. To produce 1.1 tonnes of H_2 gas, 2.2 tonnes of methane is required, with the release of nearly 6.0 tonnes of CO_2 into the atmosphere. Additional processing steps are employed to eliminate the accompanying gases like CO as they may risk poisoning noble metal Pt electrodes in fuel cells. Substantial economic and resource investments are needed before introducing this hydrogen for fuel cell application. The major drawback lies in the reliance on non-renewable resources and the significant emission of CO_2.

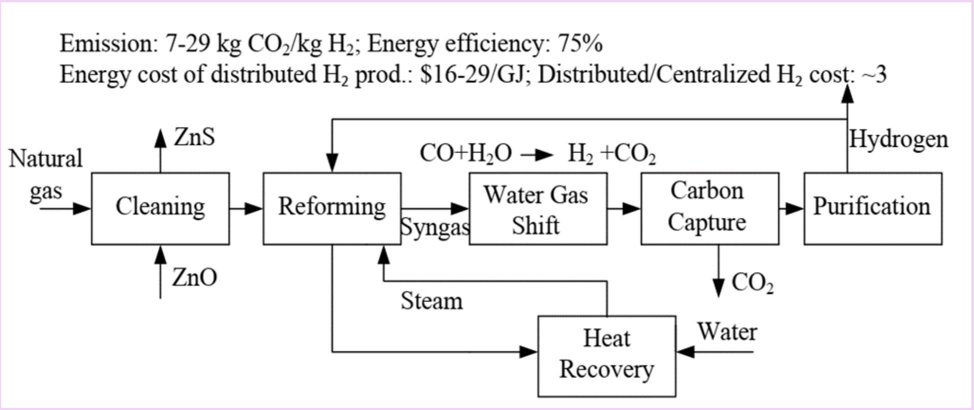

Figure 1.1. 3. Hydrogen production through steam reforming process. Reproduced with permission from Ref. (7).

(ii) **Biomass gasification:** The process of converting fossil-based carbonaceous materials or biomass feedstocks at high temperatures (> 700 °C) without combustion is called gasification ***(Figure 1.1.4.)***. A controlled amount of steam or oxygen is passed during this process, and gases like CO, CO_2, and H_2 are produced.

E.g. $C_6H_{12}O_6 + O_2 + H_2O \rightarrow CO + CO_2 + H_2$ + other species.

(iii) **Biomass-derived liquid reforming:** In this process, liquid biofuels, such as cellulosic ethanol or bio-oils, undergo a reaction with steam at high temperatures to produce H_2 and excess of CO. This CO then undergoes a water gas shift reaction to produce additional H_2 and CO_2, which are subsequently separated and purified.

$C_2H_5OH + H_2O$ + heat $\rightarrow 2CO + 4H_2$

$CO + H_2O \rightarrow CO_2 + H_2$ + heat (water-gas shift reaction)

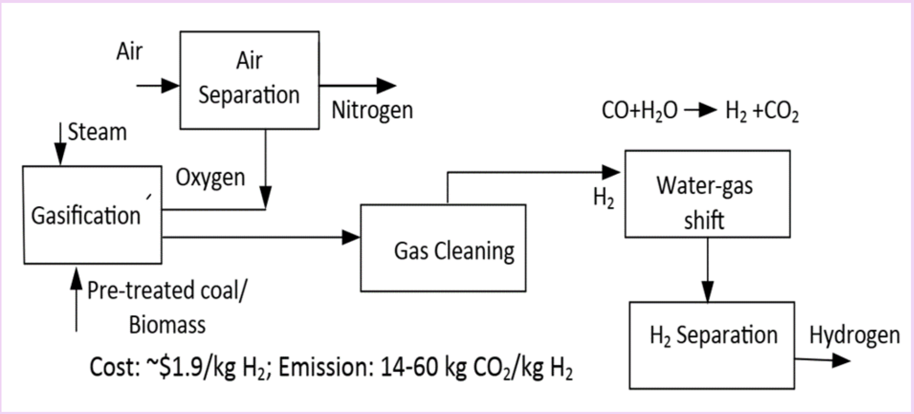

Figure 1.1. 4. Hydrogen production through the gasification process. Reproduced with permission from Ref. (7).

(iv) **Solar thermochemical hydrogen:** High-temperature heat (500-2000 °C) is harnessed from solar power or nuclear power reactions, and hydrogen is produced through water splitting with this intense heat with no or low emission of greenhouse gases.

b. **Biological:** Microbes are crucial in consuming and digesting biomasses through biological reactions to release hydrogen. These microbes either break down the organic matter or ferment the complex molecules, generating energy and H_2 fuel.

c. **Electrolytic process or Water electrolysis:** This process employs electricity sourced from either renewable or non-renewable sources to electrolyze water into H_2 and O_2.(*8*) An electrolyzer unit typically consists of an anode (on which oxidation occurs), a cathode (on which reduction occurs), and an electrolyte facilitating ion flow **(*Figure 1.1.5.*)**. The hydrogen produced through this method is carbon-free since no carbon-containing sources are employed. Water oxidation to O_2 occurs at the anode, while H_2 is produced at the cathode by reduction of water molecules. The electrons facilitate the flow of charges in the external circuit, while the movement of ions in the electrolyte maintains the charge transfer. The electrolyzers can be classified as alkaline, acidic, or solid oxide, depending on the type of electrolyte used.

In an alkaline electrolyzer:

At the anode: $4OH^- \rightarrow 2H_2O + O_2 + 4e^-$

At the cathode: $4H_2O + 4e^- \rightarrow 2H_2 + 4OH^-$

Overall: $2H_2O \rightarrow 2H_2 + O_2$

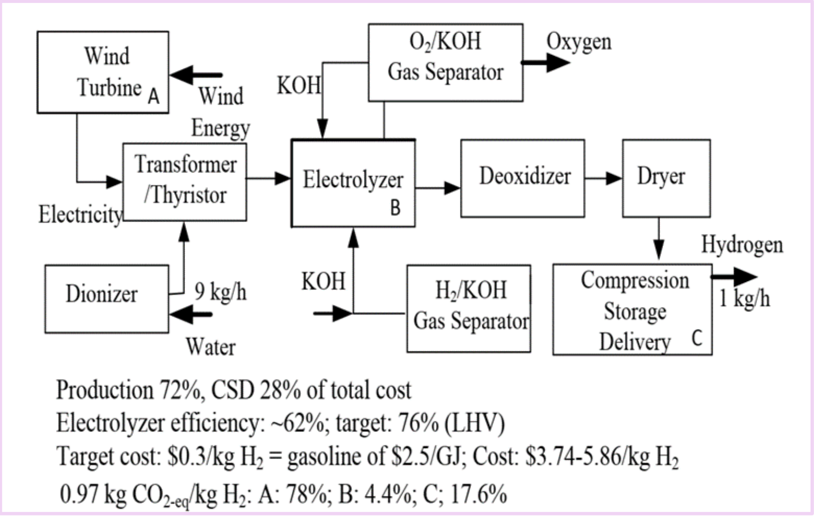

Figure 1.1. 5. Electrochemical hydrogen production through water splitting. Reproduced with permission from Ref. (7).

Among all these procedures, electrochemical water splitting emerges as an energy-efficient, eco-friendly, and sustainable approach for producing high-purity hydrogen fuel. This also offers an environmentally conscious alternative, utilizing electrons as the reductant and water as the greener medium.

The merits of electrochemical water splitting are listed below:(*9*)

i) Production of high-purity hydrogen

ii) Operation at room temperatures and atmospheric pressures

iii) No carbon dioxide emissions

iv) Water as the feedstock

v) Sustainable reactor design

1.1.2. Introduction to electrochemical water splitting:

The conventional electrochemical route of water splitting involves two half-cell reactions, where a high-purity hydrogen evolution reaction (HER) is facilitated at the cathode and the oxygen evolution reaction (OER) at the anode. To evaluate the performance of the reaction occurring in the half-cell, three-electrode arrangements has been considered (***Figure 1.1.6.***).

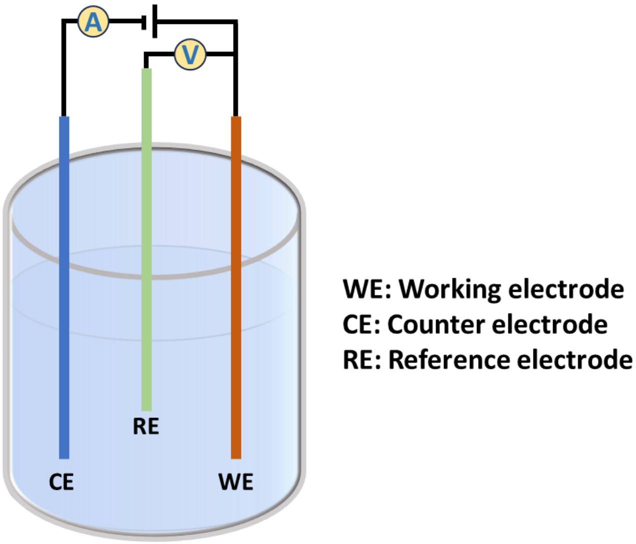

Figure 1.1. 6. Three-electrode arrangement for electrochemical analysis.

The reference electrode (with a fixed potential) fixes the potential input at the working electrode. The thermodynamic potential required for electrochemical water splitting is 1.23 V (237 kJ mol^{-1}), as depicted in the equation.(*10*)

$$2H_2O \rightarrow H_2 + O_2,\ E^0 = E^0_{OER} - E^0_{HER}, \qquad E^0 = 1.23\ \text{V (under standard conditions)}$$

In addition to this thermodynamic barrier (of 1.23 V) various kinetic barriers are also associated with the electrochemical splitting of water. These kinetic barriers attributed to various polarizations contributed from ohmic losses, activation to the charge transfer kinetics, and concentration (***Figure 1.1.7.***).(*11*) This leads to extra energy requirement for overpotential to achieve a particular current density (corresponding reaction rate). The ohmic polarization originates from the resistance the solution offers to the flow of charge carriers, the wire resistance, voids in the electrolyte, and the solution resistance. The activation polarization originates from the threshold activation energy required for a particular catalyst to conduct a reaction. Finally, the concentration polarization is linked to the diffusion of active species at the electrode surface. Alkaline or acidic conditions are typically employed to improve the conductivity of the electrolyte, thereby affecting the overall rate of the reaction.

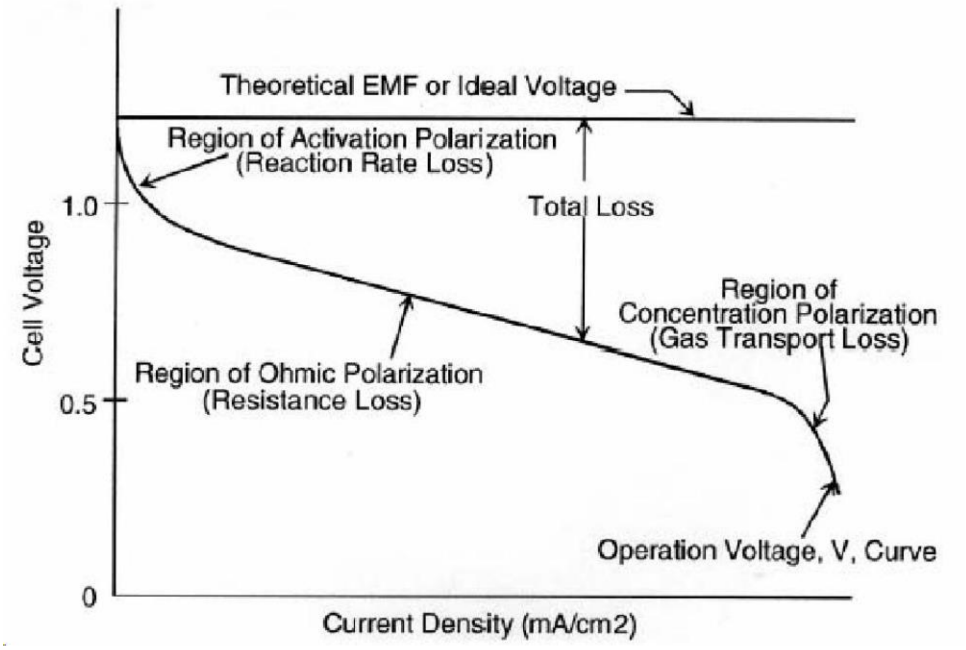

Figure 1.1. 7. Current-potential plot illustrates various polarizations during electrochemical analysis. Reproduced with permission from Ref. (11) and adapted from IEEE Explore.

The OER at the anode and HER at the cathode exhibit different mechanisms, as shown in ***Figure 1.1.8*** *and* ***Figure 1.1.9.***, *respectively.*

During HER,(*12*) the upcoming H species (H^+ or from H_2O) first adsorb at the active surface site (Volmer step). The adsorbed intermediate species combine (Heyrovsky step) with H from the H_2O molecule or H_3O^+ from the solution. Another way of producing hydrogen is through a combination of two adjacent H species adsorbed at the active surface site (Tafel step).

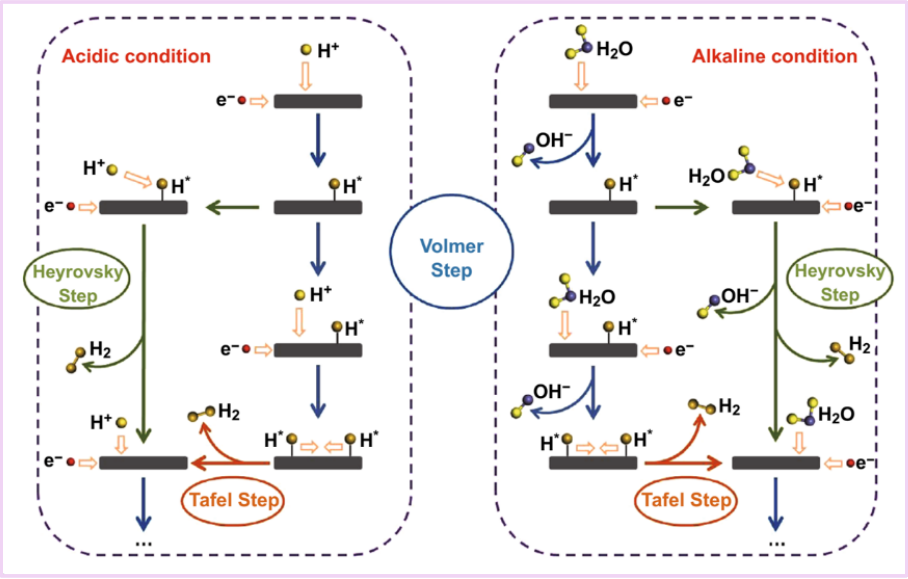

Figure 1.1. 8. Mechanistic view of hydrogen evolution reaction (HER) in acidic and alkaline conditions. Reproduced with permission from Ref. (12).

During OER,(*13*) the first step involves the adsorption of OH species (from OH^- or H_2O) at the active site, followed by the abstraction of hydrogen to form reactive MO species. These MO species lead to the formation of superoxide species and in the last step, the O_2 molecule desorbs from the surface.

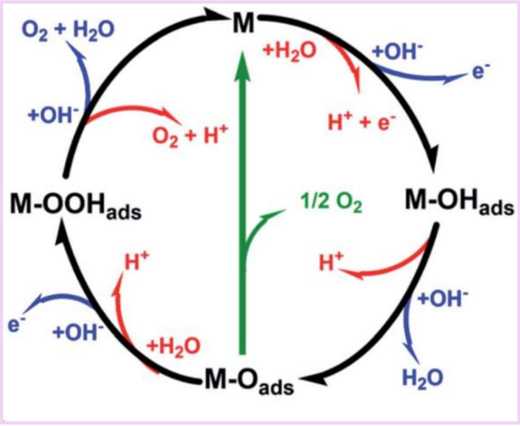

Figure 1.1. 9. Mechanistic overview of oxygen evolution reaction (OER) in acidic and alkaline conditions. Reproduced with permission from Ref. (13).

Often, the bottleneck of water splitting reaction lies in anodic OER owing to its four-electron, four-proton coupled sluggish kinetics. This high barrier results in decreased overall efficacy and, consequently, hydrogen production efficiency.

1.1.3. Figures of merit for evaluating performance towards water splitting:

Various general parameters are considered as the ‘figures of merit’ while reporting the electrocatalytic performance toward water splitting. Several techniques have been employed to record the electrochemical parameters, which include linear sweep voltammetry (LSV), cyclic voltammetry (CV), chronoamperometry (i-t), chronopotentiometry (v-t), and impedance analysis (Nyquist, Bode, and Mott-Schottky plots), etc. These performance metrics are discussed in detail below:

1.1.3.1. Overpotential (η):

The extra potential, over and above the thermodynamic potential to be provided to the system to carry out a reaction **(*Figure 1.1.10.*)**, is termed the overpotential (η).(*14*)

$\eta = E\text{-}E^0$ *E is the observed cell potential and* E^0 *is the thermodynamic potential.*

The overpotential is generally recorded to attain a current density of 10 mA cm^{-2}. Overpotentials at different high current densities could also be reported while recording an electrocatalytic performance. As the overpotential depicts the extra energy required compared to the thermodynamic potential. The lower the value of overpotential, the better the electrocatalyst. The value of thermodynamic potential for OER is 1.23 V (vs. RHE) whereas for HER is 0 V (vs. RHE).

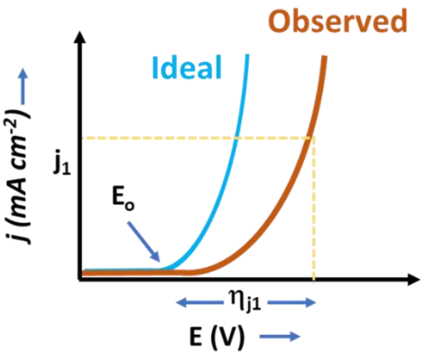

Figure 1.1. 10. Polarized linear sweep voltammetry plot (I-V curve) showing relation of current density (j) on the applied potential (E). E_0 ***is the thermodynamic equilibrium potential.***

1.1.3.2. Current density:

Another metrics to be included while reporting the performance of an electrocatalyst is the current density at a particular applied potential. According to the Butler-Volmer equation, the current density is exponentially related to the overpotential (η) and linearly related to the reaction rate (k), with the assumption that low sweep rates achieve a reversible static state.

Butler-Volmer equation: $i \approx i_0\ k \exp(\alpha nF\eta/RT)$, where i is current density, i_0 is exchange current density, k is reaction rate constant, α is transfer coefficient, n is the number of electrons transferred, F is Faraday constant, η is overpotential, R is universal gas constant, and T is temperature.

So, higher the current density at any given overpotential, higher the reaction rate and better the catalyst. It can be reported in terms of specific current density (mA cm^{-2}) or mass activity (A g^{-1}) depending on the normalization of the current density concerning the area or the mass of the catalyst taken, respectively. Higher mass activity at a particular potential depicts the maximum use of catalyst under study.

1.1.3.3. Tafel Slope (b):

The relation between overpotential (η) and logarithmic current density (log(*j*)) provides a Tafel slope (b) depicting the effect of an increase in overpotential with every decade change in current density **(*Figure 1.1.11.*)**.(*15, 16*)

Tafel equation: $\eta = a + b*\log(j)$

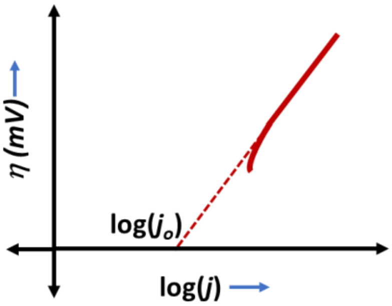

Figure 1.1. 11. Tafel plot (log(j) vs. η). (log (j₀) is the exchange current density.

Lower the observed Tafel slope (***Figure 1.1.12.***), lower the requirement of overpotentials to achieve the same current density.

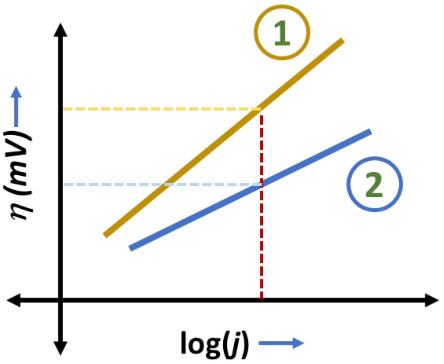

Figure 1.1. 12. Tafel slopes of two different catalysts; (1) and (2).

The range of Tafel slope value obtained in HER is used to interpret the type of mechanism. There are various electrochemical techniques such as voltammetry, steady state chronoamperometry/chronopotentiometry or electrochemical impedance spectroscopy to derive Tafel plots.

1.1.3.4. Electrochemically active surface area (ECSA):

The criteria for determining electrochemically active surface area (ECSA) depicts the intrinsic performance of an electrocatalyst. It provides the activity per unit active site of the catalyst under study. The ECSA is determined from cyclic voltammetry (CV) studies with varying scan rates in the non-faradaic region (***Figure 1.1.13.***).

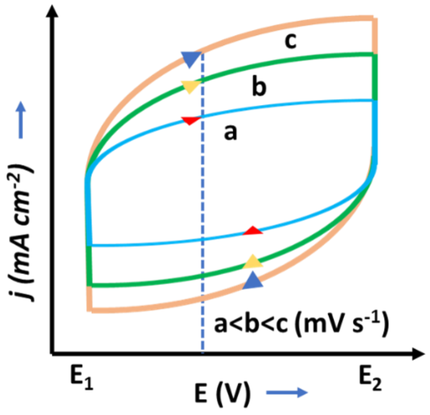

Figure 1.1. 13. Cyclic voltammetry (CV) analysis in the non-Faradaic region of potential. a, b, and c are the scan rates.

The slope of the average current with a scan rate plot **(*Figure 1.1.14.*)** gives the double-layer capacitance value.(*17, 18*)

For a linear equation, y = mx + c; slope = dy/dx

For current (I) vs. scan rate (ν) plot,

Slope = dI/dν

= (dq. dt)/ (dE/dt) [as dq = dI/dt, where q is charge, t is time, and E is potential]

= C [as dq = C.dE, where C is capacitance]

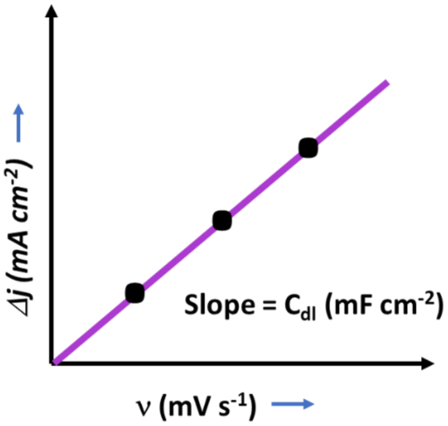

Figure 1.1. 14. Average current density vs. scan rate plot with slope as double layer capacitance (C_{dl}).

ECSA can be derived from the specific capacitance of an ideal flat surface as provided in the relation:

ECSA = C_{dl}/C_s where C_s = 40 mF cm^{-2} for flat electrodes.(*19*)

Furthermore, representing the current with respect to the ECSA depicts the intrinsic activity coming from the actual active sites at the electrochemical surfaces.

1.1.3.5. Electrochemical impedance spectroscopy:

The mechanistic aspect of an electrochemical measurement can be attained by considering the electrical elements involved during the reaction at the electrochemical interfaces. A constant DC potential is applied for a general impedance measurement, and the surface elements are analysed with a change in the AC frequency of the input potential signal. Various electrical elements could be involved, including capacitor (C), constant phase element (Q), which is similar to a capacitor with no dependency on the frequency of the potential applied, resistor (R), inductor (L), Warburg component (W), etc. The semicircles observed in the impedance plot (Nyquist) represent the RC components linked with different time constants, and the abscissa depicts the resistance offered by the solution and other independent components like leads and wires **(*Figure 1.1.15.*)**. The resistance to the flow of charge, i.e., charge transfer resistance (R_{ct}), is depicted from the abscissa values observed from the semicircles.(*20*) The linear part (45^o to the x-axis) represents the Warburg component controlling the diffusion kinetics of the process. In most cases, depressed semicircles are observed instead of perfect semicircles, dominated by surface heterogeneity with varying roughness factors represented by considering Q instead of C. A single semicircle represents the time constant from a single RC circuit with R and C in a parallel arrangement.(*21*) Various circuit arrangements are possible for a process involving more than one time-constant **(*Figure 1.1.15.*)**.

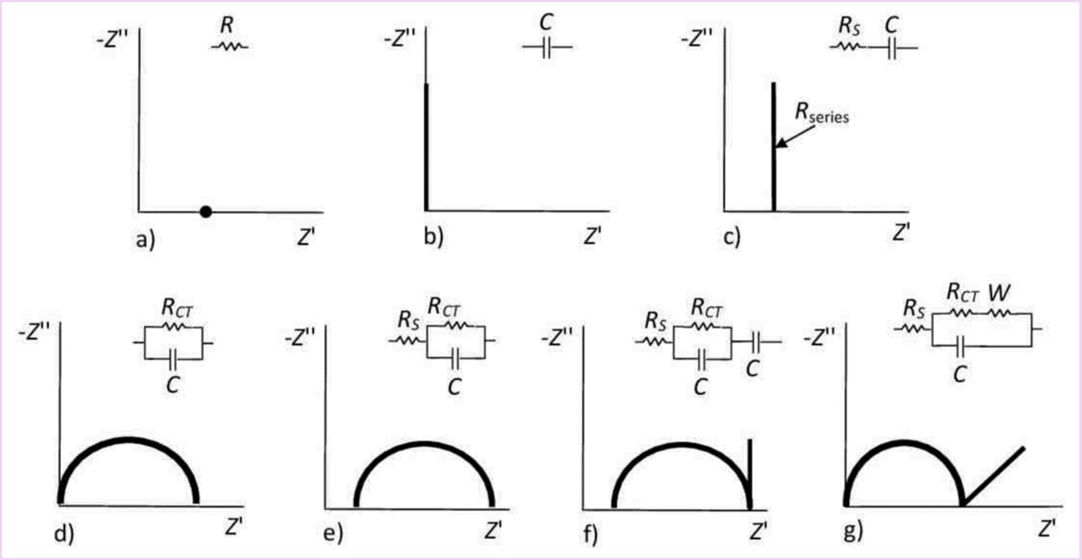

Figure 1.1. 15. Various combinations of circuit elements, resistance (R_S; solution, R_{CT}: charge transfer), capacitance (C), and Warburg component (W) in the Nyquist plot. Reproduced with permission from Ref. (21).

1.1.3.6. Stability:

For a catalyst to be employed for commercial applications, long-term stability and durability must be determined, providing the conditions of lower and higher input potentials or currents.(*22-24*) Various methods such as galvanostatic (constant current, chronopotentiometry), potentiostatic (constant potential, chronoamperometry), accelerated degradability (via cyclic voltammetry), multistep potential or current steps have been employed for studying the stability of an electrocatalyst **(*Figure 1.1.16.*)**. Retention of the constant potential or current density during galvanostatic and potentiostatic analyses, respectively, shows the stability of a catalyst. Also, the overlapping LSVs attained after CV analysis at high scan rates depict the excellent stability of an electrocatalyst.

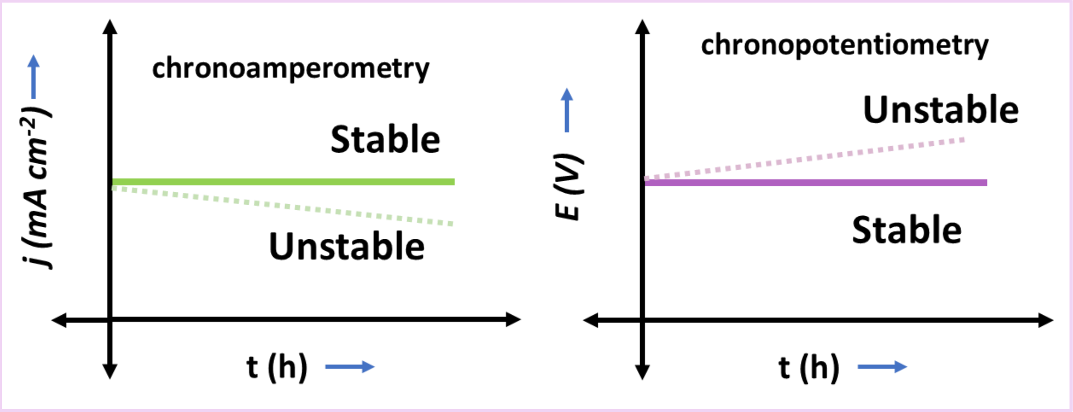

Figure 1.1. 16. Stability plots in terms of chronoamperometry and chronopotentiometry analyses.

1.1.3.7. Faradaic efficiency:

Faradaic efficiency (FE) of a reaction determines the selectivity of the reaction towards the formation of a particular product.(*25*) It describes the charge utilization efficiency towards a particular product formation. The water-gas displacement method can be used to determine the faradaic efficiency for oxygen in OER **(*Figure 1.1.17.*)**.(*26*) In this method, a burette is inverted in water, and the O_2 gas coming out from the anodic chamber of airtight H-type electrochemical cell displaces the water in the burette. The amount of water displaced equals the amount of gas evolved.

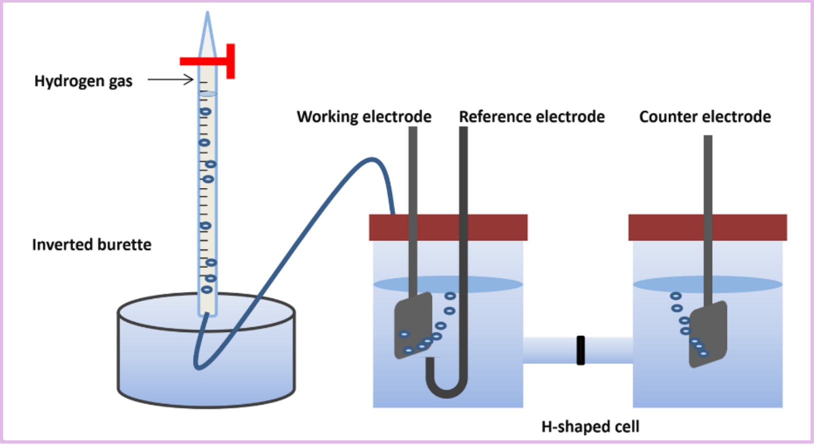

Figure 1.1. 17. Water-gas displacement method for evaluation of Faradaic efficiency. Reproduced with permission from Ref. (26).

The experiment is usually performed under potentiostatic conditions, and the amount of observed charge should be compared with that observed from the volume of water replaced by the evolved O_2 by using the following relation:

FE = $(Q_{O2}/Q_{total})*100$, where Q_{O2} and Q_{total} are experimentally observed charges and total theoretical charges associated with O_2 evolution, respectively.

$Q_{O2} = (N_{O2})/(n*F)$, where N_{O2} is the number of moles of O_2 evolved, n = the number of electrons transferred (4 for OER), and F (Faraday's constant) = 96485 C mol^{-1}.

$N_{O2} = V/V_m$, where V is the volume of water displaced, and V_m (molar volume) = 22.4 L.

Q_{total} can be calculated from the charge observed via potentiostatic measurement.

1.1.3.8. Turnover frequency (TOF):

TOF denotes the number or quantity of product molecules per unit active site per unit time.(*27*) The TOF values for different catalysts can be calculated from the following relation:

TOF = (j*A)/ (n*F*m),

where *j* is current density at a fixed potential, A is geometrical surface area (0.07068 cm^{-2} for the glassy carbon electrode), n is the number of electrons transferred (n=4, for OER), F is Faraday constant (96485 C mol^{-1}), and m is moles of active metal sites. The number of moles of active species is calculated from the number of metal species on the working electrode as $m = w/M_W$, where w is the weight of metals taken in the sample, and M_W is the molecular weight of metals in the sample.

1.1.4. Selection of electrocatalysts for oxygen evolution reaction (OER):

To improve the overall performance of the electrochemical reaction, the electrochemical performance towards OER is to be evaluated. Firstly, metal oxides were considered the most active towards OER, but there is always a low conductivity issue with oxides.(*19*) Further, different metal sulphides,(*28*) chalcogenides,(*29*) selenides,(*30*) phosphides,(*31*) and nitrides(*32*) are considered, and all these acts as the pre-catalysts which get converted to oxyhydroxide **(*Figure 1.1.18.*)** in the oxidising environment during OER.(*33*) These oxyhydroxide surfaces of metal sulphides, selenides, phosphides, and nitrides show better performance(*34*) with respect to pure metal oxides because of the effect of heteroatoms like P, S, Se, N, etc, which actively participate in creating defects and vacancies during conversion to oxyhydroxides.(*35*) Also, these heteroatoms activate the adjacent metal center by the inductive and electronegative effect, making the metal site more electrophilic and, thus, improving the adsorption kinetics of different intermediates generated at the metal sites during the reaction.(*36*)

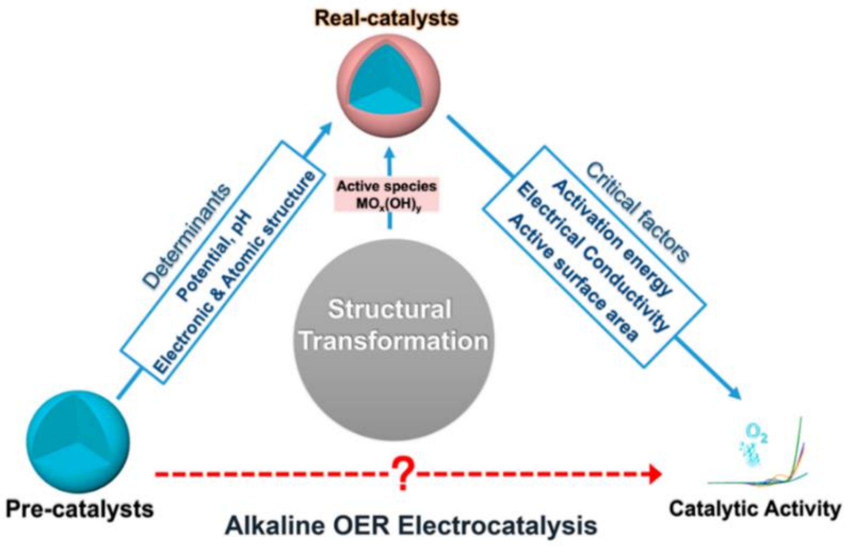

Figure 1.1. 18. Illustration of structural transformations and catalytic performance during oxygen evolution reaction (OER). Reproduced with permission from Ref. (33).

While considering these electrocatalysts, metal phosphides are considered best in terms of their stability in a wide pH range, low toxicity, ease in availability, and high conductivity. There is a need to shift from the historic flat support to porous supports like Ni foam (NF) and Carbon paper (CP). Using porous support increases the effective area and decreases the diffusion length of the electrolyte at the interface, increasing the accessibility of the reactants and the conductivity of the material.(*37*) Further, these porous supports can also affect the performance by interacting with the coated material, bringing in synergism in the band structure, thus modifying the kinetics of the reaction intermediates at the final surface. The aim in designing an OER electrocatalyst is to achieve low overpotential, high turnover frequency (TOF), mass activity and long-term stability.

1.1.5. Electrochemical measurements:

Electrochemical measurements can be carried out in a conventional two-electrode arrangement wherein one electrode acts as the anode (oxidation side) while the other acts as the cathode (reduction side). Three-electrode measurements are considered to estimate the performance of a single electrode, wherein the reference electrode is used to fix the potential at the working electrode. In contrast, the counter electrode completes the overall circuit. It is essential to calibrate the reference electrode to estimate the standard potential values. Herein, the electrochemical studies were investigated using an electrochemical workstation (66 °C, USA) obtained from CH instruments, EC-Lab, Biologic Science Instruments VSP, and 2461-US, Hi Current Interactive Source Meter Unit, Tektronix/Keithley for evaluating the electrochemical activities of catalysts towards oxygen evolution reaction (OER), hydrogen evolution reaction (HER), overall water splitting and other electrochemical analyses.

1.1.6. Calibration of Reference electrode:

The reference electrode, Hg/HgO, used in the alkaline electrolyte (KOH solution), was calibrated with respect to the reversible hydrogen electrode (RHE) using a large area of Pt foil as a working electrode and Pt coil as the counter electrode. High-purity hydrogen gas was purged in the electrolyte for 45 minutes before the experiment to achieve H_2 saturation, and constant purging of H_2 was maintained during the measurement. Cyclic voltammograms (***Figure 1.1.19.***) were recorded at a scan rate of 1 mV s^{-1}. The average of potential values (at j=0) for the forward and backward scans (HER and HOR, respectively) were considered as the standard potential of the reference (vs. RHE).(*38*)

For 1 M KOH, $E_{RHE} = E_{Hg/HgO} + E_{calibrated}$

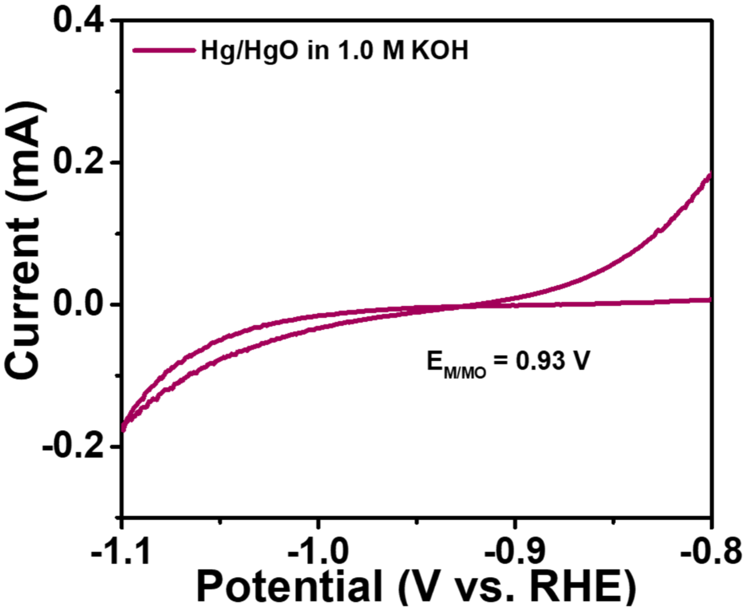

Figure 1.1. 19. Cyclic voltammetry (CV) analysis depicting the calibration of Hg/HgO reference electrode.

1.1.7. Mott-Schottky analysis:

The Mott-Schottky analysis deals with interpreting the electrochemical behavior of the surface of a material immersed in the solution. Due to the dangling bonds of the surface-active species, there exist surface states in addition to electron energy bands and impurity levels (***Figure 1.1.20.***). There is a transfer of charge carriers during the equilibration of the surface Fermi levels and the Fermi levels in the interior of the material. If the material is semiconducting, there is a generation of equal and opposite charges inside the material, forming a space charge layer (SCL) near the surface. As the two levels equilibrate, there is bending of bands near the surface in the space charge layer, which develops an electrostatic potential that can be explained in terms of the double-layer model.(*39*)

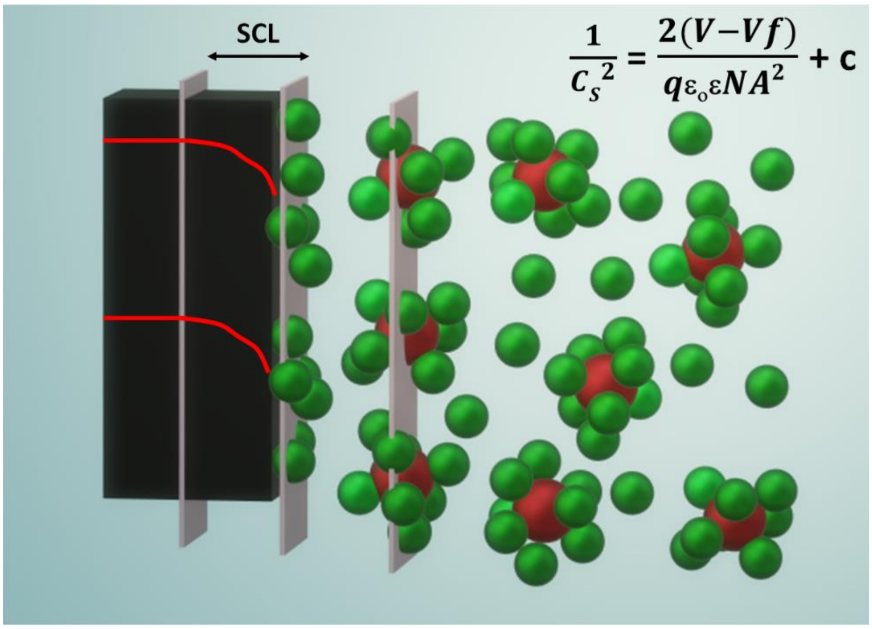

Figure 1.1. 20. Double layer model showing bending of bands in the space charge layer (SCL) inside the semiconducting electrode immersed in an electrolyte.

1.1.8. Calculation of relative charge carrier concentration from Mott-Schottky analysis:

Three different layers contribute to electrochemical activity: the space charge layer inside the semiconductor, the compact layer (CL) comprising adsorbed solvent molecules at the surface, and the diffusion layer (DL) consisting of solvated ions **(*Figure 1.1.20.*)**. The arrangement of the charge carriers leads to the existence of parallel plate capacitance in these three regions and the contribution from C_{SC} (capacitance from space charge layer) would be more for the resultant capacitance value in comparison to the other two with a semiconductor and the capacitance depends according to the equation, ($1/C_T = 1/C_{SC} + 1/C_w + 1/C_d$), where C_s, C_w, and C_d are capacitance due to SCL, CL, and DL, respectively. This value of C_{SC} can be interpreted with respect to applied potential ($V-V_b$) by the Mott-Schottky equation,

($1/C_s^2 = 2(V-V_b)/N$)(*40*)

The slope value will provide the charge carrier concentration (N), and the slope type (either negative or positive) will deliver information on whether the surface behaves as p-type or n-type semiconductor. Also, the C vs. V plot tells about the behavior of the material at the interface in an electrolyte.

1.1.9. Magnetic field-assisted oxygen evolution reaction:

Various studies highlighted the role of an external magnetic field in improving OER performance by influencing the kinetics of the reaction.(*42-52*) The magnetic field has hugely impacted various fields of study, like electrolysis, electrodeposition, propulsion in fluids, hydrodynamics, etc., in the last few decades. Magneto-electrochemistry affects the kinetics of OER by affecting the polarization effects, the magnetic spin, and the surface characteristics. The adhesion of bubbles on the electroactive surface during the gas phase reactions significantly affects these polarisations. The generation of bubbles leads to the inaccessibility of the active sites, impeding the electrochemical performance. In addition, the conductivity of the electrolyte is adversely affected by increased void space. External agitation can help in removing these adsorbed macro-bubbles, but the nano and microbubbles remain unaffected.(*53, 54*) The local convection **(*Figure 1.1.21.*)** through the induced Lorentz force (F_L), ($F_L = \sigma(v \times B)$, where σ, v and B are the charge density, velocity vector, and magnetic field, respectively) by the magnetohydrodynamic (MHD) helps in the release of bubbles at the early stage of formation.

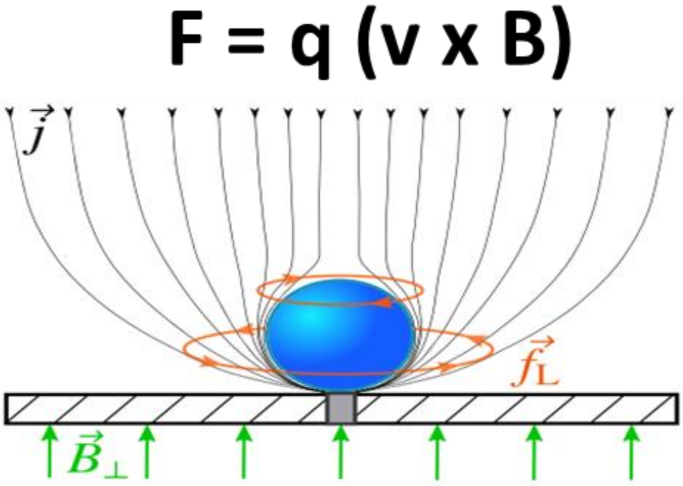

Figure 1.1. 21. Local convection induced at the bubble evolved during gas-evolving reaction. Reproduced with permission from Ref. (54).

Not only bubble removal, the magneto-electrochemistry also affects the electrode-electrolyte interface through the Maxwell stress effect (***Figure 1.1.22.***), improving the intrinsic adsorption abilities of the surface. In absence of magnetic field, the paramagnetic droplet remains spherical (***Figure 1.1.22. b***) while in presence of magnetic field in parallel or perpendicular direction (***Figure 1.1.22.a, c***), the effective surface area of interaction increases.(*55*)

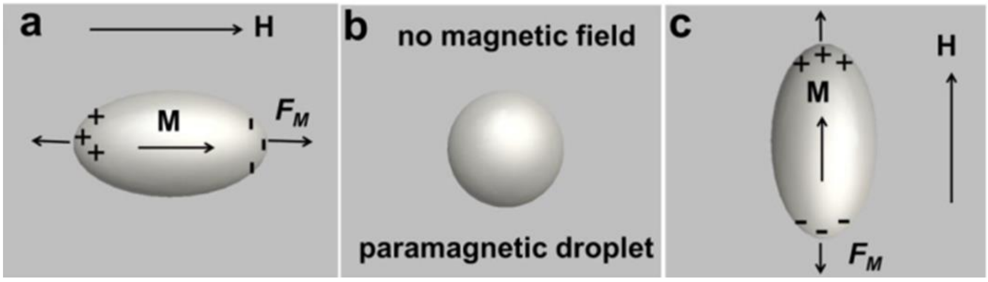

Figure 1.1. 22. Schematics showing Maxwell stress effect experienced by a paramagnetic droplet in presence of external magnetic field. Reproduced with permission from Ref. (55).

Additionally, the alignment of magnetic spins of a magnetic material facilitates the direct production of oxygen molecules in the energy-efficient spin-triplet ground state.(*52*) The spins at the adjacent metal sites (***Figure 1.1.23.***) in magnetic materials can be influenced by magnetic fields and align themselves in spin parallel orientation. The upcoming O* intermediates at these adjacent metal sites are thereby effectively adsorbed in a parallel direction only, leading to the formation of an O_2 molecule in a spin-triplet ground state.

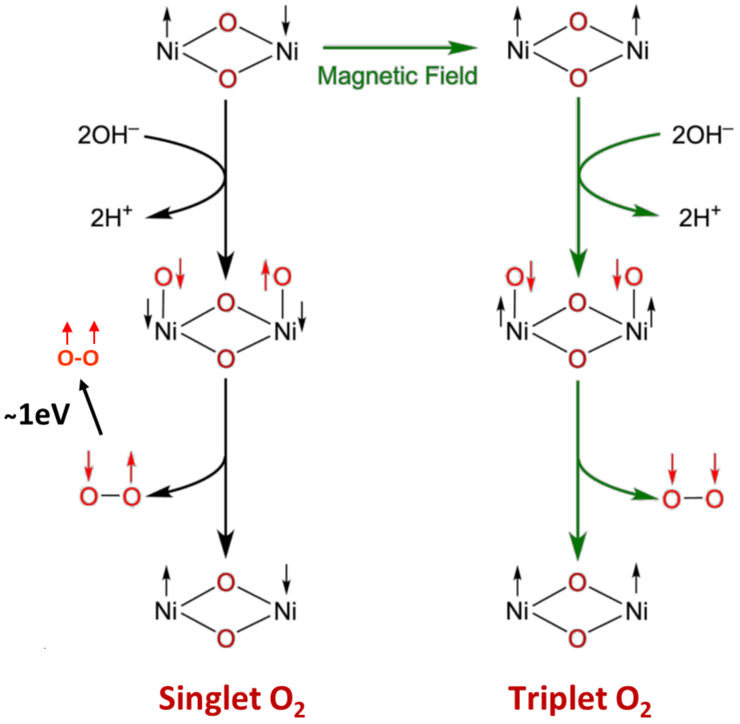

Figure 1.1. 23. Direct formation of triplet ground state of oxygen molecule at the surface of magnetic electrocatalyst in presence of external magnetic field. Modified figure from Ref. (52).

Some or all these factors may simultaneously contribute to enhanced electrochemical performance. Several studies report the reversal of performance after removing the external magnetic field. Ziren Xiong et al. recently reported that a field-free enhancement by a one-time exposure to a magnetic field permanently affects the OER performance.(*56*) However, high current density demands high overpotential. Achieving high current densities (> 1 A cm^{-2}) at low overpotentials with long-term stability (around 1000 h) is still challenging. The use of noble metal-based catalysts (Pt, RuO_2, and IrO_2) in electrolyzers and fuel cells elevates the energy requirement to a certain extent. Still, their high cost, scarcity, and low stability affect their overall performance chemically and economically. Among non-noble metal-based catalysts, Fe, being a ferromagnetic and inexpensive metal material, is the second most abundant metal in the earth's crust and can be considered a favorable choice for magnetic field-induced electrocatalysis. Furthermore, Fe in the presence of Ni was shown to exhibit synergism in OER performance; it is expected that the introduction of Fe on nickel support could influence the OER activity in the presence of the magnetic field.

1.1.10. Factors contributing to magnetic performance:

The two major contributions to the performance in the presence of magnetic field are:(*52*)

1.1.10.1. Magneto-current density (j_{MC}):

The extra current density observed by including a magnetic field in the presence of an electric field is the magneto-current density. The j_{MC} was evaluated using the relation:

$j_{MC} = j_{B\neq0} - j_{B=0}$, wherein $j_{B=0}$ and $j_{B\neq0}$ are the current densities observed in the absence and presence of B.

1.1.10.2. Percentage magneto-current (% MC):

The percentage of the ratio of magneto-current density to the initial current (in the absence of the magnetic field) is calculated as the percentage of magneto-current. % MC is calculated via the relation:

$\% \ MC = (j_{MC} / j_{B=0})*100$

Other factors are the same as considered for electrocatalytic water splitting, including overpotentials (η) at different current densities, maximum current densities, stability for long durations, multistep (potential or current) analyses, and various electrochemical controls in absence or presence of magnetic field.

1.1.11. Conclusions:

This chapter summarizes various strategies adopted to produce green hydrogen by electrochemical water splitting. Though acid and alkaline based electrolyzers are commercially available, the alkaline electrolyzers dominate the market due to their durability and low cost. This chapter also discusses about the challenges involved in selecting the non-noble based catalysts for water splitting, specifically for oxygen evolution reaction (OER). The critical parameters (overpotential, current density, Tafel slope, stability, ECSA, etc.) necessary for attaining improved performance are discussed in detail.

1.1.12. References:

1. K. T. Møller, T. R. Jensen, E. Akiba, H.-w. Li, Hydrogen - A sustainable energy carrier. *Progress in Natural Science: Materials International* **27**, 34-40 (2017).
2. E. Taibi *et al.*, Hydrogen from renewable power: Technology outlook for the energy transition. *International Renewable Energy Agency*, (2018).
3. M. Wappler *et al.*, Building the green hydrogen market – Current state and outlook on green hydrogen demand and electrolyzer manufacturing. *International Journal of Hydrogen Energy* **47**, 33551-33570 (2022).
4. S. Shiva Kumar, V. Himabindu, Hydrogen production by PEM water electrolysis – A review. *Materials Science for Energy Technologies* **2**, 442-454 (2019).
5. A. Dutta, Process Considerations for the Production of Hydrogen via Steam Reforming of Oxygenated Gases from Biomass Pyrolysis and Other Conversion Processes. *Advanced Sustainable Systems*, (2023).
6. D. I. Rinawati, A. R. Keeley, S. Takeda, S. Managi, Life-cycle assessment of hydrogen utilization in power generation: A systematic review of technological and methodological choices. *Frontiers in Sustainability* **3**, (2022).
7. Y. Demirel, Technoeconomics and Sustainability of Renewable Methanol and Ammonia Productions Using Wind Power-based Hydrogen. *Journal of Advanced Chemical Engineering* **5**, (2015).
8. B. You, Y. Sun, Innovative Strategies for Electrocatalytic Water Splitting. *Acc Chem Res* **51**, 1571-1580 (2018).
9. J. Yin *et al.*, Optimized Metal Chalcogenides for Boosting Water Splitting. *Adv Sci (Weinh)* **7**, 1903070 (2020).
10. A. Raveendran, M. Chandran, R. Dhanusuraman, A comprehensive review on the electrochemical parameters and recent material development of electrochemical water splitting electrocatalysts. *RSC Adv* **13**, 3843-3876 (2023).
11. X. Huang, Z. Zhang, J. Jiang, Fuel Cell Technology for Distributed Generation: An Overview. *IEEE Xplore*, (2006).
12. J. Wei *et al.*, Heterostructured Electrocatalysts for Hydrogen Evolution Reaction Under Alkaline Conditions. *Nanomicro Lett* **10**, 75 (2018).

13. C. Walter, P. W. Menezes, M. Driess, Perspective on intermetallics towards efficient electrocatalytic water-splitting. *Chem Sci* **12**, 8603-8631 (2021).
14. N. T. Suen *et al.*, Electrocatalysis for the oxygen evolution reaction: recent development and future perspectives. *Chem Soc Rev* **46**, 337-365 (2017).
15. S. Anantharaj *et al.*, Precision and correctness in the evaluation of electrocatalytic water splitting: revisiting activity parameters with a critical assessment. *Energy & Environmental Science* **11**, 744-771 (2018).
16. T. Shinagawa, A. T. Garcia-Esparza, K. Takanabe, Insight on Tafel slopes from a microkinetic analysis of aqueous electrocatalysis for energy conversion. *Nature Scientific Reports* **5**, (2015).
17. X. Lu, C. Zhao, Electrodeposition of hierarchically structured three-dimensional nickel-iron electrodes for efficient oxygen evolution at high current densities. *Nat Commun* **6**, 6616 (2015).
18. J. Kibsgaard *et al.*, Designing an improved transition metal phosphide catalyst for hydrogen evolution using experimental and theoretical trends. *Energy & Environmental Science* **8**, 3022-3029 (2015).
19. M. E. G. Lyons, M. P. Brandon, A comparative study of the oxygen evolution reaction on oxidised nickel, cobalt and iron electrodes in base. *Journal of Electroanalytical Chemistry* **641**, 119-130 (2010).
20. R. L. Doyle, M. E. Lyons, An electrochemical impedance study of the oxygen evolution reaction at hydrous iron oxide in base. *Phys Chem Chem Phys* **15**, 5224-5237 (2013).
21. J. Aguedo, L. Lorencova, M. Barath, P. Farkas, J. Tkac, Electrochemical Impedance Spectroscopy on 2D Nanomaterial MXene Modified Interfaces: Application as a Characterization and Transducing Tool. *Chemosensors* **8**, (2020).
22. S. Cherevko, Stability and dissolution of electrocatalysts: Building the bridge between model and “real world” systems. *Current Opinion in Electrochemistry* **8**, 118-125 (2018).
23. R. A. Marquez *et al.*, A Guide to Electrocatalyst Stability Using Lab-Scale Alkaline Water Electrolyzers. *ACS Energy Letters* **9**, 547-555 (2024).

24. D. Hochfilzer, I. Chorkendorff, J. Kibsgaard, Catalyst Stability Considerations for Electrochemical Energy Conversion with Non-Noble Metals: Do We Measure on What We Synthesized? *ACS Energy Lett* **8**, 1607-1612 (2023).

25. D. Voiry *et al.*, Best Practices for Reporting Electrocatalytic Performance of Nanomaterials. *ACS Nano* **12**, 9635-9638 (2018).

26. D. K. Singh, R. N. Jenjeti, S. Sampath, M. Eswaramoorthy, Two in one: N-doped tubular carbon nanostructure as an efficient metal-free dual electrocatalyst for hydrogen evolution and oxygen reduction reactions. *Journal of Materials Chemistry A* **5**, 6025-6031 (2017).

27. S. Anantharaj, S. Kundu, Do the Evaluation Parameters Reflect Intrinsic Activity of Electrocatalysts in Electrochemical Water Splitting? *ACS Energy Letters* **4**, 1260-1264 (2019).

28. M. Wang, L. Zhang, Y. He, H. Zhu, Recent advances in transition-metal-sulfide-based bifunctional electrocatalysts for overall water splitting. *Journal of Materials Chemistry A* **9**, 5320-5363 (2021).

29. K. C. Majhi, M. Yadav, Transition Metal-Based Chalcogenides as Electrocatalysts for Overall Water Splitting. *ACS Engineering Au* **3**, 278-284 (2023).

30. X. Xia, L. Wang, N. Sui, V. L. Colvin, W. W. Yu, Recent progress in transition metal selenide electrocatalysts for water splitting. *Nanoscale* **12**, 12249-12262 (2020).

31. A. Dutta, N. Pradhan, Developments of Metal Phosphides as Efficient OER Precatalysts. *J Phys Chem Lett* **8**, 144-152 (2017).

32. X. Peng *et al.*, Recent progress of transition metal nitrides for efficient electrocatalytic water splitting. *Sustainable Energy & Fuels* **3**, 366-381 (2019).

33. H. Ding, H. Liu, W. Chu, C. Wu, Y. Xie, Structural Transformation of Heterogeneous Materials for Electrocatalytic Oxygen Evolution Reaction. *Chem Rev* **121**, 13174-13212 (2021).

34. S. Jin, Are Metal Chalcogenides, Nitrides, and Phosphides Oxygen Evolution Catalysts or Bifunctional Catalysts? *ACS Energy Letters* **2**, 1937-1938 (2017).

35. B. R. Wygant, K. Kawashima, C. B. Mullins, Catalyst or Precatalyst? The Effect of Oxidation on Transition Metal Carbide, Pnictide, and Chalcogenide Oxygen Evolution Catalysts. *ACS Energy Letters* **3**, 2956-2966 (2018).
36. S. Anantharaj *et al.*, Recent Trends and Perspectives in Electrochemical Water Splitting with an Emphasis on Sulfide, Selenide, and Phosphide Catalysts of Fe, Co, and Ni: A Review. *ACS Catalysis* **6**, 8069-8097 (2016).
37. P. Wang, T. Jia, B. Wang, A critical review: 1D/2D nanostructured self-supported electrodes for electrochemical water splitting. *Journal of Power Sources* **474**, (2020).
38. M.-R. Gao *et al.*, Nitrogen-Doped Graphene Supported CoSe2 Nanobelt Composite Catalyst for Efficient Water Oxidation. *ACS Nano* **8**, 3970-3978 (2014).
39. N. Sato, *Electrochemistry at Metal and Semiconductor Electrodes*. E. S. B.V., Ed., (Japan, 1998).
40. S. M. Sze, K. K. Ng, *Physics Of Semiconductor Devices*. (John Wiley & Sons, Inc. , United States of America, 2007).
41. M. S. Burke, M. G. Kast, L. Trotochaud, A. M. Smith, S. W. Boettcher, Cobalt-iron (oxy)hydroxide oxygen evolution electrocatalysts: the role of structure and composition on activity, stability, and mechanism. *J Am Chem Soc* **137**, 3638-3648 (2015).
42. C. Hunt *et al.*, Quantification of the Effect of an External Magnetic Field on Water Oxidation with Cobalt Oxide Anodes. *J Am Chem Soc* **144**, 733-739 (2022).
43. C. Wei, Z. J. Xu, The possible implications of magnetic field effect on understanding the reactant of water splitting. *Chinese Journal of Catalysis* **43**, 148-157 (2022).
44. H. Liu *et al.*, Magnetic-Field-Induced Strain Enhances Electrocatalysis of FeCo Alloys on Anode Catalysts for Water Splitting. *Metals* **12**, (2022).
45. L. T. Tufa, K. J. Jeong, V. T. Tran, J. Lee, Magnetic-Field-Induced Electrochemical Performance of a Porous Magnetoplasmonic Ag@Fe(3)O(4) Nanoassembly. *ACS Appl Mater Interfaces* **12**, 6598-6606 (2020).
46. X. Qin *et al.*, Magnetic Field Enhancing OER Electrocatalysis of NiFe Layered Double Hydroxide. *Catalysis Letters* **153**, 673-681 (2022).

47. Y. Li, L. Zhang, J. Peng, W. Zhang, K. Peng, Magnetic field enhancing electrocatalysis of Co3O4/NF for oxygen evolution reaction. *Journal of Power Sources* **433**, (2019).
48. Y. Zhang *et al.*, Magnetic field assisted electrocatalytic oxygen evolution reaction of nickel-based materials. *Journal of Materials Chemistry A* **10**, 1760-1767 (2022).
49. L. Zhang, J. Peng, Y. Yuan, K. Peng, Magnetic enhancement of oxygen evolution reaction performance of NiCo-spinel oxides. *Nanotechnology* **32**, (2021).
50. H. Li, S. Liu, Y. Liu, Magnetic Enhancement of Oxygen Evolution in CoNi@C Nanosheets. *ACS Sustainable Chemistry & Engineering* **9**, 12376-12384 (2021).
51. J. Yan *et al.*, Direct Magnetic Reinforcement of Electrocatalytic ORR/OER with Electromagnetic Induction of Magnetic Catalysts. *Adv Mater* **33**, e2007525 (2021).
52. F. A. Garcés-Pineda, M. Blasco-Ahicart, D. Nieto-Castro, N. López, J. R. Galán-Mascarós, Direct magnetic enhancement of electrocatalytic water oxidation in alkaline media. *Nature Energy* **4**, 519-525 (2019).
53. A. Angulo, P. van der Linde, H. Gardeniers, M. Modestino, D. Fernández Rivas, Influence of Bubbles on the Energy Conversion Efficiency of Electrochemical Reactors. *Joule* **4**, 555-579 (2020).
54. D. Baczyzmalski *et al.*, On the Electrolyte Convection around a Hydrogen Bubble Evolving at a Microelectrode under the Influence of a Magnetic Field. *Journal of The Electrochemical Society* **163**, E248-E257 (2016).
55. Y. Zhang *et al.*, Recent Advances in Magnetic Field-Enhanced Electrocatalysis. *ACS Applied Energy Materials* **3**, 10303-10316 (2020).
56. Z. Xiong *et al.*, Field-Free Improvement of Oxygen Evolution Reaction in Magnetic Two-Dimensional Heterostructures. *Nano Lett* **21**, 10486-10493 (2021).

Chapter-1.2 Heterostructures from hetero-mixtures: metal phosphides for oxygen evolution reaction (OER)

Summary:

This chapter deals with the generation of metal phosphide heterostructures and interfaces by a very simple route of physical mixing of FeP and CoP. The catalyst shows low overpotential of 220 mV with very high current density of 1.37 A cm^{-2} *and mass activity of 18987 A g*$^{-1}$ *at an overpotential of 500 mV for oxygen evolution reaction in alkaline conditions. The catalyst also attains a great stability for 200 hours to achieve a current density of 200 mA cm*$^{-2}$*. The structural analysis of the catalyst shows that the physical mixing of individual FeP and CoP leads to heterostructure formation with effective charge transfer between the metal sites. During the reaction, the surface of the metal phosphide converges to metal oxyhydroxide with concentration of phosphorus decreasing with time. Taking in account this metal phosphide heterointerface with the surface covered with oxyhydroxides, theoretical analysis reveals favourable sorption kinetics of intermediates with lowest free energy of the reaction and zero kinetic barrier towards potential determining steps of OER.*

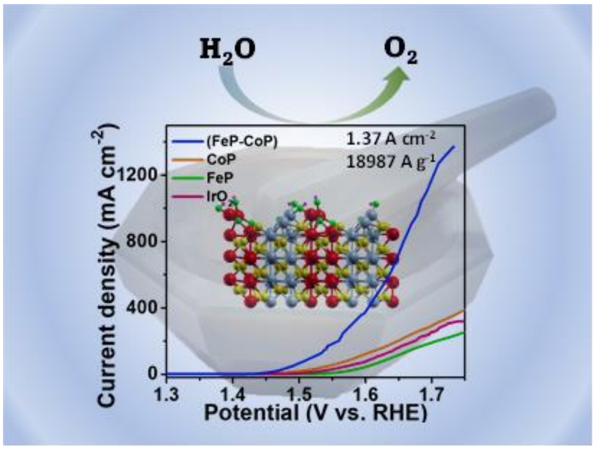

(A paper based on this work has appeared in *J. Mater. Chem. A*, 2022, **10**, 22354–22362)

1.2.1. Introduction:

Evolving oxygen at a satisfactory rate from the electrochemical route of water splitting increases the overall efficiency of the reaction, thereby diminishing the primary barrier to hydrogen generation. Intensifying this bottleneck process with sluggish kinetics is very challenging, with a need for very efficient electrocatalysts to achieve low overpotentials, high rates, and good stability.(*1*) Ir and Ru-based catalysts were taken as the state-of-the-art catalysts for OER. Their scarcity, exclusivity, and low stability in wide pH range make them inappropriate to be used.(*2*, *3*) Transition metal-based catalysts are studied as fair substitutes to these noble metal-based catalysts. Various catalysts containing metal oxides and their hybrids,(*4*, *5*) selenides,(*6*) carbides,(*7*, *8*) sulphides,(*9*) nitrides,(*10*) borides,(*11*-*13*) and phosphides(*14*, *15*) as the active species were considered in this direction. Out of these metal phosphides catalysts appear as the best in terms of stability, conductivity, low toxicity, low cost and high abundance.(*16*) Prominently, phosphorus activates the adjacent metal center in metal phosphides by influencing the electronic environment of intermediates adsorbed on the metal center.(*17, 18*) Creation of defects, doping strategies, and formation of bimetallic interfaces are taken as effective approaches to achieve high OER performance with phosphides.(*19*) Nevertheless, major challenge still lies in attaining low overpotentials with high current densities and sustained stability. Attaining heterostructures and heterointerfaces is a well grown field and attracted much attraction in recent years.(*20*-*25*) Extensive changes in the physical and chemical properties can be observed with various van der Waals, and coulombic interactions, inter-particle defects, strain and disorders in the lattice during electrochemical applications.(*26*-*29*) All these transformations originate from the modulation of the electronic structure which further modifies the electrochemical energetics of sorption of reaction intermediates at the active sites. The adsorption kinetics and thus the reaction rate of different reaction intermediates can be hugely tuned by utilising the role of heterointerfaces during a multistep OER process. Although heterostructures show enhanced catalytic activities, the tedious method of synthesis typically involves epitaxial growth,(*30*) plasma treatment,(*31*) solvothermal,(*32*, *33*) and complex ALD processes.(*34*) On the other hand, the performances of physically mixed individual components are not on par with their in-situ generated heterostructures and need further improvement.(*33*, *35*-*38*)

1.2.2. Scope of present investigation:

In this work, we establish heterostructure by simple physical mixing of two separate metal phosphide (FeP and CoP) acting as a remarkable OER catalyst as compared to individual metal phosphide constituents as well as their in-situ synthesized heterostructures.(*39*-*46*) To achieve a current density of 10 mA cm^{-2} for OER, the physically mixed metal phosphide heterostructure needed a low overpotential of 220 mV and attains high current density of 1.37 A cm^{-2} at overpotential less than 500 mV. A remarkably high mass activity of 18987 A g^{-1} and high stability for 200 h (at a current density of 200 mA cm^{-2}) were observed for mixed FeP-CoP catalyst without using any additive under alkaline reaction conditions (1.0 M KOH). It is revealed through first-principles calculations that the energy barrier of the potential determining step (final step in the OER, i.e., desorption of *OOH to evolve O_2) reduces significantly for adsorption of reaction intermediates at the Co-site of the oxygenated FeP–CoP interface. Also, favourable adsorption energies for all the reaction intermediates were realized on the oxygenated FeP-CoP interface.

1.2.3. Materials and methods:

1.2.3.1. Materials required:

Cobalt chloride hexahydrate ($CoCl_2.6H_2O$) and anhydrous ferric chloride ($FeCl_3$) were purchased from S D Fine Chemicals, $NaBH_4$, NaH_2PO_2 and 5 wt % Nafion® perflourinated resin solution purchased from Sigma-Aldrich, HCl (37%, AR grade) and KOH from Merck Chemicals. All chemicals were used as received without any further purification. Milli Q water (18.2 S cm) is used for all the synthesis and electrochemical analyses. Toray carbon paper (TGP-H-60) used for electrochemical studies was purchased from Alfa Aesar.

1.2.3.2. Synthesis of metal phosphides:

FeP and CoP were individually synthesized by a two-step procedure **(*Figure 1.2.1.a*)**. Firstly, 30 mL of 0.1 M metal chloride solution was rapidly added to freshly prepared 150 mL of 1.0 M aqueous $NaBH_4$ solution under vigorous stirring.(*47*, *48*) The solution was stirred for another 30 minutes. The product obtained was washed three times with water and ethanol and then dried at 60 °C in oven overnight. In the second step, nanostructured metal phosphides were synthesized according to previously reported procedure.(*49*) In a typical synthesis, 200 mg of as-synthesized metal hydroxide was ground with 1 g of NaH_2PO_2 in a mortar-pestle and heated at 300 ℃ for 1 h in Ar atmosphere (heating and cooling rates were 3 ℃ per minute). Then, the solid product obtained was dispersed in 120 ml 0.1 M HCl solution and stirred for 3 h to remove unreacted metal particles formed during the synthesis of metal hydroxide. The remaining solid product was washed several times with water and ethanol and dried overnight at 60 ℃ in oven. For the synthesis of bimetallic cobalt-iron hydroxides, CoFeP, individual solutions of cobalt and iron chloride were mixed according to their desired compositions (20: 80 wt. % of Co: Fe) and same procedure was followed. Also, the physically ground mixtures [FeP-CoP-(x:y), x and y being the percentage weight ratios of amount of FeP and CoP] were prepared by mixing and grinding required weight ratios of individually synthesized metal phosphides **(*Figure 1.2.1.b*)**. The mixture of FeP and CoP in ration of 80:20 is designated as FeP-CoP in further studies.

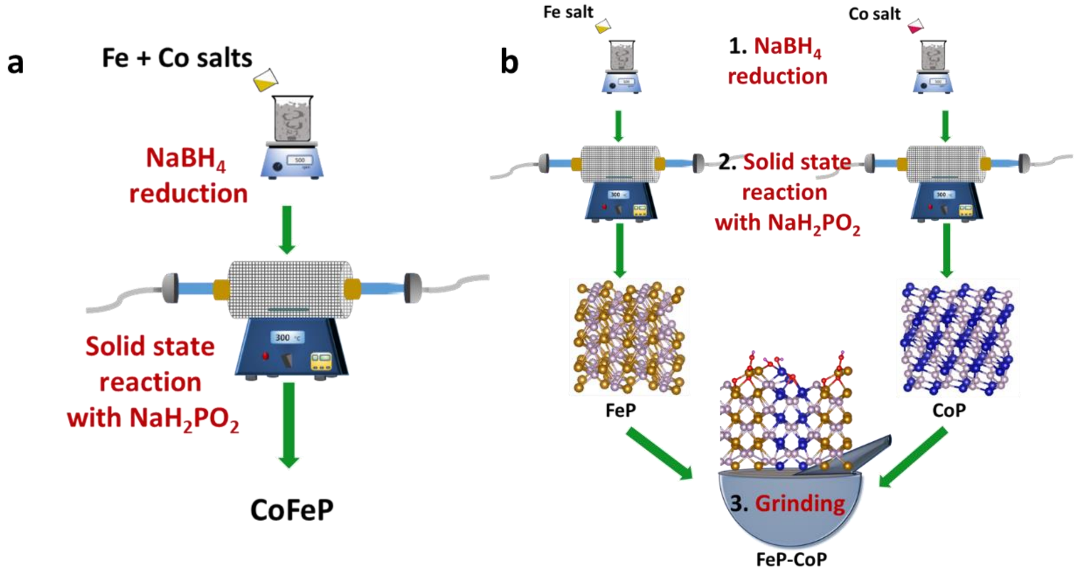

Figure 1.2. 1. (a) Synthesis of metal phosphides through borohydride reduction followed by phosphidation, and (b) physical mixing of in-situ synthesized metal phosphides.

1.2.3.3. Characterizations and electrochemical studies:

The instrumentation techniques (PXRD, FESEM, TEM, Raman, XPS, etc) used to characterize the samples are described in detail in the appendix at the end of this thesis. Electrochemical measurements were carried out using electrochemical workstation (66 0C, USA) obtained from CH instruments for evaluating the electrochemical activities of catalysts towards oxygen evolution reaction (OER), hydrogen evolution reaction (HER), overall water splitting and other electrochemical analyses. The electro active material (2 mg) was dispersed in 0.5 mL Milli Q water. Also, 5 μL of 5 wt.% Nafion solution added to the resultant dispersion was ultrasonicated to obtain a homogeneous catalyst ink. Then, 2 μL of as obtained catalyst ink was drop-casted on a clean glassy carbon (GC) electrode having a diameter of 3 mm resulting in a catalyst loading of (0.112 ± 0.006) mg cm^{-2}. The coated GC electrode was dried in ambient conditions and used as working electrode in the electrochemical studies. Toray carbon paper (0.5*0.5 cm) was used for stability studies at high current densities and for full cell studies. Electrochemical measurements were carried out using a standard three-electrode cell with a high surface area graphite rod as a counter electrode, mercury-mercuric oxide (Hg/HgO) electrode as a reference electrode (calibrated prior measurement) in alkaline medium (1 M KOH) in an alkaline cell under external agitation of 1400 rpm. The polarization curves are reported with 100% iR compensation which arises due to ohmic resistance of the cell. All the measured potentials are reported with respect to reversible hydrogen electrode (RHE). The obtained current densities were normalized to the geometrical surface area of the GC electrode (0.07068 cm^2). The linear sweep voltammograms (LSVs) were recorded in 1 M KOH at 5 mV s^{-1} under Ar saturated aqueous electrolytes.

1.2.3.4. Purification of KOH:

Commercial grade KOH, which contains a trace amount of Fe impurities (~ 1ppm, can be analyzed by ICP-OES measurement), can be purified using the $Co(OH)_2$ absorption method reported in the literature.(*41*) In a typical procedure, 2 g of $Co(NO_3)_2$ was dissolved in 4 mL Milli Q water followed by the addition of 20 mL of 0.1 M KOH solution with stirring for 5 minutes. The $Co(OH)_2$ precipitate thus obtained was separated by centrifugation and washed with Milli Q water (5 times), and used for the purification of KOH. The as-prepared $Co(OH)_2$ was added to 50 mL of 1M KOH solution and mechanically agitated for 10 minutes in order to remove Fe impurities. Then, the brown-colored suspension of $Co(OH)_2$ particles after iron adsorption was removed by centrifugation for 1 h, and the purified KOH was separated out. The process was repeated three times with the same purified KOH solution and finally used as a Fe-free KOH electrolyte for electrochemical measurements. Also, the absence of Fe in 1 M KOH solution was confirmed by ICP-AES analysis.

1.2.4. Results and discussion:

1.2.4.1. Characterization of FeP-CoP catalyst:

Powder X-ray diffraction patterns were taken to confirm the phase purity of individual phosphides. Various broad peaks were observed in PXRD pattern of FeP-CoP mixture (***Figure 1.2.2.a***) which can be individually assigned to FeP and CoP nanostructures with a crystallite size of about 17 nm calculated from the Scherrer relation provided in the appendix of this thesis. The peak intensity matches with corresponding peaks of FeP (or CoP) taken the mixture in different ratios. Although, the PXRD study of in-situ synthesized CoFeP material (***Figure 1.2.2.b***) shows major peaks for CoP nanostructure when amount of Co equals that of Fe in CoFeP, the peaks corresponding to the composition with 20% Co species can mainly be assigned to FeP nanostructure. This also highlights the existence of FeP and CoP as individual phosphides.

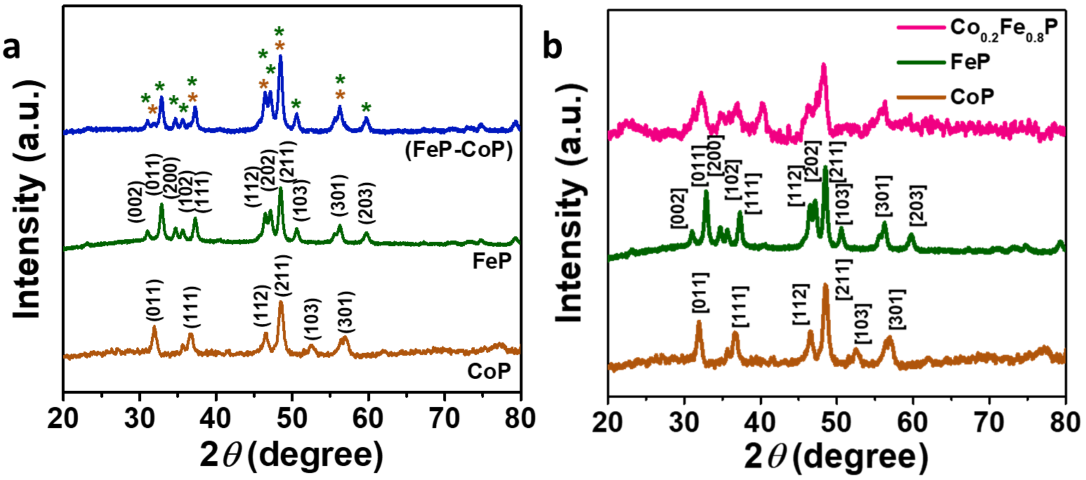

Figure 1.2. 2. Powder X-ray diffraction (PXRD) patterns of (a) CoP, FeP, and FeP-CoP mixture, and (b) in-situ synthesized CoFeP ($Co_{0.2}Fe_{0.8}P$) catalysts.

The FESEM image of the FeP-CoP catalyst shows nanoporous morphology (***Figure 1.2.3.***). Similar interconnected nanoporous morphology was observed for in-situ synthesized CoFeP and individual FeP and CoP nanostructures (***Figure 1.2.3.***).

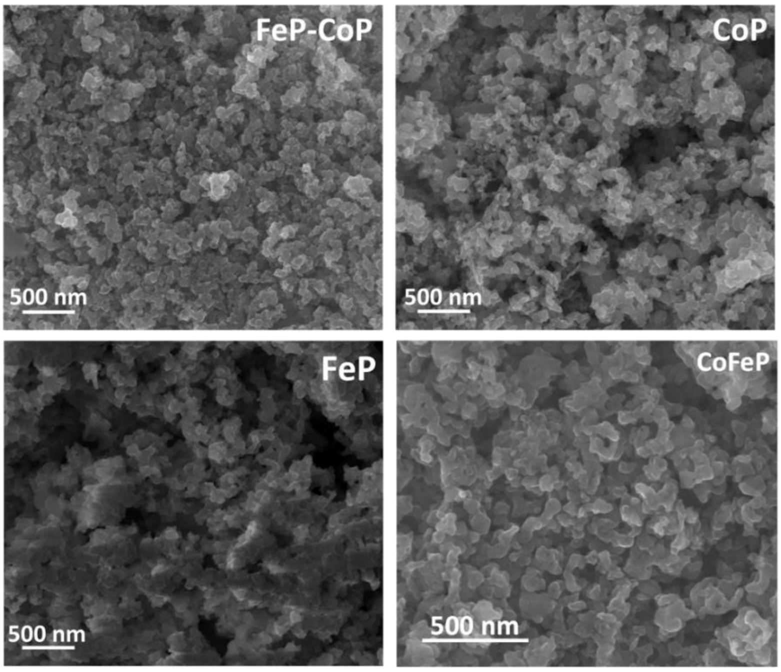

Figure 1.2. 3. Field emission scanning electron microscopy (FESEM) images of CoP, FeP-CoP, FeP, and CoFeP catalysts.

The TEM image confirms the porous morphology for FeP-CoP, FeP, CoP, and CoFeP (***Figure 1.2.4.***).

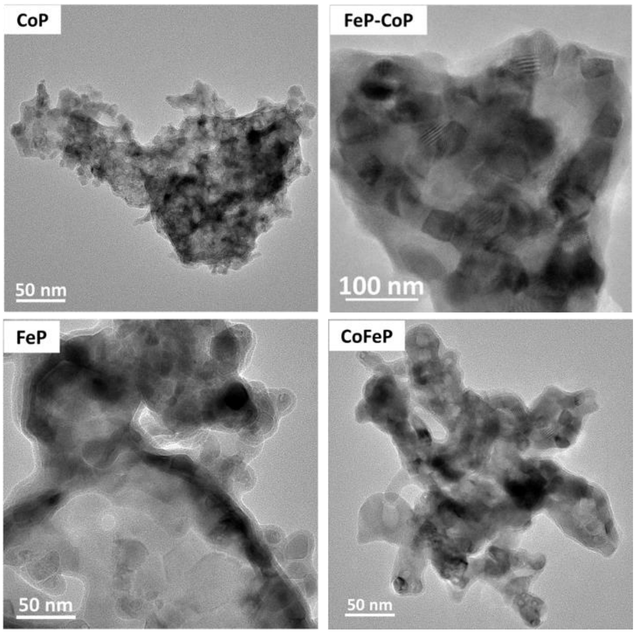

Figure 1.2. 4. Transmission electron microscopy (TEM) images of CoP, FeP-CoP, FeP, and CoFeP catalysts.

Further, in the HRTEM (***Figure 1.2.5.***) of CoFeP and FeP-CoP, lattice fringes for both CoP and FeP domains can be seen.

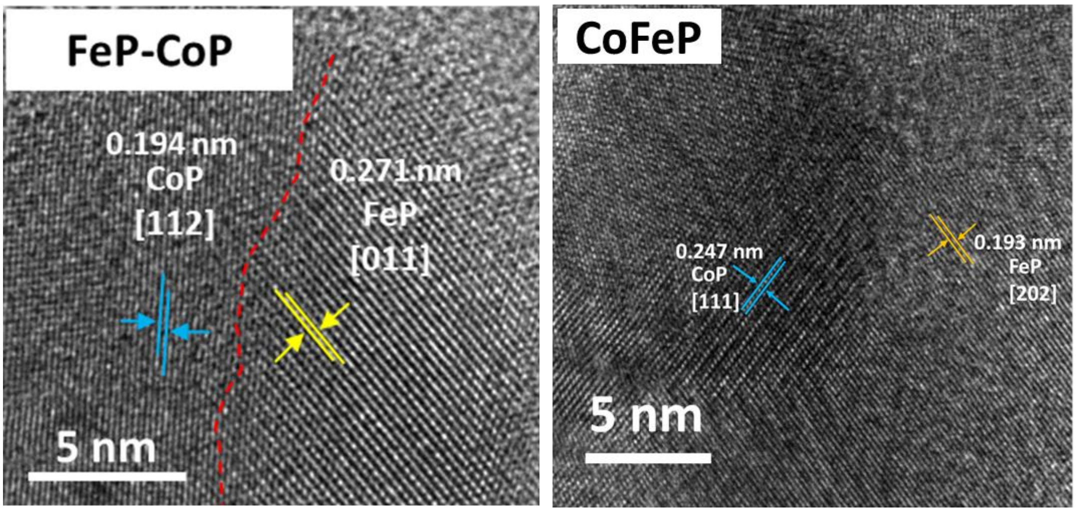

Figure 1.2. 5. High-resolution transmission electron microscopy (HRTEM) images of FeP-CoP, and CoFeP catalysts.

The line mapping (***Figure 1.2.6.***) in HAADF-STEM mode also confirmed the uniform dispersion of Co.

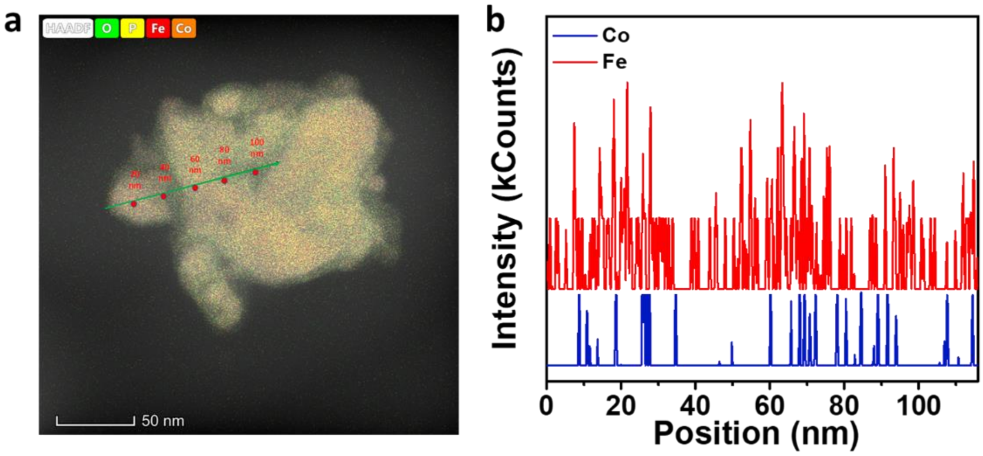

Figure 1.2. 6. (a, b) Line mapping profile of Fe, and Co in FeP-CoP catalyst.

Clear heterointerfaces were observed between the crystalline domains of CoP and FeP in FeP-CoP mixture (***Figure 1.2.7.***).

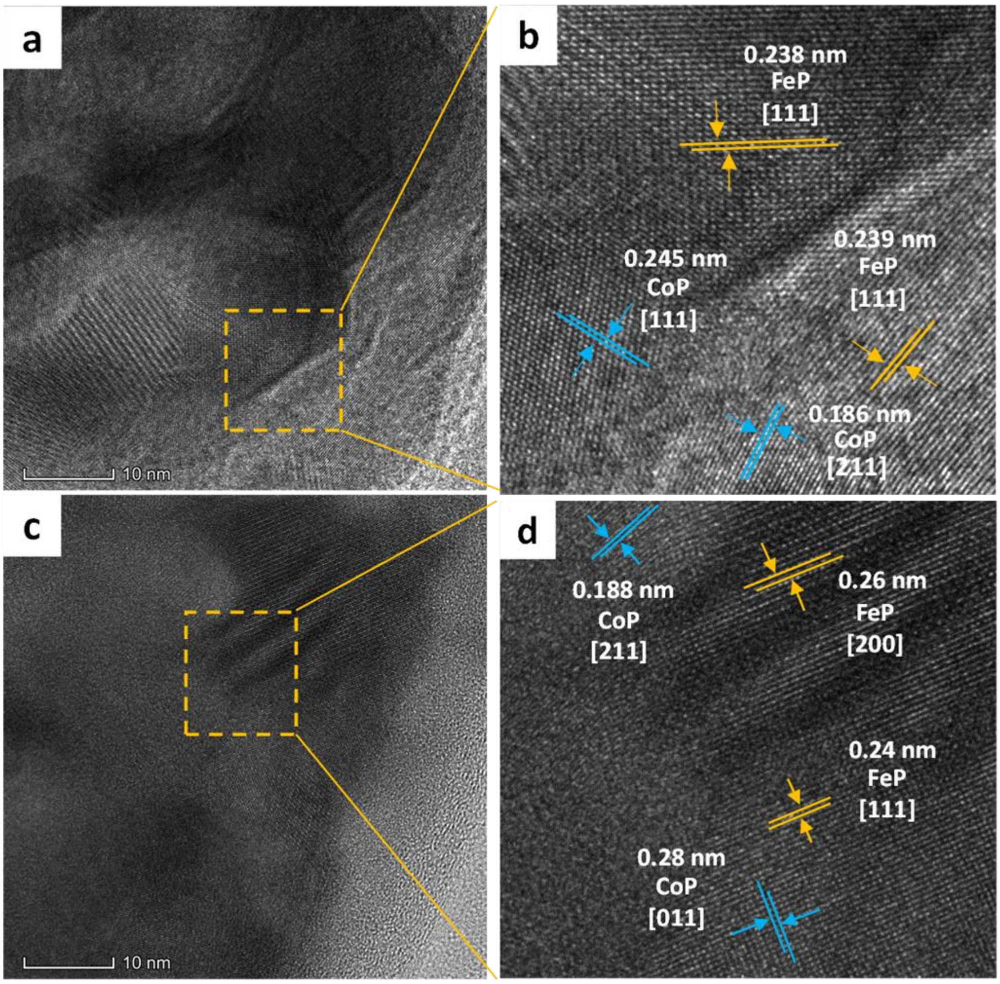

Figure 1.2. 7. High-resolution transmission electron microscopy (HRTEM) images of FeP-CoP catalyst in different regions.

The observed SAED patterns for FeP, CoP, CoFeP, and FeP-CoP show polycrystalline nature of all the materials **(*Figure 1.2.8.*)**.

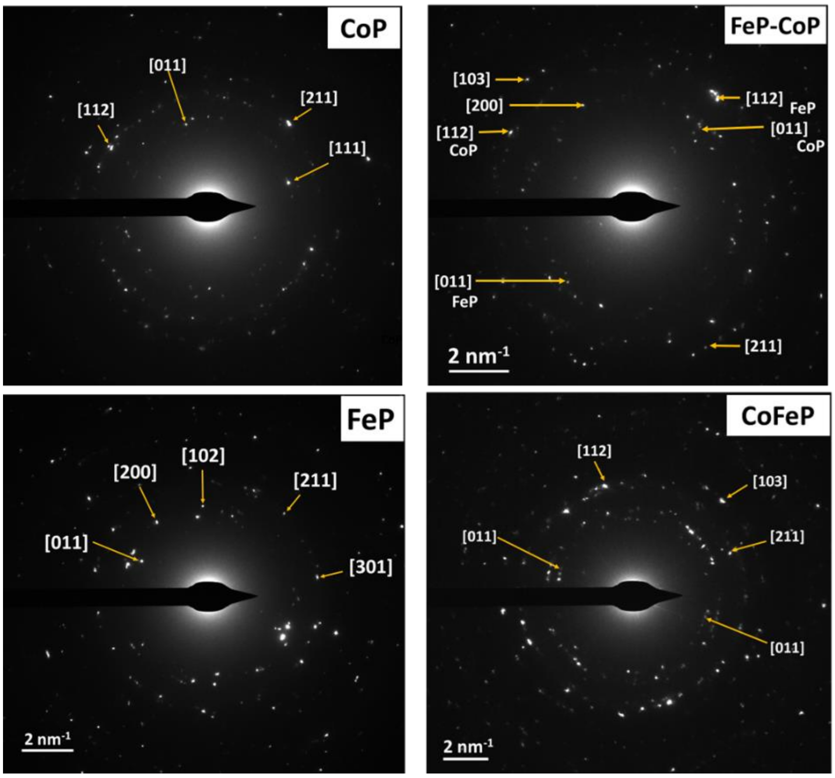

Figure 1.2. 8. Selected area electron diffraction (SAED) patterns of CoP, FeP-CoP, FeP, and CoFeP catalysts.

Good dispersion of Co and Fe in FeP-CoP can be seen from HAADF-STEM images (***Figure 1.2.9.***) with relatively low intensity of Co as expected.

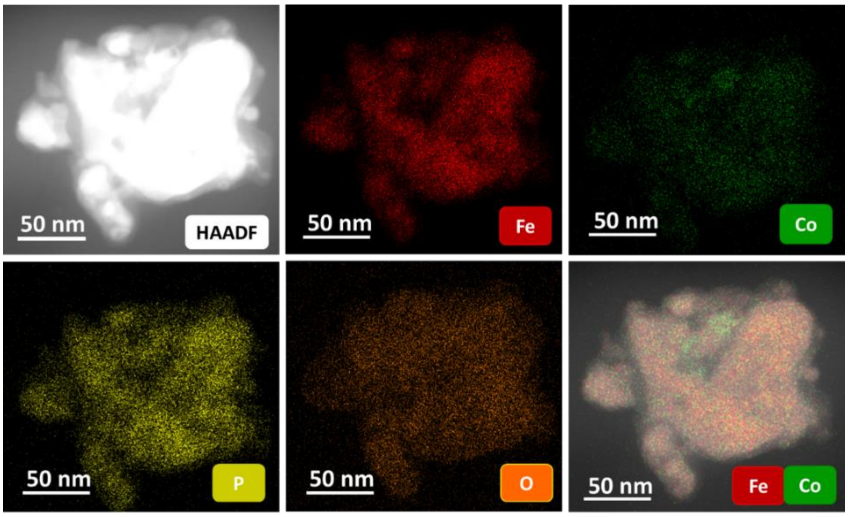

Figure 1.2. 9. High-angle annular dark field (HAADF) images in scanning transmission electron microscopy (STEM) mode of FeP-CoP catalyst.

The EDS elemental mapping further confirmed the uniform distribution of Fe, Co, and P in FeP-CoP catalyst **(*Figure 1.2.10.*)**.

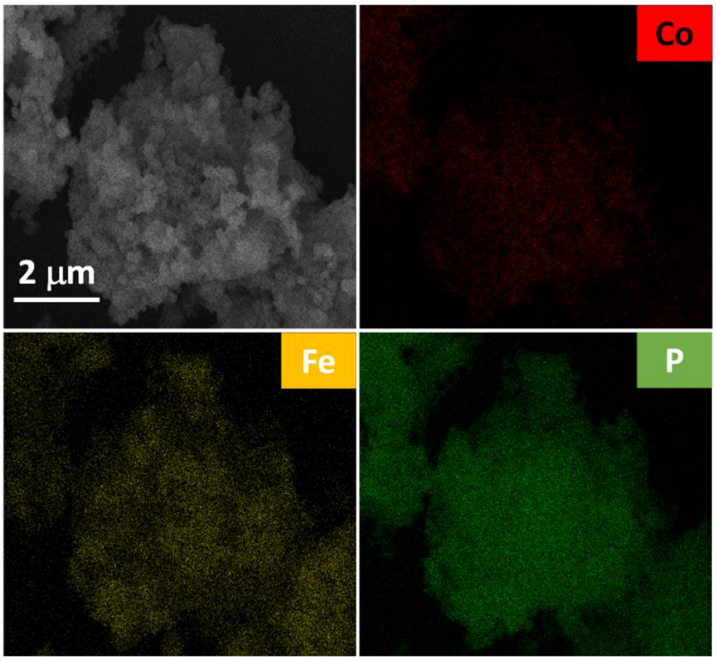

Figure 1.2. 10. Energy dispersive X-ray spectroscopy (EDS) analysis of FeP-CoP catalyst.

The chemical composition and respective metal weight ratios were confirmed by ICP-OES analyses with 22% CoP in FeP-CoP.

The chemical nature of different elements in all the FeP, CoP, CoFeP, and FeP-CoP catalysts were characterized by XPS analyses. The high-resolution Co 2p spectra of FeP-CoP shows a positive shift **(*Figure 1.2.11.a*)** for peak corresponding to Co-P bond (778.67 eV for Co2$p_{3/2}$ and 793.65 eV for Co 2$p_{1/2}$) as compared to that in CoP (778.37 eV for Co 2$p_{3/2}$ and 793.26 eV for Co 2$p_{1/2}$).(*35*, *50*) Conversely, the binding energy for peak related to Fe-P bond in the high-resolution Fe 2p spectra of FeP-CoP catalyst shows a negative shift **(*Figure 1.2.11.b*)** (707.01 eV for Fe 2$p_{3/2}$ and 719.81 eV for Fe 2$p_{1/2}$) as compared to that in FeP (707.48 eV for Fe 2$p_{3/2}$ and 720.27 eV for Fe 2$p_{1/2}$).(*42*, *51*)

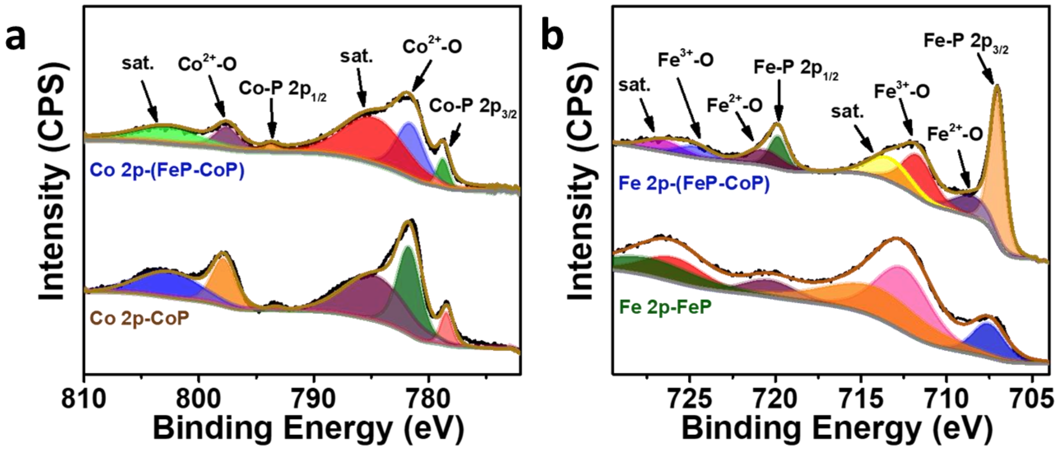

Figure 1.2. 11. X-ray photoelectron spectroscopy (XPS) (a) Co 2p spectra of CoP and FeP-CoP, and (b) Fe 2p spectra of FeP and FeP-CoP catalyst.

This shift in binding energies **(*Table 1.2.1.*)** demonstrates that there is charge transfer from Co to Fe sites in FeP-CoP catalyst. The other peaks at 781.51 eV (Co $2p_{3/2}$) and 797.51 eV (Co $2p_{1/2}$) correspond to Co^{2+}, while the peaks at 708.5 eV (Fe $2p_{3/2}$) and 720.6 eV (Fe $2p_{1/2}$) correspond to Fe^{2+} and Fe^{3+} species arising from surface oxidation and H_2O adsorption at metal sites. Also, satellite peaks at 713.36 eV (Fe $2p_{3/2}$) and 726.6 eV (Fe $2p_{1/2}$) were observed.(*52*) After the mixing of FeP and CoP, extra peaks corresponding to Fe^{2+} can be seen by comparing with the FeP sample, further validating the charge transfer from Co to Fe sites.

Table 1.2. 1. Binding energies of peaks corresponding to metal-phosphorus (M-P) bond observed from XPS analysis.

Catalyst	Binding Energies (eV)			
	Co		Fe	
	$2p_{3/2}$	$2p_{1/2}$	$2p_{3/2}$	$2p_{1/2}$
CoP	778.37	793.26	-	-
FeP	-	-	707.48	720.27
FeP-CoP	778.67	793.65	707.01	719.81

Peaks at 129.25 eV (P $2p_{3/2}$) and 130.1 eV (P $2p_{1/2}$) associated with M–P bond formation can be seen in the high-resolution spectra of P 2p **(*Figure 1.2.12.a*)**. (*53*) Similarly, peaks at 531.2 eV and 532.5 eV corresponding to the adsorption of OH^- ions and water at the metal site and P sites, respectively were observed in the high-resolution spectra of O 1s **(*Figure 1.2.12.b*)**.(*54*)

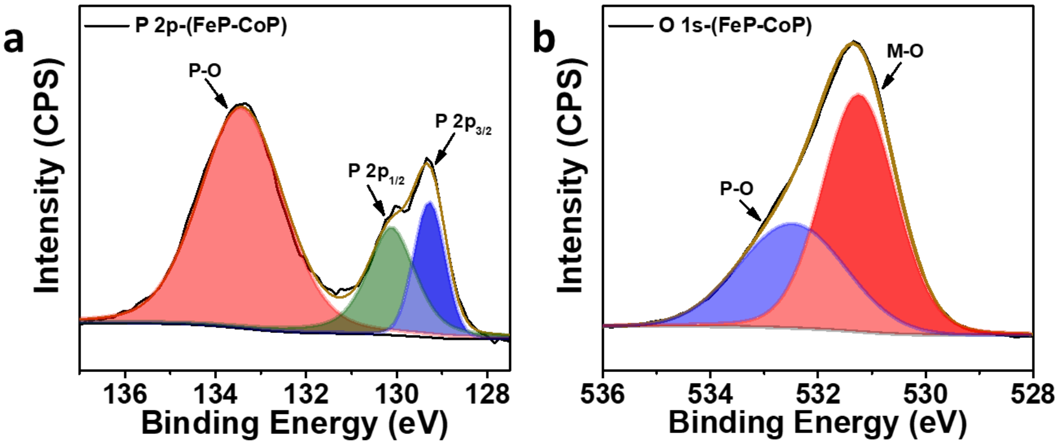

Figure 1.2. 12. X-ray photoelectron spectroscopy (XPS) (a) P 2p spectra and (b) O 1s spectra of FeP-CoP catalyst.

Similar peaks with slight shift in binding energies were observed in XPS analysis of in-situ synthesized CoFeP catalyst **(*Figure 1.2.13.*)**.

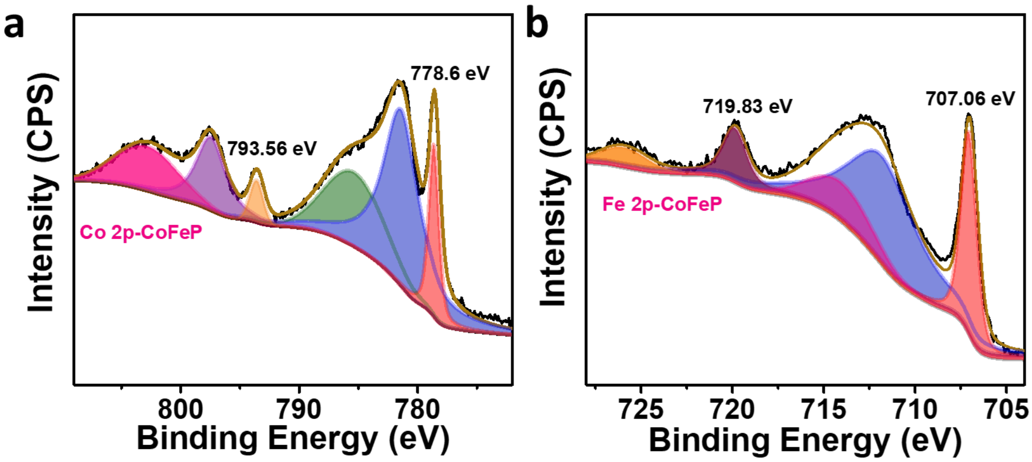

Figure 1.2. 13. X-ray photoelectron spectroscopy (XPS) (a) Co 2p spectra, and (b) Fe 2p spectra of CoFeP catalyst.

Over 90 Raman spectra were collected by mapping the FeP–CoP sample. A sum of peaks obtained from the individual spectra of CoP, FeP, and oxides of Co and Fe (***Figure 1.2.14.***) were seen for the spectra recorded at most of the spots (90%).(*55-57*)

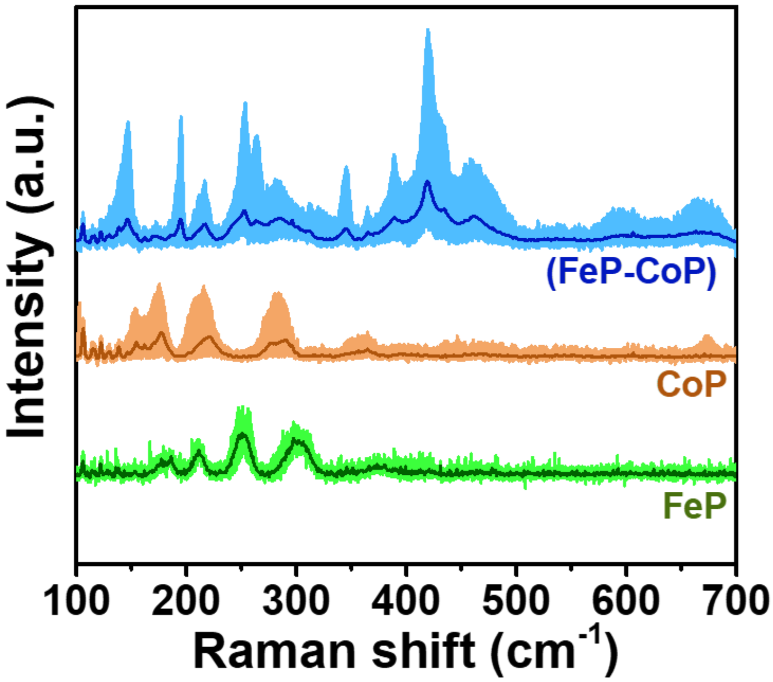

Figure 1.2. 14. Raman spectra of FeP, CoP, and FeP-CoP catalysts. The shaded regions show the data acquired over 90 points in the samples while dark line show the average data.

Possible electronic exchange, or interactions at the interfaces and new bond formation can be interpreted from a couple of new peaks observed around 194 cm^{-1} and 263 cm^{-1}. Also, a peak around 145 cm^{-1}, shifted by 8 cm^{-1} from that of CoP, indicates an induced strain in the B_{1g} vibration mode (***Table 1.2.2.***).

Table 1.2. 2. Observed peak positions in Raman spectra.

CoP	FeP	FeP-CoP
154	176	144-147
161	186	193-196
174-178	209-212	210
186-188	213-217	216
209	247-255	242
219	275-280	251-254
276	297	263-264
278	308	283
289	373	311
348	389-391	343-347
364	418	364-365
462-471	440-444	388-389
504-511	592-595	416-419
605-606	-	434
663-675	-	458-461
-	-	512
-	-	594
-	-	662-667

Also, two weak, broad peaks around 595 cm^{-1} and 665cm^{-1} are very similar to those observed in in-situ prepared CoFeP **(*Figure 1.2.15.*)**, indicating possible interactions between the hetero domains of the FeP–CoP mixture. Although, the Raman spectra of in-situ synthesized CoFeP shows very different peaks in comparison to other catalysts studied.

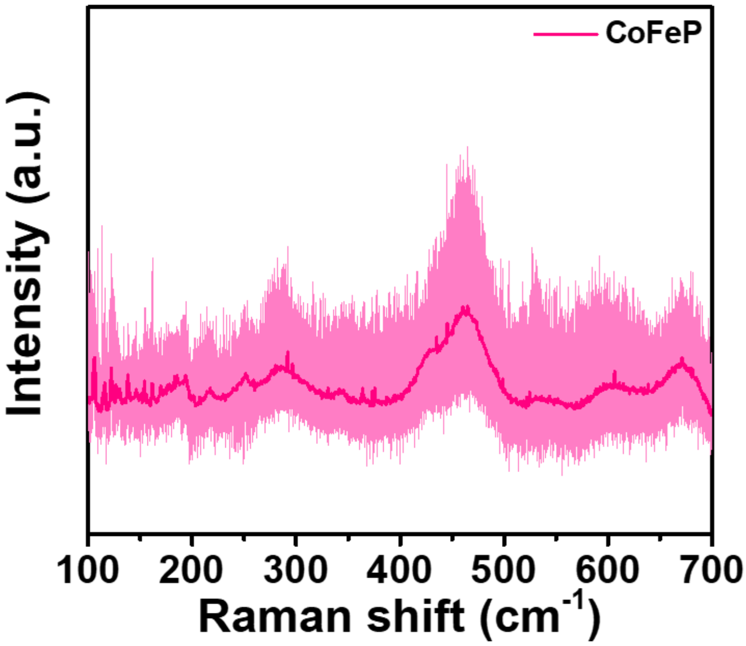

Figure 1.2. 15. Raman spectra of CoFeP catalyst. The shaded regions show the data acquired over 90 points in the samples while dark line show the average data.

1.2.4.2. Electrochemical Measurements:

The OER activities of monometallic phosphides, and commercial IrO_2 catalyst were compared with physically ground mixtures of FeP–CoP-(x : y) in various compositions (***Figure 1.2.16.***). The LSV study indicate superior performance for the FeP–CoP mixture with an 80 : 20 weight ratio (abbreviated as FeP–CoP) over other catalysts (***Figure 1.2.16., and Table 1.2.3.***). *(15, 58-80)* A low overpotential of 220 mV is required to attain a current density of 10 mA cm^{-2} for the FeP–CoP catalyst. It is clear from ***Figure 1.2.16.a*** that the addition of CoP (20 wt%) to FeP significantly reduces the overpotential of FeP from 325 mV to 220 mV, i.e. nearly 100 mV. FeP–CoP (1.45 mV) shows 63 mV lower overpotential ***(Figure 1.2.16.b)*** in comparison to IrO_2 (1.513 V) to achieve a current density of 10 mA cm^{-2}, while the differences are 97 mV and 118 mV for higher current densities of 100 mA cm^{-2} and 200 mA cm^{-2} respectively.

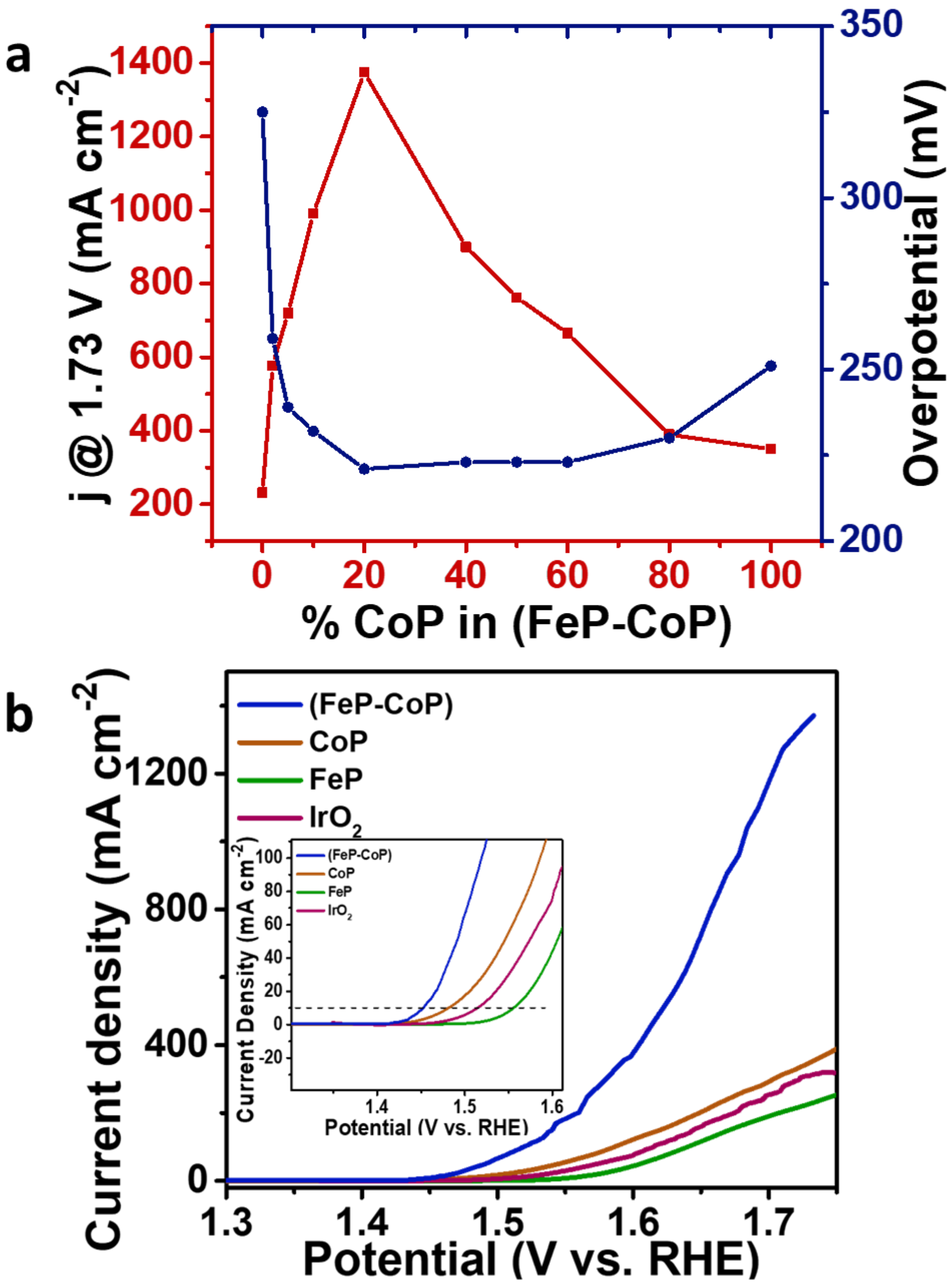

Figure 1.2. 16. (a) Histogram showing the electrochemical performance (overpotential (η_{10}) and maximum current density (j_{max})) of different compositions of FeP-CoP catalysts, and (b) polarized linear sweep voltammogram (LSV) of different catalysts towards oxygen evolution reaction (OER) in 1.0 M KOH. Inset shows the region of low current densities.

Table 1.2. 3. OER performance of reported metal phosphides. (The loading of the electrocatalysts studied in this work varies as 0.112 ± 0.006 mg cm^{-2})

Catalyst [support]	Loading (mg cm^{-2})	Overpotential (mV) at (j)	Stability (h) at (j)	j (mA cm^{-2}) @ 500 mV	Tafel slope (mV dec^{-1})	Ref.
FeP-CoP [GCE]	0.112	220 (10)	200 (200)	1375	39.4	This work
CoP [GCE]	0.112	250 (10)	20 (200)	354	55.1	This work
FeP [GCE]	0.112	325 (10)	40 (200)	227	49.7	This work
IrO_2 [GCE]	0.112	283 (10)	35 (200)	320	62.6	This work
Co_2P@NPPC[a] [GCE]	0.35	316 (10)	10 (10)	40	98.0	15
CoFeBiP [NF]	0.31	273 (10)	25 (10)	90	77.3	58
CoP@FeNiP [NF]	8.0	283 (100)	110 (10)	-	31.8	59
Ni_2P@NSG[b] [NF]	5.0	240 (10)	60 (10)	-	47.0	60
CoFeP NS@Fe-CoP NW[c] [NF]	-	250 (30)	12 (34)	250	107.0	61
FeP_2-NiP_2@PC[d] [GCE]	1.0	248 (10)	60 (40)	-	54.0	62
N-CoO@CoP [NF]	-	332 (100)	24 (100)	-	81.5	63
$NiSe_2$-Ni_2P [NF]	-	220 (50)	15 (60)	-		64
$Co(OH)_2$/Ag/ FeP [Ti foil]	-	236 (10)	50 (50, 100)	225	56	65
NiCoFeP/C [CP]	-	270 (10)	10 (10)	-	65	66

Table 1.2. 3. continued.

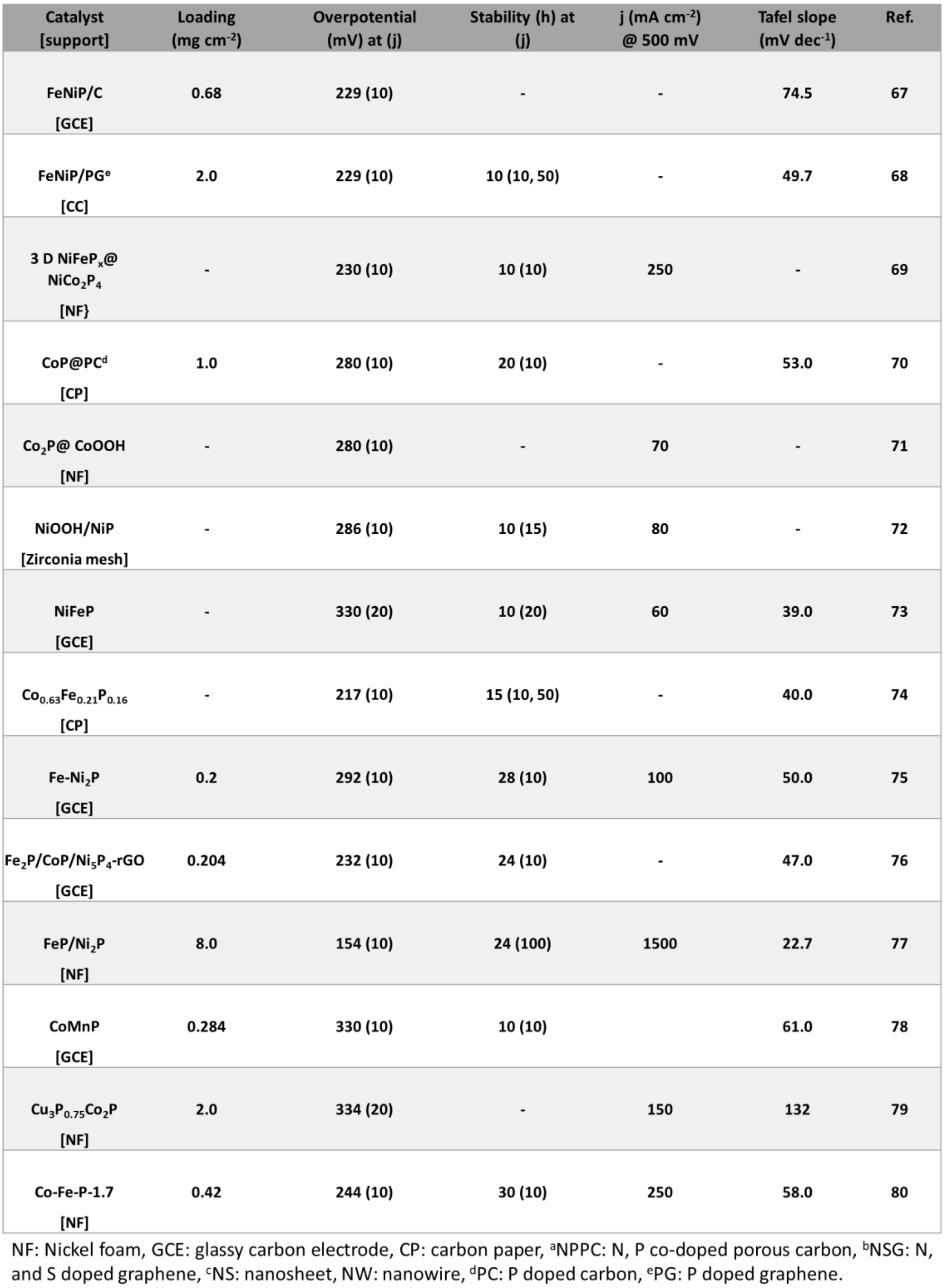

Catalyst [support]	Loading (mg cm^{-2})	Overpotential (mV) at (j)	Stability (h) at (j)	j (mA cm^{-2}) @ 500 mV	Tafel slope (mV dec^{-1})	Ref.
FeNiP/C [GCE]	0.68	229 (10)	-	-	74.5	67
FeNiP/PG[e] [CC]	2.0	229 (10)	10 (10, 50)	-	49.7	68
3 D NiFeP$_x$@ NiCo$_2$P$_4$ [NF}	-	230 (10)	10 (10)	250	-	69
CoP@PC[d] [CP]	1.0	280 (10)	20 (10)	-	53.0	70
Co$_2$P@ CoOOH [NF]	-	280 (10)	-	70	-	71
NiOOH/NiP [Zirconia mesh]	-	286 (10)	10 (15)	80	-	72
NiFeP [GCE]	-	330 (20)	10 (20)	60	39.0	73
Co$_{0.63}$Fe$_{0.21}$P$_{0.16}$ [CP]	-	217 (10)	15 (10, 50)	-	40.0	74
Fe-Ni$_2$P [GCE]	0.2	292 (10)	28 (10)	100	50.0	75
Fe$_2$P/CoP/Ni$_5$P$_4$-rGO [GCE]	0.204	232 (10)	24 (10)	-	47.0	76
FeP/Ni$_2$P [NF]	8.0	154 (10)	24 (100)	1500	22.7	77
CoMnP [GCE]	0.284	330 (10)	10 (10)		61.0	78
Cu$_3$P$_{0.75}$Co$_2$P [NF]	2.0	334 (20)	-	150	132	79
Co-Fe-P-1.7 [NF]	0.42	244 (10)	30 (10)	250	58.0	80

NF: Nickel foam, GCE: glassy carbon electrode, CP: carbon paper, [a]NPPC: N, P co-doped porous carbon, [b]NSG: N, and S doped graphene, [c]NS: nanosheet, NW: nanowire, [d]PC: P doped carbon, [e]PG: P doped graphene.

LSV without iR compensation is provided (***Figure 1.2.17.a***) for comparison. FeP-CoP (80:20 wt. ratio) prepared by in-situ method (***Figure 1.2.17.b***) shows 234 mV overpotential to achieve a current density of 10 mA cm^{-2}, a slightly higher value than the physically mixed metal phosphides. In addition, it attains a current density of 720 mA cm^{-2} at an overpotential of 500 mV (***Figure 1.2.17.b***), a far low value as compared to that of physically mixed FeP-CoP mixture.

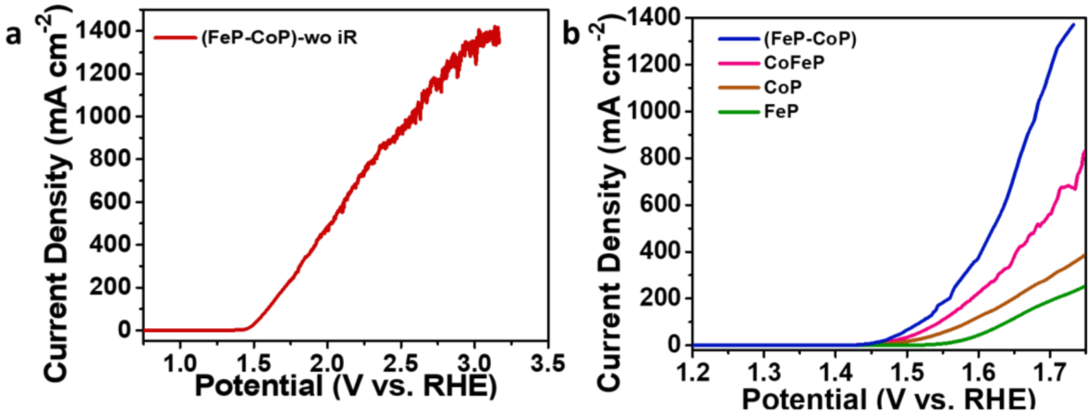

Figure 1.2. 17. Polarized linear sweep voltammograms (LSVs) of (a) FeP-CoP catalyst without iR compensation, and (b) FeP, CoP, FeP-CoP, and CoFeP catalysts, towards oxygen evolution reaction (OER) in 1.0 M KOH. (loading of catalyst = 0.112 mg cm^{-2})

Furthermore, FeP–CoP displays a very high current density of 1.37 A cm^{-2} at an overpotential of 500 mV vs. RHE. A remarkable improvement in the performance of FeP on addition of a small amount of CoP can be concluded from the six times higher current density observed for FeP-CoP than that for FeP. The creation of electrochemically active interfaces between CoP and FeP nanodomains on physical mixing of CoP with FeP could be the plausible explanation for such high current density. These interactions at the interfaces could synergistically assist the effective charge transfer kinetics across the heterointerfaces with efficient mass transport facilitated by the porous network structures. The observed shifts in binding energies corresponding to M–P peaks observed for FeP–CoP in XPS further support the synergism at the heterointerface leading to higher electrochemical performance.

Moreover, the electrochemically active surface area (ECSA) is meant to increase the kinetics of an electrochemical reaction by accelerating the charge transport across the interface.

The double layer capacitance (C_{dl}) was first evaluated by studying current density at different scan rates by cyclic voltammetry in the non-faradaic region **(*Figure 1.2.18.*)** within the potential range from 1.1 to 1.35 V (vs. RHE) recorded at different scan rates (20-100 mV s^{-1}).

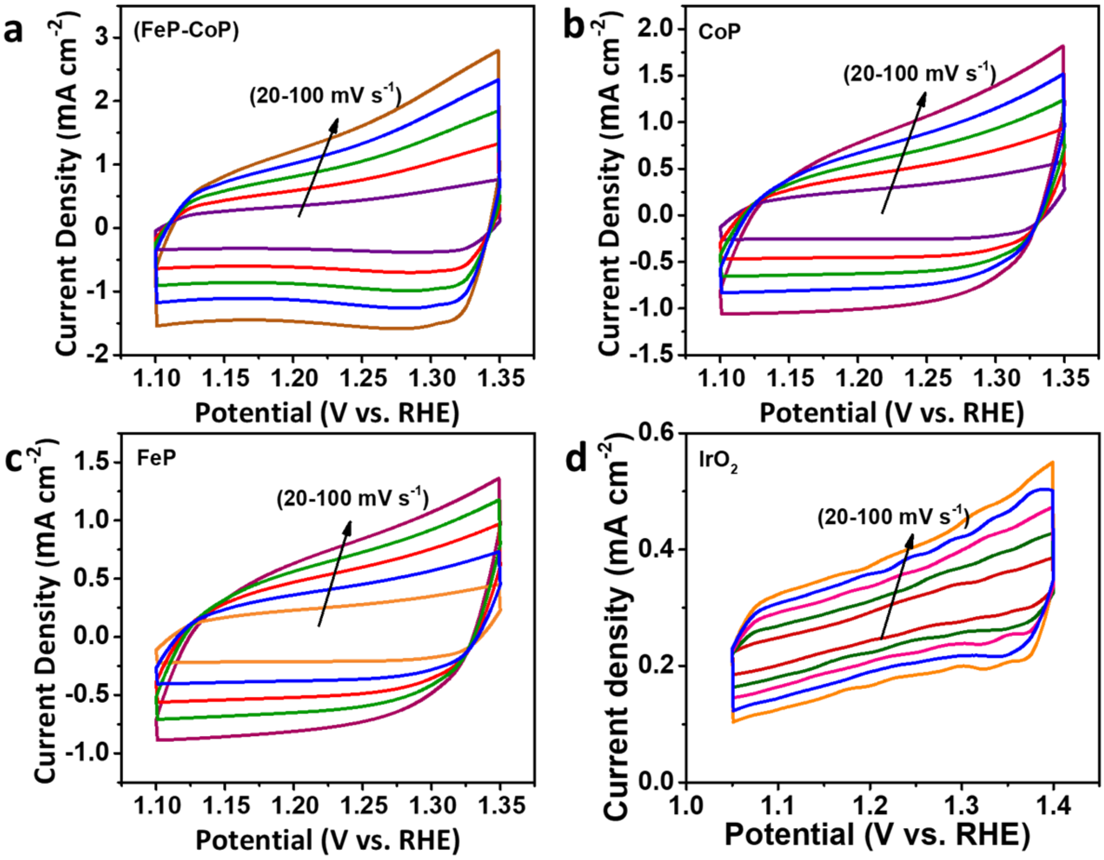

Figure 1.2. 18. Cyclic voltammogram (CV) studies in the non-Faradaic region of (a) FeP-CoP, (b) CoP, (c) FeP, and (d) IrO_2 catalysts towards oxygen evolution reaction (OER) in 1.0 M KOH. (loading of catalyst = 0.112 mg cm^{-2})

The electrochemically active surface area (ECSA) was calculated from C_{dl} value using the relation,

$$ECSA = C_{dl}/C_s,$$

where C_s is specific capacitance of flat electrode surface (40 mF cm^{-2}). The FeP–CoP catalyst shows higher C_{dl} **(*Figure 1.2.19.a*)**, and thus a higher ECSA compared to FeP and CoP **(*Table 1.2.4.*)**. The major contribution towards the OER comes from the creation of more active sites due to the generation of heterointerfaces in the mixture since the geometric area is the same for all the catalysts. Also, the LSV normalised with corresponding ECSA values (***Figure 1.2.19.b***) shows a huge increase in the current density for the FeP–CoP catalyst as compared to the individual components (FeP and CoP), strongly supporting the contribution from its intrinsic activity.

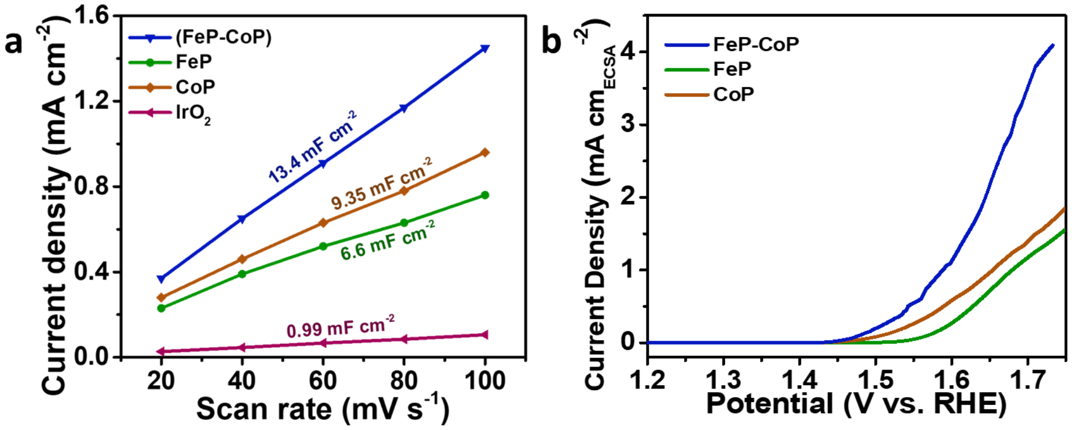

Figure 1.2. 19. (a) Double layer capacitance (C_{dl}) plot, and (b) Electrochemically active surface area (ECSA) normalized linear sweep voltammograms of FeP, CoP, and FeP-CoP catalysts towards oxygen evolution reaction (OER) in 1.0 M KOH. (loading of catalyst = 0.112 mg cm^{-2})

Table 1.2. 4. OER performance of CoP, FeP, (FeP-CoP), and IrO_2 catalysts.

Catalyst	Mass activity (@ 350 mV) (A g^{-1}_{M})	Mass activity (@ 500 mV) (A g^{-1}_{M})	ECSA (cm^2)	TOF (s^{-1})
(FeP-CoP)	**4269 ± 194**	**18987 ± 894**	**23.68**	**1.65**
CoP	**1290 ± 63**	**4893 ± 240**	**14.84**	**0.54**
FeP	**374 ± 1**	**3257 ± 150**	**11.49**	**0.27**
IrO_2	**572 ± 28**	**3264 ± 152**	**1.74**	**0.66**

To investigate the rate of the electrochemical reaction, Tafel analysis was done wherein the Tafel plots were obtained from the polarization curves using Tafel relation considering log(*j*) vs. V. The improved kinetics is further confirmed by the decreased value of the Tafel slope (***Figure 1.2.20.a***) for FeP-CoP catalyst (39.7 mV dec^{-1}) in comparison to IrO_2 (57.9 mV dec^{-1}), CoP (49.8 mV dec^{-1}), and FeP (48.6 mV dec^{-1}). Another figure of merit is the mass activity (A g^{-1}) and surprisingly FeP–CoP catalyst displays a phenomenal improvement in mass activity of 18 987 (± 894) A g_M^{-1} as compared to FeP (3257 ±150 A g_M^{-1}) and CoP (4893 ± 240 A g_M^{-1}) at an overpotential of 500 mV (***Figure 1.2.20.b***).

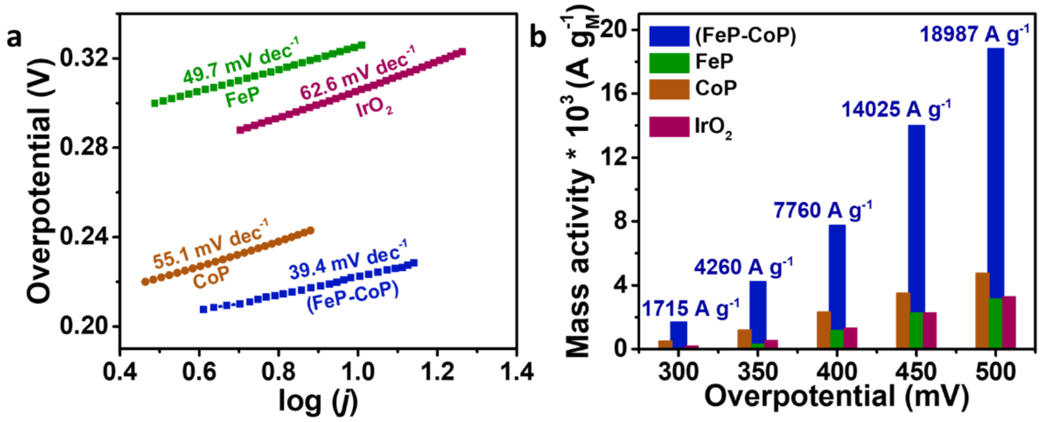

Figure 1.2. 20. (a) Tafel plot, and (b) mass activity of FeP, CoP, FeP-CoP, and IrO_2 catalysts towards oxygen evolution reaction (OER) in 1.0 M KOH. (loading of catalyst = 0.112 mg cm^{-2})

Electrochemical impedance spectroscopy (EIS) analyses were performed in frequency range of 0.01 Hz to 100 kHz with an amplitude of 5 mV at various fixed potential values. The Nyquist plot (***Figure 1.2.21.***) shows an almost three times lower value of charge transfer resistance (Rct, 14.7 Ω) for FeP–CoP as compared to FeP (45.4 Ω) and CoP (35.7 Ω) catalysts at a potential of 1.55 V vs. RHE. These R_{ct} values are manually calculated from the plot.

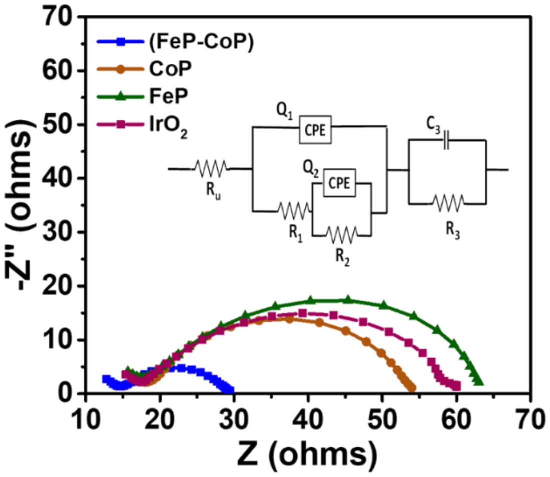

Figure 1.2. 21. Nyquist plot of CoP, FeP, and FeP-CoP catalysts towards oxygen evolution reaction (OER) in 1.0 M KOH. Inset shows the circuit fitting.

The rate of the alkaline oxygen evolution reaction (OER) involving multiple steps of hydroxide adsorption and abstraction of hydrogen followed by the formation of peroxide species is primarily affected by the sorption kinetics of hydroxide species in the system. As reported for the iron-based systems in aqueous media, there exists an inner compact anhydrous layer and an outer hydrous layer.(*81*) The outer hydrous layer is known for containing the OER active species. Electrochemical impedance spectroscopy has been used to understand the underlying electrical elements involved. Circuit fitting was done by considering three circuits **(*Figure 1.2.22.*)** to fit the EIS data. The common circuit involves a resistor (R) and capacitor (C) as the electrical elements to define a particular process at the electrode surface. In materials with high surface roughness and inhomogeneity observed from the depressed circle, the capacitor element is replaced by a constant phase element (CPE, Q). The combination of elements with low error and high probability for fitting is represented in Circuit 3. Three different relaxation processes can be observed with RC contribution from the compact layer, the charge transfer, and the adsorption of intermediates at the surface.

The simplest circuit 1 can be considered to constitute two different RC loops (C1R1 and Q2R2) along with R_u as the resistance offered by the solution and other components of the cell. C1R1 may contribute from the charge transfer while Q2R2 may contribute from the compact layer. In the case of systems with poorly separated time constants of two different relaxation processes occurring at the electrode surface, circuit 2 can be considered.

Considering circuit 3, RCPE1 corresponds to RC circuit elements linked with compact layer formation as these are not much affected by changing the samples. RCPE2 can be assigned to the RC circuit elements for charge transfer and double-layer formation, as seen from the fitting of circuit 3 for the mixture **(*Figure 1.2.23.*)**. Also, as seen from the Tafel behavior, the R_{ct} values match well with the observed order of FeP-CoP<CoP<FeP. The RC3 can be linked to the adsorption of intermediate species as the C3 values also show the order of FeP-CoP>CoP>FeP.

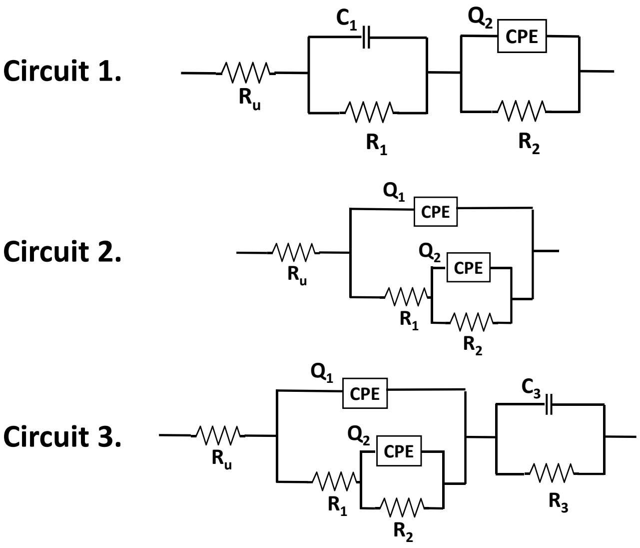

Figure 1.2. 22. Various electrochemical circuits considered for fitting of impedance data.

Various reports suggest circuit 1 for a similar sort of EIS data wherein two RC circuits are connected in series with a solution resistance (***Figure 1.2.23.- 1.2.25.***).(*82*) While fitting the data in circuit 1, the error with the electrochemical circuit fitting (ECF) is around 3 %. So, shifting to circuit 2 gives a very odd fitting with an error of 4.5 %. Finally, circuit 3 fits very well with all the samples with an error in the range of 1 % to 1.7%. All these elements show the effective contribution ***(Table 1.2.5.)*** from the electrochemical structure formed during the reaction.

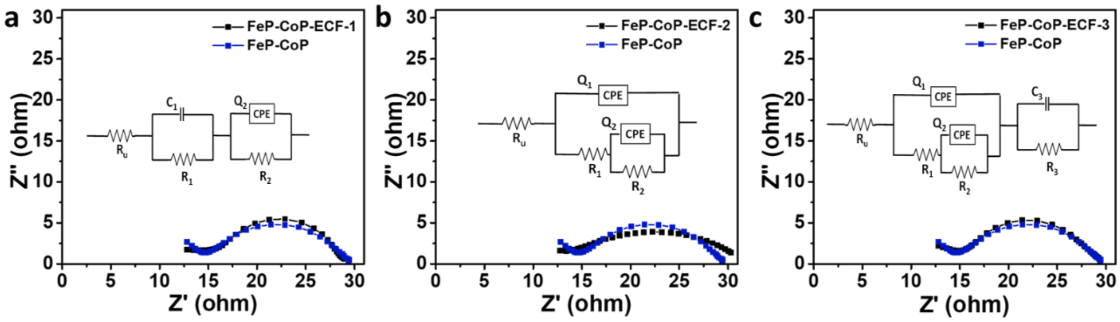

Figure 1.2. 23. (a-c) Electrochemical impedance Circuit fitting (ECF) of FeP-CoP catalyst.

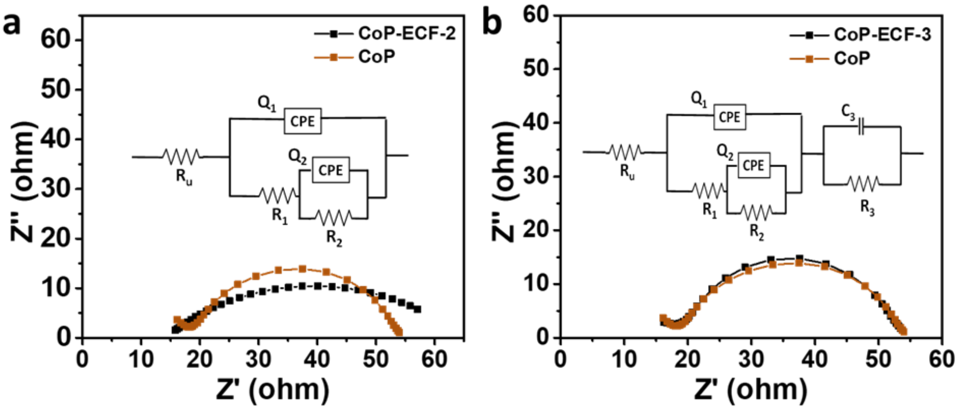

Figure 1.2. 24. (a, b) Electrochemical impedance Circuit fitting (ECF) of CoP catalyst.

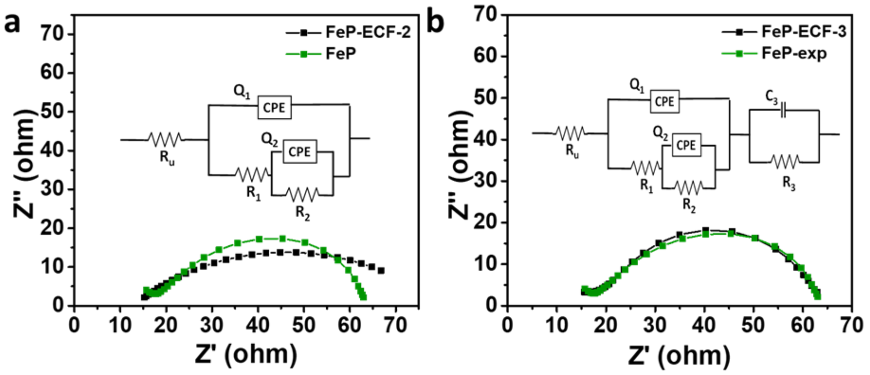

Figure 1.2. 25. (a, b) Electrochemical impedance Circuit fitting (ECF) of FeP catalyst.

Table 1.2. 5. EIS circuit fitting parameters of different catalysts.

Circuit elements	FeP	CoP	(FeP-CoP)
R_u	0.001	0.001	0.001
Q_1	2.077 e-5	2.026 e-5	2.55 e-5
R_1	18.26	19.5	15.49
Q_2	0.98 e-3	2.75 e-3	4.9 e-3
R_2	19.71	10.78	7.037
C_3	17.14 e-5	2.15 e-5	8.75 e-5
R_3	27.64	24.7	7.49

The cyclic voltammograms observed in the potential region before the onset of the OER (1.0 to 1.4 V vs. RHE) confirm the existence of Co species in higher oxidation state **(*Figure 1.2.26.*)**, thus showing the effective formation of metal oxy-hydroxides at the surface. The oxidation peaks in regions of 1.0 to 1.1 V (vs. RHE) and 1.3 to 1.4 V (vs.

RHE) corresponds to oxidation peaks from Co(II) to Co(III) and Co(III) to Co(IV), respectively.(*83*) Also, the interaction between the Fe and Co metal sites with varying percentages of CoP in FeP was evidenced by the shift in the position ***(Table 1.2.6)*** of the oxidation peak of Co.(*84*)

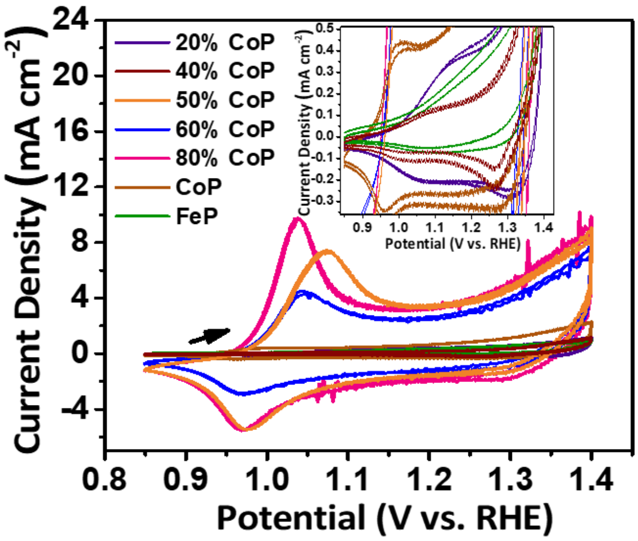

Figure 1.2. 26. Cyclic voltammograms (CV) of all catalysts with varying percentage of CoP in FeP.

Table 1.2. 6. Metal oxidation peak position from CV studied in non-faradaic region of different catalysts.

Catalyst	Peak position (V vs. RHE)
CoP	0.995
(FeP-CoP)-(20:80)	1.038
(FeP-CoP)-(40:60)	1.045
(FeP-CoP)-(50:50)	1.070
(FeP-CoP)-(60:40)	1.103
(FeP-CoP)-(80:20)	1.145
FeP	1.170

To consider a catalyst to be electrochemically active, the primary concerning factor is the stability and durability in wide potential range. The accelerated degradability test for

FeP–CoP catalyst shows only a 5% loss in activity (***Figure 1.2.27.a***) after 3000 cycles. The potentiostatic stability test to attain a current density of 200 mA cm^{-2} also shows a minimal degradation (~2 %) in current density over FeP-CoP even after a long duration of 200 h at a fixed potential of 1.57 V (***Figure 1.2.27.b***) as compared to the commercial catalyst, IrO_2 (at 1.67 V), for which 83% activity degradion from 200 mA cm^{-2} to 35 mA cm^{-2} was observes within 6.5 hours (***Figure 1.2.27.b***).

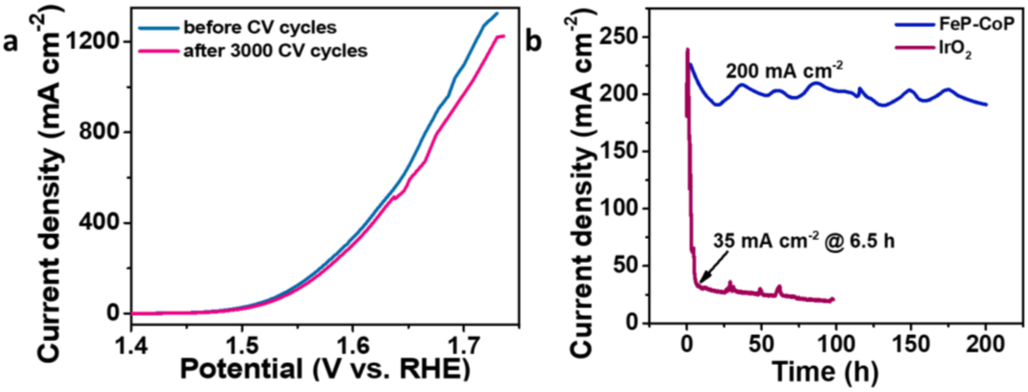

Figure 1.2. 27. (a) Accelerated degradability test for 3000 cycles, and (b) chronoamperometry analysis to achieve a current density of 200 mA cm^{-2} for FeP-CoP and IrO_2 catalysts towards oxygen evolution reaction (OER) in 1.0 M KOH.

The individual FeP and CoP catalysts also show sharp decrease in performance to achieve even lower current densities of 55 and 70 mA cm^{-2} at corresponding potentials (***Figure 1.2.28.***).

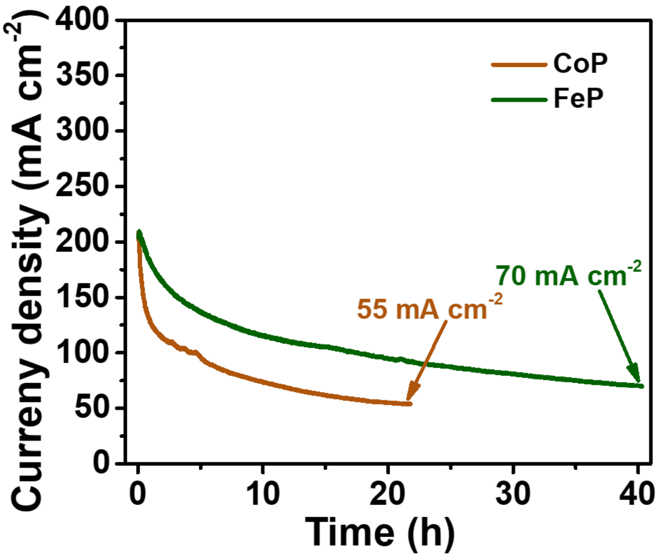

Figure 1.2. 28. Chronoamperometry studies of CoP (55 mA cm^{-2}), and FeP (70 mA cm^{-2}) towards oxygen evolution reaction (OER) in 1.0 M KOH.

Further, good durability was observed both with multistep study in conditions of varying external load (***Figure 1.2.29.a***) and galvanostatic study to achieve a low current density of 30 mA cm^{-2} for 400 h (***Figure 1.2.29.b***) of FeP-CoP.

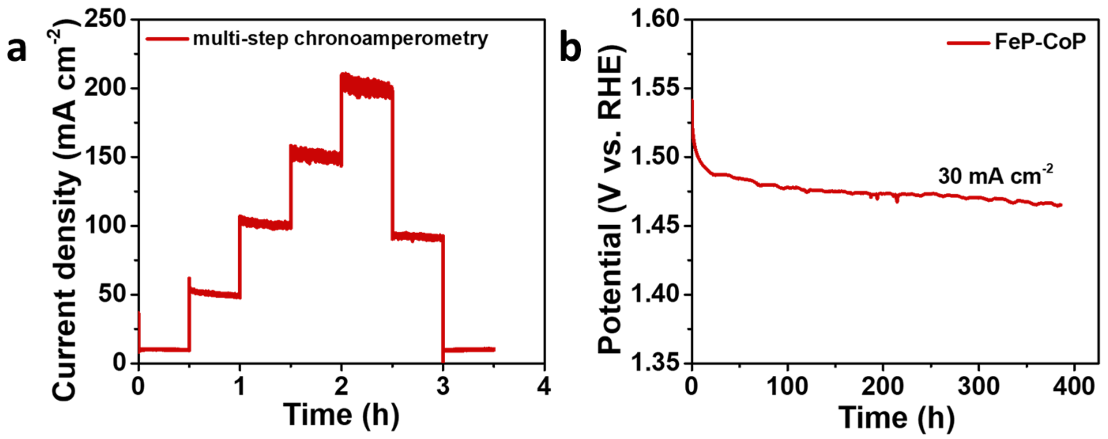

Figure 1.2. 29. (a) Multistep chronoamperometry studies, and (b) chronopotentiometry studies of FeP-CoP towards oxygen evolution reaction (OER) in 1.0 M KOH.

The rate of stirring (***Figure 1.2.30.a***) also affects the performance at higher potentials and high rate of stirring (1400 rpm) showed better activity due to the removal of adsorbed oxygen bubbles from the surface of the catalyst. It is to be noted that the FeP-CoP catalyst shows similar activities on GCE as well as on carbon paper electrode (CPE) (***Figure 1.2.30.b***) for the same catalyst loading.

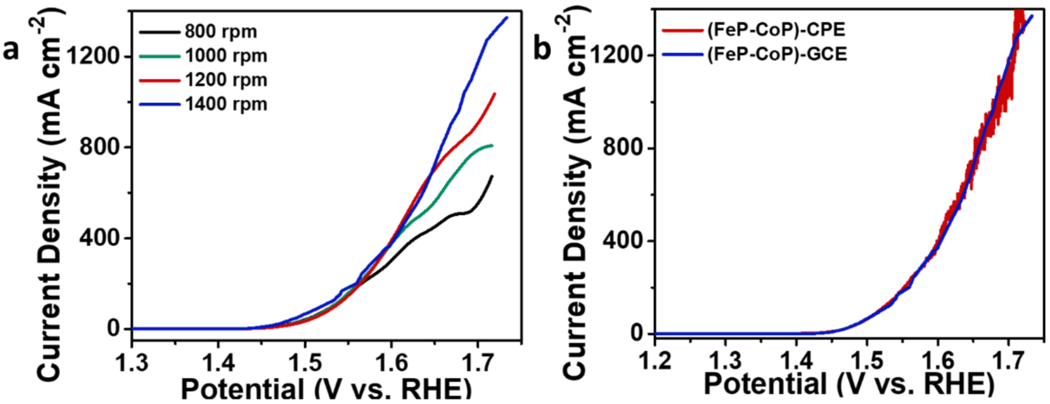

Figure 1.2. 30. (a) Effect of stirring rate, and (b) performance at glassy carbon (GCE) and carbon paper (CPE) electrodes for FeP-CoP catalyst towards oxygen evolution reaction (OER) in 1.0 M KOH.

1.2.4.3. Full cell studies:

During the full cell study carried out in a two-electrode arrangement using FeP-CoP coated Toray carbon paper as the working electrode and 20%-Pt/C as the counter electrode **(*Figure 1.2.31.*)** without iR compensation, a cell potential of 1.56 V was required to achieve a current density of 10 mA cm^{-2}. The full cell potential applied using FeP-CoP catalyst is 80 mV lower than that needed for commercial catalyst, IrO_2-Pt/C couple to attain a current density of 10 mA cm^{-2}.

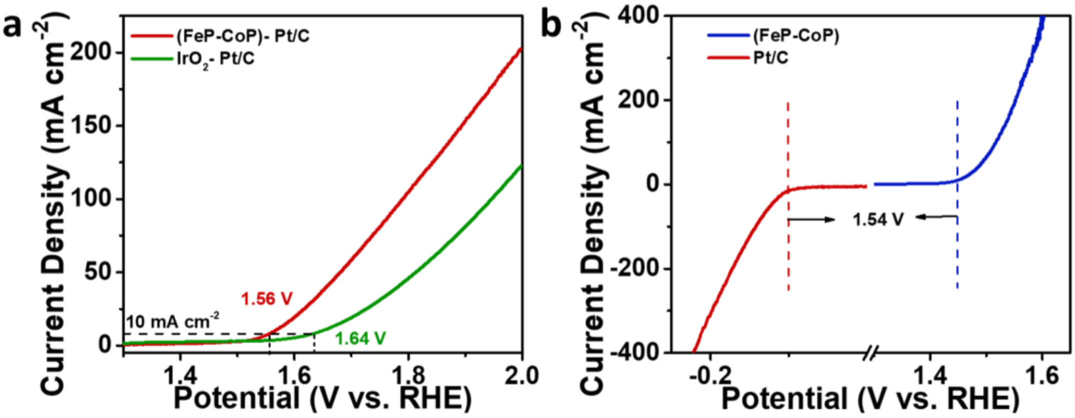

Figure 1.2. 31. (a) Full-cell (two-electrode) studies of FeP-CoP-Pt/C and state-of-the-art IrO_2-Pt/C couples, and (b) individual linear sweep voltammograms of FeP-CoP and Pt/C catalysts towards OER and HER, respectively in 1.0 M KOH.

The full cell performance of individual FeP and CoP catalysts (***Figure 1.2.32.***) was lower than that of FeP-CoP catalyst.

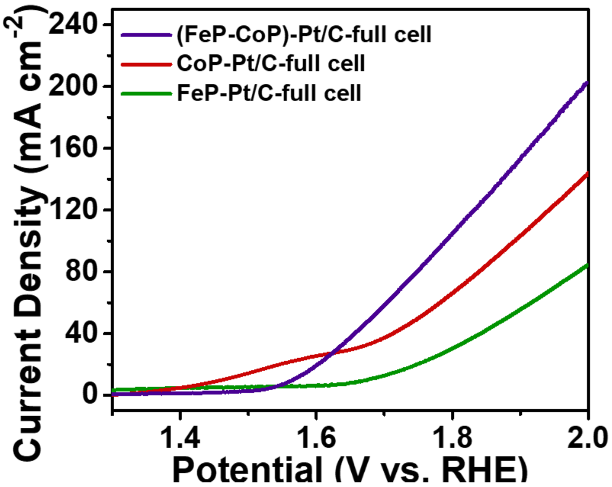

Figure 1.2. 32. Full-cell (two-electrode) studies of FeP-CoP-Pt/C, CoP-Pt/C, and FeP-Pt/C couples in 1.0 M KOH.

1.2.4.4. Role of phosphorus:

To understand the role of phosphorus in the metal phosphide, the electrochemical activity of the precursor hydroxide nanostructures prepared by the $NaBH_4$ reduction of Co- and Fe-salts was compared. The Fe-ns, Co-ns and their mixture (***Figure 1.2.33.***) display lower performance as compared to the FeP-CoP catalyst probably due to poor electrical conductivity associated with the oxide/hydroxide surface.

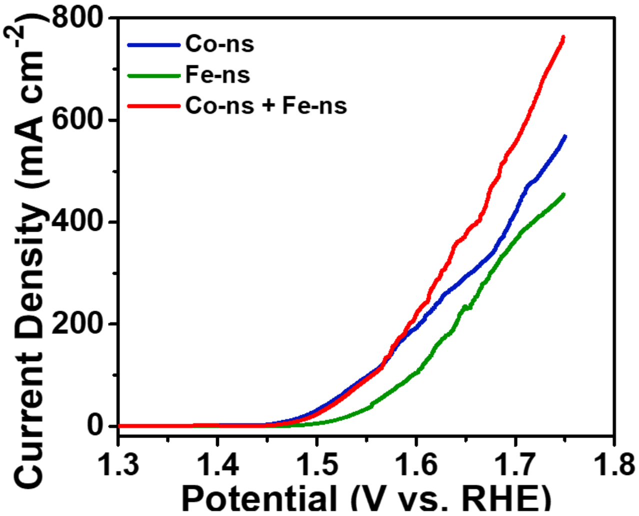

Figure 1.2. 33. Linear sweep voltammograms (LSVs) of the precursors; Co-ns, Fe-ns, and their mixture (Co-ns + Fe-ns) towards OER in 1.0 M KOH.

1.2.4.5. Mott-Schottky analysis:

To study the behaviour of active catalyst surface in 1.0 M KOH, Mott-Schottky analysis was carried out in anodic potential range of 0.3 to 1.7 V (vs. RHE) at 5 mV s^{-1}. From the Mott-Schottky plot (***Figure 1.2.34.***) the active role of both p- and n-type charge carriers at the catalyst surface in the electrolyte can be depicted.(*85*) The relative charge carrier concentration (with respect to FeP) was calculated for different catalysts. The FeP-CoP mixture shows higher concentration of carriers (***Table 1.2.7.***) and the surface p- and n-type differ much for FeP-CoP catalyst as compared to individual CoP and FeP. Also, common MOS capacitor with high leakage current type behaviour can be seen from the C vs. V plot (***Figure 1.2.34.***) with active change in phase angle towards zero degrees.(*86*) This analysis proves that metal phosphides behave as pre-catalyst in the alkaline conditions, actively converting to oxyhydroxides which may show this sort of observed behaviour.(*87*, *88*)

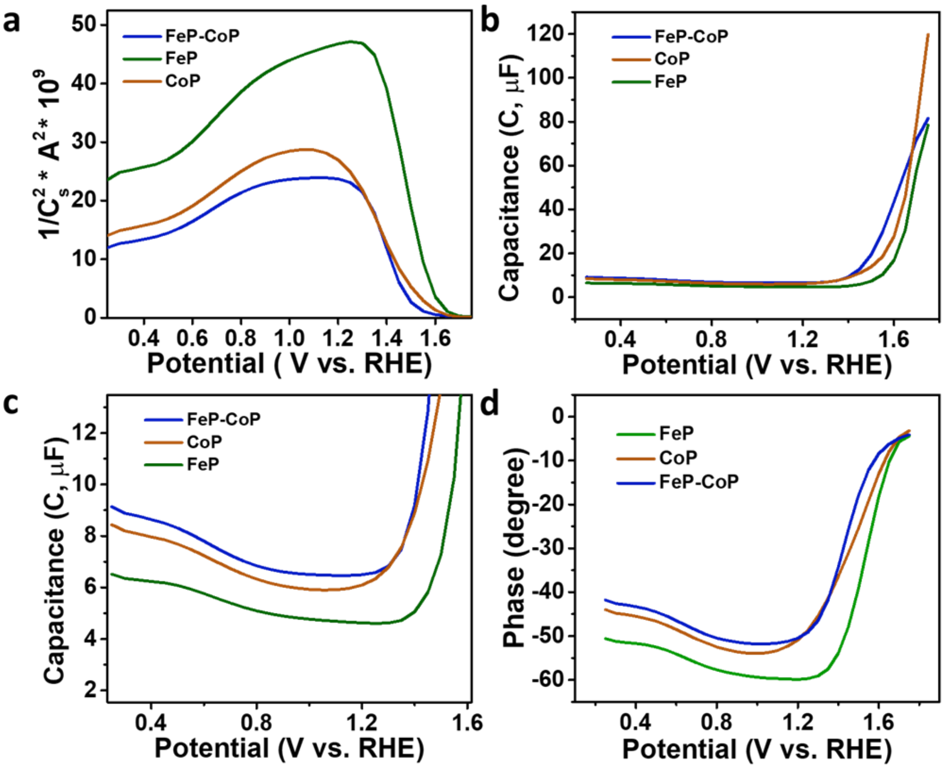

Figure 1.2. 34. Mott-Schottky analysis: (a) Capacitance versus. Potential plot (C vs. E), (b) Lower potential region of C vs. E plot, (c, d) Mott-Schottky plot of FeP-CoP towards OER in 1.0 M KOH.

Table 1.2. 7. Charge carrier concentrations (N_a, and N_d) calculated from Mott-Schottky analysis.

Catalyst	**Relative donor charge carrier conc. (cm^{-3}), N_d**	**Relative acceptor charge carrier conc. (cm^{-3}), N_a**
FeP	1.03	1.0
CoP	1.83	1.86
FeP-CoP	2.09	2.81

1.2.4.6. Faradaic efficiency determination:

The faradaic efficiency of OER was determined by water-gas displacement method. During the collection of O2 gas, 3.6 mL of O_2 gas was collected in the inverted burette corresponding to $Q_{O2} = 62.03$ C.

Q_{total} is calculated from the charge observed via potentiostatic measurement for 7200 s at 1.53 V vs. RHE and equals to 63.77 C. Thus, the faradaic efficiency comes out to be 97%.

1.2.4.7. Post-reaction analysis:

In order to get insights into real nature of the catalyst, post-OER analyses of the FeP-CoP catalyst was carried out employing various techniques. It is known and well-studied that the metal phosphides act as pre-catalysts in OER in alkaline conditions and the actual catalyst contains a surface layer of metal oxyhydroxides. To understand the modifications of the catalytic surface, the post reaction analyses were done after 2 h and 75 h. After 2 h of reaction study, the catalyst mostly consists of phosphorus rich surface with low concentration of oxygen. The existence of metal phosphides, oxides, and oxy-hydroxides can be clearly seen from the PXRD pattern (***Figure 1.2.35.a***), and XPS analysis (***Figure 1.2.35.c-f***) after the OER reaction.(*42, 89, 90*) Existence of relatively high intense peaks corresponding to Co^{3+} and Fe^{2+} species after OER clearly indicates the charge transfer from Co to Fe sites. A small decrease in phosphorus content and a slight increase in oxygen at the surface was observed from EDS analysis (***Figure 1.2.36.***) with HAADF-STEM showing existence of Fe, Co, P, and O. On the other hand, the phosphide peaks are masked in Raman spectrum (***Figure 1.2.35.b***) with signatures for the oxide surface were seen accounting for the larger Raman scattering cross section of oxides. Also, few fingerprints in the higher wavenumber region similar to in-situ synthesized CoFeP (***Figure 1.2.15.***), represent possible interactions between the metal sites.

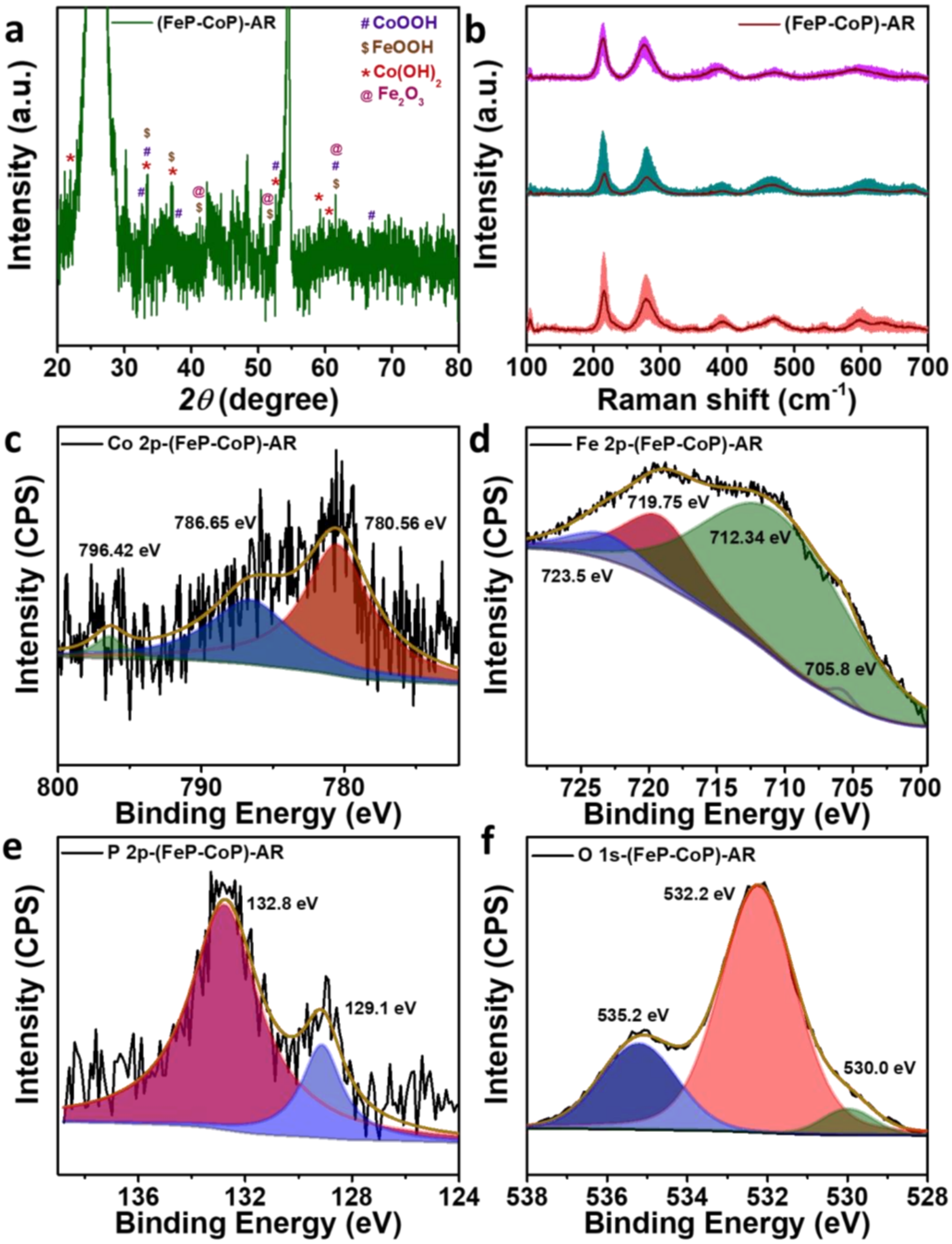

Figure 1.2. 35. (a) PXRD pattern, (b) Raman analysis, (c) High-resolution XPS spectra Co 2p, (d) Fe 2p, (e) P 2p, and (f) O 1s for (FeP-CoP) catalyst 2 h post-OER measurement.

Note: (AR means "after reaction"), and the three Raman spectra represent the spatial variations of the Raman spectra over the 90 points in the FeP-CoP sample post OER.

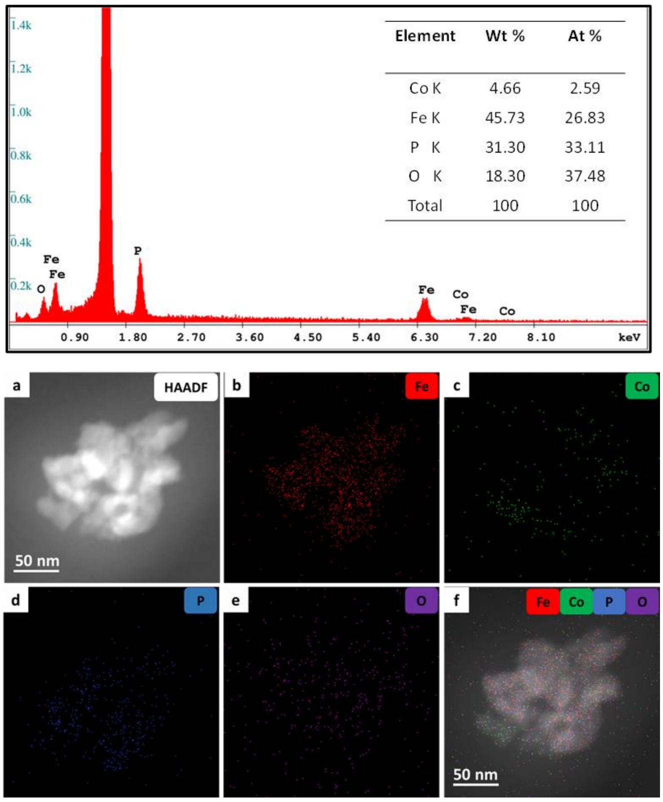

Element	Wt %	At %
Co K	4.66	2.59
Fe K	45.73	26.83
P K	31.30	33.11
O K	18.30	37.48
Total	100	100

Figure 1.2. 36. EDS elemental plot, and (a) HAADF, (b) Fe, (c) Co, (d) P, (e) O, and (f) all elements mapping of (FeP-CoP) catalyst post-OER for 2 h in HAADF-STEM mode.

TEM, SAED analyses (***Figure 1.2.37.***), and HRTEM (***Figure 1.2.38.***) shows various crystalline domains of metal phosphides and metal hydroxides distributed heterogeneously over amorphous matrix.(*91-94*)

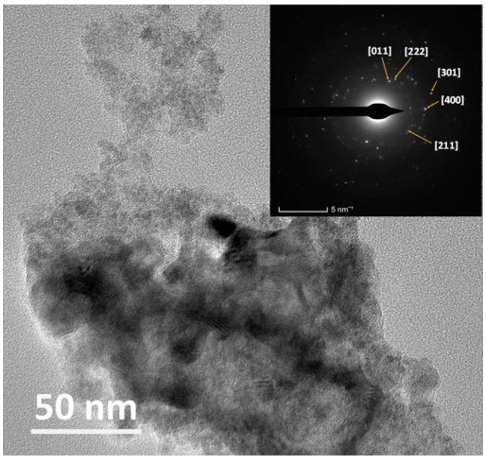

Figure 1.2. 37. (a) TEM (inset shows SAED pattern), of (FeP-CoP) catalyst post-OER for 2 h.

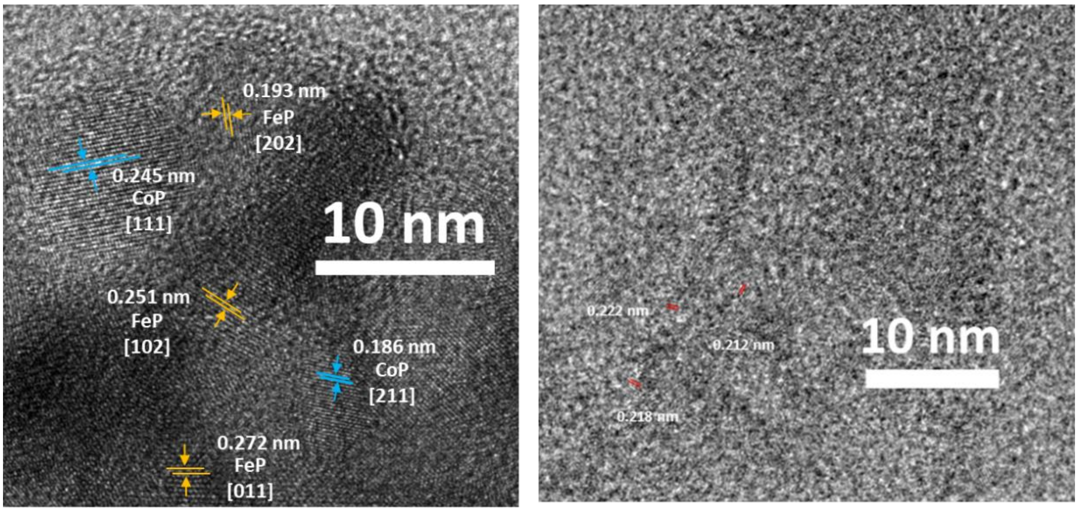

Figure 1.2. 38. HRTEM images of (FeP-CoP) catalyst post-OER for 2 h.

The dissolution and dynamic redeposition of trace amount of Fe species (as observed in earlier Fe containing metal hydr(oxy) oxides) on the surface of the catalyst leading to in-situ formed structure could also contribute to the formation of active sites.(*95*) However, CoP in the presence of a trace amount of Fe impurity (10 ppm) in purified KOH ***(Figure 1.2.39.)*** did not show any enhancement in performance with time; rather, it showed a 15 % decrease in activity in 72 h of reaction. Suppose the deposition of Fe and interaction with the catalytic surface were the reasons behind the increase in the performance of FeP-CoP. In that case, increased performance must have been observed for CoP also.

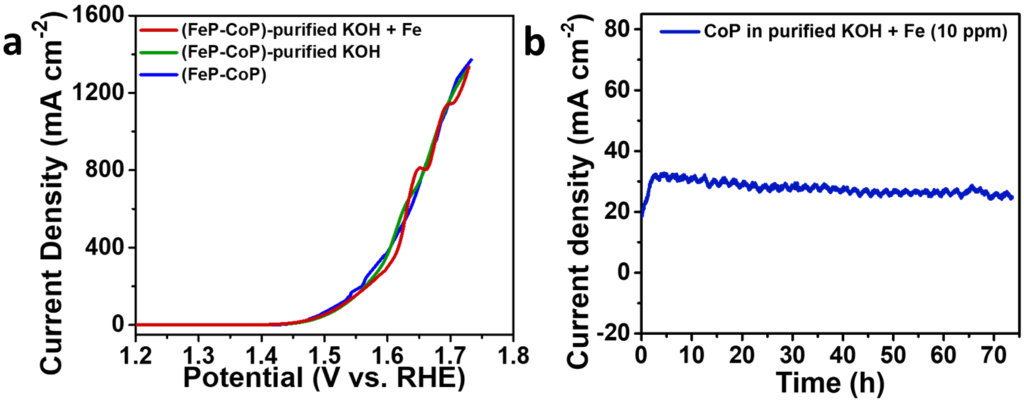

Figure 1.2. 39. (a) Polarised linear sweep voltammograms, and (b) Chronometry of CoP in presence of Fe (10 ppm) in 1 M purified KOH.

However, for practical applications it is necessary to do the post reaction analyses after longer duration of reaction. We analysed the catalyst after 75 h of reaction which shows less amount of phosphorus containing species and formation of oxides and oxyhydroxides at the surface. Very few broad peaks **(*Figure 1.2.40.*)** for the presence of metal phosphides, oxides and oxyhydroxides were observed from the PXRD analysis. The EDS **(*Figure 1.2.41.*)** and XPS analyses **(*Figure 1.2.42.*)** suggest the presence of phosphides along with oxygenated species in the catalyst post OER (75 h). These techniques confirm that the final surface consists of trace amount of phosphorus containing species (phosphides and phosphates) with great subsistence of oxygenated species. The post-reaction studies reveal that the actual contribution to the activity comes from various factors like heterointerface formation, catalyst conversion to oxyhydroxides, and inter-metallic charge transfer.

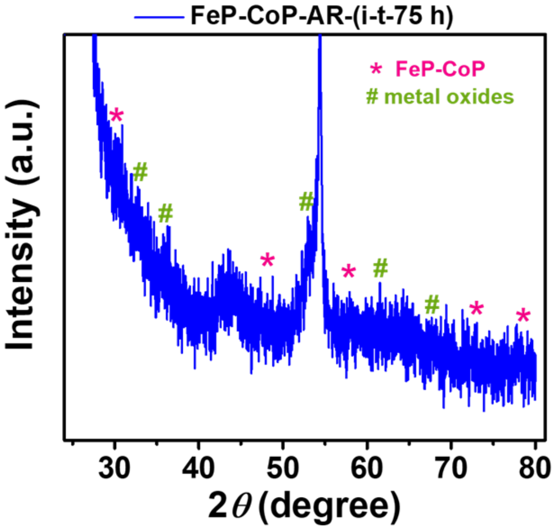

Figure 1.2. 40. PXRD pattern of FeP-CoP catalyst 75 h post-OER measurement.

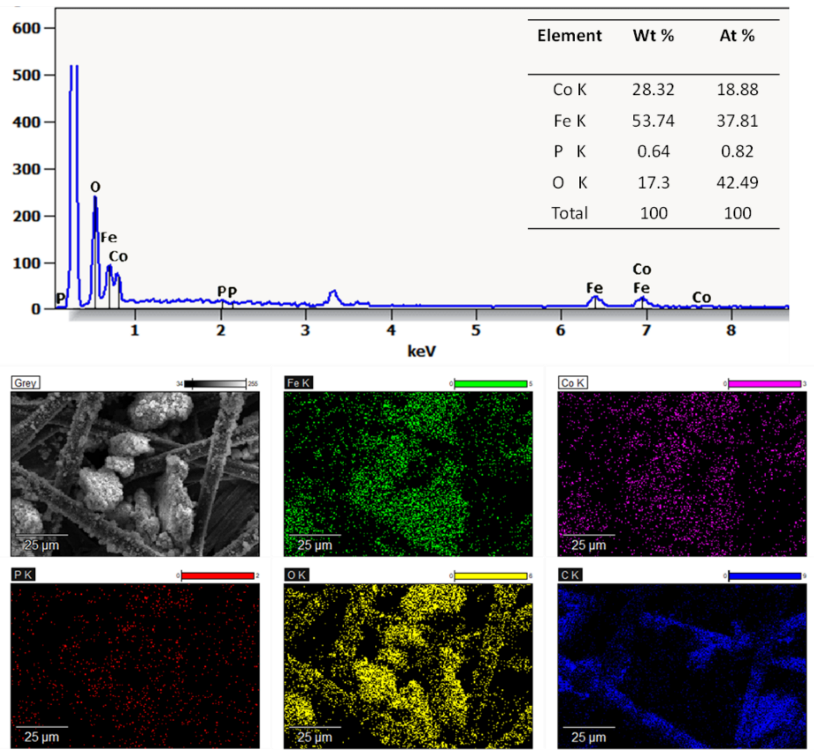

Element	Wt %	At %
Co K	28.32	18.88
Fe K	53.74	37.81
P K	0.64	0.82
O K	17.3	42.49
Total	100	100

Figure 1.2. 41. EDS elemental mapping and plot of FeP-CoP catalyst post OER after 75 h.

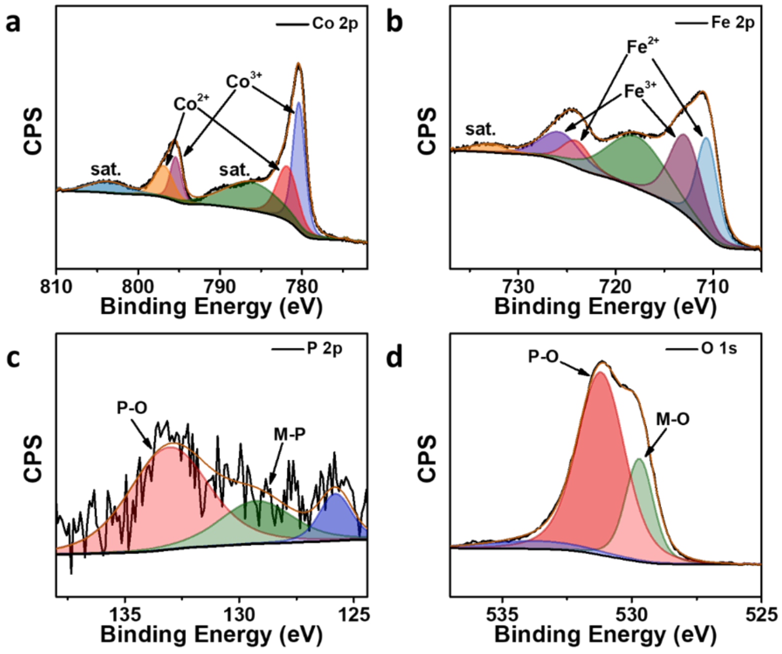

Figure 1.2. 42. High resolution XPS spectra of (a) Co 2p, (b) Fe 2p, (c) P 2p, and (d) O 1s for FeP-CoP catalyst post OER for 75 h.

1.2.4.8. DFT calculations: Computational studies:

We used Quantum ESPRESSO software package(*96*) to perform density functional theoretical calculations. We also performed NEB calculations to understand the potential determining step. To model ion-electron interaction we used projector-augmented wave (PAW) potentials. We used generalized gradient approximation as given by Perdew-Burke-Ernzerhof (PBE).(*97*) We also included Grimme-D2 corrections(*98*) to account for van der Waals interactions. A uniform mesh of 6×6×1 k-points(*99*) was used in sampling of Brillouin-zone (BZ) integrations. To model slab, we used a vacuum of 15 Å to prevent the interaction between periodic images.

The Gibbs free energies (ΔG) of intermediates were estimated in each reaction step by simulating adsorption of OH, O, and OOH intermediates, thereby understanding the mechanisms of OER on surfaces of FeP, CoP and their physical mixture with interfaces. As Although (011) surface of both CoP and FeP has higher surface energy than of (211) surface, we have considered (011) surface in our simulations as an OOH intermediate is unstable and dissociates into adsorbed O and OH on (211) surfaces of CoP and FeP **(*Table 1.2.8.*)**.

Table 1.2. 8. Surface energy of different catalysts.

Catalyst	Surface energy (kJ m^{-2})
CoP (011)	**0.152**
CoP (211)	**0.103**
FeP (011)	**0.120**
FeP (211)	**0.085**

Since our post-reaction analyses after 2 h of reaction showed a low concentration of oxygen species at the surface, we carried out simulations considering FeP-CoP interface with one surface oxygen atom **(*Figure 1.2.43.*)** and the surfaces containing oxyhydroxides **(*Figure 1.2.44.- 1.2.46.*)** as considered in an earlier work.(*18*)

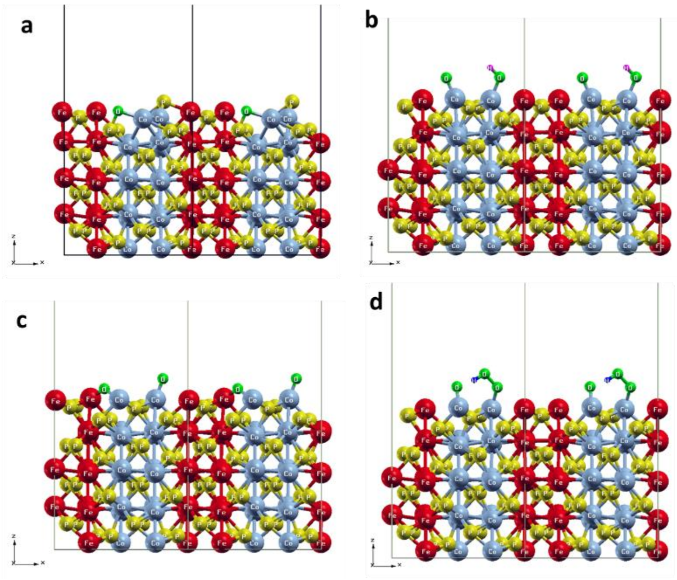

Figure 1.2. 43. Stable configurations of various intermediates on FeP-CoP interface with one surface oxygen atom.

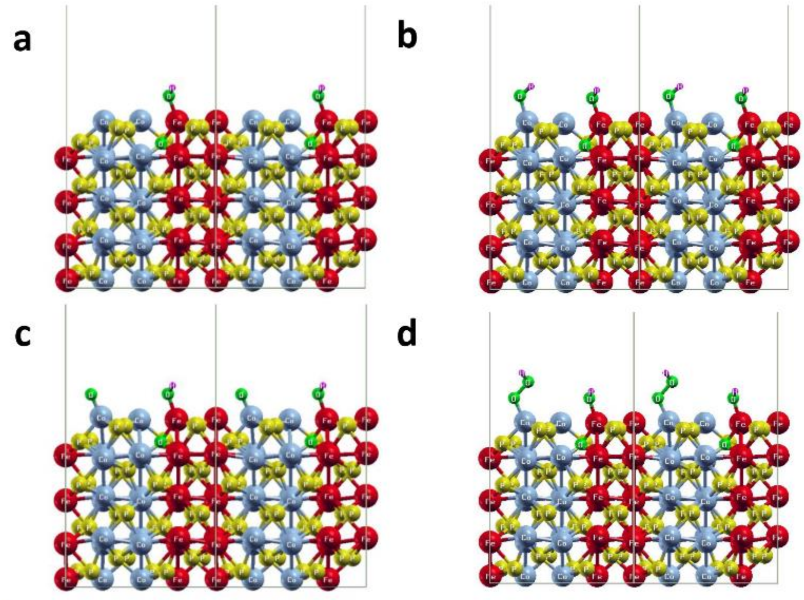

Figure 1.2. 44. Stable configurations of (a) FeOOH structure, (b-d) various intermediates considering FeOOH on the surface of FeP-CoP interface with Co as the intermediate adsorption site.

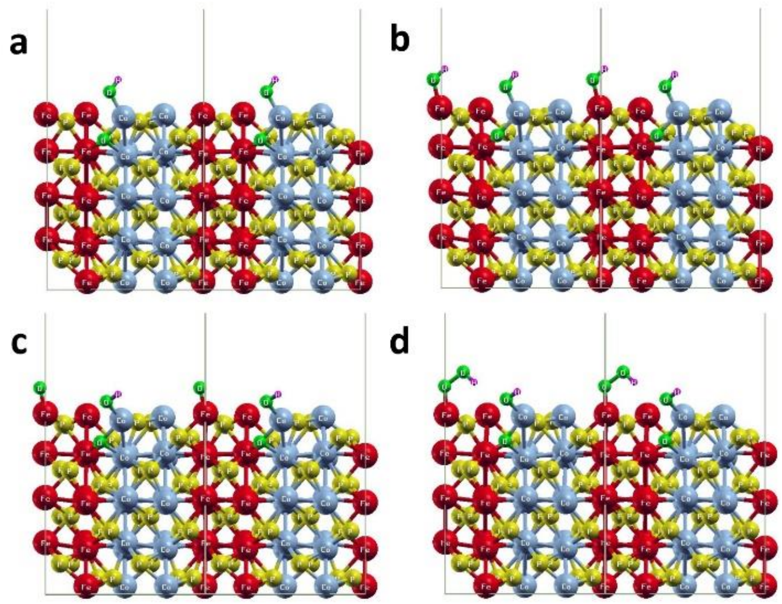

Figure 1.2. 45. Stable configurations of (a) CoOOH structure, (b-d) various intermediates considering CoOOH on the surface of FeP-CoP interface with Fe as the intermediate adsorption site.

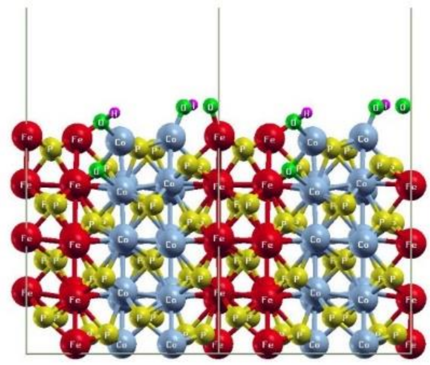

Figure 1.2. 46. Unstable configuration of adsorption of OOH intermediate on Co site considering CoOOH on the surface of FeP-CoP interface.

The study **(*Figure 1.2.47.*)** reveals low energy barrier for the final step but the potential determining step (3rd step, 2.54 eV) is similar to the other catalysts **(*Figure 1.2.48., 1.2.49.*)**. While the formation of oxyhydroxides causes reconstruction of catalyst **(*Figure 1.2.50.*)**, the active sites are retained through multiple cycles, as seen here experimentally. Thus, various reaction steps occurring at different sites are responsible for the enhanced activity of FeP-CoP mixture.

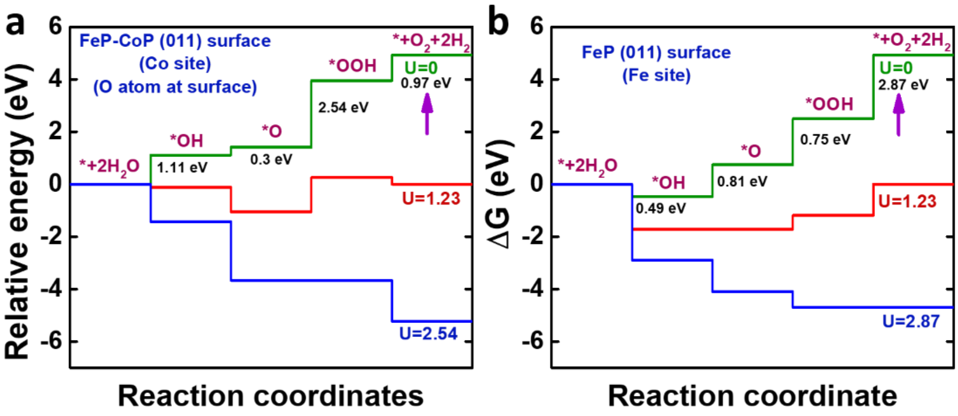

Figure 1.2. 47. Relative energy for each step in OER mechanism for (a) FeP-CoP interface with one surface oxygen atom, (b) FeP surface with Fe as the adsorption site.

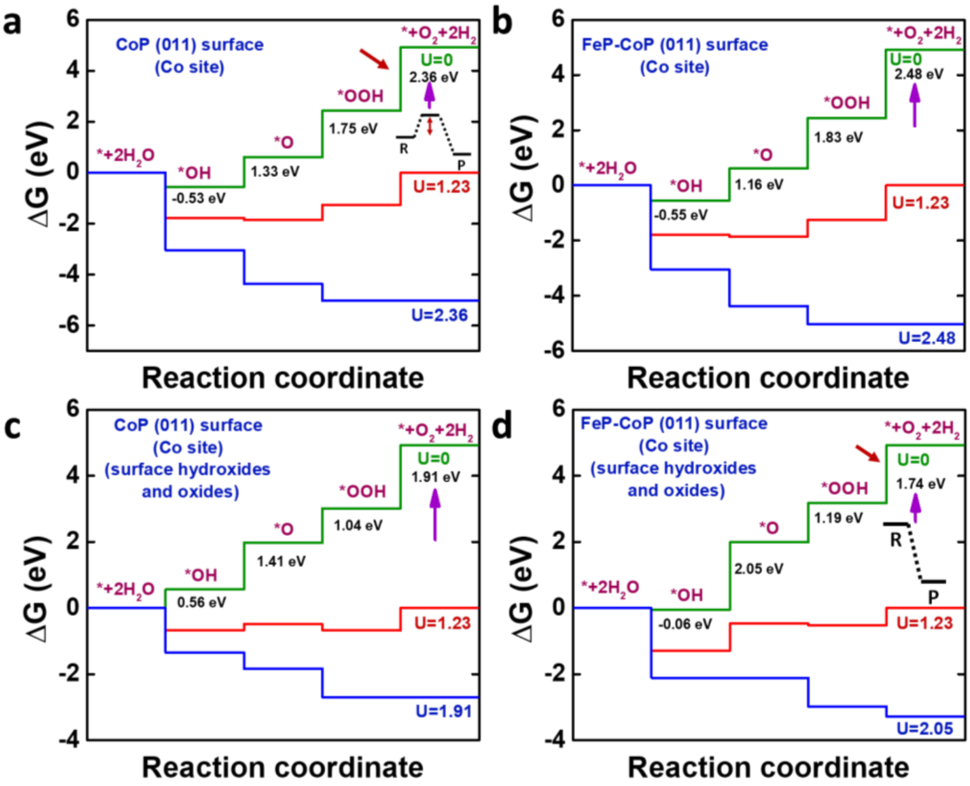

Figure 1.2. 48. Free energy changes in each step of the OER on (a) pristine CoP (inset shows schematic of energy barrier obtained from NEB calculation), (b) FeP-CoP interface, (c) oxygenated CoP, and (d) oxygenated FeP-CoP interface (inset shows schematic of energy barrier obtained from NEB calculation). The red arrows mark the step considered for NEB calculation.

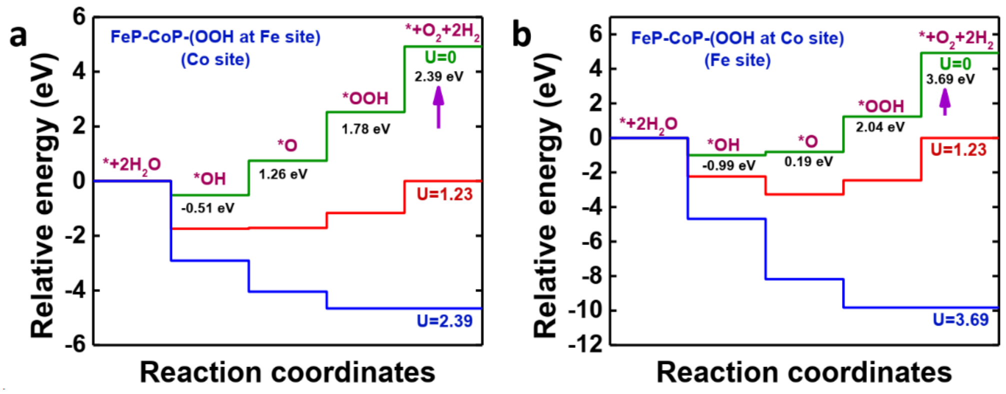

Figure 1.2. 49. Relative energy for each step in OER mechanism for (a) FeOOH at surface of FeP-CoP interface with Co as intermediate adsorption site, and (b) CoOOH at surface of FeP-CoP interface with Fe as intermediate adsorption site.

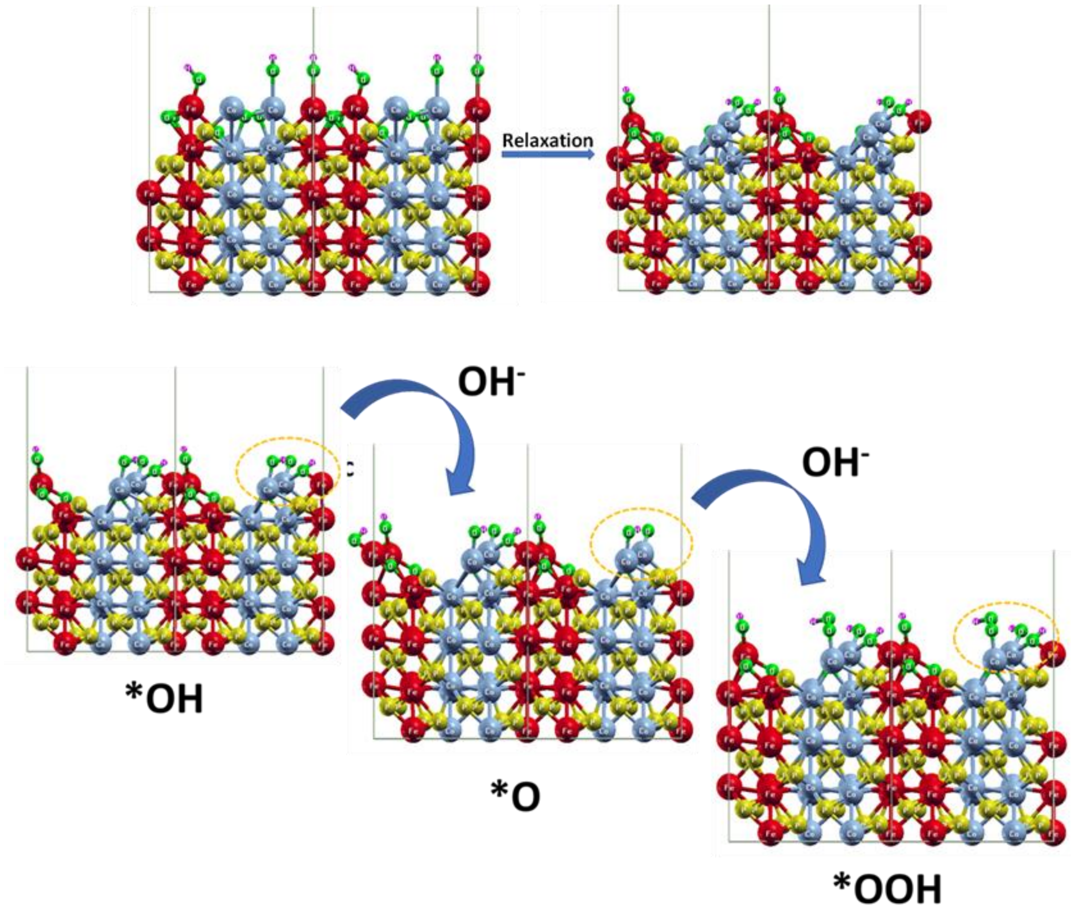

*Figure 1.2. 50. Relaxation of oxygenated surface on FeP-CoP interface, and stable configurations of various intermediates (*OH, *O, *OOH) considering oxygenated surface on FeP-CoP interface with Co as the intermediate adsorption site.*

Since the catalyst after 75 h of reaction revealed a high concentration of oxides and oxyhydroxides formed at the surface, we have analysed adsorption of reaction intermediates on the oxygenated surfaces of CoP (***Figure 1.2.51.*** and ***Figure 1.2.48.c***) and FeP-CoP lateral heterostructure (***Figure 1.2.50.*** and ***Figure 1.2.48.d***). We note that the final step (desorption of OOH to evolve O_2) is the PDS during the reactions on the surfaces shown in (***Figure 1.2.47., Figure 1.2.48.a, b,*** and ***Figure 1.2.49.)***. However, oxygenated CoP (***Figure 1.2.48.c***), oxygenated FeP-CoP interface (***Figure 1.2.48.d***), and FeP-CoP with one surface oxygen atom (***Figure 1.2.47.***) show a low barrier for this step. Although, the 2nd step (abstraction of H from *OH to form *O) is the PDS on oxygenated surface of FeP-CoP interface (***Figure 1.2.48.d***) with a low energy barrier of 2.05 eV, the barrier for the final step reduces from 1.91 eV in oxygenated CoP surface (***Figure 1.2.48.c***) to 1.74 eV in oxygenated FeP-CoP interface (***Figure 1.2.48.d***).

Further, optimal energies of adsorption of intermediates (***Table 1.2.9.***) on this surface indicate an improved activity of the oxygenated FeP-CoP interface. Oxygen binds strongly with FeP as evident in its high adsorption energy (***Table 1.2.9.***) and charge density difference (***Figure 1.2.52.***). Effective charge transfer occurs from CoP ($\phi = 4.2$ eV) to oxygenated Fe site ($\phi = 4.7$ eV) driven by the difference in work functions (***Table 1.2.10.***).

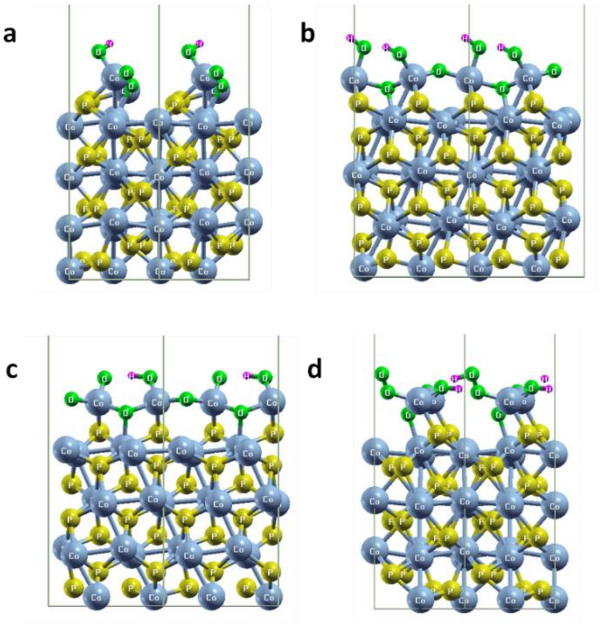

Figure 1.2. 51. Stable configurations of (a) surface, (b-d) and various intermediates (*OH, *O, *OOH) considering oxygenated surface on CoP catalyst.

Table 1.2. 9. Adsorption energy and its contribution from Grimme-D2 corrections.

System	*O		*OH		*OOH	
	E_{ads} (eV)	E_{vdW} (eV)	E_{ads} (eV)	E_{vdW} (eV)	E_{ads} (eV)	E_{vdW} (eV)
CoP (011)	**-1.54**	**-0.08**	**-0.47**	**-0.13**	**-0.81**	**-0.18**
FeP (011)	**-2.50**	**-0.09**	**-0.91**	**-0.12**	**-1.32**	**-0.18**
FeP-CoP (011) at Co	**-1.74**	**-0.07**	**-0.50**	**-0.097**	**-0.94**	**-0.15**
FeP-CoP (011) at Fe	**-2.41**	**-0.11**	**-0.91**	**-0.13**	**-1.32**	**-0.18**
Oxygenated CoP	**-0.37**	**-0.09**	**-0.61**	**-0.24**	**-0.35**	**-0.31**
Oxygenated FeP-CoP interface	**-0.36**	**-0.07**	**-0.004**	**-0.20**	**-0.19**	**-0.24**

.

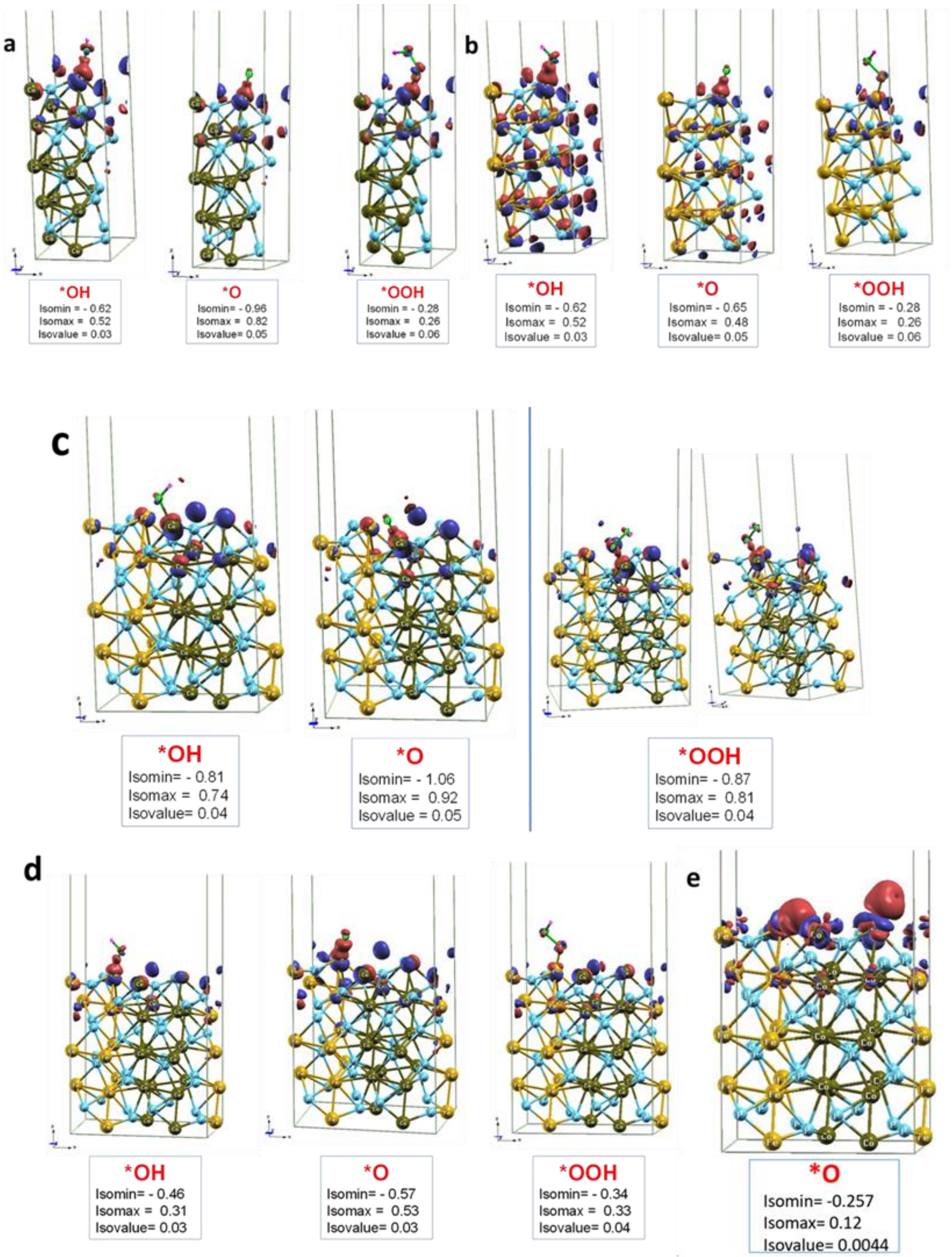

Figure 1.2. 52. Charge density difference plots for (a) CoP (011) surface, (b) FeP (011) surface, (c) FeP-CoP interface (011) at Co site, and (d) FeP-CoP interface (011) at Fe site, and (e) O adsorption at FeP-CoP interface with one O atom.

Table 1.2. 10. Work functions for considered systems.

System	Fermi level (E_F) (eV)	Vacuum Potential (eV)	Work function (ϕ) (eV)
CoP (011)	4.0135	8.255	4.2
*O at CoP (011)	3.6252	8.779	5.1
*OH at CoP (011)	3.9621	8.518	4.5
*OOH at CoP (011)	3.9853	8.719	4.7
FeP (011)	3.6797	7.587	3.9
*O at FeP (011)	3.2980	8.046	4.7
*OH at FeP (011)	3.6666	7.754	4.1
*OOH at FeP (011)	3.7614	7.772	4.0
FeP-CoP (011)	4.0429	8.104	4.1
*O at FeP-CoP (011) (Co site)	3.8636	8.373	4.5
*OH at FeP-CoP (011) (Co site)	4.0481	8.182	4.1
*OOH at FeP-CoP (011) (Co site)	4.0361	8.337	4.3
FeP-CoP (011)	4.0429	8.104	4.1
*O at FeP-CoP (011) (Fe site)	3.8440	8.336	4.5
*OH at FeP-CoP (011) (Fe site)	4.0483	8.180	4.1
*OOH at FeP-CoP (011) (Fe site)	4.1177	8.175	4.1
FeP-CoP (011) with one surface O	3.8872	8.2487	4.4
*O at FeP-CoP (011) with one surface O (Co site)	3.8064	8.4477	4.6
*OH at FeP-CoP (011) with one surface O (Co site)	3.8863	8.4168	4.5
*OOH at FeP-CoP (011) with one surface O (Co site)	3.8354	8.6079	4.77
FeP-CoP (011) with two surface O	3.9085	8.3990	4.5
*O at FeP-CoP (011) with two surface O (Fe site)	3.7973	8.6102	4.8
*OH at FeP-CoP (011) with two surface O (Fe site)	3.9524	8.4464	4.5
*OOH at FeP-CoP (011) with two surface O (Fe site)	3.9613	8.5704	4.6

Projected density of states with energy aligned to vacuum potential clearly shows that work function, $\phi = 4.7$ eV of oxygenated FeP-CoP interface **(*Figure 1.2.53.*)** is similar to other surfaces **(*Figure 1.2.54.*)** relevant to the final step. We find a large contribution of electronic states due to Fe-*d*, and Co-*d* orbitals crossing the energy level corresponding to the work function in all cases.

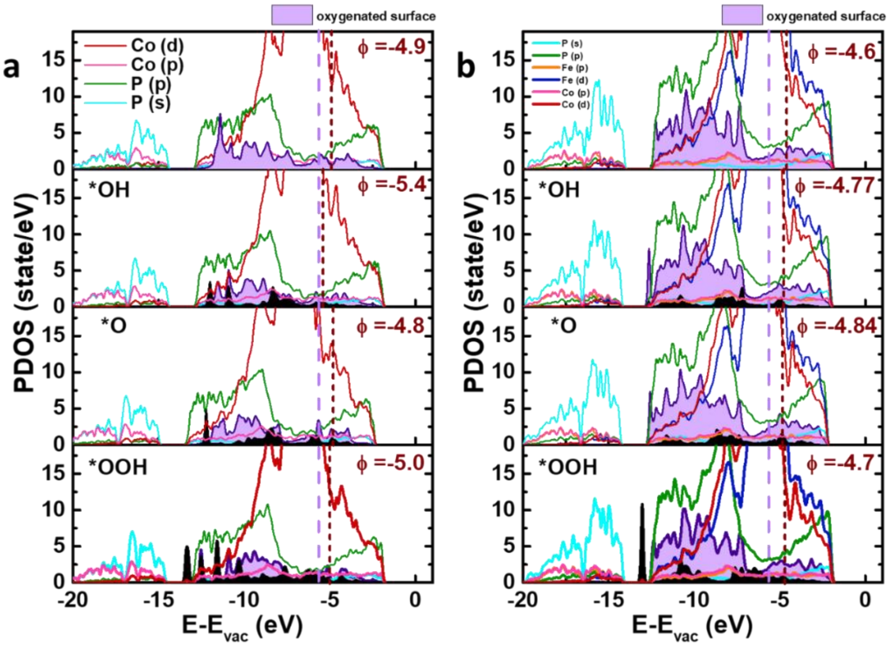

Figure 1.2. 53. Projected density of states (PDOS) of (a) oxygenated CoP, and (b) oxygenated FeP-CoP interface along with the adsorbed intermediates. (The vertical violet line marks the OER potential at 5.67 eV and brown line denotes work function (ϕ). The black regions show density of states of adsorbed species.)

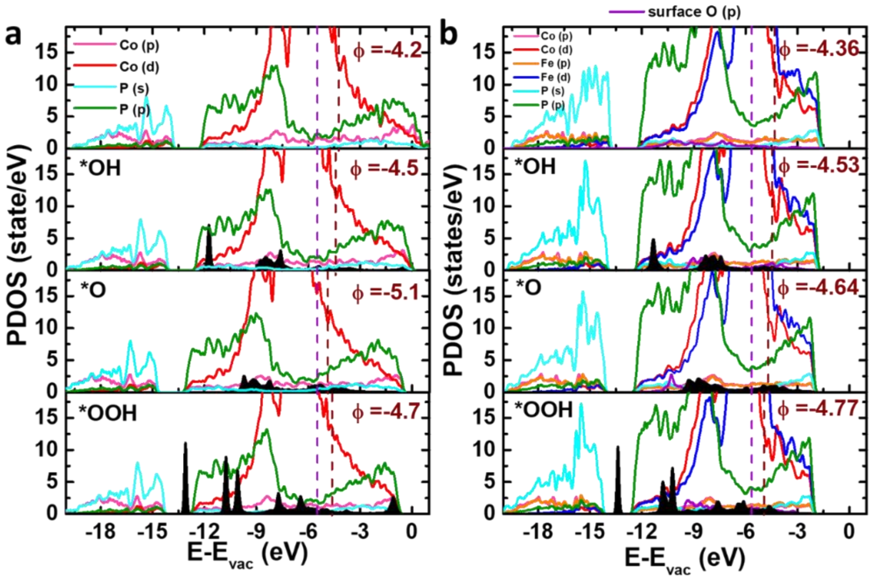

Figure 1.2. 54. Projected density of states (PDOS) of (a) pristine CoP, and (b) FeP-CoP interface with one surface oxygen along with the adsorbed intermediates. (The vertical violet line marks the OER potential at 5.67 eV and brown line denotes work function (ϕ). The black regions show density of states of adsorbed species.)

The NEB calculations to analyze the kinetic behavior and transition state reveal the barrierless final step for the oxygenated FeP-CoP interface (***Figure 1.2.55.***) while a barrier of 3.98 eV is encountered in the pristine CoP surface. This suggests that the final step is kinetically feasible at the oxygenated FeP-CoP heterointerface. While other steps of OER may occur at different sites in the physical mixture, the interface formed between FeP and CoP and the existence of oxygenated surfaces plays a key role in driving the final potential determining step.

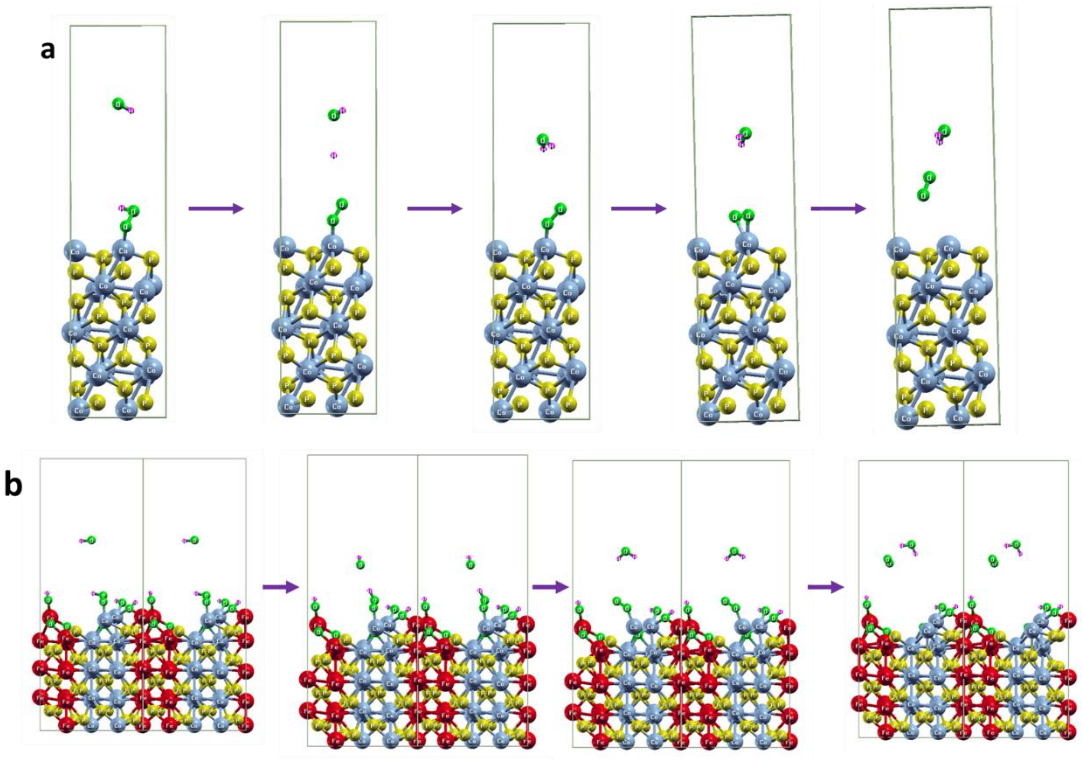

Figure 1.2. 55. NEB images for (a) final step of pristine CoP showing formation of O_2 and H_2O, and (b) showing barrierless formation of O_2 and H_2O on oxygenated surface of FeP-CoP interface.

1.2.5. Conclusions:

This work proposed the effective interfaces formed by the simple mixing of two different metal phosphides work in tandem for the adsorption and stabilization of different intermediates formed during the reaction. Further the charge transfer between the Co- and Fe- metal sites create a favourable environment for the sorption of intermediates, modifying the reaction kinetics. The oxygenated surface formed during the reaction at the metal site in the pre-catalyst helps in relieving the activation barrier for oxygen evolution. Our theoretical analysis shows that the interface formed between the CoP and FeP and the presence of oxygenated surface at the interface lead to a notable reduction in the energy barrier of the final potential determining step in OER. The observed high current density and prominent stability make the catalyst effective towards its use in electrolyzer and as a sustainable material for future applications in the field of viable utilization of energy.

1.2.6. References:

1. A. D. Doyle, M. Bajdich, A. Vojvodic, Theoretical Insights to Bulk Activity Towards Oxygen Evolution in Oxyhydroxides. *Catalysis Letters* **147**, 1533-1539 (2017).
2. Z. Ma *et al.*, Reaction mechanism for oxygen evolution on RuO2, IrO2, and RuO2@IrO2 core-shell nanocatalysts. *Journal of Electroanalytical Chemistry* **819**, 296-305 (2018).
3. H.-Y. Qu, X. He, Y. Wang, S. Hou, Electrocatalysis for the Oxygen Evolution Reaction in Acidic Media: Progress and Challenges. *Applied Sciences* **11**, (2021).
4. H. Wang *et al.*, Porous Two-Dimensional Materials for Photocatalytic and Electrocatalytic Applications. *Matter* **2**, 1377-1413 (2020).
5. M. E. G. Lyons, M. P. Brandon, A comparative study of the oxygen evolution reaction on oxidised nickel, cobalt and iron electrodes in base. *Journal of Electroanalytical Chemistry* **641**, 119-130 (2010).
6. S. Anantharaj, S. Noda, Nickel selenides as pre-catalysts for electrochemical oxygen evolution reaction: A review. *International Journal of Hydrogen Energy* **45**, 15763-15784 (2020).
7. H. Wang *et al.*, Transition metal carbides in electrocatalytic oxygen evolution reaction. *Chinese Chemical Letters* **32**, 291-298 (2021).
8. Y. Wu, Z. Xiao, Z. Jin, X. Li, Y. Chen, The cobalt carbide/bimetallic CoFe phosphide dispersed on carbon nanospheres as advanced bifunctional electrocatalysts for the ORR, OER, and rechargeable Zn-air batteries. *J Colloid Interface Sci* **590**, 321-329 (2021).
9. X. He *et al.*, NiS□FeS/N, S co-doped carbon hybrid: Synergistic effect between NiS and FeS facilitating electrochemical oxygen evolution reaction. *International Journal of Energy Research* **44**, 7057-7067 (2020).

10. X. Peng *et al.*, Recent progress of transition metal nitrides for efficient electrocatalytic water splitting. *Sustainable Energy & Fuels* **3**, 366-381 (2019).
11. Z. Chen *et al.*, Tuning electronic property and surface reconstruction of amorphous iron borides via W-P co-doping for highly efficient oxygen evolution. *Applied Catalysis B: Environmental* **288**, (2021).
12. Y. Li *et al.*, A high-performance oxygen evolution electrocatalyst based on partially amorphous bimetallic cobalt iron boride nanosheet. *International Journal of Hydrogen Energy* **45**, 28586-28597 (2020).
13. S. Intikhab *et al.*, Electrocatalytic oxygen evolution reaction (OER) on mixed nanoporous RuIr borides. *Journal of Applied Electrochemistry* **51**, 1101-1108 (2021).
14. J. Theerthagiri *et al.*, Recent progress on synthetic strategies and applications of transition metal phosphides in energy storage and conversion. *Ceramics International* **47**, 4404-4425 (2021).
15. C. Wang *et al.*, A general MOF-intermediated synthesis of hollow CoFe-based trimetallic phosphides composed of ultrathin nanosheets for boosting water oxidation electrocatalysis. *Nanoscale* **13**, 7279-7284 (2021).
16. J. F. Callejas, C. G. Read, C. W. Roske, N. S. Lewis, R. E. Schaak, Synthesis, Characterization, and Properties of Metal Phosphide Catalysts for the Hydrogen-Evolution Reaction. *Chemistry of Materials* **28**, 6017-6044 (2016).
17. S. Anantharaj *et al.*, Recent Trends and Perspectives in Electrochemical Water Splitting with an Emphasis on Sulfide, Selenide, and Phosphide Catalysts of Fe, Co, and Ni: A Review. *ACS Catalysis* **6**, 8069-8097 (2016).
18. Z. P. Wu *et al.*, Manipulating the Local Coordination and Electronic Structures for Efficient Electrocatalytic Oxygen Evolution. *Adv Mater* **33**, e2103004 (2021).
19. K. Zhang, R. Zou, Advanced Transition Metal-Based OER Electrocatalysts: Current Status, Opportunities, and Challenges. *Small* **17**, e2100129 (2021).
20. X. Mu *et al.*, Superior electrochemical water oxidation in vacancy defect-rich 1.5 nm ultrathin trimetal-organic framework nanosheets. *Applied Catalysis B: Environmental* **296**, (2021).
21. P. Wang *et al.*, N-Doped Carbon Nanotubes Encapsulating Ni/MoN Heterostructures Grown on Carbon Cloth for Overall Water Splitting. *ChemElectroChem* **7**, 745-752 (2020).

22. G. Yang *et al.*, Interfacial Engineering of MoO(2) -FeP Heterojunction for Highly Efficient Hydrogen Evolution Coupled with Biomass Electrooxidation. *Adv Mater* **32**, e2000455 (2020).
23. R. Liang *et al.*, Interface engineering induced selenide lattice distortion boosting catalytic activity of heterogeneous CoSe2@NiSe2 for lithium-oxygen battery. *Chemical Engineering Journal* **393**, (2020).
24. B. Wu *et al.*, Hierarchical sheet-on-sheet heterojunction array of a beta-Ni(OH)(2)/Fe(OH)(3) self-supporting anode for effective overall alkaline water splitting. *Dalton Trans* **50**, 12547-12554 (2021).
25. X. Luo *et al.*, Interface Engineering of Hierarchical Branched Mo-Doped Ni3S2/NixPy Hollow Heterostructure Nanorods for Efficient Overall Water Splitting. *Advanced Energy Materials* **10**, (2020).
26. L. Wang *et al.*, Tunable intrinsic strain in two-dimensional transition metal electrocatalysts. *Science* **363**, 870-874 (2019).
27. M. Luo, S. Guo, Strain-controlled electrocatalysis on multimetallic nanomaterials. *Nature Reviews Materials* **2**, (2017).
28. S. Schnur, A. Groß, Strain and coordination effects in the adsorption properties of early transition metals: A density-functional theory study. *Physical Review B* **81**, (2010).
29. H. Li *et al.*, A durable half-metallic diatomic catalyst for efficient oxygen reduction. *Energy & Environmental Science* **15**, 1601-1610 (2022).
30. J. D. Baniecki *et al.*, Enhanced Stability and Thickness-Independent Oxygen Evolution Electrocatalysis of Heterostructured Anodes with Buried Epitaxial Bilayers. *Advanced Energy Materials* **9**, (2019).
31. Z. Liu *et al.*, Defects-Induced In-Plane Heterophase in Cobalt Oxide Nanosheets for Oxygen Evolution Reaction. *Small* **15**, e1904903 (2019).
32. X. Ma *et al.*, Synthesis of Co-based Prussian Blue Analogues/Dual-Doped Hollow Carbon Microsphere Hybrids as High-Performance Bifunctional Electrocatalysts for Oxygen Evolution and Overall Water Splitting. *ACS Sustainable Chemistry & Engineering* **8**, 8318-8326 (2020).

33. Y. Yang *et al.*, An Interfacial Electron Transfer on Tetrahedral NiS(2) /NiSe(2) Heterocages with Dual-Phase Synergy for Efficiently Triggering the Oxygen Evolution Reaction. *Small* **16**, e1905083 (2020).
34. Z. He *et al.*, NiSx@MoS2 heterostructure prepared by atomic layer deposition as high-performance hydrogen evolution reaction electrocatalysts in alkaline media. *Journal of Materials Research* **35**, 822-830 (2019).
35. Y. Niu *et al.*, A "trimurti" heterostructured hybrid with an intimate CoO/CoxP interface as a robust bifunctional air electrode for rechargeable Zn–air batteries. *Journal of Materials Chemistry A* **8**, 9177-9184 (2020).
36. C. Huang *et al.*, Mo2C/VC heterojunction embedded in graphitic carbon network: An advanced electrocatalyst for hydrogen evolution. *Nano Energy* **60**, 520-526 (2019).
37. L. Yan, B. Zhang, S. Wu, J. Yu, A general approach to the synthesis of transition metal phosphide nanoarrays on MXene nanosheets for pH-universal hydrogen evolution and alkaline overall water splitting. *Journal of Materials Chemistry A* **8**, 14234-14242 (2020).
38. M. Gorlin *et al.*, Formation of unexpectedly active Ni-Fe oxygen evolution electrocatalysts by physically mixing Ni and Fe oxyhydroxides. *Chem Commun (Camb)* **55**, 818-821 (2019).
39. L. Kumar, B. Antil, A. Kumar, M. R. Das, S. Deka, A Superior and Stable Electrocatalytic Oxygen Evolution Reaction by One-Dimensional FeCoP Colloidal Nanostructures. *ACS Appl Mater Interfaces* **14**, 5468-5477 (2022).
40. Y. Wang *et al.*, A sequential template strategy toward hierarchical hetero-metal phosphide hollow nanoboxes for electrocatalytic oxygen evolution. *Journal of Materials Chemistry A* **9**, 3482-3491 (2021).
41. A. Mendoza-Garcia, D. Su, S. Sun, Sea urchin-like cobalt-iron phosphide as an active catalyst for oxygen evolution reaction. *Nanoscale* **8**, 3244-3247 (2016).
42. J. Chen *et al.*, Metal–Organic Framework-Derived CoxFe1–xP Nanoparticles Encapsulated in N-Doped Carbon as Efficient Bifunctional Electrocatalysts for Overall Water Splitting. *ACS Applied Energy Materials* **2**, 2734-2742 (2019).
43. L. M. Cao *et al.*, Fe-CoP Electrocatalyst Derived from a Bimetallic Prussian Blue Analogue for Large-Current-Density Oxygen Evolution and Overall Water Splitting. *Adv Sci (Weinh)* **5**, 1800949 (2018).

44. X. Zhang *et al.*, Co(3) O(4) /Fe(0.33) Co(0.66) P Interface Nanowire for Enhancing Water Oxidation Catalysis at High Current Density. *Adv Mater* **30**, e1803551 (2018).

45. Q. Xu *et al.*, Atomic heterointerface engineering overcomes the activity limitation of electrocatalysts and promises highly-efficient alkaline water splitting. *Energy & Environmental Science* **14**, 5228-5259 (2021).

46. S. H. Ye, Z. X. Shi, J. X. Feng, Y. X. Tong, G. R. Li, Activating CoOOH Porous Nanosheet Arrays by Partial Iron Substitution for Efficient Oxygen Evolution Reaction. *Angew Chem Int Ed Engl* **57**, 2672-2676 (2018).

47. S. Maity *et al.*, High surface area NiCoP nanostructure as efficient water splitting electrocatalyst for the oxygen evolution reaction. *Materials Research Bulletin* **140**, (2021).

48. J. Xu *et al.*, Trends in activity for the oxygen evolution reaction on transition metal (M = Fe, Co, Ni) phosphide pre-catalysts. *Chem Sci* **9**, 3470-3476 (2018).

49. Q. Liu *et al.*, Carbon nanotubes decorated with CoP nanocrystals: a highly active non-noble-metal nanohybrid electrocatalyst for hydrogen evolution. *Angew Chem Int Ed Engl* **53**, 6710-6714 (2014).

50. S. Zhang *et al.*, Understanding the Role of Nanoscale Heterointerfaces in Core/Shell Structures for Water Splitting: Covalent Bonding Interaction Boosts the Activity of Binary Transition-Metal Sulfides. *ACS Appl Mater Interfaces* **12**, 6250-6261 (2020).

51. Y. Wang, B. Ma, Y. Chen, Iron phosphides supported on three-dimensional iron foam as an efficient electrocatalyst for water splitting reactions. *Journal of Materials Science* **54**, 14872-14883 (2019).

52. J. Ma, Y. Wang, W. Pan, J. Zhang, Preparation of Hierarchical Cube-on-plate Metal Phosphides as Bifunctional Electrocatalysts for Overall Water Splitting. *Chem Asian J* **15**, 1500-1504 (2020).

53. W. Li *et al.*, C-CoP hollow microporous nanocages based on phosphating regulation: a high-performance bifunctional electrocatalyst for overall water splitting. *Nanoscale* **11**, 17084-17092 (2019).

54. J. Zhang, Y. Hu, D. Liu, Y. Yu, B. Zhang, Enhancing Oxygen Evolution Reaction at High Current Densities on Amorphous-Like Ni-Fe-S Ultrathin Nanosheets via

Oxygen Incorporation and Electrochemical Tuning. *Adv Sci (Weinh)* **4**, 1600343 (2017).

55. A. Goryachev *et al.*, Stability of CoP (x) Electrocatalysts in Continuous and Interrupted Acidic Electrolysis of Water. *ChemElectroChem* **5**, 1230-1239 (2018).
56. O. S. Vereshchagin *et al.*, Raman spectroscopy: A promising tool for the characterization of transition metal phosphides. *Journal of Alloys and Compounds* **853**, (2021).
57. F. H. Saadi *et al.*, Operando Spectroscopic Analysis of CoP Films Electrocatalyzing the Hydrogen-Evolution Reaction. *J Am Chem Soc* **139**, 12927-12930 (2017).
58. H. W. Man *et al.*, Tailored transition metal-doped nickel phosphide nanoparticles for the electrochemical oxygen evolution reaction (OER). *Chem Commun (Camb)* **54**, 8630-8633 (2018).
59. Z. Wang, N. Heng, X. Wang, J. He, Y. Zhao, Surface and morphology structure evolution of metal phosphide for designing overall water splitting electrocatalyst. *Journal of Catalysis* **374**, 51-59 (2019).
60. H. Bi *et al.*, Supersaturation-triggered synthesis of 2D/1D phosphide heterostructures as multi-functional catalysts for water splitting. *Applied Physics Letters* **118**, (2021).
61. L. Liu *et al.*, Quasi-layer Co(2)P-polarized Cu(3)P nanocomposites with enhanced intrinsic interfacial charge transfer for efficient overall water splitting. *Nanoscale* **11**, 6394-6400 (2019).
62. D. Li, Z. Li, J. Ma, X. Peng, C. Liu, One-step construction of Co2P nanoparticles encapsulated in N, P co-doped biomass-based porous carbon as bifunctional efficient electrocatalysts for overall water splitting. *Sustainable Energy & Fuels* **5**, 2477-2485 (2021).
63. L. Mengjie *et al.*, MOF-derived nitrogen-doped CoO@CoP arrays as bifunctional electrocatalysts for efficient overall water splitting. *Electrochimica Acta* **330**, (2020).
64. F. Bu *et al.*, Microwave-assisted ultrafast synthesis of adjustable bimetal phosphide/graphene heterostructures from MOFs for efficient electrochemical water splitting. *Journal of Materials Chemistry A* **7**, 14526-14535 (2019).

65. X. Ding *et al.*, Interface Engineering of Co(OH)(2)/Ag/FeP Hierarchical Superstructure as Efficient and Robust Electrocatalyst for Overall Water Splitting. *ACS Appl Mater Interfaces* **11**, 7936-7945 (2019).
66. T. Zhang, J. Du, P. Xi, C. Xu, Hybrids of Cobalt/Iron Phosphides Derived from Bimetal-Organic Frameworks as Highly Efficient Electrocatalysts for Oxygen Evolution Reaction. *ACS Appl Mater Interfaces* **9**, 362-370 (2017).
67. F. Yu *et al.*, High-performance bifunctional porous non-noble metal phosphide catalyst for overall water splitting. *Nat Commun* **9**, 2551 (2018).
68. J. Wang *et al.*, High topological tri-metal phosphide of CoP@FeNiP toward enhanced activities in oxygen evolution reaction. *Nanoscale* **13**, 1354-1363 (2021).
69. X. Xu *et al.*, Hierarchical Design of NiOOH@Amorphous Ni-P Bilayer on a 3D Mesh Substrate for High-Efficiency Oxygen Evolution Reaction. *ACS Appl Mater Interfaces* **10**, 30273-30282 (2018).
70. G. Liu, D. He, Y. Zhai, J. Li, Enhancing the water oxidation activity of Ni2P nanocatalysts by iron-doping and electrochemical activation. *Electrochimica Acta* **253**, 498-505 (2017).
71. D. Li, H. Baydoun, C. N. Verani, S. L. Brock, Efficient Water Oxidation Using CoMnP Nanoparticles. *J Am Chem Soc* **138**, 4006-4009 (2016).
72. J. Wu *et al.*, An Efficient Cobalt Phosphide Electrocatalyst Derived from Cobalt Phosphonate Complex for All-pH Hydrogen Evolution Reaction and Overall Water Splitting in Alkaline Solution. *Small* **16**, e1900550 (2020).
73. P. Ji *et al.*, Double Metal Diphosphide Pair Nanocages Coupled with P-Doped Carbon for Accelerated Oxygen and Hydrogen Evolution Kinetics. *ACS Appl Mater Interfaces* **12**, 727-733 (2020).
74. P. Wang *et al.*, Coupling NiSe2-Ni2P heterostructure nanowrinkles for highly efficient overall water splitting. *Journal of Catalysis* **377**, 600-608 (2019).
75. Y. Du *et al.*, Core–Shell FeCo Prussian Blue Analogue/Ni(OH)2 Derived Porous Ternary Transition Metal Phosphides Connected by Graphene for Effectively Electrocatalytic Water Splitting. *ACS Sustainable Chemistry & Engineering* **7**, 13523-13531 (2019).

76. U. P. Suryawanshi *et al.*, Colloidal Ni2P Nanocrystals Encapsulated in Heteroatom-Doped Graphene Nanosheets: A Synergy of 0D@2D Heterostructure Toward Overall Water Splitting. *Chemistry of Materials* **33**, 234-245 (2020).
77. H. Li *et al.*, Colloidal Cobalt Phosphide Nanocrystals as Trifunctional Electrocatalysts for Overall Water Splitting Powered by a Zinc-Air Battery. *Adv Mater* **30**, (2018).
78. X. Wang *et al.*, Chemical and morphological transformation of MOF-derived bimetallic phosphide for efficient oxygen evolution. *Nano Energy* **62**, 745-753 (2019).
79. X. Wei *et al.*, Carbon-incorporated porous honeycomb NiCoFe phosphide nanospheres derived from a MOF precursor for overall water splitting. *Chem Commun (Camb)* **55**, 10896-10899 (2019).
80. T. Wang *et al.*, Amorphous Co–Fe–P nanospheres for efficient water oxidation. *Journal of Materials Chemistry A* **5**, 25378-25384 (2017).
81. R. L. Doyle, M. E. Lyons, An electrochemical impedance study of the oxygen evolution reaction at hydrous iron oxide in base. *Phys Chem Chem Phys* **15**, 5224-5237 (2013).
82. İ. B. Pehlivan, M. A. Arvizu, Z. Qiu, G. A. Niklasson, T. Edvinsson, Impedance Spectroscopy Modeling of Nickel–Molybdenum Alloys on Porous and Flat Substrates for Applications in Water Splitting. *The Journal of Physical Chemistry C* **123**, 23890-23897 (2019).
83. Y. Lian *et al.*, Carved nanoframes of cobalt-iron bimetal phosphide as a bifunctional electrocatalyst for efficient overall water splitting. *Chem Sci* **10**, 464-474 (2019).
84. K. Li *et al.*, Bimetallic Iron–Cobalt Catalysts and Their Applications in Energy-Related Electrochemical Reactions. *Catalysts* **9**, (2019).
85. N. Sato, *Electrochemistry at Metal and Semiconductor Electrodes*. E. S. B.V., Ed., (Japan, 1998).
86. O. N. Ogidi-Ekoko *et al.*, Electrical properties of MgO/GaN metal-oxide-semiconductor structures. *Solid-State Electronics* **172**, (2020).

87. W. Li, D. Xiong, X. Gao, L. Liu, The oxygen evolution reaction enabled by transition metal phosphide and chalcogenide pre-catalysts with dynamic changes. *Chem Commun (Camb)* **55**, 8744-8763 (2019).

88. B. R. Wygant, K. Kawashima, C. B. Mullins, Catalyst or Precatalyst? The Effect of Oxidation on Transition Metal Carbide, Pnictide, and Chalcogenide Oxygen Evolution Catalysts. *ACS Energy Letters* **3**, 2956-2966 (2018).

89. X. Zhao, X. Guo, Z. Yang, H. Liu, Q. Qian, Phase-controlled preparation of iron (oxyhydr)oxide nanocrystallines for heavy metal removal. *Journal of Nanoparticle Research* **13**, 2853-2864 (2010).

90. F. Hui *et al.*, Defects Promoted Topotactic Transformation from Co(OH)2 Nanodiscs To Co3O4 Nano Octahedra. *Materials Science* **25**, 335-339 (2019).

91. B. Qu *et al.*, Ultrasmall Fe(2)O(3) nanoparticles/MoS(2) nanosheets composite as high-performance anode material for lithium ion batteries. *Sci Rep* **7**, 42772 (2017).

92. S. Agarwala, Z. H. Lim, E. Nicholson, G. W. Ho, Probing the morphology-device relation of Fe(2)O(3) nanostructures towards photovoltaic and sensing applications. *Nanoscale* **4**, 194-205 (2012).

93. D. Su, X. Xie, P. Munroe, S. Dou, G. Wang, Mesoporous hexagonal Co3O4 for high performance lithium ion batteries. *Sci Rep* **4**, 6519 (2014).

94. Q. Xu *et al.*, Improving the triethylamine sensing performance based on debye length: A case study on α-Fe2O3@NiO(CuO) core-shell nanorods sensor working at near room-temperature. *Sensors and Actuators B: Chemical* **245**, 375-385 (2017).

95. D. Y. Chung *et al.*, Dynamic stability of active sites in hydr(oxy)oxides for the oxygen evolution reaction. *Nature Energy* **5**, 222-230 (2020).

96. P. Giannozzi *et al.*, QUANTUM ESPRESSO: a modular and open-source software project for quantum simulations of materials. *J Phys Condens Matter* **21**, 395502 (2009).

97. J. P. Perdew, K. Burke, M. Ernzerhof, Generalized Gradient Approximation Made Simple. *Physical Review Letters* **77**, (1996).

98. S. Grimme, Semiempirical GGA-type density functional constructed with a long-range dispersion correction. *J Comput Chem* **27**, 1787-1799 (2006).

99. P. Wisesa, K. A. McGill, T. Mueller, Efficient generation of generalized Monkhorst-Pack grids through the use of informatics. *Physical Review B* **93**, (2016).

Chapter- 1.3 Magnetically activated iron nanostructures for water splitting

Summary:

Magnetically influenced water splitting satisfactorily avoids the sluggish kinetics of OER with consideration of magnetohydrodynamics and spin contribution from the magnetic electrocatalyst. The induced magnetism in the nanodomains reflects the hidden potential of the sites with their enduring magnetic role towards the electromagnetic behavior. Herein, the iron nano-ligaments obtained via single-step borohydride reduction synergize with the metal support and form a new spinel $NiFe_2O_4$ *phase at room temperature during electrocatalysis. The magnetically active phase aligns with the one-time activation and demonstrates remarkable performance at low overpotentials, gives high current density, and immense stability. Very low overpotentials were required with astonishing stability for 4200 hours at a high external load of 1 A* cm^{-2} *towards OER. Ultra-high current densities of 17 A* cm^{-2} *and 12 A* cm^{-2} *were achieved for OER and HER, respectively. Full cell arrangement also showed robustness for 1300 h. Testing the one-time magnetized catalyst under harsh conditions of high concentrations (110 mV for 1 A* cm^{-2} *in 10 M KOH) of alkaline electrolytes and high temperatures (180 mV for 1 A* cm^{-2} *at 80 °C) also delivered excellent performance. The in-situ studies and ex-situ post-reaction analyses reveal that the catalyst surface transforms to oxyhydroxide species with coexisting in-situ generated spinel Ni ferrites and metallic Fe at room temperature. These components act as the active catalytic sites, which is the probable reason behind the remarkable performance.*

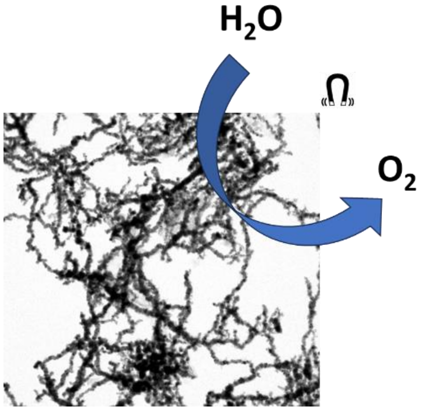

(A patent based on this work has been submitted and a manuscript under preparation)

1.3.1. Introduction:

Hydrogen production through electrochemical water splitting is fast emerging as an alternative to conventional steam reforming. The sluggish kinetics associated with the counter oxygen evolution reaction (OER) is one of the major impediments to transforming this process into a large-scale industrial hydrogen production. The kinetics of the OER are often influenced by various polarization effects, viz, concentration, activation, ohmic, etc. One of the primary contribution to these polarizations arises from the resistance offered by the gas bubbles generated that evolved during the reaction. As the gas bubble attaches to the active surface of the catalyst, the electrochemical surface becomes inaccessible for the reaction to occur. Also, the conductivity of the electrolyte gets adversely affected by increased void space, hampering the overall performance.(*1, 2*) A simple way to avoid bubble accumulation is using external agitation during the electrochemical analysis, but it is effective only when the bubble growth reaches a definite size.

Recent studies utilize the magnetic field(*3-5*) to induce a Lorentz force which facilitates the removal of bubbles at the early stages of formation, a process known as magnetohydrodynamics (MHD).(*6*) Further, the adsorbed species at the electrode-electrolyte interface are subjected to the Maxwell stress effect in the presence of the magnetic field, affecting the double-layer capacitance and, thus, the active surface area.(*7, 8*) In the case of magnetic materials, the alignment of magnetic spins (spin parity) also facilitates the direct production of oxygen molecules in an energy-efficient spin-triplet ground state.(*9-11*) The spins at the adjacent metal sites in magnetic materials can be influenced by magnetic fields and align themselves in spin parallel orientation. The upcoming O* intermediates at these adjacent metal sites are thereby effectively adsorbed in a parallel direction only, leading to the formation of an O_2 molecule in a spin-triplet ground state.(*12*)

Although various strategies have been employed to enhance the kinetics of the 4 electron OER process, developing a highly stable, non-noble metal catalyst and generating a high current density (> 1A cm^{-2}) at low overpotential is still challenging to realize their commercial potential. Several reports claimed a current density of 1 A cm^{-2} but only at an overpotential of around 350 mV and lack long-term stability.(*13-22*) Y Liu et al. reported LDH nanodomains on Fe foam by corrosion engineering in the presence of divalent metal ions and showed OER stability for over 6000 h at 1 A cm^{-2} current density but with a high overpotential of 340mV (in 1M KOH).(*23*) The highest OER activity reported for NiFe-based catalysts so far is 3 A cm^{-2} at 370 mV **(*Table 1.3.1.*)**.(*24*) Nevertheless, it showed an overpotential of 300 mV at a current density of 1.1 A cm$^{-2,}$ and the chronoamperometry test to indicate the catalytic stability was shown only for 12 h. Several reports depict the degradation of the catalysts during the stability test (within 50 h run time) performed at high current densities.

Table 1.3. 1. Reported electrocatalysts showing high current densities towards oxygen evolution reaction (OER).

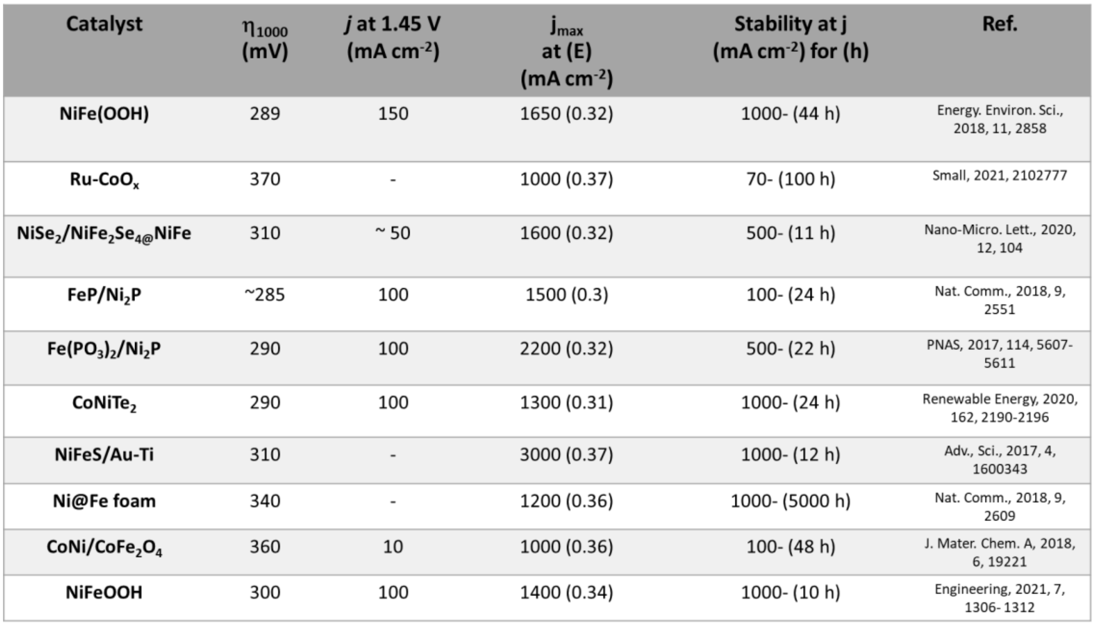

Catalyst	η_{1000} (mV)	*j* at 1.45 V (mA cm^{-2})	j_{max} at (E) (mA cm^{-2})	Stability at j (mA cm^{-2}) for (h)	Ref.
NiFe(OOH)	289	150	1650 (0.32)	1000- (44 h)	Energy. Environ. Sci., 2018, 11, 2858
Ru-CoO$_x$	370	-	1000 (0.37)	70- (100 h)	Small, 2021, 2102777
NiSe$_2$/NiFe$_2$Se$_{4@}$NiFe	310	~ 50	1600 (0.32)	500- (11 h)	Nano-Micro. Lett., 2020, 12, 104
FeP/Ni$_2$P	~285	100	1500 (0.3)	100- (24 h)	Nat. Comm., 2018, 9, 2551
Fe(PO$_3$)$_2$/Ni$_2$P	290	100	2200 (0.32)	500- (22 h)	PNAS, 2017, 114, 5607-5611
CoNiTe$_2$	290	100	1300 (0.31)	1000- (24 h)	Renewable Energy, 2020, 162, 2190-2196
NiFeS/Au-Ti	310	-	3000 (0.37)	1000- (12 h)	Adv., Sci., 2017, 4, 1600343
Ni@Fe foam	340	-	1200 (0.36)	1000- (5000 h)	Nat. Comm., 2018, 9, 2609
CoNi/CoFe$_2$O$_4$	360	10	1000 (0.36)	100- (48 h)	J. Mater. Chem. A, 2018, 6, 19221
NiFeOOH	300	100	1400 (0.34)	1000- (10 h)	Engineering, 2021, 7, 1306- 1312

1.3.2. Scope of the present investigation:

In this report, we have demonstrated iron nano-ligaments (Fe-L) formed by the assembly of iron nanoparticles on incorporation into a nickel foam (Fe@NF), act as an efficient electrocatalyst for OER in alkaline conditions. The Fe@NF on one-time exposure to a magnetic field (0.13 T) exhibits extraordinary enhancement for OER with a 700% increase in magnetic current density. Post-reaction analysis shows *in situ* formed Fe@NiFe$_2$O$_4$ species during the OER cycles. It shows an overpotential of 110 mV for 1A cm^{-2} in 10 M KOH. Furthermore, it shows more than 4200 h stability at 1 A cm^{-2} and more than 800 h at 5 A cm^{-2} current density. Indeed, it shows an increase in current density of 5.7 A cm^{-2} after 800 h. This is the highest all-round performance reported by a non-noble-based catalyst towards OER. The magnetic influence on the catalyst was permanent, and a stable catalytic response was achieved for more than 6 months.

1.3.3. Materials and methods:

1.3.3.1. Materials required:

The materials required for the synthesis of various catalysts and their application in electrochemical analysis were purchased from different sources. Anhydrous ferric chloride ($FeCl_3$), and nickel chloride hexahydrate ($NiCl_2$. 6 H_2O) from S D Fine Chemicals, standard Fe_2O_3, and Fe_3O_4 catalysts, $NaBH_4$, and 5 wt % Nafion® perfluorinated resin solution purchased from Sigma-Aldrich, HCl (37%, AR grade), KOH, and isopropyl alcohol (IPA) from Merck Chemicals. All chemicals were used as received without any further purification. Milli Q water (18.2 S cm) is used for all the synthesis and electrochemical analyses. Ni foam (1.6 mm thick) used as the support for electrochemical studies was purchased from MTI, USA.

1.3.3.2. Synthesis of electrocatalysts:

i) Synthesis of iron nanostructures:

Iron nano-ligaments (Fe-L) were synthesized **(*Figure 1.3.1.*)** by a one-step borohydride reduction route.(*25, 26*) For the synthesis, 30 mL of 0.1 M metal chloride solution was rapidly added to freshly prepared 150 mL of 1.0 M aqueous $NaBH_4$ solution under vigorous stirring. The final solution was stirred for another 30 minutes. The obtained product was washed three times with water and ethanol and then dried at around 60 ℃ overnight in an oven. A similar procedure was followed for the synthesis of Ni nanostructures (Ni-ns), wherein the Fe salt solution was replaced with Ni salt solution. The reduced form of Ni-ns was used for control studies, synthesized by heating Ni-ns in H_2 environment at 500 ℃ in a tubular furnace.

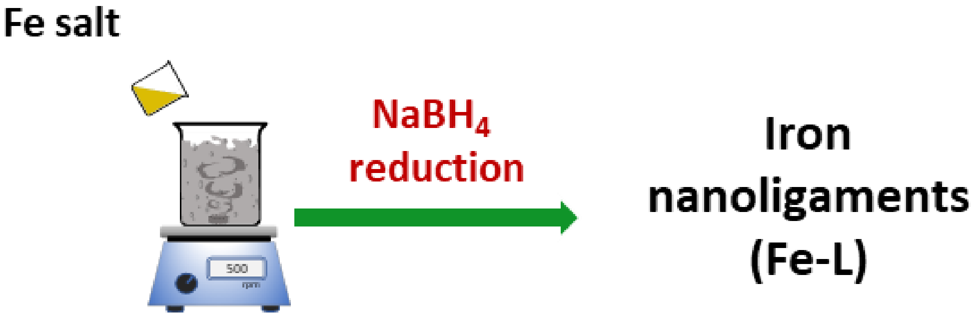

Figure 1.3. 1. Schematics showing synthesis of iron nanoligaments (Fe-L) through borohydride reduction.

ii) Preparation of FeOOH and NiOOH:

The FeOOH catalyst was synthesized by the reported procedure.(*27*) In a typical synthesis, 1.2 g of $Fe(NO_3)_2$. $9H_2O$ was dissolved in 25 mL water. To this 0.2 g of PVP (to improve the dispersity of particles) was added followed by 9 mL of 5 M NaOH under vigorous stirring. After 3 h of stirring, the solution was transferred to a Teflon-lined autoclave and heated at 120 °C for 12 h. The product was washed with water and ethanol and dried. Also, NiOOH catalyst was synthesized(*28*) by adding 100 mL 1.0 M NaOH to 1.4 g of Ni-ns under stirring. $K_2S_2O_8$ was added to the solution, which was kept under stirring for 24 h. The precipitate was collected by centrifugation and washing three times with water and ethanol. The observed light green powder was dried at 80 °C under vacuum.

iii) Synthesis of Fe_3O_4 and $NiFe_2O_4$:

The Fe_3O_4 catalyst was synthesized by oxidizing Fe-L powder in the air at 350 °C in a muffle furnace. $NiFe_2O_4$ spinel was synthesized following the reported procedure(*11*) wherein 50 mL of 50 mM ferric nitrate solution was stirred with glycine (1.2 times that of metal concentration) till dissolution. The resultant solution was heated to 200 °C till evaporation. The porous dark brown solid was sintered at 1100 °C for 1 h in a box furnace in the air.

1.3.3.3. Characterizations and electrochemical studies:

The instrumentation techniques (PXRD, FESEM, TEM, Raman, XPS, etc) used to characterize the samples are described in detail in the appendix at the end of this thesis.

Electrochemical measurements were investigated using electrochemical workstations, (660C, USA) obtained from CH instruments. for evaluating the electrochemical activities of catalysts towards oxygen evolution reaction (OER), hydrogen evolution reaction (HER), overall water splitting and other electrochemical analyses. However, measurements at high current-potentials were carried out using 2461-US, Hi Current Interactive Source Meter Unit, Tektronix/Keithley. Primary electrochemical measurements were carried out in a self-designed standard three-electrode acrylic cuboidal cell (2x2x5 cm). The working electrode was prepared by dispersing iron nano ligaments (Fe-L) in isopropyl alcohol was drop-casted on Ni foam (catalyst loading was 2.46 mg cm^{-2}) with a high surface area graphite rod/ Pt coil, and mercury-mercuric oxide (Hg/HgO) used as the counter and reference electrodes, respectively. All the polarization curves are reported with 85% iR compensation (wherever mentioned if iR uncompensated) arising due to the ohmic resistance of the cell. All the measured potentials are reported with respect to the reversible hydrogen electrode (RHE). The obtained current densities were normalized to the geometrical surface area of the NF electrode. The magnetic field was applied using two permanent (NdFeB) magnets of dimension 1x2x4 cm.

1.3.4. Results and discussion:

1.3.4.1. Characterization of Fe-L catalyst:

The phase purity of the as-synthesized Fe-L catalyst was analyzed by powder X-ray diffraction (PXRD) study. The PXRD pattern **(*Figure 1.3.2.a*)** shows strong peaks for α-Fe (# PDF no. 24963) at 2θ values 44.9, 65, and 82.6 degrees associated with the (110), (200), and (211) planes. In addition, a small peak associated with the (311) plane of Fe_3O_4 (# PDF no. 31770) was also observed. The iron crystallite size calculated from the Scherrer equation was found to be 10 nm. The field emission scanning electron microscopy (FESEM) image **(*Figure 1.3.2.b*)** shows ligament-like morphology formed by the assembly of iron nanoparticles, which was further confirmed by TEM images.

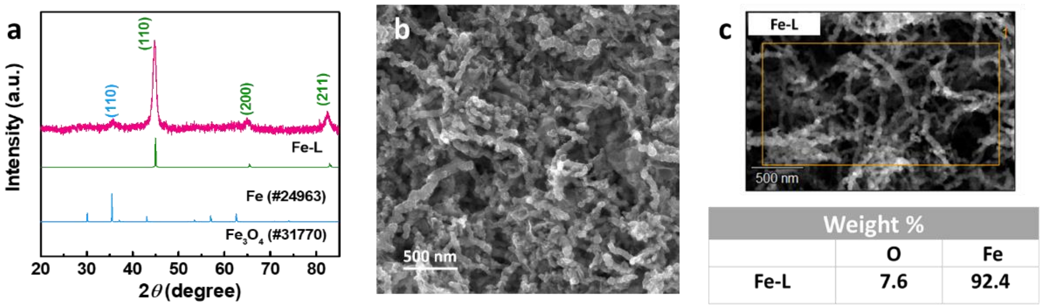

	O	Fe
Fe-L	7.6	92.4

Figure 1.3. 2. (a) Powder X-ray diffraction (PXRD) pattern, (b) field emission scanning electron microscopy (FESEM) image, and (c) EDS analysis of Fe-L catalyst.

The average width of the nano-ligaments lies in the range of 20-60 nm, and the length is 500 nm to 1 μm. These ligaments **(*Figure 1.3.3.a*)** are composed of iron nanoparticles of size ranging from 5-10 nm. The high-resolution transmission electron microscopy (HRTEM) image **(*Figure 1.3.3.b*)** shows major lattice fringes corresponding to elemental Fe species. The selected area electron diffraction (SAED) pattern **(*Figure 1.3.3.c*)** shows major planes corresponding to the elemental Fe. The percentage of Fe to O **(*Figure 1.3.2.c*** and ***Figure 1.3.3.d-f*)**, as observed from the energy dispersive X-ray (EDS) analysis, was 12:1 in the system. This analysis validates the coexistence of iron in metallic and oxidized states as observed in PXRD.

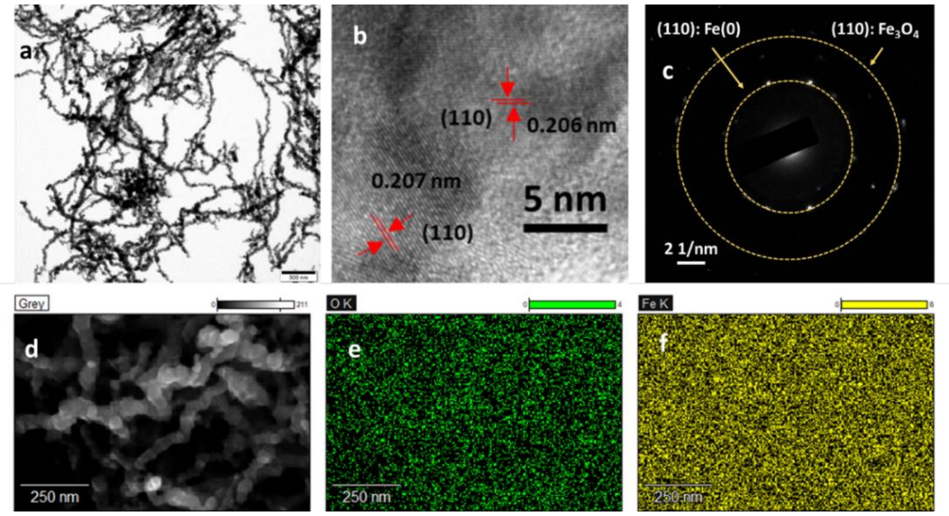

Figure 1.3. 3. (a) Transmission electron microscopy (TEM) image, (b) High-resolution transmission electron microscopy (HRTEM) image (c) selected area electron diffraction pattern(SAED), and (d-f) energy dispersive X-ray spectroscopy images of Fe-L catalyst.

Raman analysis of different regions shows various transitions with peaks foe the presence of Fe_3O_4 at 212 cm^{-1}, 274 cm^{-1}, 386 cm^{-1}, 482 cm^{-1}, 585 cm^{-1}, and 1283 cm^{-1} corresponding to A_{1g} (1), E_g (1) + E_g (2), E_g (3), A_{1g} (2), E_g (4) transitions, and second order scattering, respectively (***Figure 1.3.4.a***).(*29*, *30*) The intensity of peaks observed for Fe-L sample were 20 % of the oxidised sample, Fe_3O_4 (***Figure 1.3.4.b***). The PXRD of oxidized sample (***Figure 1.3.4.c***) showed peaks corresponding to Fe_3O_4 species.

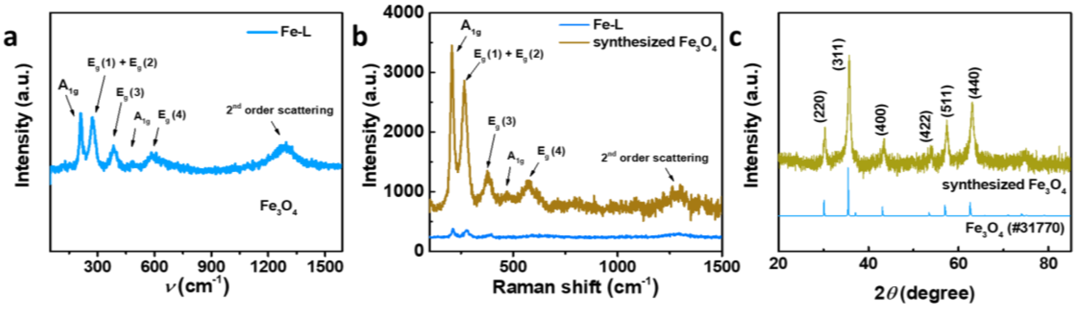

Figure 1.3. 4. Raman spectra of (a) Fe-L powder, and (b) FeO_x and Fe-L samples, and (c) PXRD of synthesized Fe_3O_4 sample.

The chemical nature of elements in the Fe-L catalyst was characterized by X-ray photoelectron spectroscopy (XPS).(*31*) The high-resolution spectra of Fe 2p (***Figure 1.3.5.a***) show Fe (0) peaks at 706.5 eV (Fe $2p_{3/2}$) and 719.5 eV (Fe $2p_{1/2}$) along with the satellite peaks at 713.6 eV, 716.9 eV, 726.6 eV, and 730 eV. In addition, it shows peaks for Fe^{3+} species (at 709.3 eV and 722.3 eV assigned to Fe $2p_{3/2}$ and Fe $2p_{1/2}$) and Fe^{2+} species (at 711 eV and 724 eV for Fe $2p_{3/2}$ and Fe $2p_{1/2}$ respectively) associated with Fe_3O_4. The O 1s high-resolution spectra (***Figure 1.3.5.b***) show two peaks at 529 eV and 531 eV assigned to the presence of lattice oxygen and adsorbed oxide species, respectively.

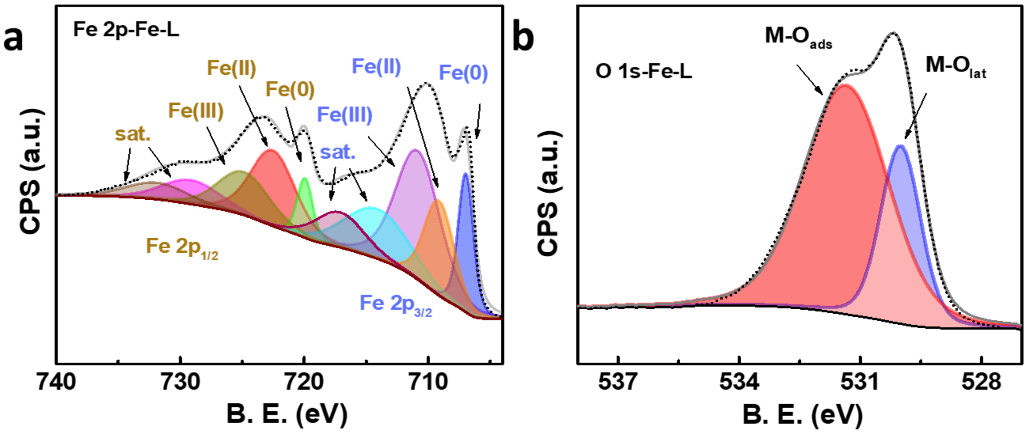

Figure 1.3. 5. High-resolution X-ray photoelectron spectroscopy (XPS) with (a) Fe 2p, and (b) O 1s spectra of Fe-L sample.

1.3.4.2. Electrochemical studies:

The electrochemical measurements were carried out in a self-designed electrochemical setup **(*Figure 1.3.6.*).**

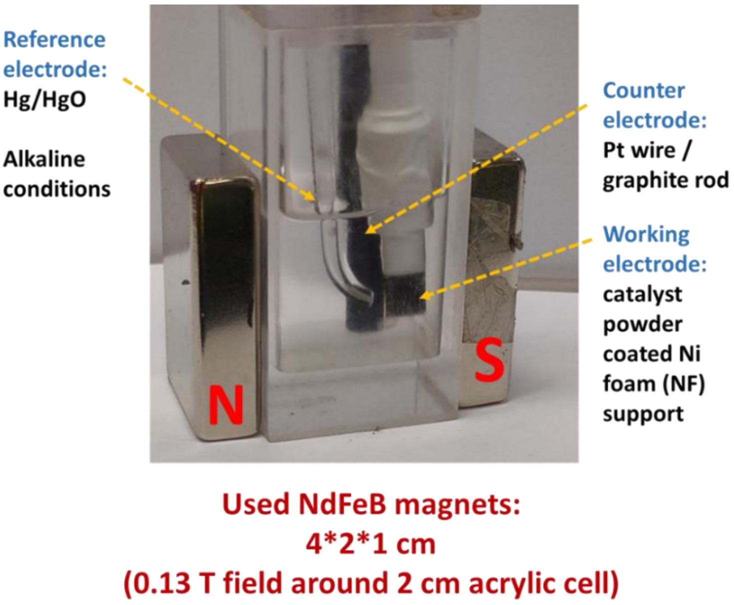

Figure 1.3. 6. Electrochemical setup (acrylic cell with powder coated Ni foam as working, graphite rod as the counter, and Hg/HgO as the reference electrodes.

Polarised linear sweep voltammograms (LSVs) were carried out for first 15 cycles in absence of magnetic field at 5 mV s^{-1} to get stable overlapping LSVs. Fe@NF catalyst showed an overpotential of 190 mV for the current density of 200 mA cm^{-2} **(*Figure***

***1.3.7.*)**. Then the Fe@NF was placed in a magnetic field (0.13T) using two rectangular permanent magnets (NdFeB) for 10 minutes. The one-time, magnetic field-treated Fe@NF is abbreviated as Fe@NF(M) catalyst **(*Figure 1.3.7.*)**.

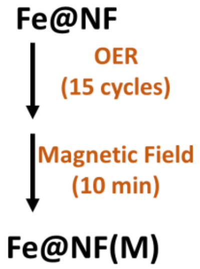

Figure 1.3. 7. Way of electrochemical measurement.

This magnetic field-treated Fe@NF catalyst shows a huge jump in current density (from 200 mAcm^{-2} to 1.6 Acm^{-2}), a 700% increase **(*Figure 1.3.8.*)** in magnetocurrent density at an overpotential of 190 mV. A high reproducibility **(*Figure 1.3.9.b*)** in its performance is evident from the similar values (the overpotential varies within the range of 20 mV) observed for different synthesized batches of Fe@NF(M) catalysts.

It is to be noted that this increase in current density after one-time magnetic field activation is permanent and is stable for more than 6 months. The Fe@NF(M) catalyst attained a high current density of 5.5 A cm^{-2} at a very low overpotential of 230 mV in 1 M KOH **(*Figure 1.3.9.a*)**, which is, to our knowledge, the lowest value ever reported.

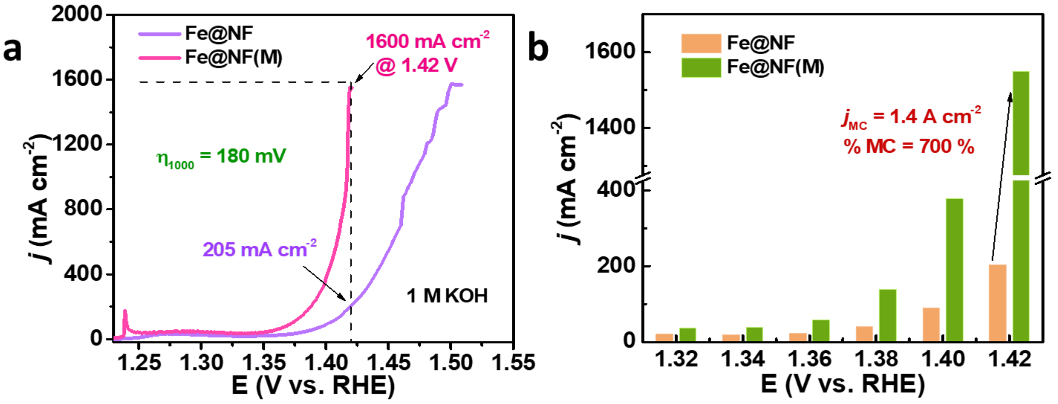

Figure 1.3. 8. (a) Polarized linear sweep voltammograms (LSVs) of Fe@NF catalyst before and after magnetic field influence, and (b) magneto-current density (j_{MC}) and % magnetocurrent (% j_{MC}) of Fe@NF catalyst in 1.0 M KOH.

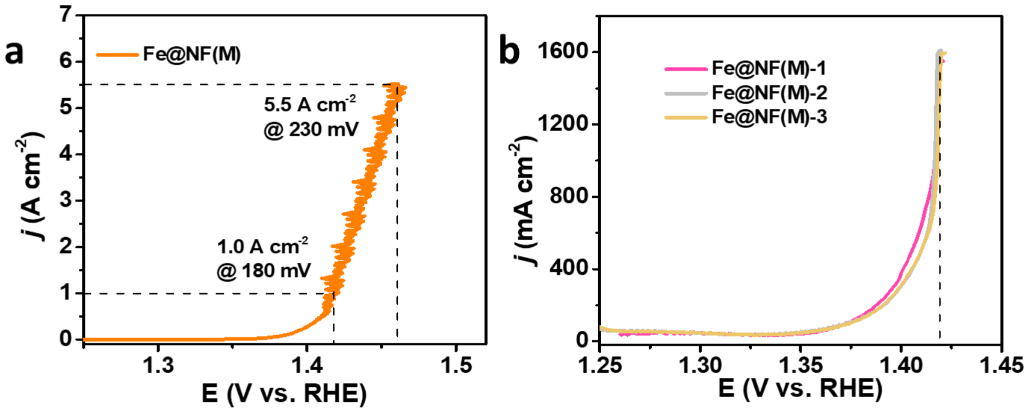

Figure 1.3. 9. (a) High current study, and (b) reproducibility of Fe@NF(M) catalyst in 1.0 M KOH.

The performance of IrO_2 and blank NF **(*Figure 1.3.10.*)** were minimal (11 mA cm^{-2} and 16 mA cm^{-2}) whereas Fe@NF(M) catalyst showed comparably high current density of 1.6 A cm^{-2} at 1.42 V.

The Fe@NF(M) catalyst showed **(*Figure 1.3.12.a*)** a significantly low Tafel slope (47.0 mV dec^{-1}) as compared to the Fe@NF catalyst (60.4 mV dec^{-1}), indicating the improved kinetics in the treatment of Fe@NF with a magnetic field. The double-layer capacitance (C_{dl}) studies (by CV analysis, ***Figure 1.3.11.***) show an increased C_{dl} value **(*Figure 1.3.12.b*)** for Fe@NF(M) (10.0 mF cm^{-2}) as compared to Fe@NF (5.5 mF cm^{-2}).

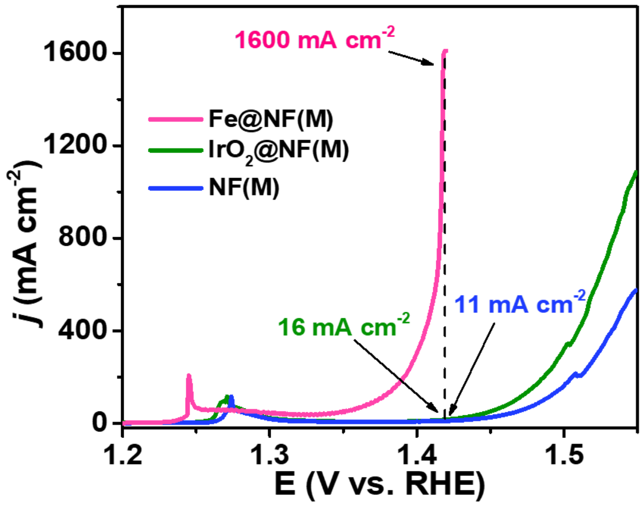

Figure 1.3. 10. Polarized linear sweep voltammograms (LSVs) of Fe@NF, Fe@NF(M), IrO_2, and blank NF.

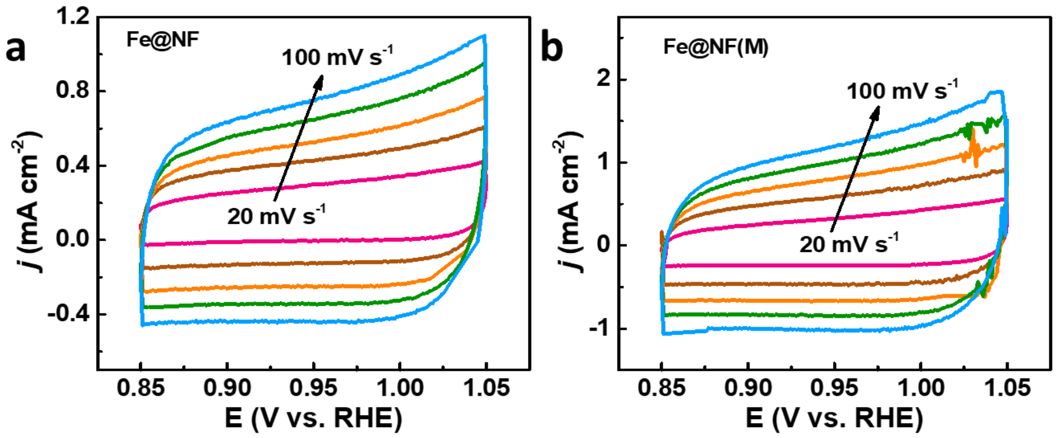

Figure 1.3. 11. Cyclic voltammetry studies in non-Faradaic region for C_{dl} analysis of (a) Fe@NF, and (b) Fe@NF(M) catalysts.

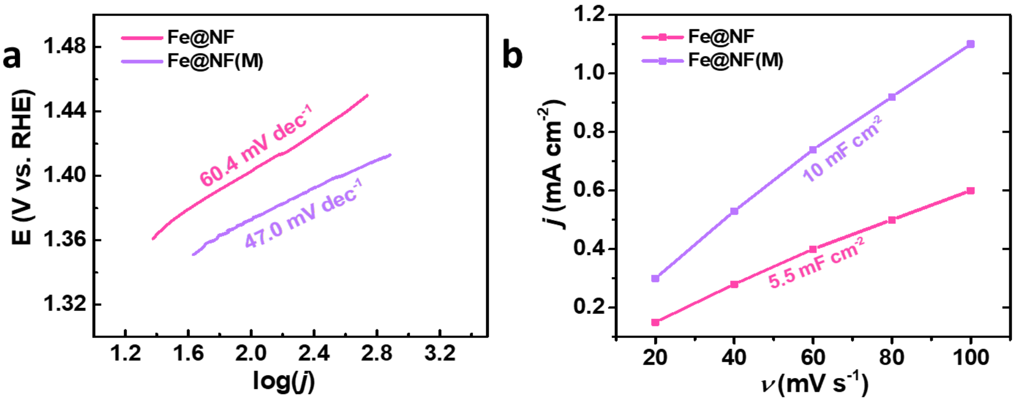

Figure 1.3. 12. (a) Tafel, and (b) double layer capacitance analysis of Fe@NF catalysts in 1.0 M KOH.

The corresponding electrochemically active surface area (ECSA) obtained from C_{dl} shows a value of 35 cm^2 for Fe@NF and 62.5 cm^2 for Fe@NF(M)), a huge increase in ECSA on exposure to magnetic field. The current density normalized to ECSA **(*Figure 1.3.13.a*)** shows an increase in active sites and an improvement in intrinsic activity. Further, the electrochemical impedance study **(*Figure 1.3.13.b*)** reveals a low charge transfer resistance (R_{ct}) for Fe@NF(M), suggesting improved charge transfer kinetics of Fe@NF on treatment with the magnetic field.

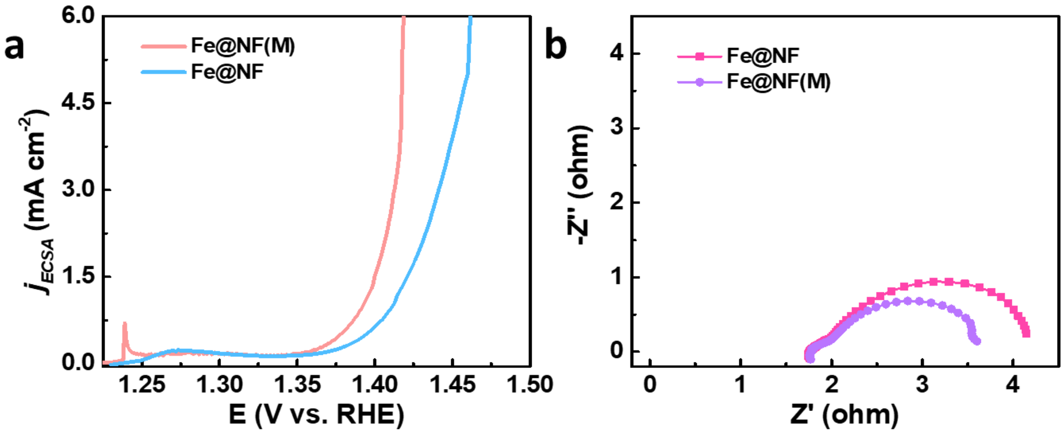

Figure 1.3. 13. (a) Electrochemically active surface area (ECSA) normalized LSVs, and (b) impedance analysis of Fe@NF, and Fe@NF(M) catalysts.

The stability and durability of the Fe@NF(M) catalyst towards OER were tested in both potentiostatic and galvanostatic modes. Fe@NF(M) maintained a constant current density of 1 A cm^{-2} without any change in the potential for more than 4200 h **(*Figure 1.3.14.a*)** in the galvanostatic mode. In comparison, the potential of the IrO_2 catalyst and blank NF support rises in just 100 h **(*Figure 1.3.14.b, c*)** to retain the current density of 1 A cm^{-2}.

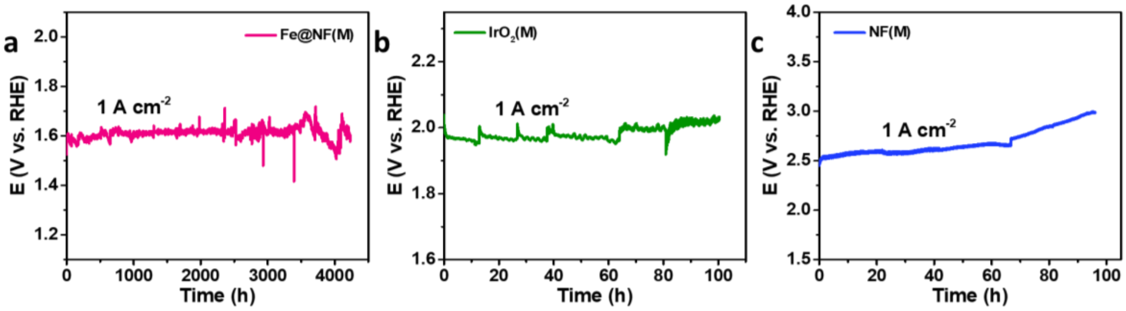

Figure 1.3. 14. Galvaostatic studies of (a) Fe@NF(M), (b) IrO_2, and (c) NF catalysts towards OER in 1.0 M KOH.

Potentiostatic mode stability tests **(*Figure 1.3.15.*)** were also done over Fe@NF(M) catalyst at various constant potentials to achieve current densities from 500 mA cm^{-2} to 5 A cm^{-2}. It is to be noted that Fe@NF(M) shows extraordinary stability, more than 800 h (more than a month), even at a very high current density of 5 A cm^{-2} at 1.46 V. To our knowledge, this is the highest ever reported stability test, at a high current density with a very low overpotential.

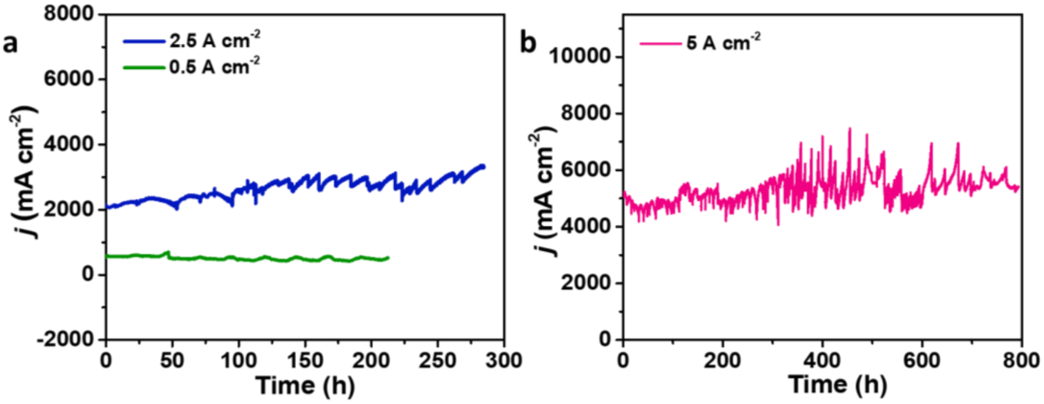

Figure 1.3. 15. Potentiostatic studies of Fe@NF(M) catalyst at (a) 0.5 A cm^{-2} (at 1.41 V vs. RHE), and 2.5 A cm^{-2}(at 1.43 V vs. RHE), and (b) 5 A cm^{-2} (at 1.46 V vs. RHE).

Furthermore, an accelerated degradability test (***Figure 1.3.16.a***) was performed for 10,000 cycles, and the catalyst Fe@NF(M) retained its performance very well. Also, the multistep technique in potentiostatic mode (***Figure 1.3.16.b***) was employed (step size of 1 h), and the catalyst demonstrates great durability even at higher loads. For all these stability studies, no degradation in the performance of the catalyst was observed.

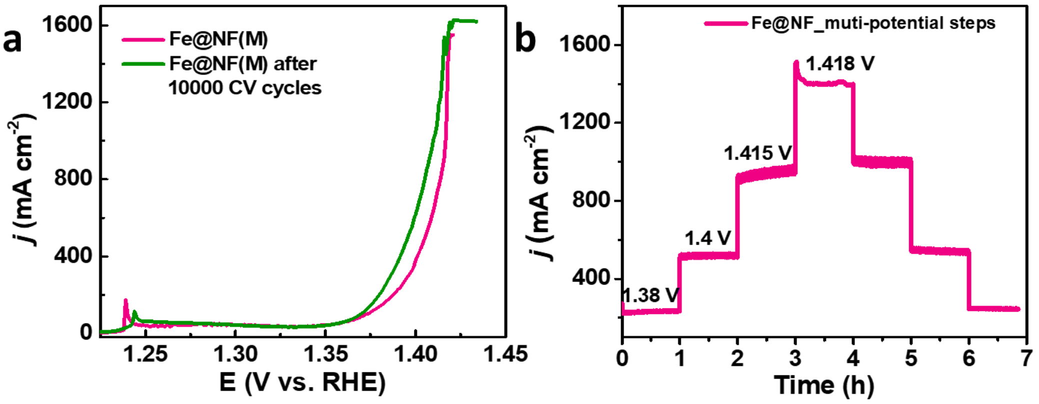

Figure 1.3. 16. (a) Accelerated degradability test (ADT), and (b) multistep chronoamperometry analysis of Fe@NF(M) catalyst.

It is to be noted that the temperature of the electrolyte reaction reached around 70 °C during the chronoamperometry tests at a high current density of 5 A cm^{-2}. The stability was retained even at this high temperature of the system. Moreover, when the electrolyte concentration is at 10M (***Figure 1.3.17.***), often industrial scale process demand, the overpotential is reduced to 110 mV to attain a current density of 1 A cm^{-2}.

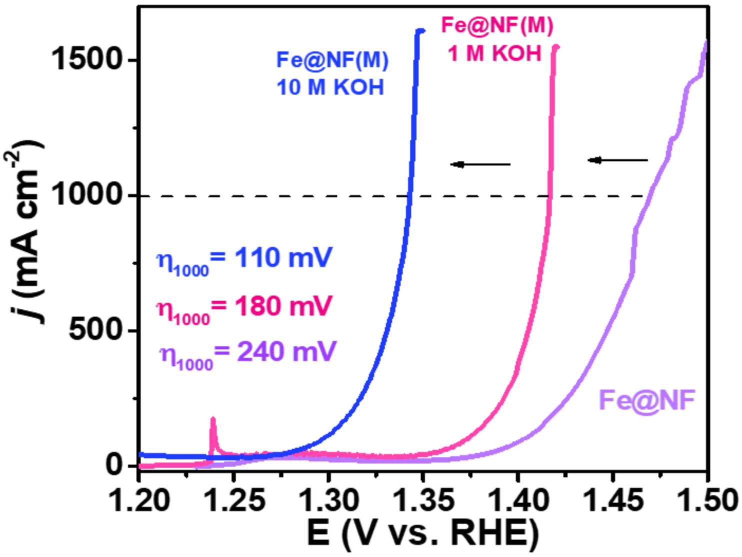

Figure 1.3. 17. Linear sweep voltammogram of Fe@NF(M) in 10 M KOH.

To check the performance of the material under harsh conditions of high external potentials, the OER activity of the Fe@NF(M) catalyst was analyzed using a high current-potential determining source meter unit without considering iR compensation. Very high current densities (***Figure 1.3.18.***) as high as 17 A cm^{-2} at 5.8 V (vs. RHE) in three-electrode arrangement.

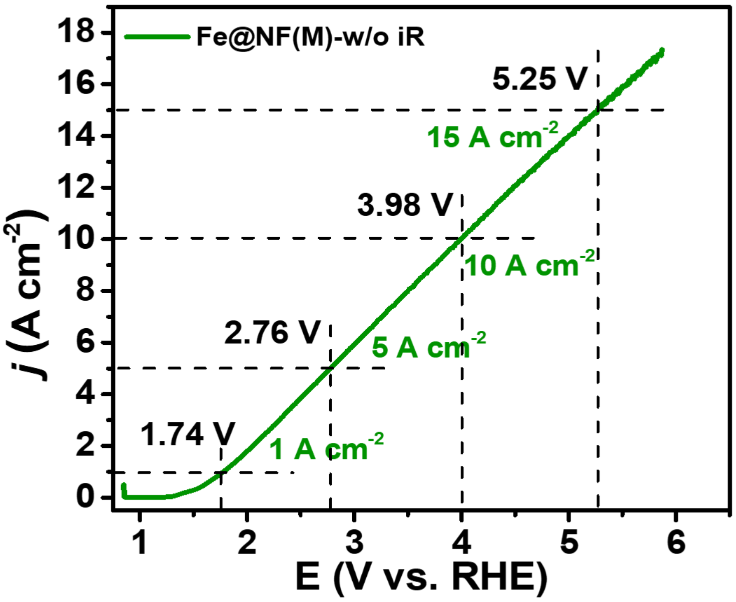

Figure 1.3. 18. High current potential measurements without iR compensation of Fe@NF(M) catalyst in 1.0 M KOH towards OER.

1.3.4.3. Determining the contributions from various magnetically assisting factors:

The contribution of the MHD effect and the Maxwell stress for the enhanced OER performance in Fe@NF(M) is ruled out, as we have seen no difference (***Figure 1.3.19.***) in performance for Fe@NF(M) in the presence and absence of a magnetic field. The significant contribution to the high performance of Fe@NF(M) compared to the Fe@NF catalyst originated from the spin contribution on exposure of Fe@NF to the magnetic field, leading to the generation of oxygen molecules in its triplet ground state.(*11*, *12*) This was further confirmed by carrying out the OER in a neutral medium (1.0 M PBS) as well as electrochemical oxidation of methanol over Fe@NF as control experiments. In contrast to alkaline OER, where OH^- acts as the reactant, in a neutral medium, H_2O serves as the reactant, and the spin-dependent pathway is not the potential determining step. Consequently, the OER activity of Fe@NF remains unchanged in the neutral medium (***Figure 1.3.19.a***) in the presence of the magnetic field. Also, the spin-dependent kinetics is not favorable for methanol electrooxidation. Hence, there is no improvement (***Figure 1.3.19.b***) in the performance of Fe@NF towards methanol oxidation reaction (MOR) in the presence of a magnetic field, further proving the dominant spin contribution for OER in alkaline conditions.

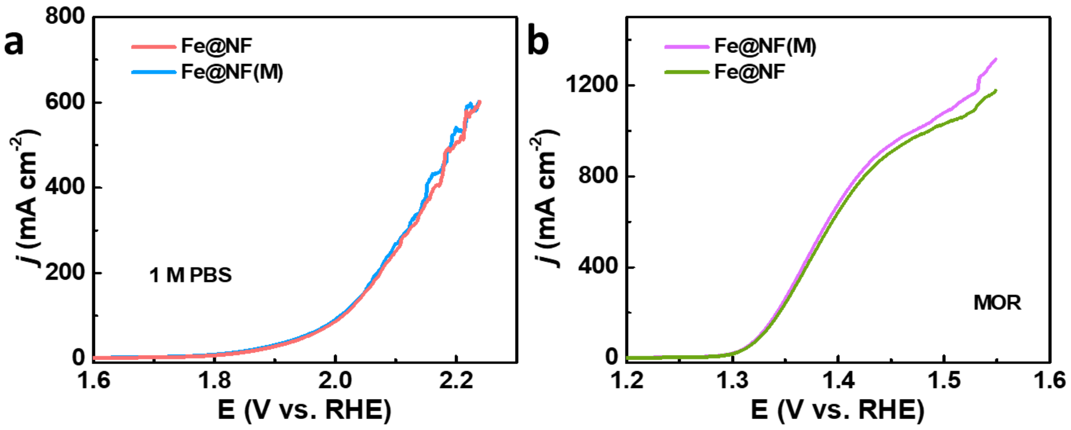

Figure 1.3. 19. Linear sweep voltammograms (LSVs) in (a) neutral 1.0 M PBS, and (b) methanol oxidation (1.0 M MeOH in 1.0 M KOH) reaction of Fe@NF catalysts.

1.3.4.4. HER studies in three-electrode arrangement:

Furthermore, the Fe@NF(M) showed good performance for HER in an alkaline medium. It attained a current density of 1.6 A cm^{-2} at an overpotential of 550 mV in 1.0 M KOH electrolyte (***Figure 1.3.20.a***). Chronopotentiometry study shows a stable HER performance for 1500 h (***Figure 1.3.20.b***) at a current density of 1 A cm^{-2} (at -0.6 V) while Pt/C and blank NF (***Figure 1.3.20.c, d***) showed stability but at high potentials.

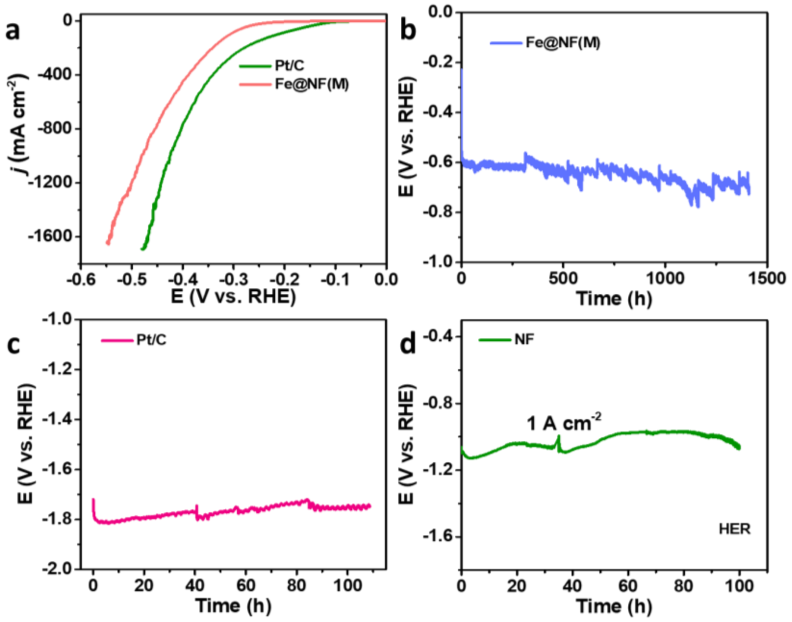

Figure 1.3. 20. (a) Linear sweep voltammograms (LSVs) of Fe@NF(M), and Pt/C catalysts, and chronopotentiometry analysis of (b) Fe@NF(M), (c) Pt/C, and (d) NF catalysts in 1.0 M KOH towards HER.

The multistep study (***Figure 1.3.21.a***) done at various potentials shows excellent stability of the Fe@NF(M) catalyst towards HER in 1.0 M KOH. With high external potential of -3.38 V (vs. RHE), the Fe@NF(M) catalyst showed (***Figure 1.3.21.b***) very high current density of -12 A cm^{-2} in three-electrode arrangement.

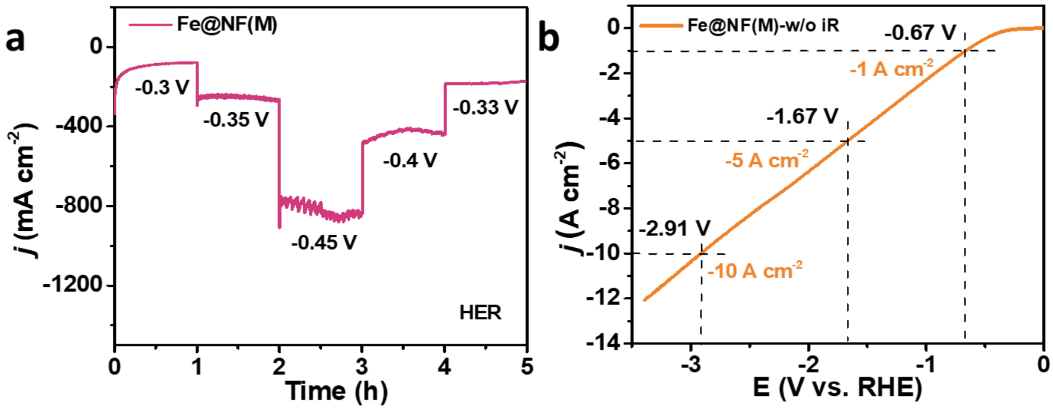

Figure 1.3. 21. (a) Multistep analysis in potentiostatic mode, and (b) linear sweep voltammetry observed during high current-potential study of Fe@NF(M) towards HER in 1.0 M KOH.

1.3.4.5. Full cell studies in two-electrode arrangement:

The full cell assembly, considering Fe@NF(M) catalyst as both anode and cathode (***Figure 1.3.22.a***), showed a current density of 715 mA cm^{-2} at 2.5 V in 1.0 M KOH. However, in 6.0 M KOH, the catalyst attained a current density of 1.58 A cm^{-2} at 2.5 V. Stable current density of 250 mA cm^{-2} (***Figure 1.3.22.b***) was attained for 1300 h in 6 M KOH. The stability of the standard Pt/C-IrO_2 couple (***Figure 1.3.22.c***) decreases in just 100 h in full cell arrangement.

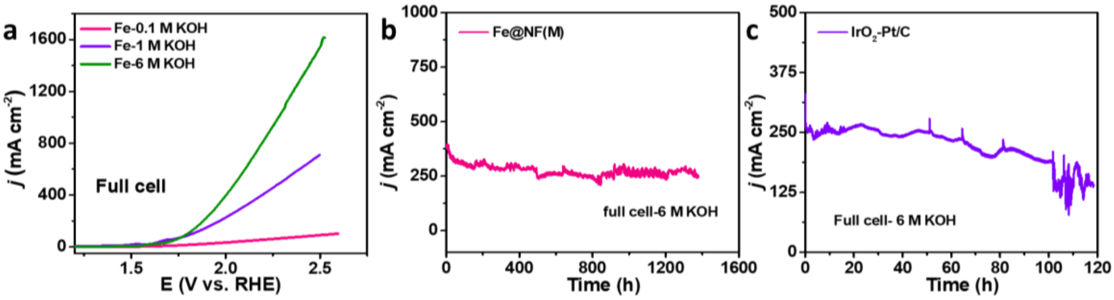

Figure 1.3. 22. (a) Linear sweep voltammetry (LSV), and (b) chronoamperometry analysis of Fe@NF(M), and (c) IrO2-Pt/C couples in full cell in 6.0 M KOH.

1.3.4.6. Varying temperature studies:

As the electrocatalysts in commercial electrolyzers are used at high temperatures (around 90 °C), we carried out the electrochemical studies at varying temperatures (40 °C, 60 °C, and 80 °C) by employing the same NF-coated electrodes in a small-sized glass cell. It is well stated that the activation energy required to attain a particular current density decreases with an increase in the temperature of the system, and similar is observed in this case of using Fe@NF catalyst. Overpotentials of 248 mV, 218 mV, 194 mV mV (***Figure 1.3.23.***) were required to achieve a current density of 100 mA cm^{-2} with temperatures at 40 °C, 60 °C, and 80 °C, respectively. Also, very low overpotentials of 190 mV, and 220 mV were required to achieve current densities of 1 A cm^{-2}, and 1.6 A cm^{-2} for an electrochemical OER carried out at 80 °C. A major concerning factor for electrochemical studies at high temperatures is low stability. An increase in temperature to nearly 70 °C was observed during the chronoamperometry studies of the Fe@NF(M) catalyst at a high current density of 5 A cm^{-2}, and the catalyst was stable for 800 h highlighting its robust nature.

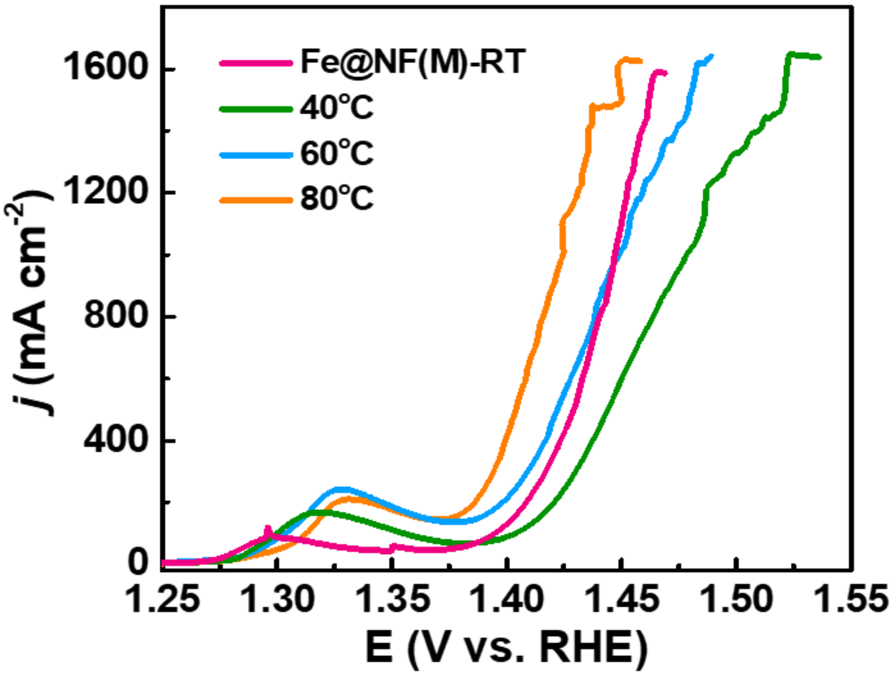

Figure 1.3. 23. Linear sweep voltammograms of Fe@NF catalyst at different temperatures in 1.0 M KOH.

1.3.4.7. Post-reaction analysis:

Post-reaction characterization was performed over Fe@NF and Fe@NF(M) catalysts after 1 h and 72 h OER measurements separately. The particles were removed from the NF electrode via sonication in absolute ethanol. PXRD analysis of the particles obtained after 1 h OER (***Figure 1.3.24., Figure 1.3.25.***) showed prominent peaks corresponding to the formation of $NiFe_2O_4$ spinel species (#PDF. 35596) in addition to Fe peaks. However, the sample collected after 72 h of the reaction (***Figure 1.3.25.***) showed very broad $NiFe_2O_4$ peaks, indicating the amorphization of the spinel phase in the long run. Interestingly, the peak corresponding to elemental Fe species was still retained even after 72 h.

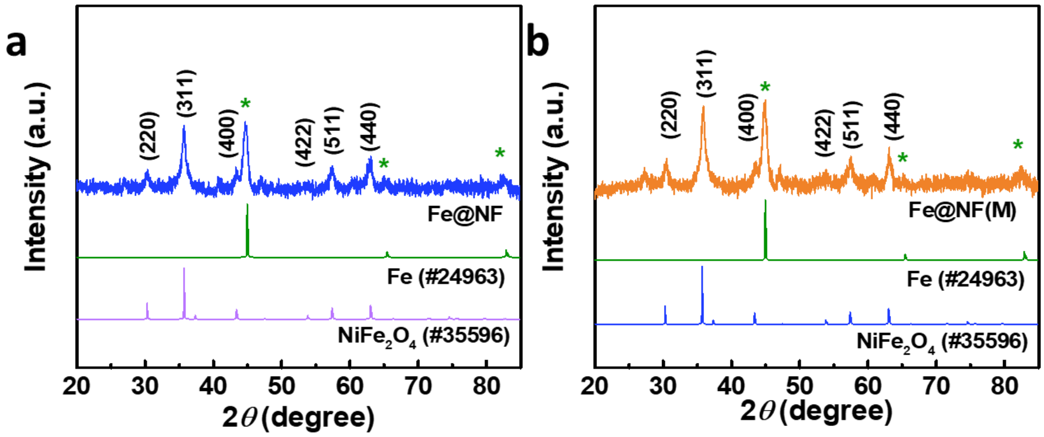

Figure 1.3. 24. Powder X-ray diffraction (PXRD) pattern of (a) Fe@NF, and (b) Fe@NF(M) catalysts post OER.

TEM and HRTEM analysis (***Figure 1.3.26.***) of samples collected after 1h shows lattice fringes corresponding to the a-Fe phase and crystalline $NiFe_2O_4$.

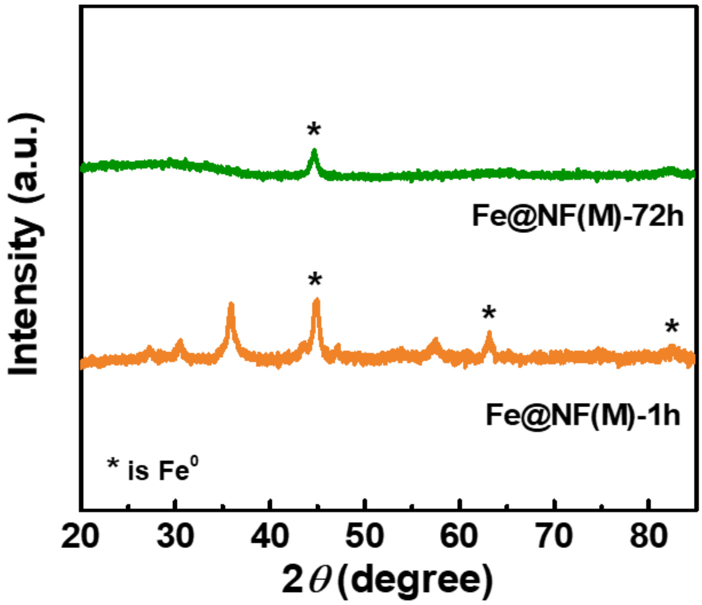

Figure 1.3. 25. Powder X-ray diffraction (PXRD) pattern after 1 h, and 72 h post OER of Fe@NF(M) catalyst.

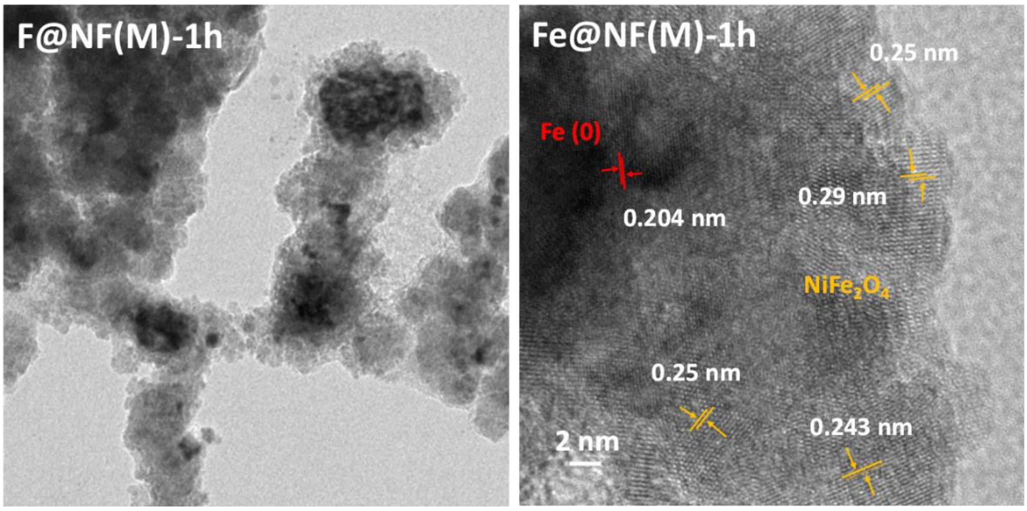

Figure 1.3. 26. (a) Transmission electron microscopy (TEM), and (b) High-resolution transmission electron microscopy (HRTEM) images of Fe@NF(M) catalyst 1 h post-OER.

However, the sample collected after 72 h reaction (***Figure 1.3.27.***) shows core iron nanoparticles covered with amorphized spinel oxide.

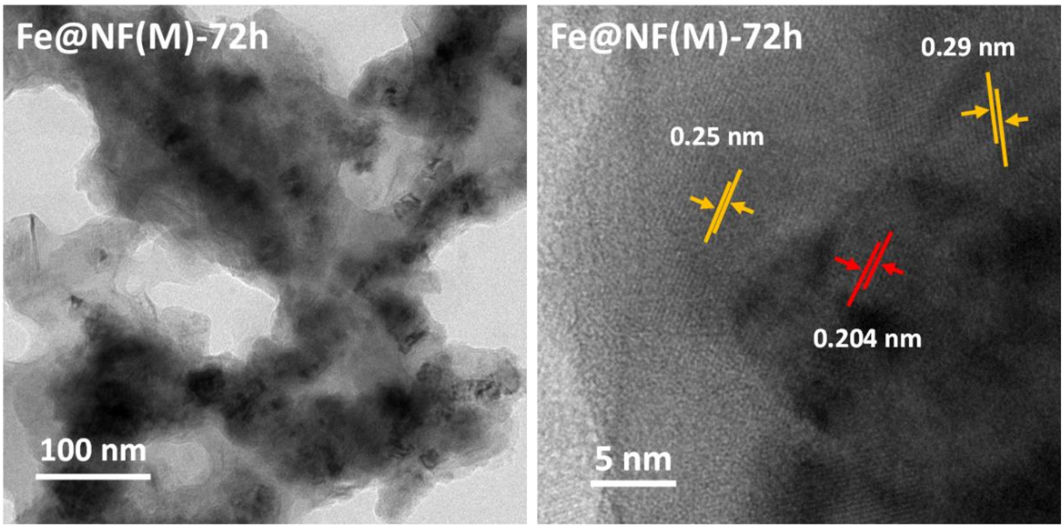

Figure 1.3. 27. (a) Transmission electron microscopy (TEM), and (b) High-resolution transmission electron microscopy (HRTEM) images of Fe@NF(M) catalyst 72 h post-OER.

There are few regions where lattice fringes corresponding to $NiFe_2O_4$ were seen. The EDS analysis confirmed the presence of nickel (10% to Fe) in the recovered powdered sample (***Figure 1.3.28.***).

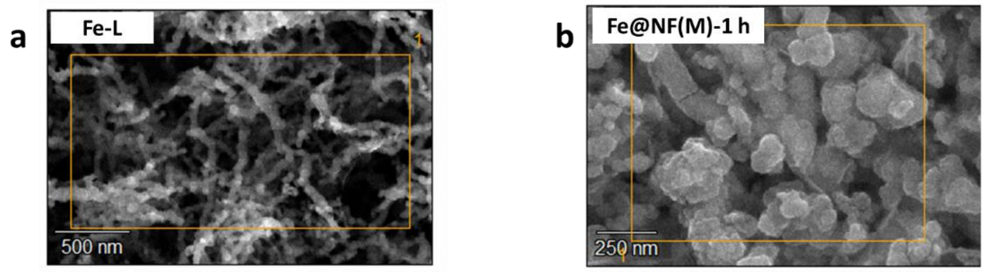

Weight %		
	O	Fe
Fe-L	7.6	92.4

Weight %			
	O	Fe	Ni
Fe@NF(M)-1 h	37.54	61.78	0.68

Figure 1.3. 28. Energy dispersive X-ray spectroscopy (EDS) analysis of (a) pristine Fe-L, and (b) Fe@NF(M) catalyst 1 h post-OER analysis.

XPS analysis over the sample collected after 1 h showed Fe^0, Fe^{3+}, Fe^{2+}, and Ni^{2+} species (***Figure 1.3.29.***).

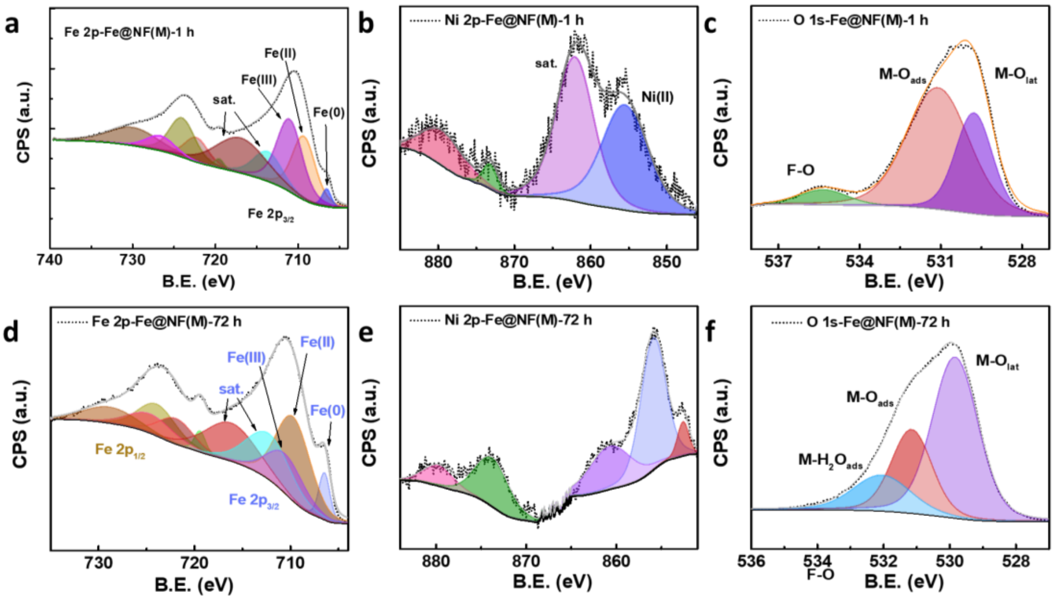

Figure 1.3. 29. X-ray photoelectron spectroscopy (XPS) analysis of Fe@NF(M) catalyst (a-c) 1 h, and (d-f) 72 h post-OER analysis.

Raman (***Figure 1.3.30.***) studies after 1 h also showed the sharp peaks corresponding to the existence of $NiFe_2O_4$.

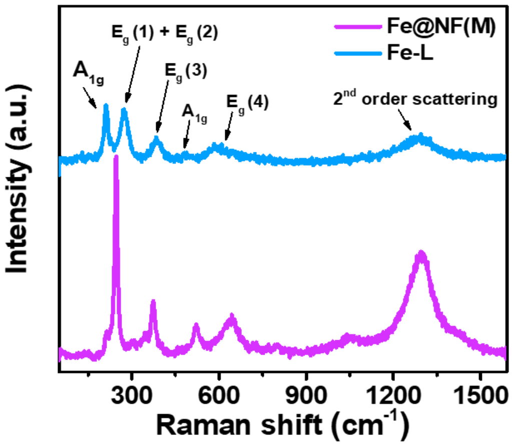

Figure 1.3. 30. Raman analysis of Fe-L and Fe@NF(M) catalysts.

Quantitative EXAFS analysis of catalysts post-reaction was performed over Fe@NF and Fe@NF(M) after 1 h of OER reaction in 1.0 M KOH medium (abbreviated as Fe@NF-1h and Fe@NF(M)-1h) to get the insights of the internal structure and elucidate the catalyst-support interaction. The EXAFS analysis of as-prepared iron nano-ligaments (Fe-L) was also carried out for comparison. The Fourier-transformed data derived from EXAFS measurements matches the theoretical standards **(*Figure 1.3.31.*)** obtained from the ICSD and Materials Project. The magnitude of the Fourier-transformed data of the representative sample is shown in ***Figure 1.3.32*** *and* ***Figure 1.3.33.*** along with the paths used to model the data. Fe-L sample could be reliably modelled **(*Figure 1.3.32.*)** using three Fe-Fe interactions from the Fe^0 phase (ICSD ref. #24963) and a small Fe-O interaction from the Fe_3O_4 phase (mp-31770), representing the surface atoms.

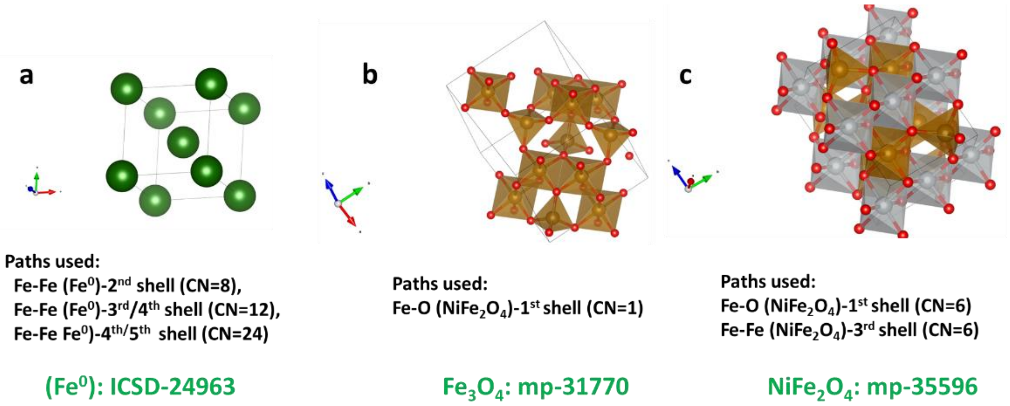

Paths used:
Fe-Fe (Fe^0)-2nd shell (CN=8),
Fe-Fe (Fe^0)-3rd/4th shell (CN=12),
Fe-Fe Fe^0)-4th/5th shell (CN=24)

(Fe^0): ICSD-24963

Paths used:
Fe-O ($NiFe_2O_4$)-1st shell (CN=1)

Fe_3O_4: mp-31770

Paths used:
Fe-O ($NiFe_2O_4$)-1st shell (CN=6)
Fe-Fe ($NiFe_2O_4$)-3rd shell (CN=6)

$NiFe_2O_4$: mp-35596

Figure 1.3. 31. Theoretical models used for XAS fitting (a) Fe (0), (b) Fe_3O_4, and (c) $NiFe_2O_4$ crystal systems.

In comparison to pristine Fe-L powder, the samples collected from Fe@NF and Fe@NF(M) after 1 h of reaction have similar Fe-O interaction from the $NiFe_2O_4$ phase (mp-35596) and an additional Fe-Fe interaction around 3 Å (violet curve, ***Figure 1.3.33.***) originating from $NiFe_2O_4$ phase, suggesting an enhanced interaction between the catalyst and the support during the OER.

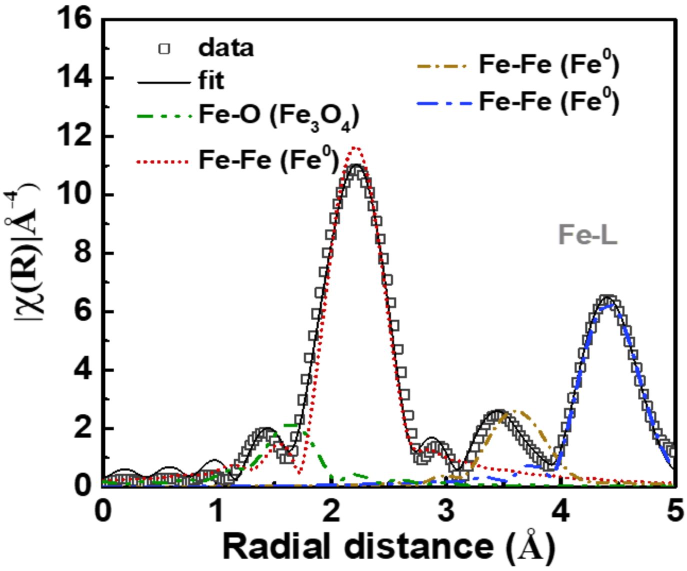

Figure 1.3. 32. The magnitude of Fourier-transformed Fe_K edge EXAFS spectrum of Fe-L catalyst (hollow black squares), best fit (black line) along with the theoretical paths used for fitting. The theoretical standards in each case are shown in parenthesis.

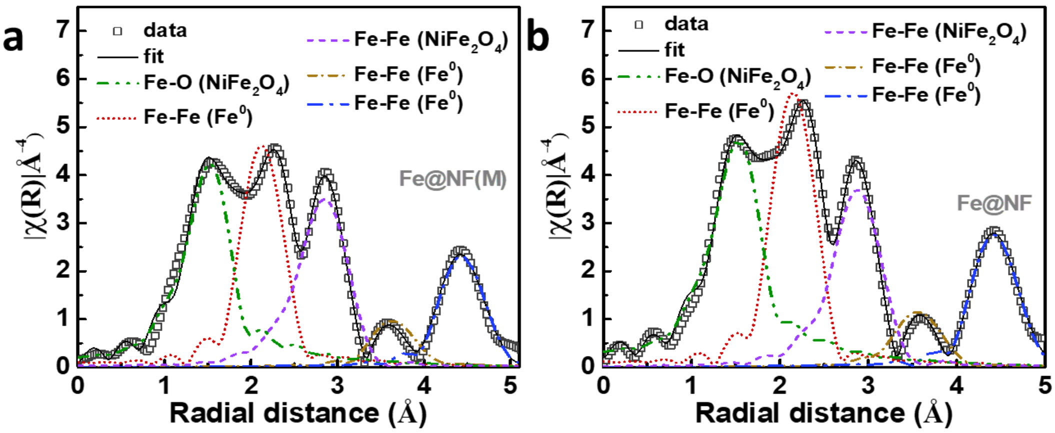

Figure 1.3. 33. The magnitude of Fourier-transformed Fe_K edge EXAFS spectrum of (a) Fe@NF, and (b) Fe@NF(M) catalysts (hollow black squares), best fit (black line) along with the theoretical paths used for fitting. The theoretical standards in each case are shown in parenthesis.

Importantly, our attempts to model the data with theoretical paths generated from the Fe_3O_4 phase led to unusually high bond lengths **(*Table 1.3.2.*)** and, hence, unphysical models, ruling out the possibility of the formation of Fe_3O_4 in the support.

Table 1.3. 2. XAS analysis of different samples fitted with Fe_3O_4 and Fe^0 models.

Sample	shell	N	CN	σ^2	R (Å)	δE_0	k range (Å^{-1})	R range (Å)
Fe	Fe-O (Fe_3O_4)	1	0.71 ± 0.340	0.001	2.06 ± 0.04	-20.00 ± 3.57	3, 11.4	1, 6
Fe@NF	Fe-O (Fe_3O_4)	1	3.57 ± 0.550	0.011	2.06 ± 0.07	3.55 ± 1.95	3, 11.2	1, 6
Fe	Fe-Fe (Fe^0)	8	1.95 ± 0.460	0.002	2.47 ± 0.07	12.56 ± 2.07	3, 11.4	1, 6
Fe@NF	Fe-Fe (Fe^0)	8	1.58 ± 0.530	0.006	2.47 ± 0.05	6.76 ± 3.30	3, 11.2	1, 6
Fe	Fe-Fe (Fe_3O_4)	-	-	-	-	-	-	-
Fe@NF	Fe-Fe (Fe_3O_4)	4	5.30 ± 3.76	0.016	3.00 ± 0.13	13.72 ± 2.10	3, 11.2	1, 6
Fe	Fe-Fe (Fe^0)	12	3.00 ± 1.85	3.55	4.03 ± 0.02	-3.54 ± 4.17	3, 11.4	1, 6
Fe@NF	Fe-Fe (Fe^0)	12	1.20 ± 1.90	0.007	4.03 ± 0.08	5.25 ± 2.23	3, 11.2	1, 6
Fe	Fe-Fe (Fe^0)	24	9.65 ± 2.54	0.006	4.73 ± 0.08	2.24 ± 1.47	3, 11.4	1, 6
Fe@NF	Fe-Fe (Fe^0)	24	0.24 ± 2.9	0.011	4.73 ± 0.10	2.68 ± 0.12	3, 11.2	1, 6

The data for all three samples are compared **(*Figure 1.3.34.*)** with each contribution and the parent theoretical phases marked, which shows an apparent decrease of the contributions from the Fe^0 phase and an increase from the $NiFe_2O_4$ phase in samples collected from both Fe@NF and Fe@NF(M) compared to the pristine Fe-L, reciprocating the already hinted increased interaction between the catalyst and the support.

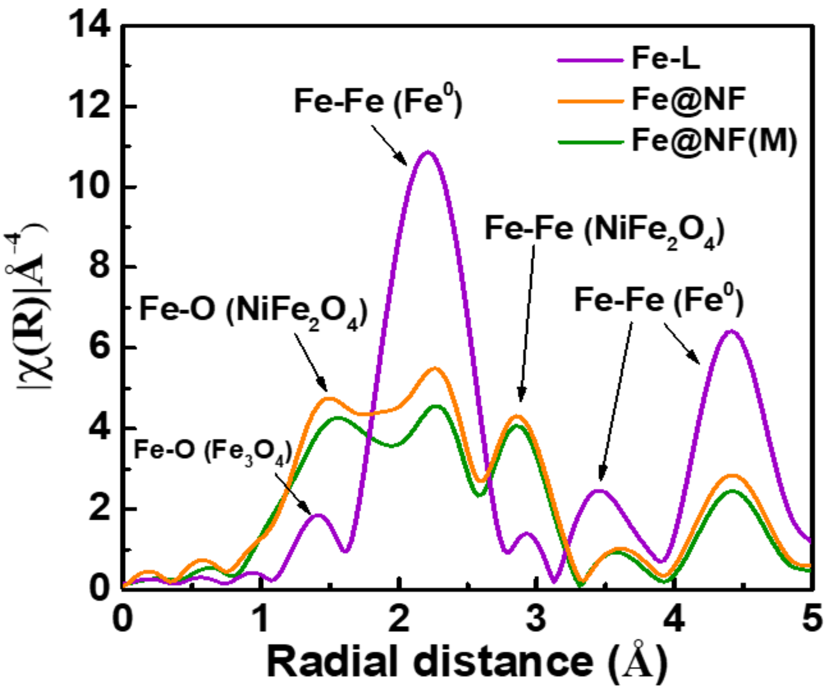

Figure 1.3. 34. The magnitude of Fourier-transformed Fe_K edge EXAFS spectra of Fe-L. Fe@NF, and Fe@NF(M) catalysts. The atomic interactions are shown with arrows. Notice the decreasing intensities of the interactions originating from $NiFe_2O_4$ in Fe@NF and Fe@NF(M) samples compared to the pristine Fe-L and vice-versa for the interactions originating from Fe^0 phase.

This is also reflected in the comparison plots of the coordination number **(*Figure 1.3.35.*)** and the area under the deconvoluted path normalized to the experimental data **(*Figure 1.3.35.*)**.

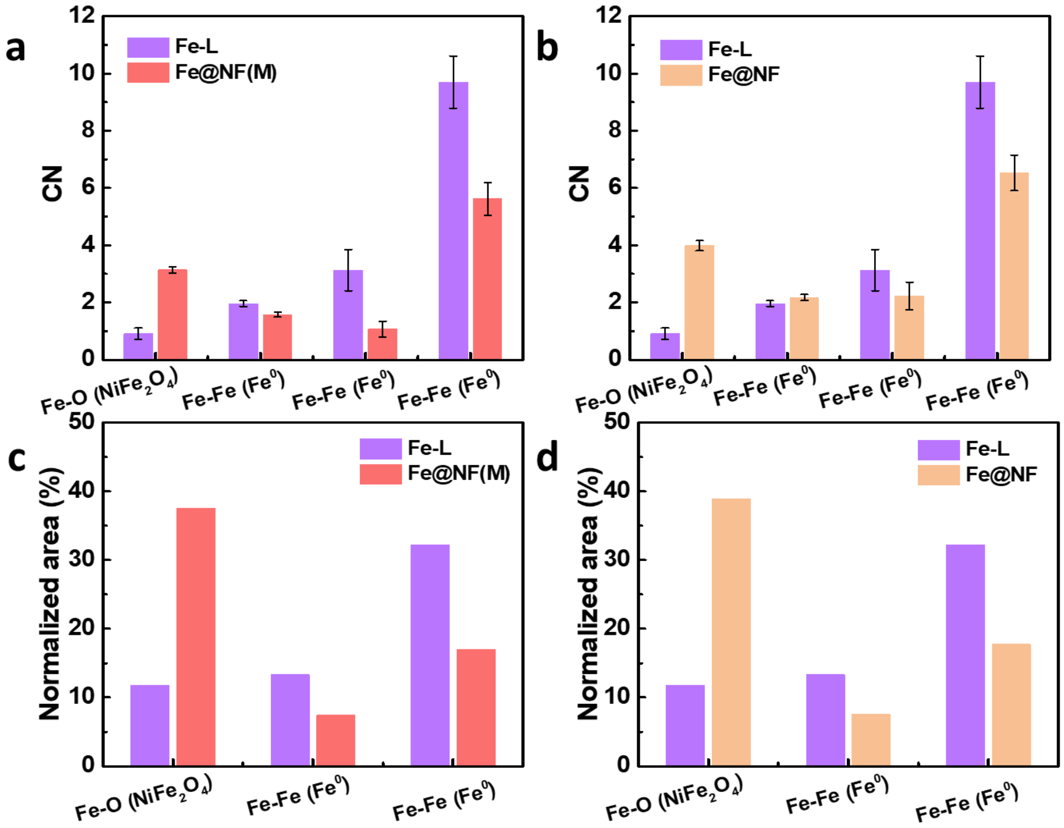

Figure 1.3. 35. The comparison of the coordination numbers (CN) obtained from the fits for each theoretical path between (a) Fe-L and Fe@NF(M) samples, (b) Fe-L and Fe@NF samples, and the comparison of the normalized area under the curve (%) obtained from the fits for each theoretical path between (c) Fe-L and Fe@NF(M) samples, and (d) Fe-L and Fe@NF samples.

As hinted from ***Figure 1.3.35.*** *and* ***Table 1.3.3.***, the Fe-O (NiFe$_2$O$_4$) CN increases in case of Fe@NF(M), and Fe@NF catalysts while the contributions from Fe-Fe (Fe^0) decreases.

Also, as hinted from the change in CN, the Fe-O (NiFe$_2$O$_4$) area increases in case of Fe@NF(M), and Fe@NF catalysts while the contributions from Fe-Fe (Fe^0) decreases.

Table 1.3. 3. XAS analysis of different samples fitted with $NiFe_2O_4$ and Fe^0 models.

Sample	shell	N	CN	σ^2	R (Å)	δE_0	k range ($Å^{-1}$)	R range (Å)
Fe	Fe-O (Fe_3O_4)	1	0.91 ± 0.200	0.005	2.04 ± 0.03	10.00 ± 0.01	3, 11.4	1, 5
Fe@NF	Fe-O ($NiFe_2O_4$)	6	3.98 ± 0.180	0.013	1.97 ± 0.07	3.03 ± 1.57	3, 11.2	1, 5
Fe@NF(M)	Fe-O ($NiFe_2O_4$)	6	3.14 ± 0.114	0.011	1.96 ± 0.08	1.45 ± 1.28	3, 11.282	1, 5
Fe	Fe-Fe (Fe^0)	8	1.96 ± 0.102	0.002	2.52 ± 0.05	9.72 ± 1.51	3, 11.4	1, 5
Fe@NF	Fe-Fe (Fe^0)	8	2.18 ± 0.104	0.008	2.51 ± 0.04	3.79 ± 1.53	3, 11.2	1, 5
Fe@NF(M)	Fe-Fe (Fe^0)	8	1.58 ± 0.088	0.007	2.49 ± 0.03	0.48 ± 1.95	3, 11.282	1, 5
Fe	Fe-Fe ($NiFe_2O_4$)	-	-	-	-	-	-	-
Fe@NF	Fe-Fe ($NiFe_2O_4$)	6	6.00 ± 0.06	0.013	3.37 ± 0.07	8.84 ± 1.64	3, 11.2	1, 5
Fe@NF(M)	Fe-Fe ($NiFe_2O_4$)	6	7.82 ± 0.50	0.016	3.37 ± 0.07	10.54 ± 1.30	3, 11.282	1, 5
Fe	Fe-Fe (Fe^0)	12	3.13 ± 0.72	0.007	4.04 ± 0.01	3.96 ± 3.86	3, 11.4	1, 5
Fe@NF	Fe-Fe (Fe^0)	12	2.23 ± 0.48	0.011	4.02 ± 0.01	5.43 ± 4.30	3, 11.2	1, 5
Fe@NF(M)	Fe-Fe (Fe^0)	12	1.07 ± 0.28	0.006	4.05 ± 0.02	2.30 ± 4.22	3, 11.282	1, 5
Fe	Fe-Fe (Fe^0)	24	9.69 ± 0.912	0.006	4.81 ± 0.08	2.34 ± 1.43	3, 11.4	1, 5
Fe@NF	Fe-Fe (Fe^0)	24	6.53 ± 0.624	0.009	4.82 ± 0.09	2.70 ± 1.41	3, 11.2	1, 5
Fe@NF(M)	Fe-Fe (Fe^0)	24	5.62 ± 0.574	0.010	4.83 ± 0.11	2.73 ± 1.35	3, 11.282	1, 5

We found that in the Fe@NF catalyst, the iron nanoparticles react with nickel foam in the oxidizing environment and produce $NiFe_2O_4$ surface species during the LSV cycle. The core-shell type $Fe@NiFe_2O_4$ structure observed in the HRTEM image of the Fe@NF sample after 1h reaction supports this type of transformation (***Figure 1.3.26.*** *and* ***Figure 1.3.27.***). It also proves that it is not the Fe nanoparticles that are catalytically active but the surface-modified Fe in the presence of Ni that is catalytically active for OER. Indeed, the Fe nano-ligaments supported on carbon paper (Fe@CP) did not show any OER activity (***Figure 1.3.36.a***) even after an hour of reaction. Nor does it show any enhancement when exposed to the external magnetic field. On the other hand, when Fe nano-ligament was mixed with Ni nanoparticles and loaded on to a carbon paper (FeNi@CP), the OER activity is increased from 50 mA cm^{-2} for Fe@C to 400 mA cm^{-2} for NiFe@C at 1.7 V. This clearly proves that the in-situ formed, reactive NiFe-mixed oxide species at the nanoscale play a major role in the OER activity. The amorphization of initially formed $NiFe_2O_4$ after 72 hours did not reduce the OER performance of Fe@NF(M). On the other hand, when commercially available Fe_3O_4 was used (***Figure 1.3.36.b***) in place of Fe nano-ligaments, the enhancement was not that significant (h_{1000}

= 300 mV). Also, when the iron oxide obtained by heat treatment of Fe-L in the air (350 °C for 1 h) was used as the catalyst, an overpotential of 320 mV was observed for a current density of 1 A cm^{-2}. These results indicate that the defect-rich iron nanoparticles in Fe-L are more reactive toward nickel than iron oxide particles to generate the catalytically active species.

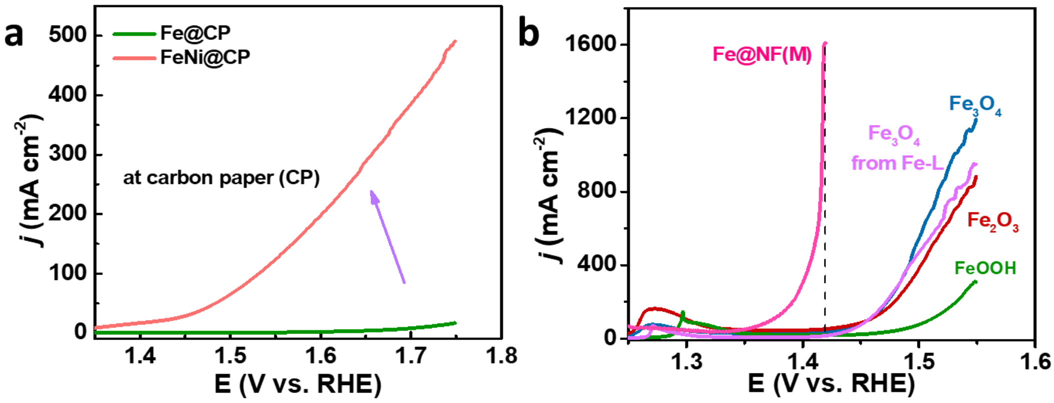

Figure 1.3. 36. Linear sweep voltammograms (LSVs) of (a) Fe-L, FeNi at carbon paper (CP), and (b) oxides of Fe at NF in 1.0 M KOH.

We observed room-temperature ferromagnetic behavior (***Figure 1.3.37.***) for as prepared Fe-L sample with a saturation magnetization of 80 emu g^{-1} and coercivity of 1640 Oe at 300 K. At a lower temperature of 2 K, high saturation magnetization of 105 emu g^{-1} and coercivity of 2380 Oe was observed.

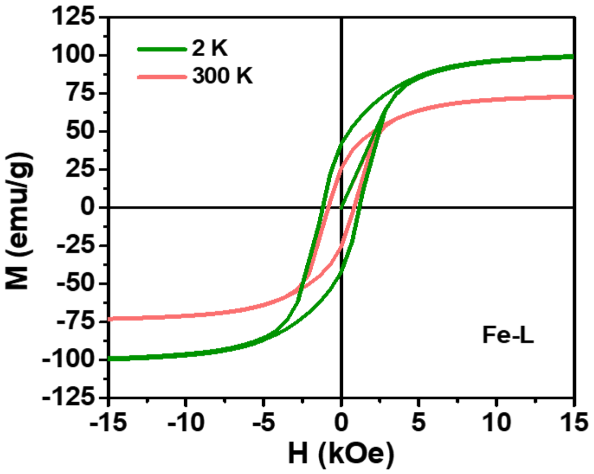

Figure 1.3. 37. Magnetic measurements of Fe-L sample at 2 K and 300 K.

The magnetic measurements carried out over Fe@NF and Fe@NF(M) after 1 h of OER in 1.0 M KOH are shown in (***Figure 1.3.38.***). The coercivity of the materials collected post-reaction was retained though saturation magnetization is decreased, probably due to the formation of ferrimagnetic $NiFe_2O_4$ species. The Fe@NF(M) catalyst showed higher saturation magnetization than Fe@NF, confirming the spin alignment in the system subjected to magnetic field exposure.

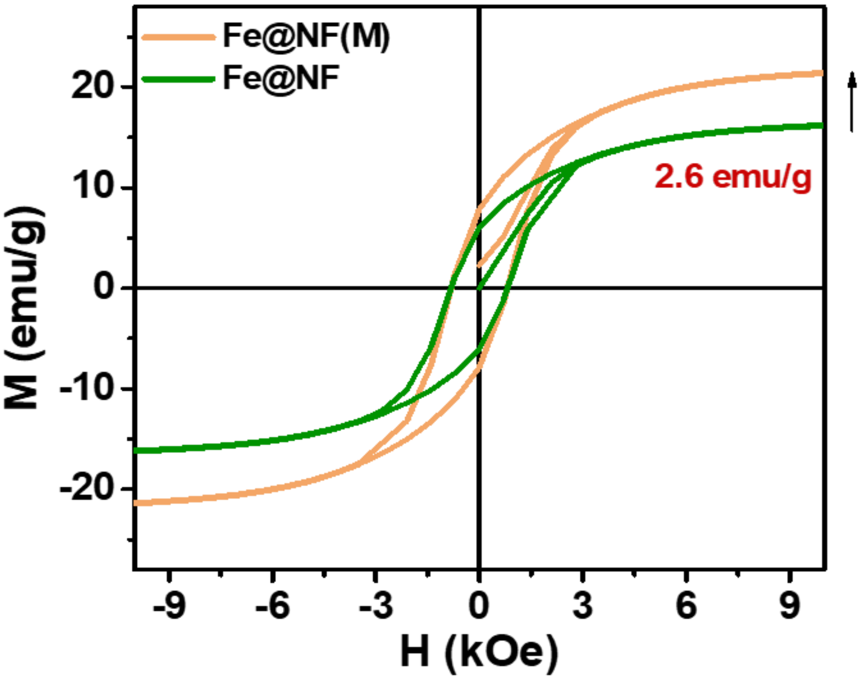

Figure 1.3. 38. Magnetic measurements of catalysts recovered from Fe@NF, and Fe@NF(M) electrodes.

With this increased M_s on magnetization, one can consider the alignment of spins of the $NiFe_2O_4$ phase formed during the OER analysis. So, aligning these species from the beginning of the measurement might affect the performance.

The in-situ Raman analysis (***Figure 1.3.39.***) of the Fe-L catalyst shows peaks corresponding to the existence of NiOOH species after 1.35 V. Also, the onset of OER appeared after 1.35 V, showing that NiOOH could be the active site for intermediate adsorption along with the sites accessible from the $NiFe_2O_4$ species.

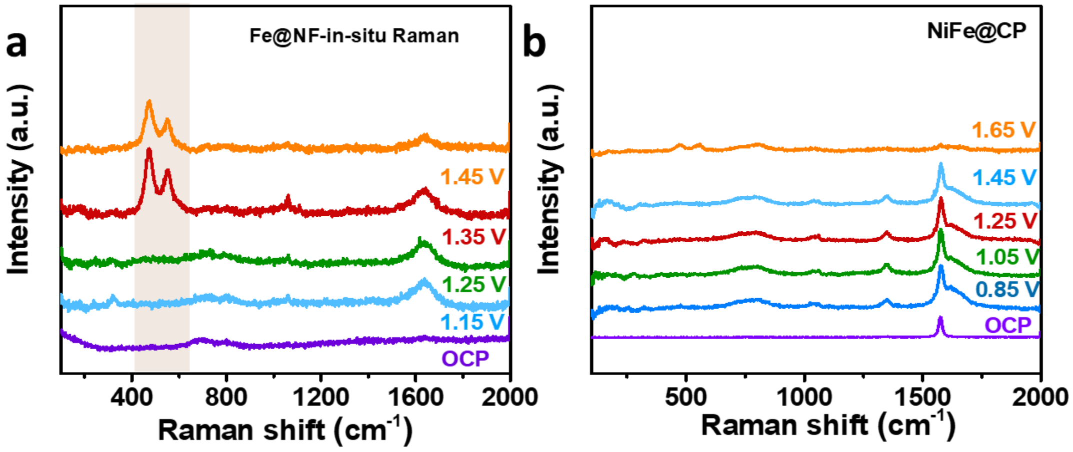

Figure 1.3. 39. In-situ Raman analysis of (a) Fe@NF catalyst, and (b) FeNi catalyst supported on carbon paper (CP) electrode.

1.3.5. Conclusion:

In conclusion, the effective interfaces formed during the electrochemical analysis by the interaction of Fe nano-ligaments with NF support act as a highly active and stable OER catalyst. The one-time magnetic field exposure leads to the alignment of spins in the system, facilitating the direct formation and desorption of O_2 molecules in the ground triplet state. The dynamic interaction of Fe-L in the presence of NF undergoes electrochemical generation of the $NiFe_2O_4$ phase during OER under alkaline conditions. The formed oxide surface under these conditions is highly active for OER with more than 4200 h stability at 1 A cm^{-2}. Remarkably, it shows an ultralow overpotential of 110 mV for a current density of 1 A cm^{-2} in 10 M KOH. The catalyst showed extraordinarily stable performance even at a high current density of 5.5 A cm^{-2} at an overpotential of 230 mV for 800 h. The full-cell fabricated from Fe@NF(M) showed a current density of 1.58 A cm^{-2} at 2.5 V in 6 M KOH. This catalyst can be considered a potential candidate for future commercial applications in the field of viable utilization of energy.

1.3.6. References:

1. R. Aogaki *et al.*, Origin of Nanobubbles Electrochemically Formed in a Magnetic Field: Ionic Vacancy Production in Electrode Reaction. *Sci Rep* **6**, 28927 (2016).
2. A. Angulo, P. v. d. Linde, G. Han, M. Modestino, D. F. Rivas, Influence of Bubbles on the Energy Conversion Efficiency of Electrochemical Reactors. *Joule* **4**, 555-579 (2020).

3. Z. Feng *et al.*, Recent Development of External Magnetic Field Assisted Oxygen Evolution Reaction-A Mini Review. *ChemCatChem* **15**, (2023).
4. G. Li *et al.*, Magnetocatalysis: The Interplay between the Magnetic Field and Electrocatalysis. *CCS Chemistry* **3**, 2259-2267 (2021).
5. S. Luo, K. Elouarzaki, Z. J. Xu, Electrochemistry in Magnetic Fields. *Angew Chem Int Ed Engl* **61**, e202203564 (2022).
6. H.-b. Liu, H. Xu, L.-m. Pan, D.-h. Zhong, Y. Liu, Porous electrode improving energy efficiency under electrode-normal magnetic field in water electrolysis. *International Journal of Hydrogen Energy* **44**, 22780-22786 (2019).
7. Y. Zhang *et al.*, Recent Advances in Magnetic Field-Enhanced Electrocatalysis. *ACS Applied Energy Materials* **3**, 10303-10316 (2020).
8. P. Dunne, J. M. D. Coey, Influence of a Magnetic Field on the Electrochemical Double Layer. *The Journal of Physical Chemistry C* **123**, 24181-24192 (2019).
9. X. Ren *et al.*, Spin-polarized oxygen evolution reaction under magnetic field. *Nat Commun* **12**, 2608 (2021).
10. J. Yan *et al.*, Direct Magnetic Reinforcement of Electrocatalytic ORR/OER with Electromagnetic Induction of Magnetic Catalysts. *Adv Mater* **33**, e2007525 (2021).
11. F. A. Garcés-Pineda, M. Blasco-Ahicart, D. Nieto-Castro, N. López, J. R. Galán-Mascarós, Direct magnetic enhancement of electrocatalytic water oxidation in alkaline media. *Nature Energy* **4**, 519-525 (2019).
12. T. Wu, Z. J. Xu, Oxygen evolution in spin-sensitive pathways. *Current Opinion in Electrochemistry* **30**, (2021).
13. H. Zhou *et al.*, Water splitting by electrolysis at high current densities under 1.6 volts. *Energy & Environmental Science* **11**, 2858-2864 (2018).
14. Y. Hu *et al.*, Large current density for oxygen evolution from pyramidally-coordinated Co oxide. *Applied Catalysis B: Environmental* **333**, (2023).
15. S. Li *et al.*, Bifunctional CoNi/CoFe2O4 /Ni foam electrodes for efficient overall water splitting at a high current density. *Journal of Materials Chemistry A* **6**, 19221-19230 (2018).

16. J. Yuan *et al.*, A Superaerophobic Bimetallic Selenides Heterostructure for Efficient Industrial-Level Oxygen Evolution at Ultra-High Current Densities. *Nanomicro Lett* **12**, 104 (2020).
17. D. Wu, D. Chen, J. Zhu, S. Mu, Ultralow Ru Incorporated Amorphous Cobalt-Based Oxides for High-Current-Density Overall Water Splitting in Alkaline and Seawater Media. *Small* **17**, e2102777 (2021).
18. J. Yuan *et al.*, Bimetallic Oxyhydroxide as a High-Performance Water Oxidation Electrocatalyst under Industry-Relevant Conditions. *Engineering* **7**, 1306-1312 (2021).
19. G. Qian *et al.*, Free-standing bimetallic CoNiTe2 nanosheets as efficient catalysts with high stability at large current density for oxygen evolution reaction. *Renewable Energy* **162**, 2190-2196 (2020).
20. H. Zhou *et al.*, Highly active catalyst derived from a 3D foam of Fe(PO(3))(2)/Ni(2)P for extremely efficient water oxidation. *Proc Natl Acad Sci U S A* **114**, 5607-5611 (2017).
21. J. Lian, Y. Wu, J. Sun, High current density electrodeposition of NiFe/Nickel Foam as a bifunctional electrocatalyst for overall water splitting in alkaline electrolyte. *Journal of Materials Science* **55**, 15140-15151 (2020).
22. F. Yu *et al.*, High-performance bifunctional porous non-noble metal phosphide catalyst for overall water splitting. *Nat Commun* **9**, 2551 (2018).
23. Y. Liu *et al.*, Corrosion engineering towards efficient oxygen evolution electrodes with stable catalytic activity for over 6000 hours. *Nat Commun* **9**, 2609 (2018).
24. J. Zhang, Y. Hu, D. Liu, Y. Yu, B. Zhang, Enhancing Oxygen Evolution Reaction at High Current Densities on Amorphous-Like Ni-Fe-S Ultrathin Nanosheets via Oxygen Incorporation and Electrochemical Tuning. *Adv Sci (Weinh)* **4**, 1600343 (2017).
25. C. S. S. S. Katla Sai Krishna, ‡ Reji Philip,‡ and Muthusamy Eswaramoorthy, Mixing Does the Magic: A Rapid Synthesis ofHigh Surface Area Noble Metal Nanosponges Showing Broadband Nonlinear Optical Response. *ACS Nano* **5**, 2681-2688 (2010).
26. G. N. Glavee, K. J. Klabunde, C. M. Sorensen, G. C. Hadjipanayis, Chemistry of Borohydride Reduction of Iron(II) and Iron(III) Ions in Aqueous and Nonaqueous

Media. Formation of Nanoscale Fe, FeB, and FeaB Powders. *Inorg Chem* **34**, 24-35 (1995).

27. M. Hua *et al.*, Hexamethylenetetramine-assisted hydrothermal synthesis of octahedral nickel ferrite oxide nanocrystallines with excellent supercapacitive performance. *Journal of Materials Science* **53**, 7621-7636 (2018).
28. Y. Y. Sun *et al.*, In Situ Synthesis of Surface-Mounted Novel Nickel(II) Trimer-Based MOF on Nickel Oxide Hydroxide Heterostructures for Enhanced Methanol Electro-Oxidation. *Front Chem* **9**, 780688 (2021).
29. Z. Ž. Lazarević *et al.*, Study of NiFe2O4and ZnFe2O4Spinel Ferrites Prepared by Soft Mechanochemical Synthesis. *Ferroelectrics* **448**, 1-11 (2013).
30. Y. P. Yew *et al.*, An Eco-Friendly Means of Biosynthesis of Superparamagnetic Magnetite Nanoparticles via Marine Polymer. *IEEE Transactions on Nanotechnology* **16**, 1047-1052 (2017).
31. S. V. Bhosale, P. S. Ekambe, S. V. Bhoraskar, V. L. Mathe, Effect of surface properties of NiFe2O4 nanoparticles synthesized by dc thermal plasma route on antimicrobial activity. *Applied Surface Science* **441**, 724-733 (2018).

PART 2

Chapter 2.1. An introduction to hybrid water electrolysis.

Chapter 2.2. Influence of chromium on Ni foam towards benzyl alcohol oxidation reaction (BOR).

Chapter 2.3. Specular CuO nanostructures towards glucose oxidation and sensing.

Chapter- 2.1 An introduction to hybrid water electrolysis

Summary:

This chapter introduces the criteria behind chemical-assisted electrochemical hydrogen generation and the parameters deciding the overall performance. Highlighting the limitations to the kinetically sluggish conventional oxygen evolution reaction (OER), hybrid water electrolysis expands the field to low energy-demanding oxidation reactions. This way of electrolysis leads to the simultaneous generation of hydrogen fuel with the electrosynthesis of value-added chemicals. The state-of-the-art catalysts, their performances, and limitations to their use are significantly overviewed with their replacement with active non-noble analogs.

Further, this chapter discusses all the parameters affecting the selectivity and yield of electro-synthesized products, along with a description of the product analysis.

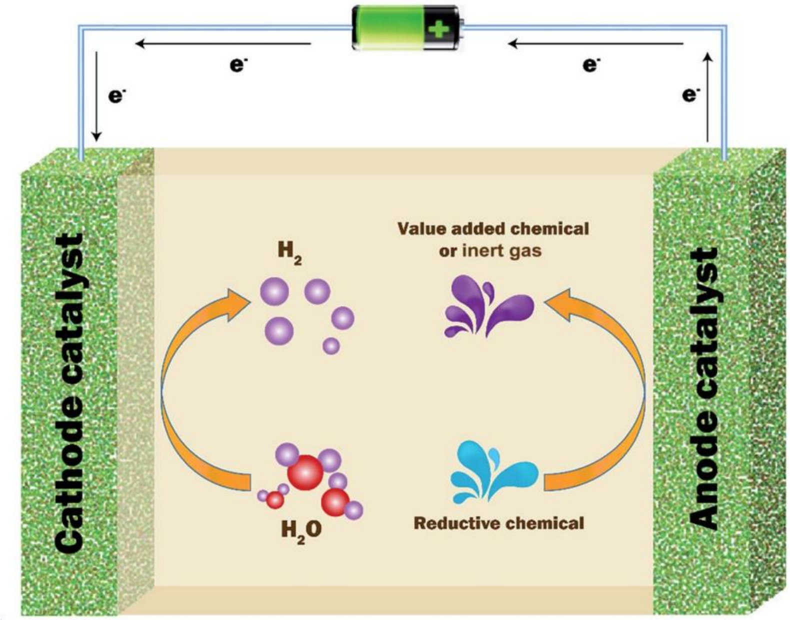

This figure has been adapted from Ref. (1).

2.1.1. Introduction to Hybrid electrocatalysis:

The ever-increasing energy demand with the growing population relies extensively on limited fossil fuels causing an energy crisis all over the globe with a rapid increase in global warming. Hydrogen, a greener alternative, has become a carbon-neutral fuel with very high gravimetric energy density of 142 MJ kg^{-1}. Also, the electrochemical generation of hydrogen from water electrolysis is much more efficient than the commercial steam reforming method. Although there is room for high-purity H_2 evolution through the electrochemical route, the major limitation to electrochemical water splitting lies in the sluggish kinetics associated with the oxygen evolution reaction (OER).(*2*) High-cost noble metal-based catalysts have generally been used to reduce the overpotential in water oxidation reactions. Alternatives are currently explored to make water-splitting reactions cost-effective at the industrial scale. Developing non-noble metal catalysts that could display a very low overpotential for OER and/or replacing OER with other oxidation reactions with low thermodynamic potentials **(*Figure 2.1.1.*)**. The selection of an organic oxidation reaction with a significantly low thermodynamic potential (as compared to OER) at the anode **(*Figure 2.1.2.*)** bestowed the possibility of reducing the overall cell potential in a water-splitting reaction.(*3*)

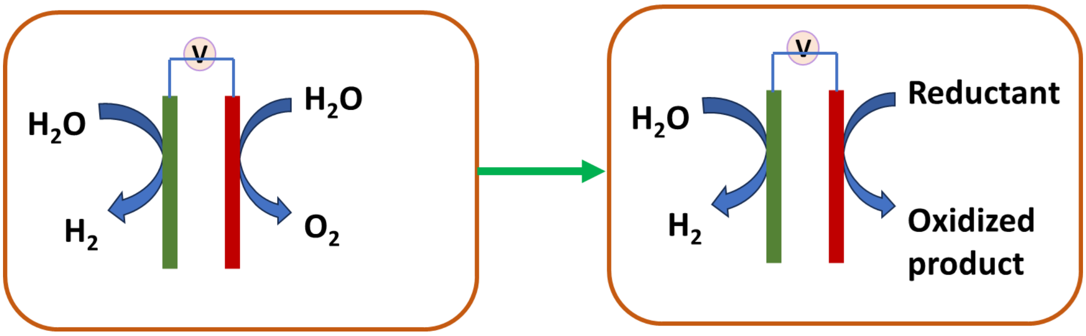

Figure 2.1. 1. Illustration of shift from conventional to hybrid water electrolysis.

Various anodic oxidation reactions having low energy barriers, such as oxidation of alcohols,(*4, 5*) urea,(*6, 7*) hydrazine,(*8, 9*) and biomasses,(*10, 11*) have been explored in this direction. The partial oxidation of organic chemicals has a great application in the production of value-added chemicals during hydrogen generation reactions. In contrast, complete oxidation produces a high amount of energy in fuel cell applications.(*3, 12-14*)

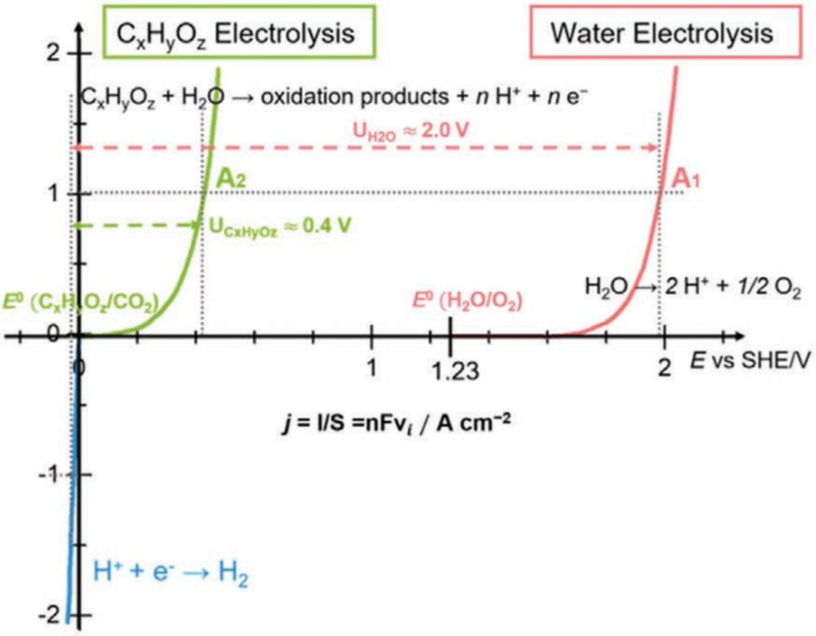

Figure 2.1. 2. Voltamogram showing low potential requirements for energy efficient hybrid water electrolysis. Reproduced with permission from Ref. (3)

Besides, the generation of value-added products with simultaneous hydrogen production makes this approach even more attractive.(*1, 15-18*)

2.1.2. Alcohol oxidation:

Alcohols such as ethanol, methanol, glycols, and glycerol are commonly used for anode oxidation.(*19-24*) Nevertheless, safety risks, toxicity, flammability, low energy density, high cross-over through membranes, and high costs limit their effective use as a substitute for OER.(*25*) Aromatic benzyl alcohol (BA) can be considered as a better alternative as its partial oxidation leads to the production of benzaldehyde (PhCHO) or benzoic acid (PhCOOH).(*5, 26-29*) These carbonyl products find application in food industries (as pH adjusters), dye industries and in pharmaceutical industries (as analgesics and antimicrobials). The commercial production of PhCHO and PhCOOH is carried out by a toluene oxidation process wherein highly corrosive concentrated acids (usually conc. HNO_3) are used as oxidants at high temperature (150-170 °C) and pressure (1 MPa) with energy-intensive separation and distillation processes.(*30-32*) The electrochemical route is an efficient alternative to this chemical toluene oxidation process.

2.1.3. Biomass oxidation:

Biomass represents abundant carbon resource on Earth and serves as feedstock for the production of various chemicals. Its interesting structure, enriched with diversity in functional groups, has spurred extensive research for its utilization. Among various biomass sources, the class of cellulosic biomass stands out for its widespread abundance, affordability and availability.(*3*, *11*, *13*, *33-37*) Various transformation strategies have resulted in a variety of chemicals from glucose and cellulose.

The abundant cellulosic biomass is highly suitable for chemical production among the several biomass feedstocks. Its easy valorization and widely available sources make these biomasses prevalent for value-added chemical production. Glucose as a reactant is a cost-effective, non-toxic, eco-friendly, renewable, and abundant monosaccharide. Glucose oxidation reaction (GOR) is an economically viable, sustainable, and promising method for generating high-quality, value-added products. It is considered as a current energy storage vector with a high energy density of 4.43 kW h kg^{-1} and a lower theoretical oxidation potential of 0.05 V. The complete oxidation of glucose (equations (1)-(3)) in alkaline conditions involves the transfer of 24 electrons, generating 2.87 MJ mol^{-1} of energy.(*36*, *38*, *39*) The reactions occurring at the anode and cathode for complete oxidation of glucose can be described as:

Anode reaction : $C_6H_{12}O_6 + 24\ OH^- \rightarrow 6\ CO_2 + 18\ H_2O + 24\ e^-$ ………………..(1)

Cathode reaction : $6\ O_2 + 12\ H_2O + 24\ e^- \rightarrow 24\ OH^-$ …………………………...(2)

Overall reaction : $C_6H_{12}O_6 + 6\ O_2 \rightarrow 6\ CO_2 + 6\ H_2O$ ………………………..(3)

The partial oxidation of glucose **(*Figure 2.1.3.*)** leads to the generation of value-added products like gluconic acid (GNA), glucaric acid (GRA), formic acid (FA), and others, which involve less than 24 electron transfer kinetics. Among these products, GRA is a high-grade, top-class value-added product (VAP) used as a critical intermediate in the production of detergents, complexing agents, and chemotherapeutic agents. (*40*)

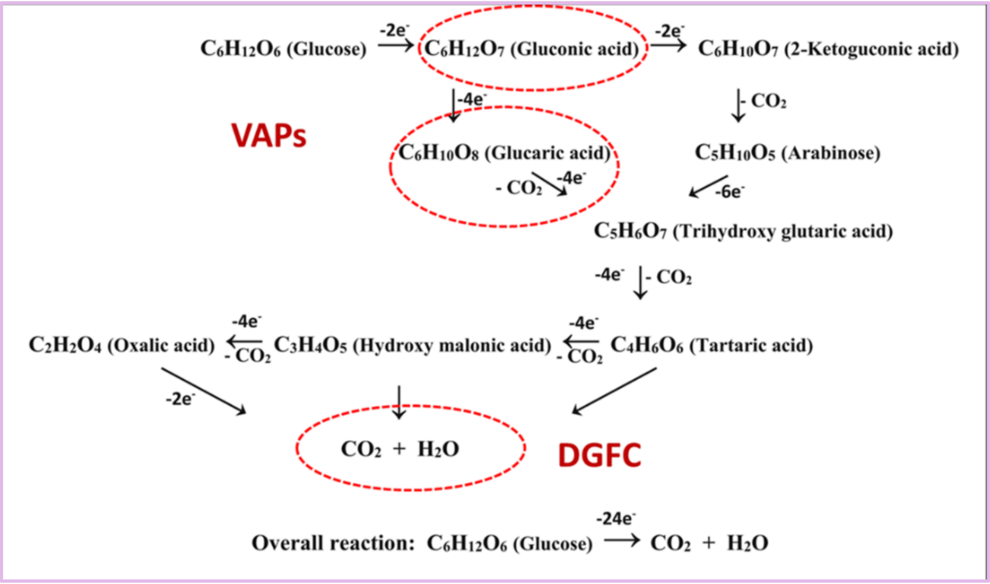

Figure 2.1. 3. Partial (VAPs) and complete electrochemical oxidation (DGFCs) of glucose to different products. Reproduced with permission from Ref. (40).

The conventional glucose oxidation method involves harsh conditions of high O_2/air pressure, high temperature (50-120 °C), and corrosive oxidants (HNO_3). The glucose oxidation occurs via catalytic (with Au, Pt, Ag or Pd catalysts) or non-catalytic (just HNO_3 as the oxidant) or microbial fermentation. A major limitation to these processes lies in low selectivity (< 60%), difficult separation, use of toxic oxidants, and long duration of the reaction. The electrochemical route involves electrons as the charge carriers and water as the oxidation medium. Complete oxidation of glucose is not electrochemically feasible, and thus, the product of interest can be obtained by selectively fluctuating the applied potentials. However, complete oxidation of glucose is preferred in the direct glucose fuel cells (DGFCs) to attain high energy output. In addition, the easily tuneable surface and morphology of the electrocatalysts significantly impact the productivity, selectivity, and efficiency of the electrochemical oxidation process of glucose.

Formic acid is also considered an essential intermediate in the pharmaceutical, rubber, dye, food, and agriculture industries. It is eco-friendly, biodegradable, non-toxic, and non-corrosive, utilized as the building block in various organic syntheses, and acts as a solvent and oxidant. Formic acid, also called methanoic acid, is a hydrogen carrier molecule and, thus, a source of effective hydrogen utilization with a volumetric capacity of 53.4 g L^{-1}.(*41*) The industrial production of FA involves two steps of methanol carbonylation (using CO) at high pressure (~ 40 bar) followed by hydrolysis of produced formylate.(*42*) Various methods, including hydrolysis, wet oxidation, or catalytic oxidation of biomass/ glucose, have been employed for the past few decades as an alternative to the commercial chemical route. The major limitations of these processes include low yields, toxic oxidants (acids, H_2O_2, alkalis), high temperature (140-250 °C), and high pressure (~ 75 bar) reaction conditions. In this way, dual-site hydrogen can be generated with the evolution of H_2 at the cathode and chemical H_2 storage molecules (in terms of formic acid) at the anodic side, benefiting the overall efficiency of the process.(*41*, *43*)

As can be seen, glucose oxidation reactions can be classified into three categories **(*Figure 2.1.4.*)** depending on the area of interest.(*44*) One can completely oxidize glucose and harvest high-output electrical energy in direct glucose fuel cells (DGFCs). The second category is the generation of VAPs through partial oxidation of glucose. In the third category, glucose oxidation can power various implantable devices in the human body and sensor applications for blood sugar detection. This field of glucose oxidation is further classified into two categories: enzymatic and non-enzymatic.(*45*) Various studies have indicated that better stability, durability, selectivity, and lifetime prevail for non-enzymatic oxidation reactions (using metal oxides and nanostructured catalysts) as compared to enzymatic reactions.

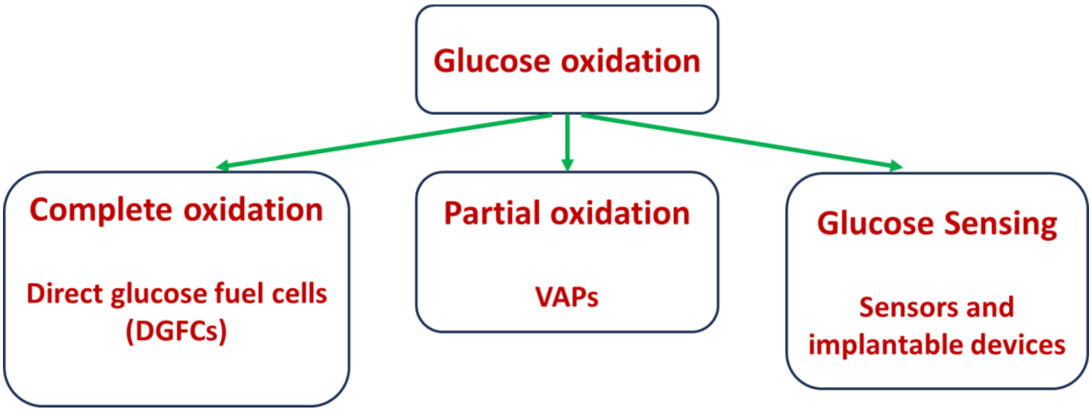

Figure 2.1. 4. Utilization of electrochemical glucose oxidation in various sectors. VAPs denotes value added products.

2.1.3.1. Non-enzymatic glucose oxidation:

Enzymatic way of glucose oxidation limits its application because of its lower shelf life, high cost, low reproducibility, and frequent denaturation of the enzymes.(*44*) Noble metal-based catalysts, like Pt, Au, and Pd, and their alloys have been considered the best-performing non-enzymatic GOR catalysts. Their scarcity, low selectivity, and stability significantly affect the economic value and sustainability of the overall process. Also, the poisoning effect of the intermediate adsorption poses a major hurdle to organic oxidation reactions.(*14*, *36*, *37*) The inclusion of non-metal as a dopant or heterometal site has hugely impacted the performance. Still, the novelty with high currents at low overpotentials and good stability and conversion has not yet been attained. Exploring non-noble metals and their nanostructured alternatives for large-scale application of GOR is crucial. Various studies have reported the use of Ni, Fe, and Cu-based catalysts for GOR.(*36*, *40*, *42*, *46*-*48*) Although glucose-coupled hydrogen generation is promising, high current densities (> 500 mA cm^{-2}) at low overpotentials are not yet achieved. Various parameters such as potential, current density, pH, and the nature of metals affect the conversion and selectivity towards a particular product, which is not yet clearly understood.

Glucose fuel cells can be employed in another emerging technology of implantable fuel cell studies. As glucose is a very common molecule found in human blood (65-110 mg/100 mL), it can be oxidized to generate electricity, thereby acting as a source of energy to power up various implantable devices and artificial organs.(*12*, *49*, *50*) Further, glucose produced by the metabolism of carbohydrates can also be used as an energy source. Three different categories of direct glucose fuel cells (DGFCs) can be considered including viz. enzymatic, microbial, and non-enzymatic (abiotically catalysed) fuel cells. Electrocatalysts are required for the long-term application of fuel cells at lower input potentials. Metal oxide-based systems have been employed in fuel cells and biosensors as an alternative to noble metal-based catalysts. Various studies have proven the enhancement in performance while using porous supports with improved diffusion kinetics and effective surface area.

2.1.3.2. Non-enzymatic glucose sensing:

Diabetes Mellitus has become a chronic condition affecting more than 150 million people worldwide. The disturbances in insulin supply led to fluctuation in glucose levels (normal range is 4.4-6.6 mM) in the human body, which increases the chances of getting diabetes. In a worst-case scenario, complications like blindness, nerve damage, heart attack, etc, may arise with a diabetic patient. There is no cure for diabetes, and it can only be controlled by gradual monitoring of glucose levels and providing medical treatments to reduce and control the emergencies and complications involved.(*35*, *37*, *51*) Various optical, fluorescent, enzymatic, and electrochemical methods have been employed to detect and quantify glucose levels. Moving on from the simplest 1st generation **(*Figure 2.1.5.*)** glucose sensors to the commercialization of 3rd generation sensors still lags with various limitations to use of enzymes. The commercially available enzyme-based devices and sensors have a shorter shelf life, are highly expensive, and work under limited pH and temperature conditions. Thus, non-enzymatic electrochemical glucose sensors have drawn much attention in this field.

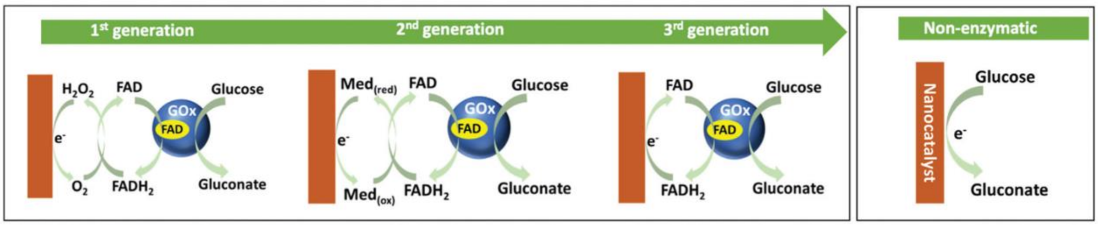

Figure 2.1. 5. Progress in different generations of glucose sensors and development in the field of non-enzymatic glucose sensors. Reproduced with permission from Ref. (35).

Electrochemical detection is cost-effective, reliable, highly sensitive, and quick to respond. Noble metals like Au, Pt, Ag, and Pd and their alloys were extensively employed as catalysts in these biosensors. The poisoning issue with the intermediates, non-selectivity, and high-cost leads to the search for new alternatives.(*52*) Earth-abundant transition metal-oxides-based non-enzymatic glucose sensors have come up as great alternatives to noble metals-based sensors. However, with the dissolubility problem, the high performance, stability, and durability still make them promising candidates for glucose-sensing applications in alkaline conditions only. Cu-based catalysts known for their non-toxicity and low cost have inherently been utilized for their great activity towards GOR. Adding a second metal can modify the electronic structure and improve the intrinsic characteristics. The Ni-Cu combination is expected to play a synergistic role in improving glucose sensing performance as Ni and copper catalysts individually show catalytic activity towards glucose sensing.(*53-58*) The exciting redox couple, Ni^{2+}/Ni^{3+}, is known for its easy existence, favorable redox properties, and facile charge transfer kinetics with the oxidizing species in the analyte.(*59*) Different mechanisms have been proposed on Ni **(*Figure 2.1.6.*)** and Cu sites **(*Figure 2.1.7.*)** of the catalysts.(*34*)

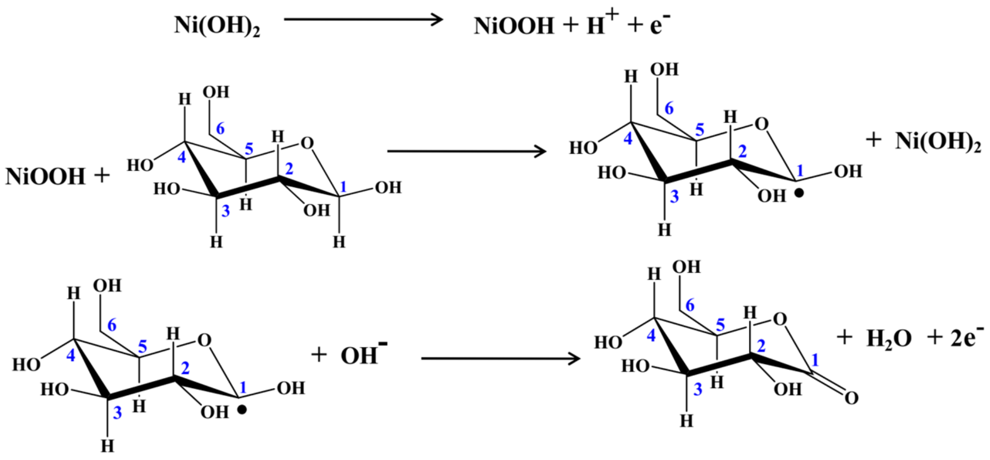

Figure 2.1. 6. Proposed glucose oxidation mechanism on Ni site. Reproduced with permission from Ref. (34).

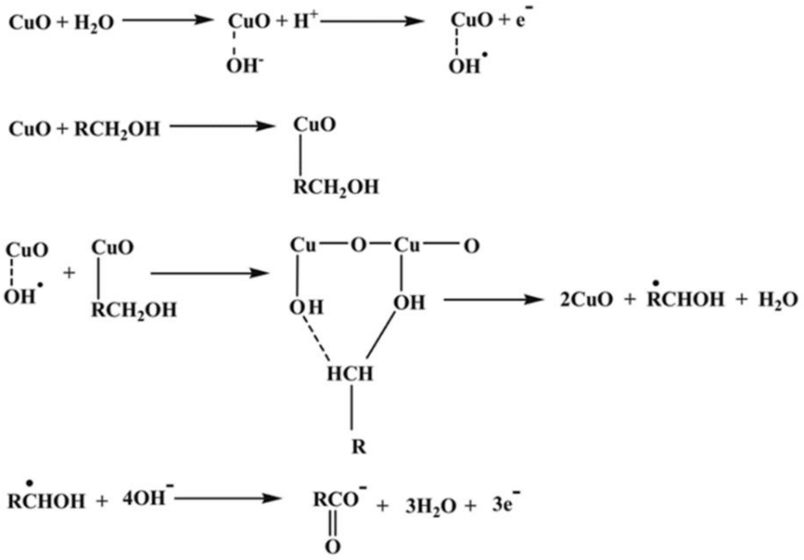

Figure 2.1. 7. Proposed glucose oxidation mechanism on Cu site. Reproduced with permission from Ref. (34).

There are still possibilities of agglomeration of nano catalytic sites, which may hinder the performance of the matrix.(*60, 61*) Also, oxides are known to be low conducting in nature. The porous metallic substrate can affect the dispersion of active sites for feasible diffusion of electrolytes and intermediates and provide good conductivity. Electrocatalysis is a surface phenomenon; the surface morphology of the catalyst and the designed high surface area of the nanostructures could significantly affect the performance and stability. Binder-free direct growth of active material on a self-standing current collector enhances the performance with easier charge migration without any insulating barrier. Also, template-free electrocatalysts are preferred over powdered catalysts taken on some current collector as there are high chances of their detachment with time and at high currents.

Non-enzymatic glucose sensors also have significance in other fields like food and ecological monitoring and development. Co-detection methods have also been employed to detect more than one biological component with single catalysts. For example, in a person with Parkinson's disease, the presence of dopamine along with glucose should be determined. Similarly, uric acid and glucose should be determined for a hyperuricemia patient. Likewise, in the presence of other interfering species like ascorbic acid, glycine, and sucrose, the sensor should not be affected.(*62*)

2.1.4. Figure of merits in the synthesis of value-added chemicals:

Various parameters should be considered while evaluating the performance of a hybrid electrocatalytic reaction. As there are two half-reactions, namely, the oxidation of organics (BOR or GOR) at the anode and the reduction of water (HER) at the cathode, the activity of the individual reactions must be evaluated. In this part of the study, we are concerned with determining the parameters assigned to the oxidation process, and the figures of merit are individually explained.(*63*)

For a reaction occurring as A → B + C, where A is the reactant, B and C are the products.

2.1.4.1. Conversion:

The amount of reactant consumed at a particular time with respect to the initial amount of the reactant defines the rate of conversion and can be evaluated as:

Percentage conversion **(% C)** = $(A_0-A_t)*100/A_0$,

where A_0 and A_t are the initial and final amount of the reactant at time t.

2.1.4.2. Selectivity:

The selectivity towards a particular product is defined as the ratio of the amount of product generated to the amount of reactant consumed and can be evaluated as:

Percentage selectivity **(% S)** = $B_t*100/(A_0-A_t)$,

where B_t is the amount of product formed, A_0 and A_t are the initial and final reactants at time t.

2.1.4.3. Yield:

The amount of product produced in grams per hour is the yield. The percentage yield can be determined from the ratio of the product formed to the maximum amount of product that can be formed and can be evaluated as:

Percentage yield **(% Y)** = $(B_t/B_{max})*100$

2.1.4.4. Faradaic efficiency:

This parameter determines the effective utilization of charge for a particular process and can be evaluated as:

% FE = $(nF* B_t * V)/ (Q * 10)$

where n = no. of electrons transferred, F = Faraday's constant (96485 C mol^{-1}), B_t = amount of product obtained at time t (mol L^{-1}), V = volume of the solution taken (mL), and Q = charge utilized for a reaction to occur (C, observed from the chronoamperometry analysis).

2.1.4.5. Cycle stability:

The number of cycles for which the catalyst is stable to carry out the reaction. After each run, the catalyst electrode must be cleaned and checked in a new electrolyte for the next run.

2.1.4.6. Reproducibility:

Retainability of the performance of different synthesized batches of the material towards a reaction contributes to its reproducibility.

Considering the glucose oxidation for sensing applications, a calibration plot (concentration of glucose versus current) must be analyzed **(*Figure 2.1.8.*)** considering known concentrations of glucose, and various parameters should be evaluated as described below:(*64, 65*)

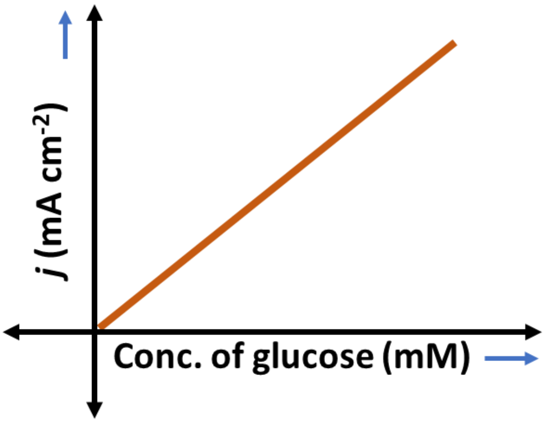

Figure 2.1. 8. Calibration plot for electrochemical glucose detection.

2.1.4.7. Linear response range:

The range of glucose concentration in which the response of the sensor is linear (from the calibration plot) is termed the linear range of response. Lower the linear range, better the sensor.

2.1.4.8. Sensitivity:

Sensitivity can be calculated in a linear range of detection from the slope of the calibration curve and is reported in terms of μA mM^{-1} cm^{-2}. Higher the sensitivity, better the sensor.

2.1.4.9. Limit of detection:

The limit of detection (LOD) is usually evaluated as:

$$LOD = 3.3\ \sigma/s$$

where σ is the standard deviation of peak currents observed for blank solution, and s is the slope of the calibration curve. Lower the value of LOD, better the sensor.

2.1.4.10. Response time:

The time taken by the sensor to detect a particular concentration of glucose is called the response time. Lesser the response time, better the sensor.

2.1.4.11. Rate constant:

During the organic oxidation reactions, the amount of reactant decreases with time and the rate of reaction is affected by the movement of product away from the electrode surface to the bulk of the solution.(*66*) There exists a barrier to charge transfer due to the diffusion contributions and the reaction behaves as a decay process explained by Cottrell's equation wherein,

$I_C / I_L = (k\ c_0\ t)^{1/2}$

where I_C = catalytic current (in presence of organic reductant), I_L = limiting current (blank solution), k = rate constant, c_0 = initial concentration of the reactant, and t = time

The rate constant determines the ability of the catalyst to surpass a kinetic barrier for the reaction.

2.1.5. Conclusions:

This chapter broadly summarizes the aspects of hybrid water electrolysis technology. Replacing the energy-intensive oxygen evolution reaction (OER) at the anode with low energy demanding organic and biomass oxidation reactions favours the low potential requirements necessary for hydrogen generation along with value-added products (VAPs). Various alcohols used for anodic oxidation were highlighted with particular emphasis on benzyl alcohol. Among the biomasses, glucose oxidation for its application in DGFCs and sensing was elaborated. Critical parameters (figures of merit) required for determining the performance of DGFCs and glucose sensors are described in detail.

2.1.6. References:

1. L. Chen, J. Shi, Chemical-assisted hydrogen electrocatalytic evolution reaction (CAHER). *Journal of Materials Chemistry A* **6**, 13538-13548 (2018).
2. A. Raveendran, M. Chandran, R. Dhanusuraman, A comprehensive review on the electrochemical parameters and recent material development of electrochemical water splitting electrocatalysts. *RSC Adv* **13**, 3843-3876 (2023).
3. H. Luo *et al.*, Progress and Perspectives in Photo- and Electrochemical-Oxidation of Biomass for Sustainable Chemicals and Hydrogen Production. *Advanced Energy Materials* **11**, (2021).
4. R. Li, K. Xiang, Z. Peng, Y. Zou, S. Wang, Recent Advances on Electrolysis for Simultaneous Generation of Valuable Chemicals at both Anode and Cathode. *Advanced Energy Materials* **11**, (2021).

5. F. Arshad, T. u. Haq, I. Hussain, F. Sher, Recent Advances in Electrocatalysts toward Alcohol-Assisted, Energy-Saving Hydrogen Production. *ACS Applied Energy Materials* **4**, 8685-8701 (2021).
6. K. Ye, G. Wang, D. Cao, G. Wang, Recent Advances in the Electro-Oxidation of Urea for Direct Urea Fuel Cell and Urea Electrolysis. *Top Curr Chem (Cham)* **376**, 42 (2018).
7. W. Ge *et al.*, Electrocatalytic urea oxidation: advances in mechanistic insights, nanocatalyst design, and applications. *Journal of Materials Chemistry A* **11**, 15100-15121 (2023).
8. X. Liu, W. Sun, X. Hu, J. Chen, Z. Wen, Self-powered H2 generation implemented by hydrazine oxidation assisting hybrid electrochemical cell. *Chemical Engineering Journal* **474**, (2023).
9. E. M. Almutairi, M. A. Ghanem, A. Al-Warthan, M. Kuniyil, S. F. Adil, Hydrazine High-Performance Oxidation and Sensing Using a Copper Oxide Nanosheet Electrocatalyst Prepared via a Foam-Surfactant Dual Template. *Nanomaterials (Basel)* **13**, (2022).
10. L. Gidi, J. Amalraj, C. Tenreiro, G. Ramirez, Recent progress, trends, and new challenges in the electrochemical production of green hydrogen coupled to selective electrooxidation of 5-hydroxymethylfurfural (HMF). *RSC Adv* **13**, 28307-28336 (2023).
11. Y. Holade *et al.*, Recent advances in the electrooxidation of biomass-based organic molecules for energy, chemicals and hydrogen production. *Catalysis Science & Technology* **10**, 3071-3112 (2020).
12. W. Liu, C. Liu, P. Gogoi, Y. Deng, Overview of Biomass Conversion to Electricity and Hydrogen and Recent Developments in Low-Temperature Electrochemical Approaches. *Engineering* **6**, 1351-1363 (2020).
13. J. M. Haan, J. R. Ragadi, K. Hohl, L. Hernandez, J. L. Haan, High performance direct liquid fuel cells powered by xylose or glucose. *International Journal of Hydrogen Energy* **48**, 18041-18053 (2023).
14. J. Chen *et al.*, An alkaline direct oxidation glucose fuel cell using three-dimensional structural Au/Ni-foam as catalytic electrodes. *RSC Advances* **7**, 3035-3042 (2017).

15. Y. Xu, B. Zhang, Recent Advances in Electrochemical Hydrogen Production from Water Assisted by Alternative Oxidation Reactions. *ChemElectroChem* **6**, 3214-3226 (2019).

16. C. A. Martínez-Huitle, M. A. Rodrigo, I. Sirés, O. Scialdone, A critical review on latest innovations and future challenges of electrochemical technology for the abatement of organics in water. *Applied Catalysis B: Environmental* **328**, (2023).

17. T. Wang *et al.*, Combined anodic and cathodic hydrogen production from aldehyde oxidation and hydrogen evolution reaction. *Nature Catalysis* **5**, 66-73 (2021).

18. L. Chen, J. Shi, Co-electrolysis toward value-added chemicals. *Science China Materials* **65**, 1-9 (2021).

19. Y. Wang, S. Zou, W.-B. Cai, Recent Advances on Electro-Oxidation of Ethanol on Pt- and Pd-Based Catalysts: From Reaction Mechanisms to Catalytic Materials. *Catalysts* **5**, 1507-1534 (2015).

20. L. Demarconnay, S. Brimaud, C. Coutanceau, J. M. Léger, Ethylene glycol electrooxidation in alkaline medium at multi-metallic Pt based catalysts. *Journal of Electroanalytical Chemistry* **601**, 169-180 (2007).

21. L. Yaqoob, T. Noor, N. Iqbal, A comprehensive and critical review of the recent progress in electrocatalysts for the ethanol oxidation reaction. *RSC Adv* **11**, 16768-16804 (2021).

22. S.-C. Chang, Y. Ho, M. J. Weaver, Applications of Real-Time FTIR Spectroscopy to the Elucidation of Complex Electroorganic Pathways: Electrooxidation of Ethylene Glycol on Gold, Platinum, and Nickel in Alkaline Solution. *J. Am. Chem. Soc.* **113**, 9506-9513 (1991).

23. Y. Xu *et al.*, Methanol electroreforming coupled to green hydrogen production over bifunctional NiIr-based metal-organic framework nanosheet arrays. *Applied Catalysis B: Environmental* **300**, (2022).

24. M. K. Goetz, M. T. Bender, K. S. Choi, Predictive control of selective secondary alcohol oxidation of glycerol on NiOOH. *Nat Commun* **13**, 5848 (2022).

25. B. Ulas, Y. Yilmaz, S. Koc, H. Kivrak, Supported PbHfCd electrocatalysts over carbon-hydroxyapatite composite fabricated by precipitation and NaBH4

reduction methods for glucose electrooxidation. *Journal of Solid State Electrochemistry* **27**, 3425-3437 (2023).

26. J. Zhong, Y. Shen, P. Zhu, S. Yao, C. An, Size-effect on Ni electrocatalyst: The case of electrochemical benzyl alcohol oxidation. *Nano Research* **16**, 202-208 (2022).
27. P. Mente *et al.*, Oxidation of Benzyl Alcohol Using Cobalt Oxide Supported Inside and Outside Hollow Carbon Spheres. *ChemistryOpen* **10**, 618-626 (2021).
28. H. Huang *et al.*, Ni, Co hydroxide triggers electrocatalytic production of high-purity benzoic acid over 400 mA cm−2. *Energy & Environmental Science* **13**, 4990-4999 (2020).
29. G. Liu *et al.*, Electrocatalytic oxidation of benzyl alcohol for simultaneously promoting H2 evolution by a Co0.83Ni0.17/activated carbon electrocatalyst. *New Journal of Chemistry* **42**, 6381-6388 (2018).
30. H. Li *et al.*, Selective oxidation of benzyl alcohols to benzoic acid catalyzed by eco-friendly cobalt thioporphyrazine catalyst supported on silica-coated magnetic nanospheres. *J Environ Sci (China)* **60**, 84-90 (2017).
31. B. You, Z. Cheng, Y. Tian, S. Wang, B. Wang, Highly Efficient and Selective Oxidation of Benzyl Alcohol by WO42− Catalyst Immobilized by a Phosphonium-Containing Porous Aromatic Framework. *Catalysts* **13**, (2023).
32. M. Sankar *et al.*, The benzaldehyde oxidation paradox explained by the interception of peroxy radical by benzyl alcohol. *Nat Commun* **5**, 3332 (2014).
33. L. E. Rebolledo-Perales, P. Hernández, G. A. Álvarez-Romero, D. Hernández-Ramírez, Trends on the Development of Non-Enzymatic Electrochemical Sensors Modified with Metal-Organic Frameworks for the Quantification of Glucose. *Journal of The Electrochemical Society* **170**, (2023).
34. K. Dhara, D. R. Mahapatra, Electrochemical nonenzymatic sensing of glucose using advanced nanomaterials. *Mikrochim Acta* **185**, 49 (2017).
35. H. Teymourian, A. Barfidokht, J. Wang, Electrochemical glucose sensors in diabetes management: an updated review (2010-2020). *Chem Soc Rev* **49**, 7671-7709 (2020).
36. A. Brouzgou, P. Tsiakaras, Electrocatalysts for Glucose Electrooxidation Reaction: A Review. *Topics in Catalysis* **58**, 1311-1327 (2015).

37. H. Huu Do, S. Y. Kim, Q. V. Le, Development of non-precious metal oxide-based electrodes for enzyme-free glucose detection: A review. *Microchemical Journal* **193**, (2023).
38. X. Shi *et al.*, Complete Glucose Electrooxidation Enabled by Coordinatively Unsaturated Copper Sites in Metal-Organic Frameworks. *Angew Chem Int Ed Engl* **62**, e202316257 (2023).
39. A. Mohammadpour-Haratbar, S. Mohammadpour-Haratbar, Y. Zare, K. Y. Rhee, S. J. Park, A Review on Non-Enzymatic Electrochemical Biosensors of Glucose Using Carbon Nanofiber Nanocomposites. *Biosensors (Basel)* **12**, (2022).
40. M. Zhiani, A. Abedini, S. Majidi, Comparison of Electro-Catalytic Activity of Fe-Ni-Co/C and Pd/C Nanoparticles for Glucose Electro-Oxidation in Alkaline Half-Cell and Direct Glucose Fuel Cell. *Electrocatalysis* **9**, 735-743 (2018).
41. Y. Chen *et al.*, Sustainable production of formic acid and acetic acid from biomass. *Molecular Catalysis* **545**, (2023).
42. X. Lin, H. Zhong, W. Hu, J. Du, Nickel-Cobalt Selenide Electrocatalytic Electrode toward Glucose Oxidation Coupling with Alkaline Hydrogen Production. *Inorg Chem* **62**, 10513-10521 (2023).
43. C. Wang *et al.*, Room temperature, near-quantitative conversion of glucose into formic acid. *Green Chemistry* **21**, 6089-6096 (2019).
44. S. Radhakrishnan *et al.*, Recent Developments and Future Perspective on Electrochemical Glucose Sensors Based on 2D Materials. *Biosensors (Basel)* **12**, (2022).
45. E. H. Yoo, S. Y. Lee, Glucose biosensors: an overview of use in clinical practice. *Sensors (Basel)* **10**, 4558-4576 (2010).
46. J. Yang, M. Cho, Y. Lee, Synthesis of hierarchical NiCo2O4 hollow nanorods via sacrificial-template accelerate hydrolysis for electrochemical glucose oxidation. *Biosens Bioelectron* **75**, 15-22 (2016).
47. P. Du, J. Zhang, Y. Liu, M. Huang, Hydrogen generation from catalytic glucose oxidation by Fe-based electrocatalysts. *Electrochemistry Communications* **83**, 11-15 (2017).
48. W. J. Liu *et al.*, Efficient electrochemical production of glucaric acid and H(2) via glucose electrolysis. *Nat Commun* **11**, 265 (2020).

49. B. Zhu, X. Li, L. Zhou, B. Su, An Overview of Wearable and Implantable Electrochemical Glucose Sensors. *Electroanalysis* **34**, 237-245 (2021).
50. M. A. Khaleque *et al.*, Nanostructured wearable electrochemical and biosensor towards healthcare management: a review. *RSC Adv* **13**, 22973-22997 (2023).
51. A. Heller, B. Feldman, Electrochemical Glucose Sensors and Their Applications in Diabetes Management. *Chem. Rev.* **108**, 2482-2505 (2008).
52. X. Niu, M. Lan, H. Zhao, C. Chen, Highly sensitive and selective nonenzymatic detection of glucose using three-dimensional porous nickel nanostructures. *Anal Chem* **85**, 3561-3569 (2013).
53. K. Yamagiwa, N. Suzuki, T. Wakatabe, D. Satou, Self-formed nanocatalyst layers on Ni–Cu alloy substrates and their characteristics for electrochemical glucose oxidation. *Japanese Journal of Applied Physics* **59**, (2020).
54. X. Wu, W. Lu, High-performance electrochemical glucose sensing enabled by Cu(TCNQ) nanorod array. *Nanotechnology* **29**, 135502 (2018).
55. N. Miya, L. F. E. Machogo-Phao, B. Ntsendwana, Exploring Copper Oxide and Copper Sulfide for Non-Enzymatic Glucose Sensors: Current Progress and Future Directions. *Micromachines (Basel)* **14**, (2023).
56. M. M. Abuzaied, Y. M. Asal, A. M. Mohammad, I. M. Al-Akraa, Enhanced Glucose Electrooxidation at Ni-Cu Binary Oxide Nanocatalyst. *International Journal of Electrochemical Science* **15**, 2449-2457 (2020).
57. D. AnnieCanisius *et al.*, Analysing the bifunctional ability of CuO/BiOBr/rGO as an electrode for non-enzymatic glucose sensor and supercapacitor. *Materials Letters* **346**, (2023).
58. N. K. Shrestha, S. A. Patil, A. S. Salunke, A. I. Inamdar, H. Im, Accelerating glucose electrolysis on Cu-doped MIL-88B for an energy efficient anodic reaction in water splitting. *Dalton Trans* **52**, 10933-10941 (2023).
59. M. T. Bender, Y. C. Lam, S. Hammes-Schiffer, K. S. Choi, Unraveling Two Pathways for Electrochemical Alcohol and Aldehyde Oxidation on NiOOH. *J Am Chem Soc* **142**, 21538-21547 (2020).
60. A. Salimi, M. Roushani, S. Soltanian, R. Hallaj, Picomolar Detection of Insulin at Renewable Nickel Powder-Doped Carbon Composite Electrode. *Anal. Chem.* **79**, 7431-7438 (2007).

61. A. Salimi, M. Roushani, Non-enzymatic glucose detection free of ascorbic acid interference using nickel powder and nafion sol–gel dispersed renewable carbon ceramic electrode. *Electrochemistry Communications* **7**, 879-887 (2005).
62. D. A. Gough, F. L. Anderson, J. Giner, C. K. Colton, J. S. Soeldner, Effect of Coreactants on Electrochemical Glucose Oxidation. *ANALYTICAL CHEMISTRY* **50**, 941-944 (1978).
63. G. Sanghez de Luna *et al.*, Electrification of glucose valorization over NiO/Ni foam. *Sustainable Energy & Fuels* **7**, 4474-4485 (2023).
64. L. Goodnight, D. Butler, T. Xia, A. Ebrahimi, Non-Enzymatic Detection of Glucose in Neutral Solution Using PBS-Treated Electrodeposited Copper-Nickel Electrodes. *Biosensors (Basel)* **11**, (2021).
65. Z. Haghparas, Z. Kordrostami, M. Sorouri, M. Rajabzadeh, R. Khalifeh, Highly sensitive non-enzymatic electrochemical glucose sensor based on dumbbell-shaped double-shelled hollow nanoporous CuO/ZnO microstructures. *Sci Rep* **11**, 344 (2021).
66. N. Sattarahmady, H. Heli, A non-enzymatic amperometric sensor for glucose based on cobalt oxide nanoparticles. *Journal of Experimental Nanoscience* **7**, 529-546 (2012).

Chapter- 2.2 Electrochemical oxidation of benzyl alcohol (BOR): Influence of chromium on Ni foam

Summary:

Hybrid water electrolysis with the simultaneous generation of hydrogen and value-added chemicals enhances the viability of the commercial water electrolysis process. A remarkably high current density of 1.4 A cm^{-2} towards benzyl alcohol oxidation (BOR) at a low potential of 1.45 V reported in this work suggests that the oxygen evolution reaction (OER) can be replaced with BOR by selecting a suitable catalyst. A chromium oxide-treated Ni foam (CTNF) synthesized through a simple hydrothermal route offers 100 % conversion and 99.5 % faradaic efficiency towards benzoic acid. Including Cr oxide assists the generation of hydrophilic sites and improves the pore-forming tendencies, enhancing the active surface sites. In-situ Raman analysis confirms the reversible electrochemical conversion of Ni hydroxides to NiOOH, which converts benzyl alcohol to benzoic acid by chemical oxidation. Cr oxide on the nickel foam acts as a pore-forming agent and promoter, facilitating the feasible sorption of intermediates. The catalyst exhibited sustained conversion with high selectivity in the full-cell arrangement also. In a two-electrode arrangement, the catalyst demonstrates excellent performance, achieving a current density of 100 mA cm^{-2} at an applied potential of 1.22 V. Furthermore, at 2.33 V, it attains a higher current density of 750 mA cm^{-2}.

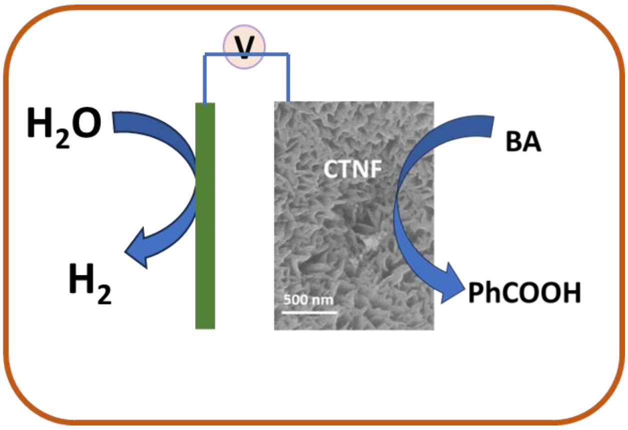

(A manuscript based on this work is under preparation)

2.2.1. Introduction:

The chemical method for producing value-added chemicals is undergoing a significant transformation with a notable shift towards green synthesis through electrochemistry. The conventional approach to achieving a high-purity H_2 generation, free from carbon emissions, involved the electrochemical process of evolving O_2 molecules at the anode (OER).(*1*) However, oxygen lacks market value and demands high theoretical energy requirements (1.23 V) due to sluggish kinetics. To address this, energy-intensive OER can be replaced by a low potential demanding oxidation reaction, generating value-added products (VAPs) at the anode.(*2-7*) This enhances the overall performance and efficiency of hydrogen production. In this way, the overall process will benefit from low energy requirements and the formation of high-quality products at both electrodes (H_2 at the cathode and a value-added product at the anode). For instance, electrochemical synthesis of carbonyl products can be achieved at lower potential from thermodynamically feasible alcohol oxidation at the anode. Diverse products can be obtained by the anodic oxidation of various alcohols like ethanol, glycol, glycerol, benzyl alcohol, methanol, etc in place of OER.(*4, 8*)

Among these, the partial oxidation reaction of benzyl alcohol (BOR) to yield benzaldehyde or benzoic acid **(*Figure 2.2.1.*)** stands out as a highly demanding process. Benzoic acid is a valuable intermediate for producing various chemicals utilized in pharmaceuticals and synthetic sectors. The industrial production of benzoic acid through the toluene oxidation process involves harsh conditions of high temperature and pressure using highly toxic chemical oxidants, necessitating energy-intensive separation techniques.(*7, 9*)

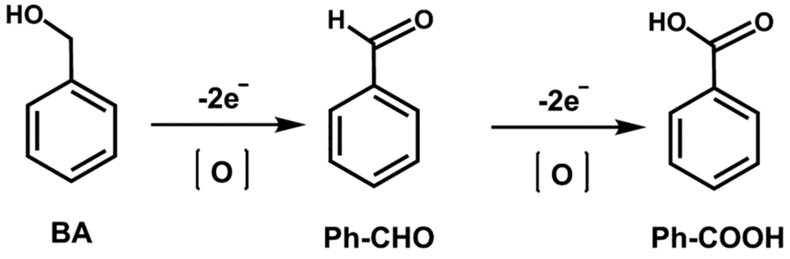

Figure 2.2. 1. Electrochemical benzyl alcohol oxidation to intermediate benzaldehyde (PhCHO), and final benzoic acid (PhCOOH) as the products. Reproduced with permission from Ref. (9).

Electrochemical oxidation of benzyl alcohol to benzoic acid involves water as the solvent. In addition, the selectivity of the product can be controlled with the applied potentials.(*10-13*) However, the competitive oxygen evolution reaction (OER) poses a significant challenge under higher potentials on positive biasing. Thus, lower potentials are preferred to circumvent the interference from OER and maximize the charge utilization, thereby improving the efficiency of the overall process **(*Figure 2.2.2.*)**.

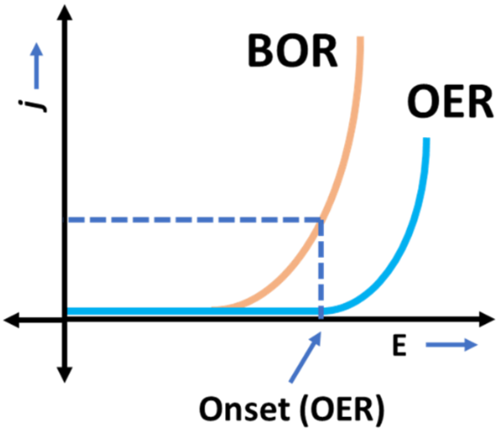

Figure 2.2. 2. Maximum charge utilization for benzyl alcohol considered before the onset of OER.

Extensive research highlighted the efficient role of noble metal-based catalysts (Pt, Ru, and Au) in benzyl alcohol oxidation.(*14*) Transition metal-based catalysts (***Table 2.2.1.)*** have been explored as alternatives, considering the high cost of noble metals and their scarcity. *(9, 10, 15-23)* However, achieving industrial scale performance (current densities ≥ 400 mA cm^{-2} at low potentials) is still challenging at a potential where OER can be arrested.

Table 2.2. 1. Reported catalysts for electrochemical benzyl alcohol oxidation reaction (BOR).(9, 10, 15-23)

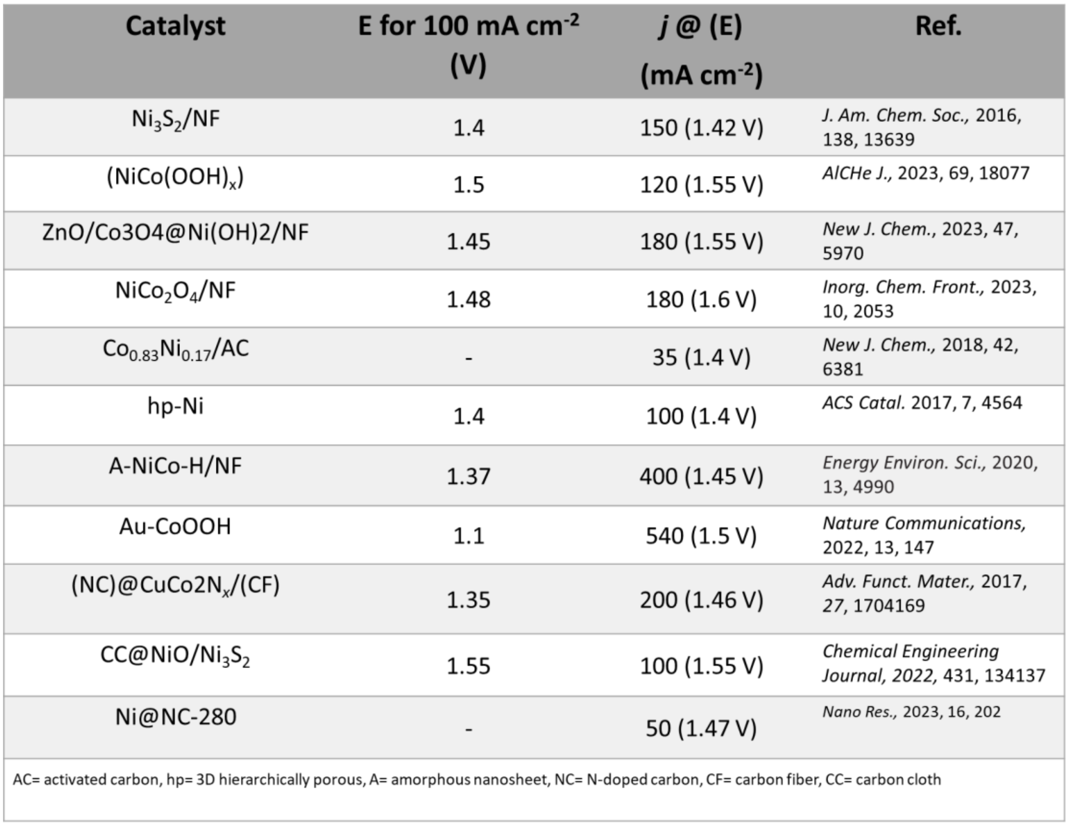

Catalyst	E for 100 mA cm^{-2} (V)	*j* @ (E) (mA cm^{-2})	Ref.
Ni_3S_2/NF	1.4	150 (1.42 V)	*J. Am. Chem. Soc.*, 2016, 138, 13639
($NiCo(OOH)_x$)	1.5	120 (1.55 V)	*AlChe J.*, 2023, 69, 18077
ZnO/Co3O4@Ni(OH)2/NF	1.45	180 (1.55 V)	*New J. Chem.*, 2023, 47, 5970
$NiCo_2O_4$/NF	1.48	180 (1.6 V)	*Inorg. Chem. Front.*, 2023, 10, 2053
$Co_{0.83}Ni_{0.17}$/AC	-	35 (1.4 V)	*New J. Chem.*, 2018, 42, 6381
hp-Ni	1.4	100 (1.4 V)	*ACS Catal.* 2017, 7, 4564
A-NiCo-H/NF	1.37	400 (1.45 V)	*Energy Environ. Sci.*, 2020, 13, 4990
Au-CoOOH	1.1	540 (1.5 V)	*Nature Communications*, 2022, 13, 147
(NC)@$CuCo2N_x$/(CF)	1.35	200 (1.46 V)	*Adv. Funct. Mater.*, 2017, *27*, 1704169
CC@NiO/Ni_3S_2	1.55	100 (1.55 V)	*Chemical Engineering Journal, 2022*, 431, 134137
Ni@NC-280	-	50 (1.47 V)	*Nano Res.*, 2023, 16, 202

AC= activated carbon, hp= 3D hierarchically porous, A= amorphous nanosheet, NC= N-doped carbon, CF= carbon fiber, CC= carbon cloth

Furthermore, porous supports (like porous Ni, Cu, Fe, etc.) are known to enhance the effective charge transfer, lower the diffusion barrier, and hence improving the mass flow of the reactants to the active sites.(*15*) Among the various porous supports, Ni foam has been extensively used owing to its high stability and chemical reactivity. The surface of the Ni foam gets converted to $Ni(OH)_2$ in the alkaline medium, which then oxidizes to NiO(OH) when subjected to oxidation potentials.(*12, 24*) This NiO(OH) is known to oxidize the alcohol chemically into an aldehyde or acid and subsequently undergoes reduction to form a $Ni(OH)_2$ surface **(*Figure 2.2.3.*)**.

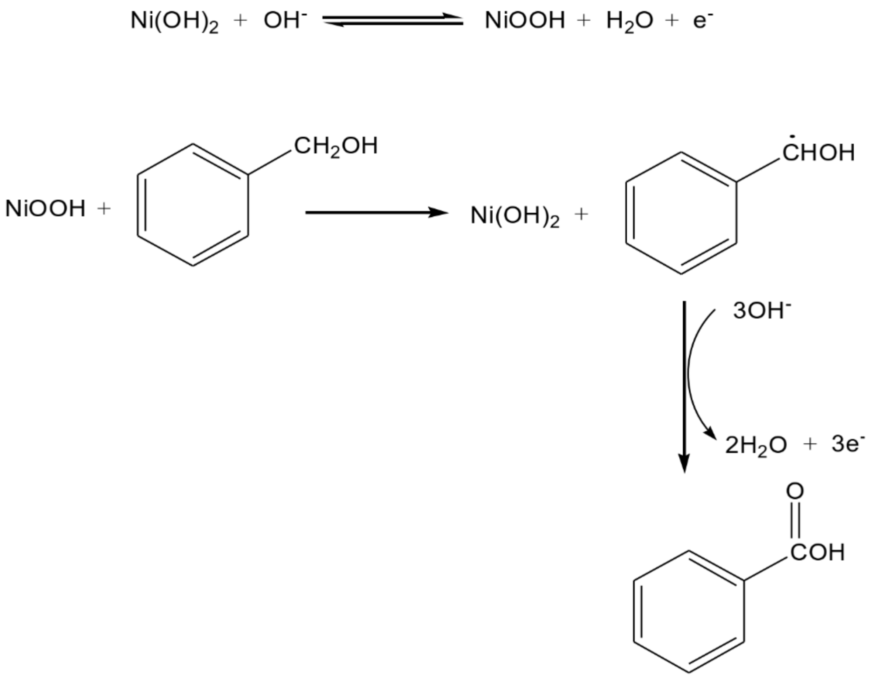

Figure 2.2. 3. Mechanistic illustration of Ni active site for benzyl alcohol oxidation reaction. Reproduced with permission from Ref. (12).

Nevertheless, the performance of the porous nickel towards organic oxidation is still hampered by low current density, which in turn limits the hydrogen evolution reaction. High valent metals like Mo, W, and Cr have been employed to lower the transformation energy for forming active metal species in a high oxidation state.(*25-28*) Cr due to its leaching tendency in alkaline environments, has been used as a pore-forming agent at the anode in electrochemical oxidation reactions. Furthermore, the synergism between Cr and Ni may lead to desirable changes in the band structure of final electrocatalyst, leading to favorable sorption kinetics for the precursor, benzyl alcohol, and the reaction intermediates.

2.2.2. Scope of the present investigation:

Herein, we report an ultra-low chromium oxide-containing Ni foam (CTNF) electrocatalyst exhibiting an impressive performance for benzyl alcohol oxidation (BOR) with a high current density of 1.4 A cm^{-2} at a low potential of 1.45 V vs. RHE. This is the highest value reported so far for any catalyst towards electrochemical BOR. It shows nearly 99.5 % faradaic efficiency towards benzoic acid with 100% conversion of benzyl alcohol. In-situ Raman studies confirm the generation of NiOOH sites as the active site for the chemical oxidation of benzyl alcohol in CTNF. The high production rate of benzoic acid and good cycling stability make CTNF as a potential candidate for benzyl alcohol assisted water electrolysis.

2.2.3. Materials and methods:

2.2.3.1. Materials required:

The materials required for synthesizing various catalysts and their application in electrochemical analysis were purchased from different sources. Chromium chloride dihydrate ($CrCl_3 . 2H_2O$) was purchased from Sigma-Aldrich, nickel chloride hexahydrate ($NiCl_2 . 6 H_2O$) from Loba Chemie, urea from S D Fine chemicals, and 5 wt % Nafion® perfluorinated resin solution, benzyl alcohol, benzaldehyde, and benzoic acid were purchased from Sigma-Aldrich, HCl (37%, AR grade), KOH, and isopropyl alcohol (IPA) from Merck Chemicals. All chemicals were used as received without any further purification. Milli Q water (18.2 S cm) is used for all the synthesis and electrochemical analyses. Ni foam (1.2 mm thick) used as the support for electrochemical studies was purchased from MTI, USA.

2.2.3.2. Synthesis of the catalysts:

Ni foam (NF) was cleaned with acetone and 3 M HCl solution and dried at room temperature for 15-20 min. A urea-mediated hydrothermal route **(*Figure 2.2.4.*)** was used to synthesized the Cr oxide-treated NF (CTNF) catalyst.(*29*) For the synthesis, 12.5 mL 0.16 M solution of $CrCl_3 . 6H_2O$ salt (2 mmol of Cr) was taken in a Teflon-lined autoclave, followed by the addition of 900 mg of urea (15 mmol). To this solution, 12.5 mL of ethanol was added with a piece (2x2 cm) of cleaned Ni foam. The tightened autoclave was kept at 160 ℃ in the oven for seven hours. After that, the autoclave was allowed to cool in ambient conditions, and the NF was washed with water and ethanol and dried.

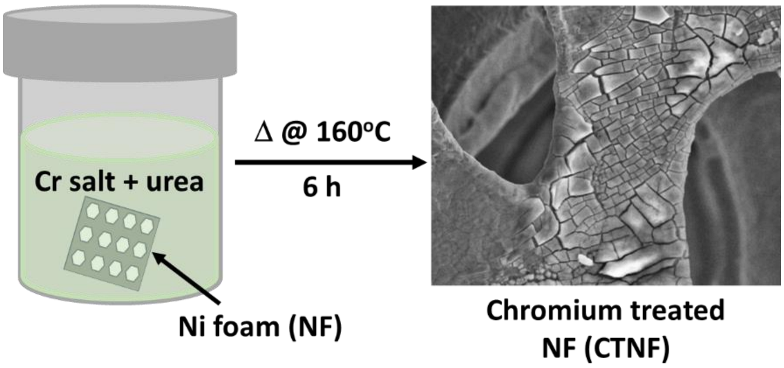

Figure 2.2. 4. Schematics of urea-mediated hydrothermal synthesis of Chromium treated-Ni foam (CTNF) catalyst.

The control powdered samples containing Cr and Ni were also synthesized through a similar procedure without adding NF to the Teflon-lined autoclave. $NiCl_2$. $6H_2O$ salt was the Ni source for synthesizing the powdered Ni-containing samples. catalysts. Urea-treated NF (NF-U) was synthesized with a similar procedure without adding chromium salt. MoNi-based catalyst for hydrogen evolution reaction (HER) analysis was also synthesized in order to fabricate a full cell using a modified procedure reported in literature.(*30*) In a typical synthesis, 185 mg (0.01 M) of $(NH_4)_6Mo_7O_{24}.4H_2O$, 175 mg (0.04 M) of $Ni(NO_3)_2$. $6H_2O$, and a piece of Ni foam (2x2 cm) were taken in 15 mL DI water taken in a Teflon-lined autoclave and heated at 150 °C for six hours. The obtained sample was dried at 60 °C for two days and then treated under an H_2 environment at 500 °C for two hours.

2.2.3.3. Characterization and electrochemical details:

The instrumentation techniques (PXRD, FESEM, TEM, Raman, XPS, etc) used to characterize the samples are described in detail in the appendix at the end of this thesis.

Electrochemical measurements were carried out using an electrochemical workstation obtained from EC-Lab, Biologic Science Instruments VSP for evaluating the electrochemical activities of catalysts towards oxygen evolution reaction (OER), hydrogen evolution reaction (HER) in the presence and absence of benzyl alcohol and other electrochemical analyses. All the primary electrochemical measurements were carried out in a small cell (10.0 mL volume) with a standard three-electrode arrangement while full cell studies were done in a two-electrode arrangement. Hydrothermally synthesized electrodes or powder-coated carbon paper (CP) electrodes were considered as the working electrodes, a high surface area graphite rod was taken as a counter electrode, and a mercury-mercuric oxide (Hg/HgO) electrode as a reference electrode in alkaline (1 M KOH) conditions. All the polarization curves were recorded at 20 mV s^{-1} with 85% iR compensation (wherever mentioned if iR uncompensated) arising due to the ohmic resistance of the cell. All the measured potentials are reported with respect to reversible hydrogen electrode (RHE). The specific activities were reported with geometrical surface area normalized current densities, while intrinsic performance was shown with current densities normalized to electrochemically active surface areas.

2.2.3.4. Product analysis:

The product observed during BOR studies were analysed using ^{1}H-nuclear magnetic resonance (^{1}H-NMR) studies at 400 MHz frequency in Bruker 400. ^{1}H-NMR studies of different concentration of standard samples (benzyl alcohol, and benzoic acid) were done using 50 μL of D_2O as the solvent and 20 μL of DMSO as the internal standard. The area under the signals **(*Figure 2.2.5.*)** corresponding to the existence of benzyl alcohol (δ8.02 ppm) and benzoic acid (δ7.41 ppm) in the ^{1}H-NMR spectra were quantified with respect to the area under DMSO peak (δ2.71 ppm). The peak area under the DMSO peak was calibrated and set as 6. The calibration plot **(*Figure 2.2.6.*)** using peak integrals of standard samples was plotted.

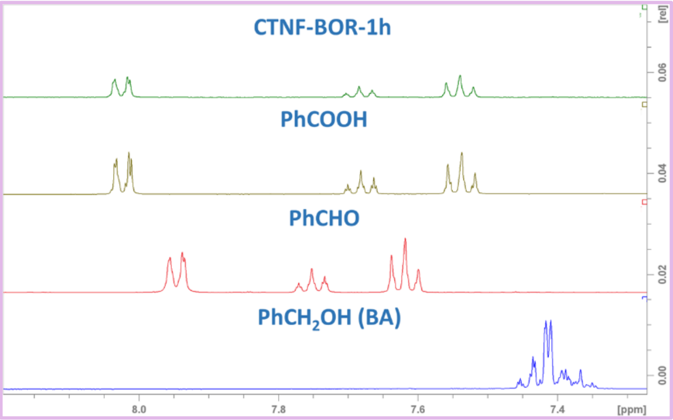

Figure 2.2. 5. ^{1}H nuclear magnetic resonance (NMR) peaks for different standard samples.

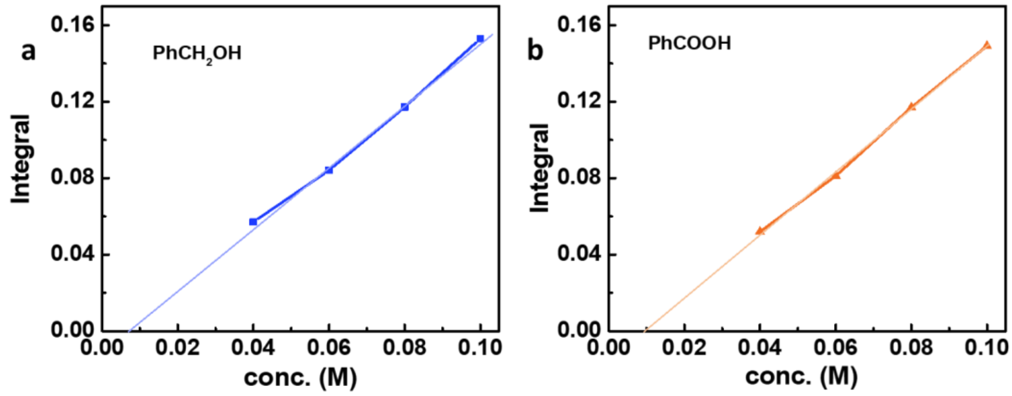

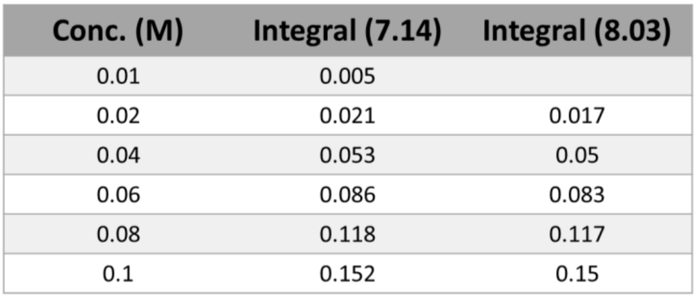

Conc. (M)	Integral (7.14)	Integral (8.03)
0.01	0.005	
0.02	0.021	0.017
0.04	0.053	0.05
0.06	0.086	0.083
0.08	0.118	0.117
0.1	0.152	0.15

Figure 2.2. 6. Calibration plots of standard samples of (a) benzyl alcohol (BA), and (b) benzoic acid (PhCOOH) detected through ^{1}H NMR analysis.

Chronoamperometric analysis was done on different catalysts and the products are collected from the electrolyte. 0.2-micron filters were used to filter the samples collected from the electroanalysis. 200 μL of collected sample was neutralized with 500 μL of H_2SO_4. 20 μL of DMSO (internal standard) and 50 μL of D_2O (solvent) were added to 700 μL of the above-neutralized sample. The sample was transferred to an NMR tube for ^{1}H NMR analysis. The quantitative analysis of various species in the collected sample was determined from the calibration plot of normalized area versus concentration.

2.2.4. Results and discussion:

2.2.4.1. Characterization of the CTNF catalyst:

The powder X-ray diffraction (PXRD) patterns of CTNF and NF-U catalysts **(*Figure 2.2.7.*)** show sharp peaks at 44.8°, 52°, and 76.5° and these can be assigned to (110), (200), and (220) planes of Ni from Ni foam support. No peaks corresponding to Cr species were observed. The obvious reason behind the non-existence of Cr-related peaks was the ultra-low content of around 2% Cr in the final synthesized sample (CTNF), as determined by inductively coupled plasma-optical emission spectroscopy (ICP-OES).

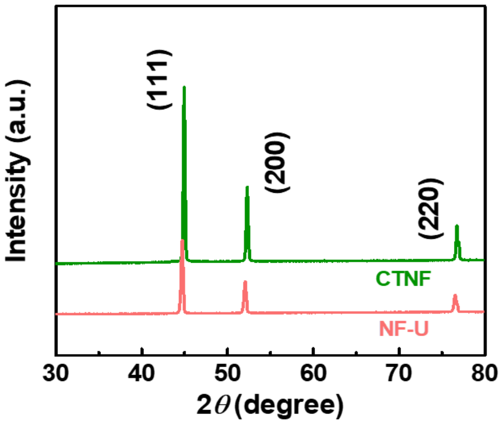

Figure 2.2. 7. Powder X-ray diffraction (PXRD) pattern of CTNF, and NF-U catalysts.

Field emission scanning electron microscopy (FESEM) images of blank NF showed a flat surface, while urea-treated NF (NF-U) showed the generation of a rough surface. Compared to blank NF and NF-U catalysts **(*Figure 2.2.8.a-d*)**, nanoporous plate-like morphology was observed for the CTNF catalyst covering the surface of Ni foam with an average sheet thickness **(*Figure 2.2.8.e, f*)** lying in a broad range of 30-100 nm with pore size lying in 20-60 nm range.

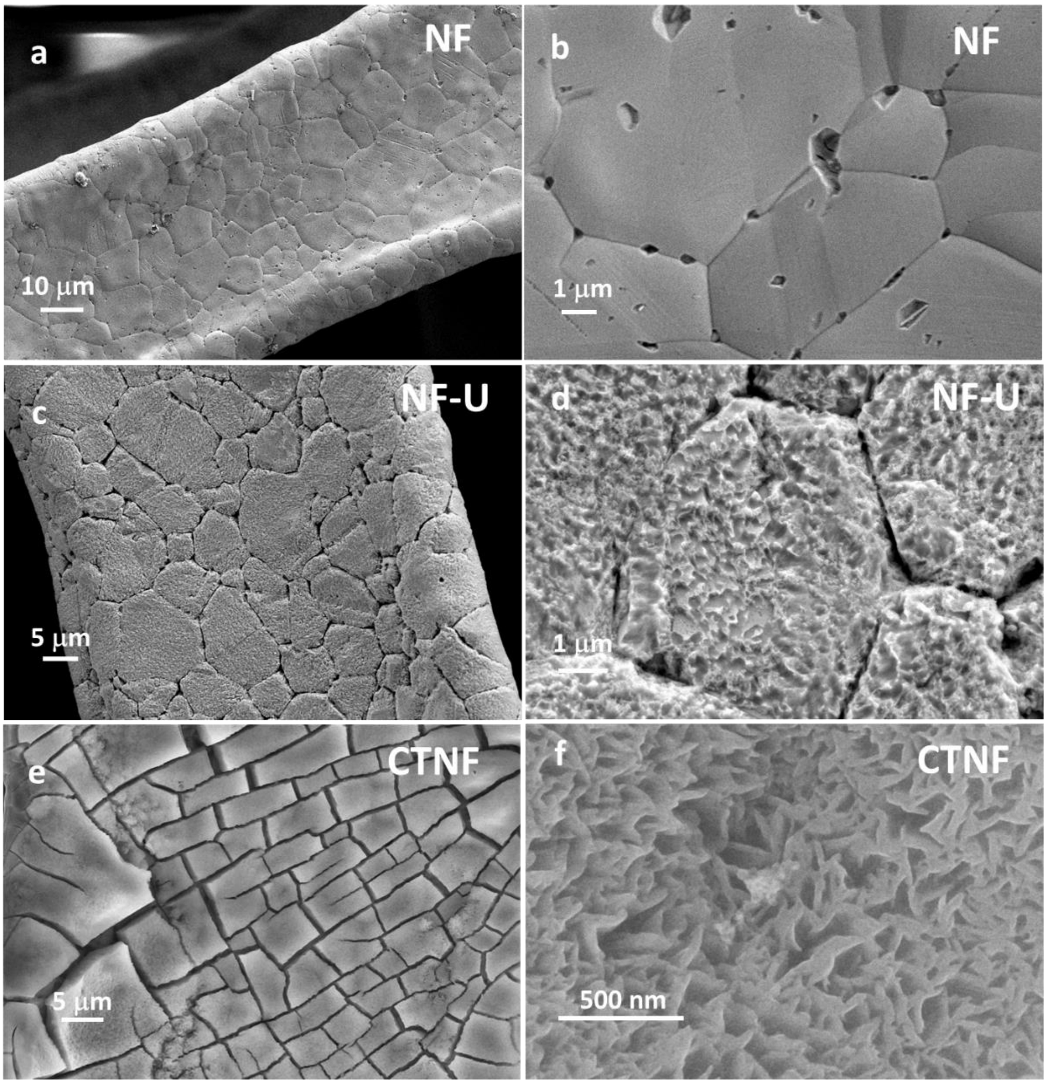

Figure 2.2. 8. Field emission scanning electron microscopy (FESEM) images of (a, b) NF, (c, d) urea-treated NF (NF-U), and (e, f) chromium oxide-treated NF (CTNF) catalysts.

EDS analysis **(*Figure 2.2.9.*)** shows uniform dispersion of Cr, O, and Ni with Cr content estimated to be around 2.0 wt %.

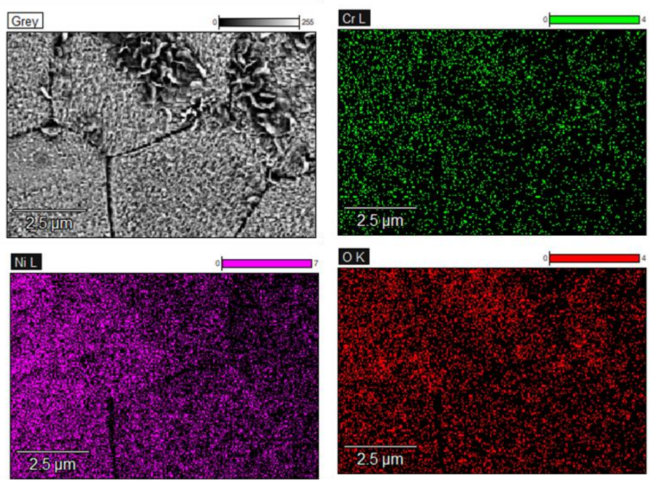

Catalyst	% Weight		
	Cr	Ni	O
CTNF	2.2	89.4	8.4

Figure 2.2. 9. Energy dispersive X-ray (EDS) analysis of CTNF catalyst.

Further, the transmission electron microscopy (TEM) image (***Figure 2.2.10.***) of CTNF confirmed the existence of plate-like morphology.

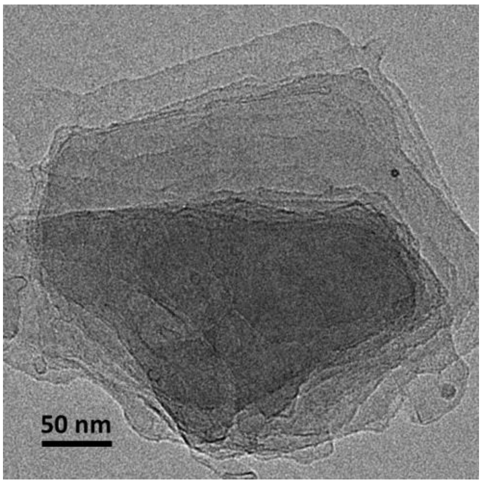

Figure 2.2. 10. Transmission electron microscopy (TEM) image of CTNF catalyst.

The high-resolution transmission electron microscopy (HRTEM) image **(*Figure 2.2.11.a*)** showed lattice fringes of 0.21 nm, 0.24 nm, and 0.25 nm. However, fringes of oxides and hydroxides of Cr and Ni fall very closely and, thus, cannot be differentiated.

The selected area electron diffraction (SAED) pattern (***Figure 2.2.11.b***) further shows planes corresponding to oxides and hydroxides Cr and Ni.

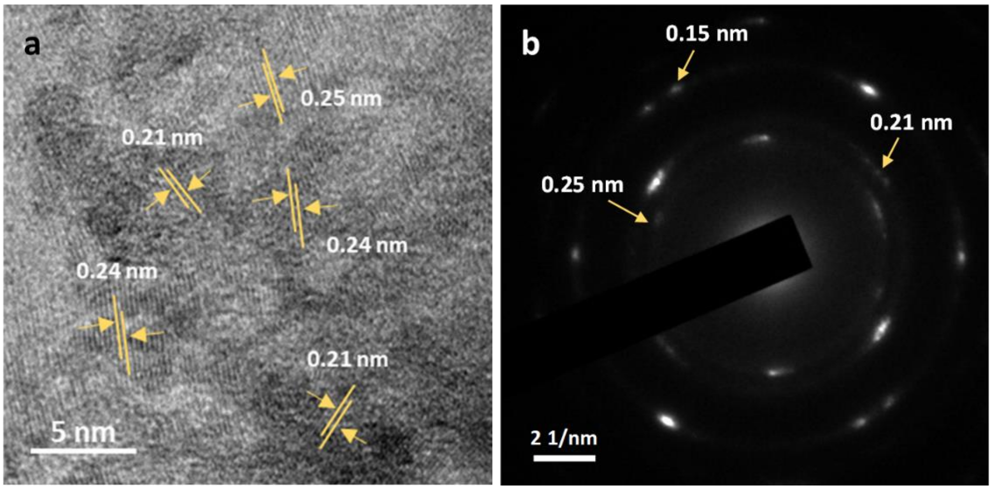

Figure 2.2. 11. (a) High-resolution transmission electron microscopy (HRTEM) and (b) selected area electron diffraction (SAED) analyses of CTNF catalyst.

The Raman spectra (***Figure 2.2.12.***) of CTNF catalyst shows the peaks corresponding to A_{1g} (555 cm^{-1}), and E_g (625 cm^{-1}) mode of Cr_2O_3 with B_{2g} (830 cm^{-1}) mode of CrO_2. Other peaks at 455 cm^{-1}, 535 cm^{-1}, 995 cm^{-1}, and 1086 cm^{-1} correspond to the hydroxides of Ni, while peak at 865 cm^{-1} can be assigned to hydroxides of chromium. (*31*, *32*)

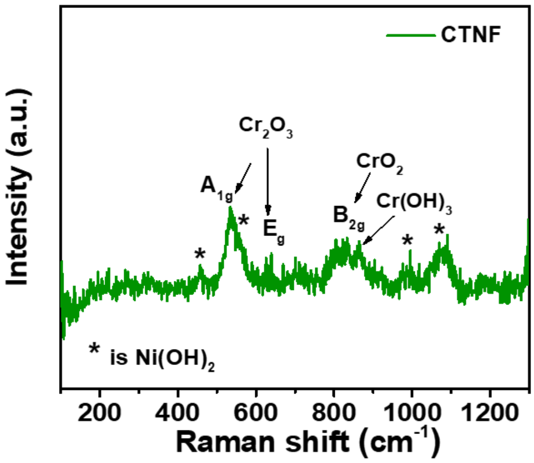

Figure 2.2. 12. Raman analysis of CTNF catalyst.

The chemical nature of elements in NF-U and CTNF catalysts was determined by X-ray photoelectron spectroscopy (XPS) analysis. In the high-resolution Ni 2p spectra of NF-

U (***Figure 2.2.13.a***), peak at 852.6 eV can be assigned to Ni^0 species. Other peaks at 853.5 eV, and 856.6 eV correspond to the existence of Ni^{2+}, and Ni^{3+} species, respectively. Satellite peaks for Ni^{2+} were observed at 860.7 eV and 878.5 eV. The Ni 2p spectra observed from the CTNF catalyst showed positive shift in binding energies for Ni^0 (852.7 eV), Ni^{2+} (854.3 eV), and Ni^{3+} (857.5 eV) (***Figure 2.2.13.b***) species. The Cr 2p spectra of CTNF catalyst show peaks at 576.9 eV, and 586.2 eV, corresponding to Cr^{3+} species of Cr_2O_3.(*33-35*) Peaks corresponding to Cr^{6+} oxides were also seen at 579.4 eV and 588.0 eV (***Figure 2.2.14.***). The positive binding energy shift for CTNF catalyst observed from Ni 2p spectra highlights the charge transfer from Ni to Cr sites.

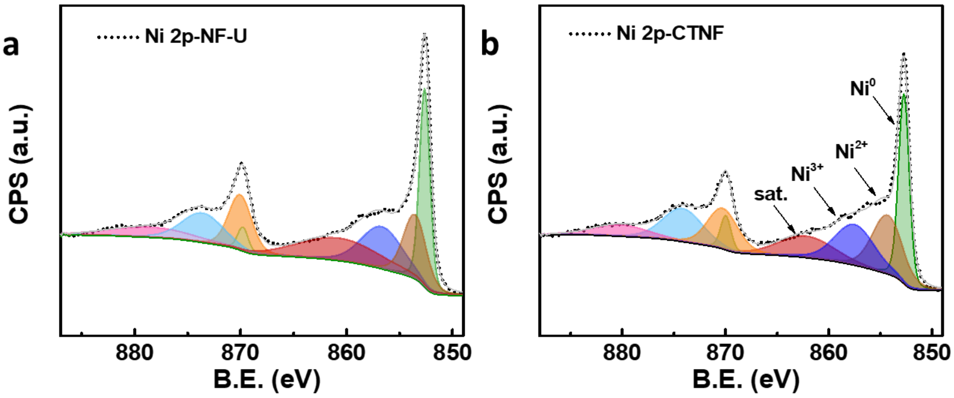

Figure 2.2. 13. X-ray photoelectron spectroscopy (XPS) Ni 2p spectra of (a) NF-U and (b) CTNF catalysts.

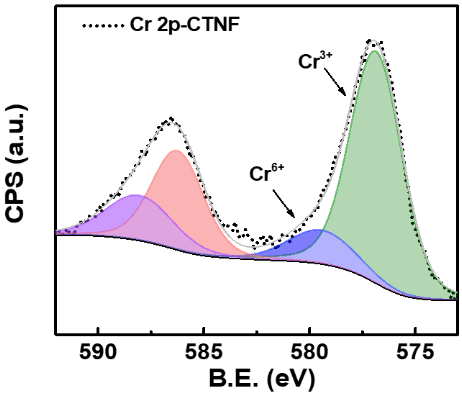

Figure 2.2. 14. High-resolution X-ray photoelectron spectroscopy (XPS) Cr 2p spectra of CTNF catalyst.

2.2.4.2. Electrochemical measurements:

The activity of CTNF and NF-U catalysts was measured in 1.0 M KOH. The LSV shows oxidation of Ni^{2+} to Ni^{3+} species at 1.3 V (***Figure 2.2.15.***). It is known that the surface $Ni(OH)_2$ species present on the Ni foam undergo oxidation to NiOOH at positive potentials in alkaline conditions. The area under the oxidation peak (Ni^{2+} to Ni^{3+} conversion) corresponds to the amount of active Ni sites. A relatively high area under the oxidation peak was observed for the CTNF catalyst compared to NF-U. Both CTNF and NF-U catalysts showed onset potential for OER at 1.45 V and for BOR (in the presence of 0.1 M BA) at around 1.25 V (***Figure 2.2.15.***). The CTNF catalyst attained a current density of 100 mA cm^{-2} at a very low potential of 1.3 V for BOR. Furthermore, a remarkably high current density of 1.4 A cm^{-2} was achieved using CTNF catalyst at a minimum potential of 1.45 V vs. RHE for BOR without any competitive OER. To our knowledge, this is the highest value reported so far for BOR in the literature, as shown in ***Table 2.2.1***. In contrast to CTNF, the NF-U catalyst shows 400 mA cm^{-2} at the same potential (1.45 V).

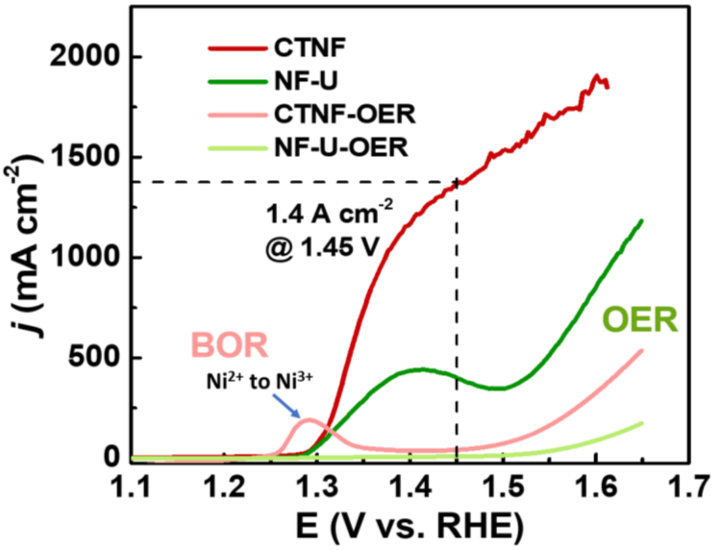

Figure 2.2. 15. Polarized linear sweep voltammograms (LSVs) of CTNF and NF-U catalysts in the presence (BOR) and absence (OER) of benzyl alcohol in 1.0 M KOH (BOR represents benzyl alcohol oxidation reaction, and OER is oxygen evolution reaction).

Control experiments with Cr_2O_3, Ni hydroxide, and mixed chromium-nickel hydroxides (***Figure 2.2.16.***) show poor performance towards BOR with sample supported on carbon paper, indicating the importance of Ni foam support for this reaction.

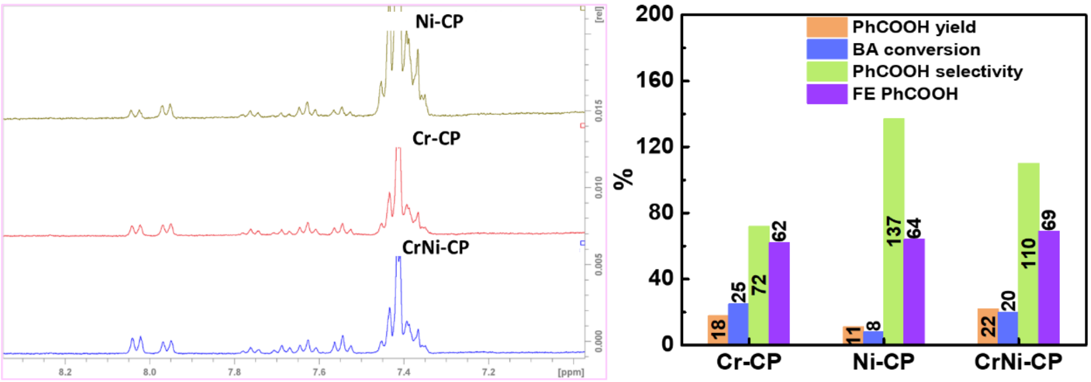

Figure 2.2. 16. (a) ^{1}H nuclear magnetic resonance (NMR) peaks for samples collected from studies of catalyst on CP after 1 h, and (b) performance determined for different catalysts at CP electrode.

The product analysis through nuclear magnetic resonance (NMR) studies reveals that more than 80 % conversion of benzyl alcohol to benzoic acid (***Figure 2.2.17.a***) occurred in around 15 min. However, the complete conversion of BA to PhCOOH (0.5 mmol h^{-1}) occurs in 60 min. On the other hand, NF-U shows only 73% conversion to PhCOOH (0.26 mmol h^{-1}) in 60 min time (***Figure 2.2.17.a***). The CTNF catalyst showed 98 % selectivity (***Figure 2.2.17.b***) toward the formation of benzoic acid. A three-fold improvement in the rate constant was observed for the CTNF catalyst (0.06 min^{-1}) compared to NF-U (-0.02 min^{-1}), considering first-order reaction kinetics (***Figure 2.2.17.c***). Different synthesized batches (***Figure 2.2.17.d***) of the CTNF catalyst showed good reproducibility.

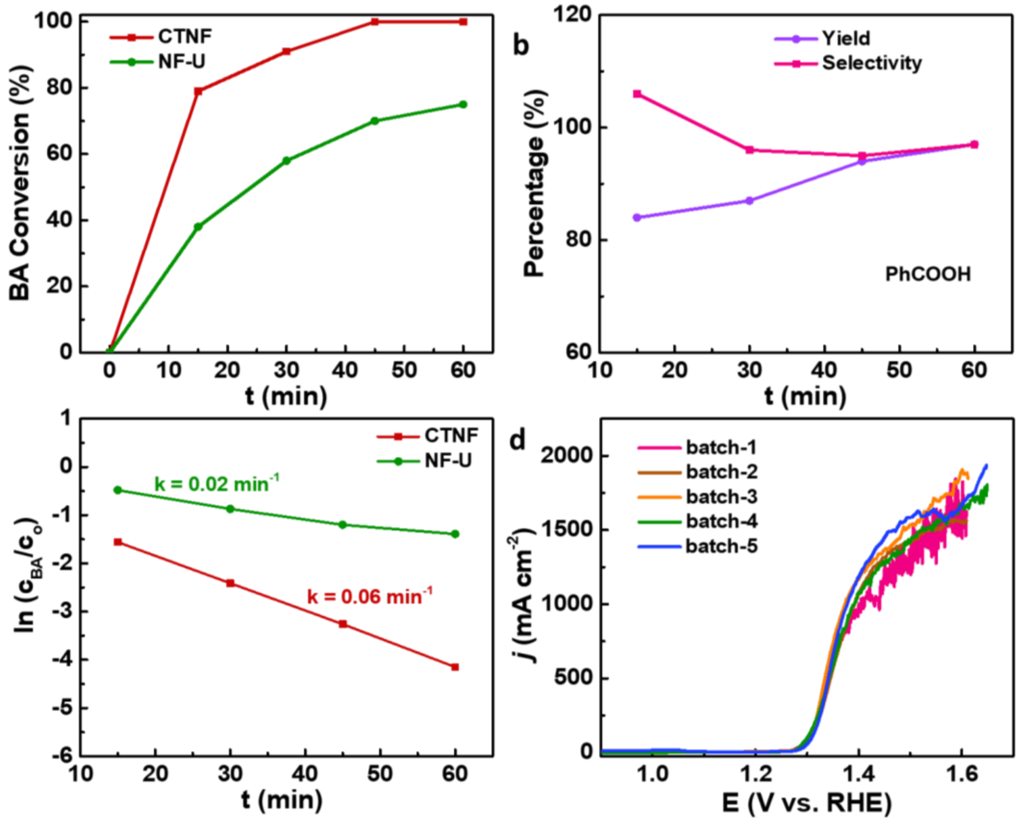

Figure 2.2. 17. (a) % BA conversion of NF-U and CTNF catalysts, (b) % yield and selectivity of PhCOOH observed with CTNF catalyst, (c) rate constant study of NF-U and CTNF catalysts, and (d) reproducibility of CTNF catalyst.

However, at higher concentrations of benzyl alcohol (0.15 M and 0.2 M), the activity decreases (***Figure 2.2.18.***), which could be due to the inability of the reactants to reach the overcrowded active site. Carrying out BOR at lower concentrations of KOH, low performance was observed (***Figure 2.2.19.a***) indicating the poor ionic conductivity of the electrolyte medium. Also, the chronoamperometry studies at higher potentials (over 1.45 V) (***Figure 2.2.19.b***) reveal reduction in conversion, yield, and selectivity towards PhCOOH formation due to competitive OER.

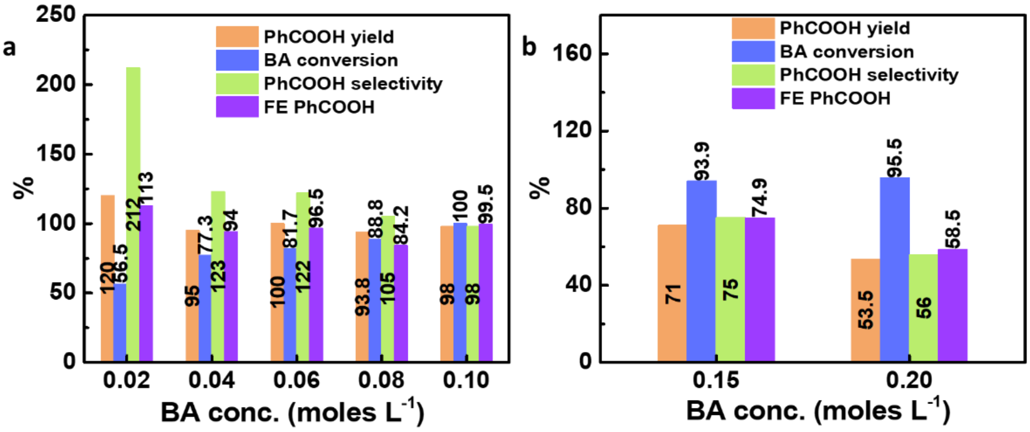

Figure 2.2. 18. Electrochemical BOR performance of CTNF catalyst with varying concentrations of BA in 1.0 M KOH.

The CTNF catalyst exhibits higher double-layer capacitance (C_{dl}) value (***Figure 2.2.20.c)*** for BOR (1.3 mF cm^{-2}) than that of NF-U (1.0 mF cm^{-2}) obtained from CV analyses **(*Figure 2.2.20.a, b)***. The electrochemically active surface area (ECSA) derived from C_{dl} analysis showed 8.1 cm^2 for CTNF which is 1.3 times higher than the value obtained for NF-U (6.25 cm^2). The LSVs normalized with ECSA **(*Figure 2.2.20.d*)** show higher performance for CTNF as compared to NF-U, indicating the increased intrinsic activity and formation of new active sites. Such increase in intrinsic activity accounts for the improved conversion of BOR in CTNF.

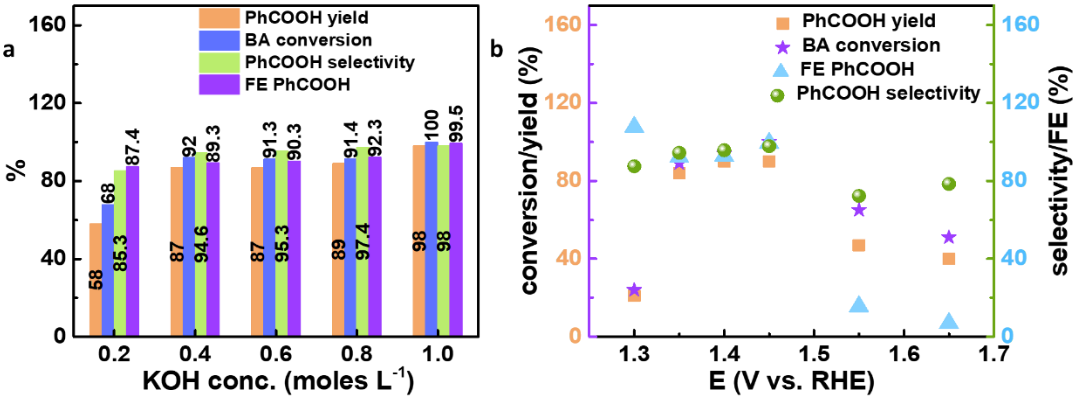

Figure 2.2. 19. Electrochemical BOR performance of CTNF catalyst with varying (a) concentrations of KOH, and (b) potential.

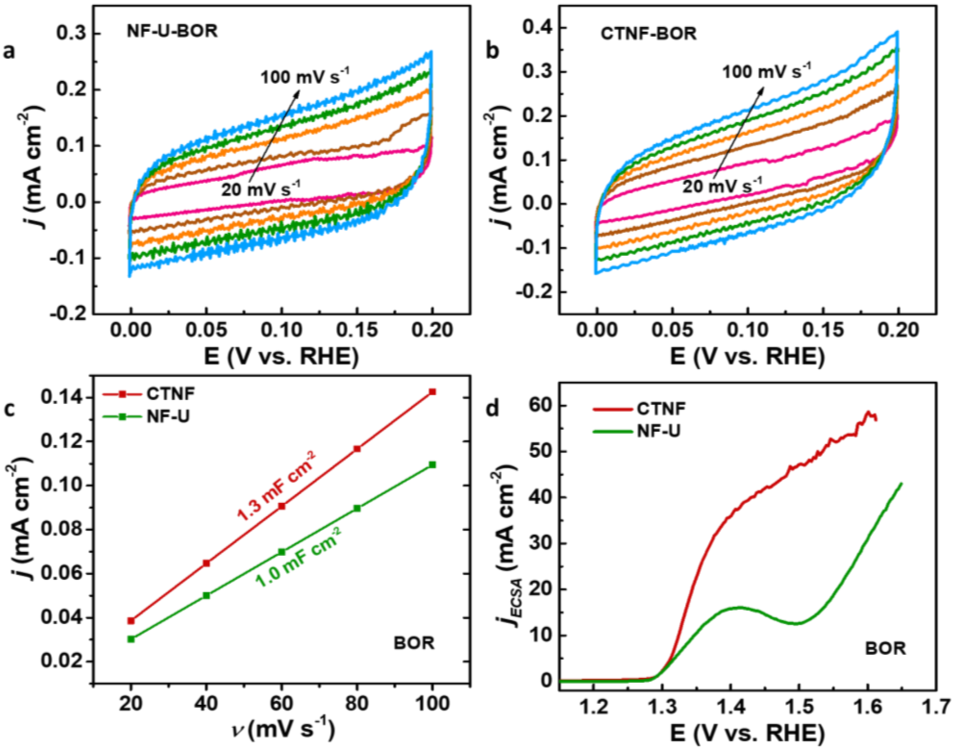

Figure 2.2. 20. (a) Cyclic voltammogram (CV) studies in the non-Faradaic region of NF-U, and (b) CTNF catalysts, (c) double layer capacitance (C_{dl}) studies, and (d) Electrochemically active surface area (ECSA) normalized LSVs of CTNF and NF-U catalyst in 0.1 M BA and 1.0 M KOH.

Various control studies were done to understand the pore-forming ability of chromium species. The concentration of active sites (NiOOH) was evaluated from the oxidation peak in LSV at 1.3 V with varying amount of chromium (0.03, 0.052, and 0.1 wt % Cr) in CTNF. As depicted from the linear sweep voltammetry (LSV) analysis **(*Figure 2.2.21.*)**, the area under the oxidation peak increases with increase in the chromium oxide content. Further, the peak potential shift towards lower values. This suggests that chromium inclusion reduces the oxidation potential associated with the Ni^{2+} to Ni^{3+} conversion to lower value (from 1.36 V to 1.29 V) as observed elsewhere.(*25-27, 31*)

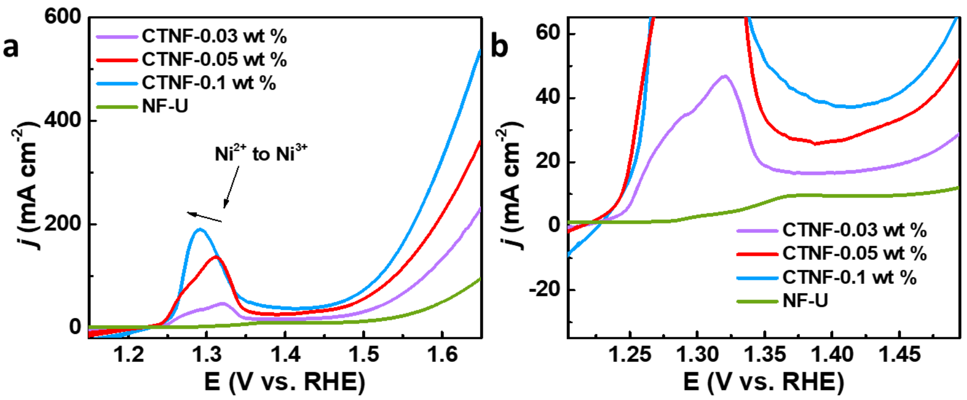

Figure 2.2. 21. (a) Linear sweep voltammetry (LSV) analysis of CTNF with varying concentration of Cr in the sample, and (b) the low current region of the LSVs. (CTNF-0.1 wt % is abbreviated as CTNF)

Since chromium oxide is prone to leach out during oxidation cycling in alkaline conditions, the ICP analysis was done to understand the amount of chromium leached from the system. A small section of pristine CTNF electrode (1x1 mm) was digested in aqua-regia overnight and ICP analysis was done for electrode and the electrolytes collected after different intervals (***Table 2.2.2.***). After 10 h almost 33 % of Cr was lost and after 20 h, 55 % Cr leached out from the electrode in the electrolyte.

Table 2.2. 2. ICP analysis of the pristine CTNF electrode and the electrolytes recovered after different intervals.

Sample	% wt of Cr
CTNF	2.0
CTNF (1 h-AR)	1.74
CTNF (3 h-AR)	1.5
CTNF (10 h-AR)	1.34
CTNF (20 h-AR)	0.9

Electrochemical impedance spectroscopy (EIS) studies were done to understand the mechanism at the interfaces. The Nyquist plot (***Figure 2.2.22.***) shows charge transfer resistance (R_{ct}) of 3 Ω for CTNF, an order of magnitude lower than the value observed for NF-U (30 Ω) resulting in lower hindrance to the flow of charges on incorporation of chromium. This could possibly arise from the easy accessibility of reactants in the porous structure generated by the nanoplate network on the surface of nickel foam support.

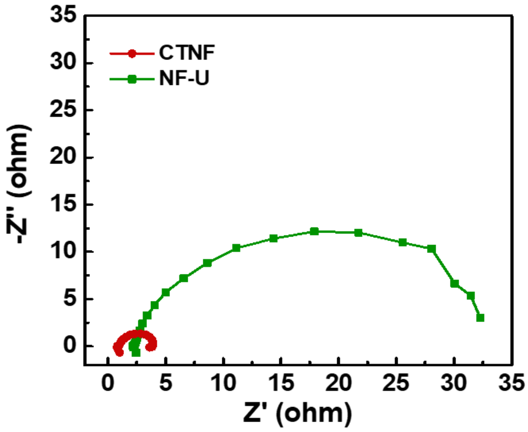

Figure 2.2. 22. Impedance analysis of CTNF, and NF-U catalysts towards BOR.

The CTNF catalyst showed stable performance for 7 cycles (***Figure 2.2.23.a***)**,** each one for an hour run at a potential of 1.45 V vs. RHE. After 9 cycles, the activity further reduces to 60 % (***Figure 2.2.24.)*** in the 10th cycle. This could be associated with the loss of significant amount of chromium (45 %) in the oxidation environment as observed from ICP analysis. An average of 0.48 mmol h^{-1} yield (***Figure 2.2.23.b***) was observed for each cycle with more than 90 % conversion, nearly 100 % selectivity, and more than 95 % faradaic efficiency towards PhCOOH formation.

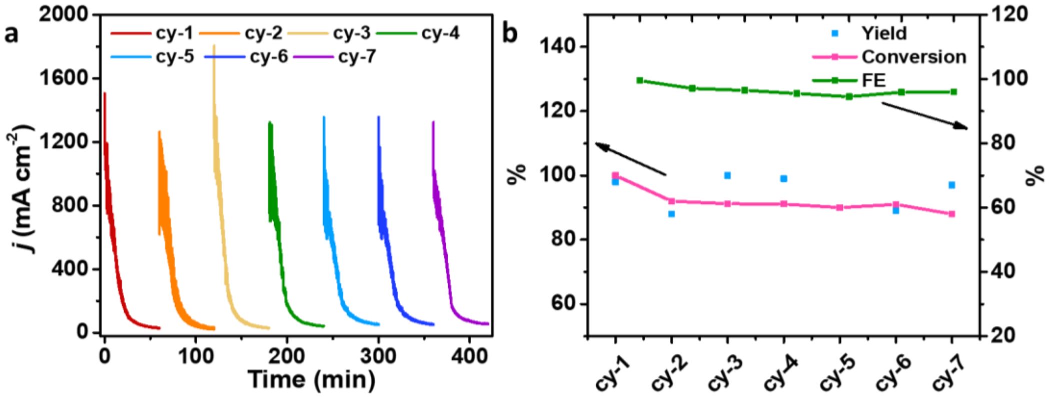

Figure 2.2. 23. (a) Chronoamperometry analysis, and (b) % yield, conversion and faradaic efficiency of CTNF catalyst towards BOR with cycles.

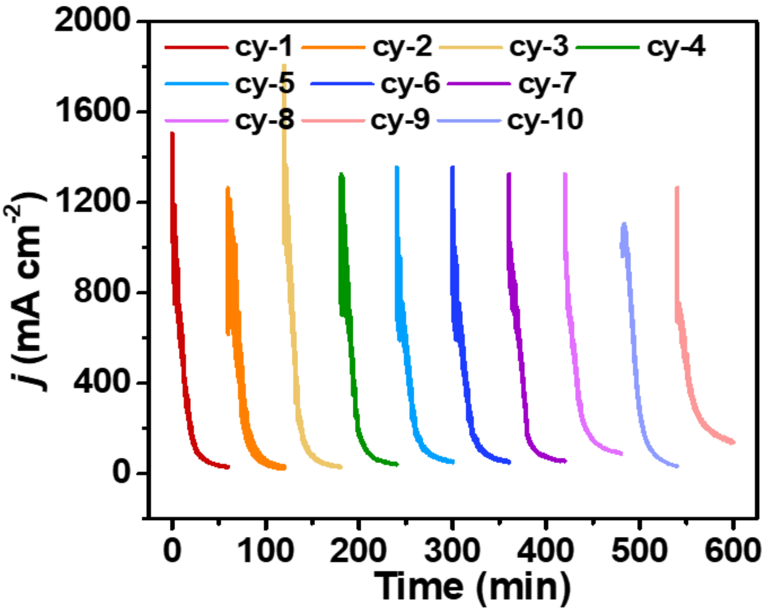

Figure 2.2. 24. Chronoamperometry analysis of CTNF catalyst till 10 cycles.

HER performance over CTNF catalyst was carried out in order to fabricate a full cell assembly. The CTNF catalyst shows an overpotential of 355 mV (***Figure 2.2.25.***) for attaining a current density of 100 mA cm^{-2} (1.0 M KOH) which is higher than the state-of-the-art Pt/C (20 wt %) catalyst (η_{100} = 150 mV). In order to get improved performance using non-noble metal-based catalysts, MoNi catalyst was synthesized using modified procedure reported in the literature. MoNi catalyst showed a current density of 100 mA cm^{-2} at an overpotential of 135 mV and a high current density of 1.8 A cm^{-2} at 465 mV overpotential.

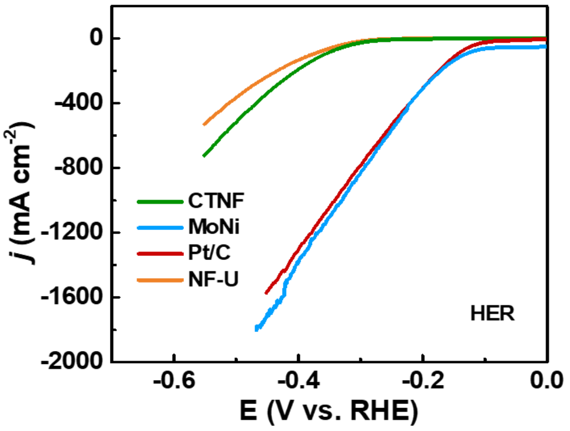

Figure 2.2. 25. Linear sweep voltammograms (LSVs) of various catalysts in 1.0 M KOH towards HER.

2.2.4.3. Full cell studies in two-electrode arrangement:

The performance of the CTNF catalyst, NF-U, and MoNi catalysts were checked in full cell (two-electrode) arrangement **(*Figure 2.2.26.*)** to mimic the commercial electrolyzers. The CTNF-MoNi couple showed best performance with a cell potential of 1.22 V required to achieve a current density of 100 mA cm^{-2}. Also, a very high current density of 750 mA cm^{-2} was observed at 2.33 V. High catalytic conversion during four cycles in full cell arrangement was achieved **(*Figure 2.2.26.*)** for each cycle for nearly 50 h stability run.

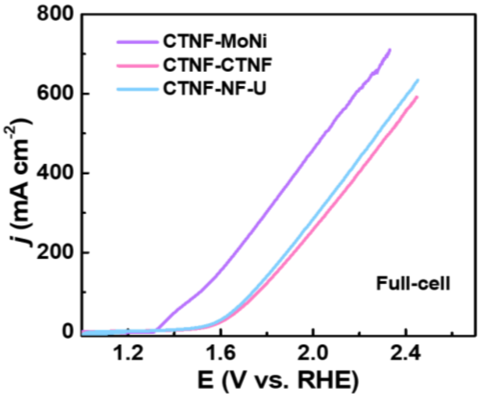

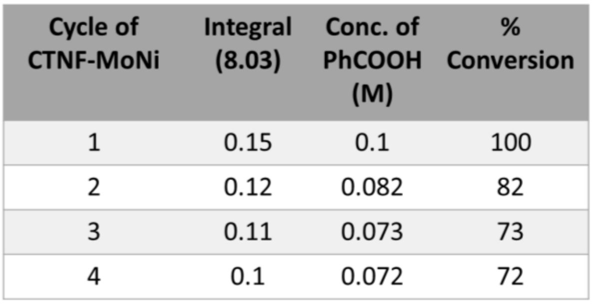

Cycle of CTNF-MoNi	Integral (8.03)	Conc. of PhCOOH (M)	% Conversion
1	0.15	0.1	100
2	0.12	0.082	82
3	0.11	0.073	73
4	0.1	0.072	72

Figure 2.2. 26. Full cell studies of various catalyst towards BOR coupled HER, and performance analysis of samples collected for 4 stability cycles for CTNF-MoNi couple.

2.2.4.4. Post-reaction analysis:

The post-reaction studies of the catalyst were done using PXRD, FESEM, HRTEM, and XPS analyses. The existence of oxides and hydroxides of Ni can be seen from the PXRD analysis **(*Figure 2.2.27.a*)**.(*36, 37*). The EDS analysis **(*Figure 2.2.27.b*)** showed leaching of Cr to 0.1 wt%.

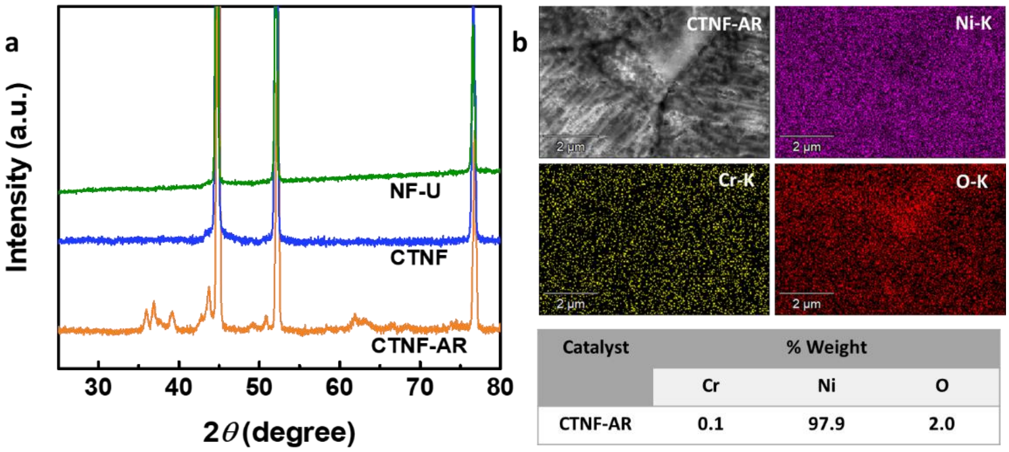

Catalyst	% Weight		
	Cr	Ni	O
CTNF-AR	0.1	97.9	2.0

Figure 2.2. 27. (a) Powder X-ray diffraction (PXRD), and (b) energy dispersive X-ray spectroscopy (EDS) of CTNF catalyst post-BOR analysis.

The high-resolution XPS analysis (***Figure 2.2.28.***) was done after 1 h post-BOR measurement. In the high-resolution Cr 2p spectra, the peak at 576.7 eV and at 580.15 eV corresponding to the Cr^{3+} and Cr^{6+} species which are negatively shifted with respect to pristine CTNF sample (***Figure 2.2.14.***). The relative amount of Cr^{3+} species decreases while that of Cr^{6+} species increases after the measurement as obvious from the positive potentials applied. The amount of Cr after the 1 h BOR measurement decreases to approx. 1.5 wt % corresponding to leaching of Cr species from the system as observed from the ICP analysis.

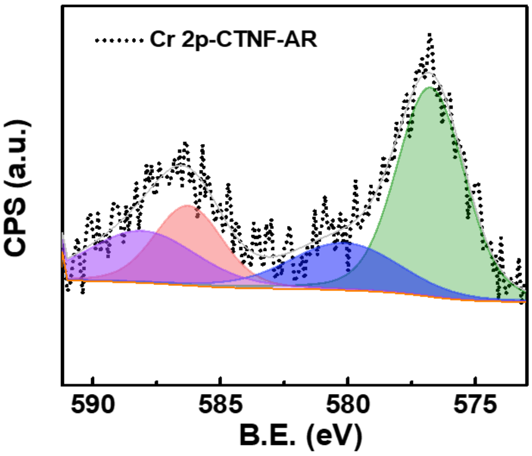

Figure 2.2. 28. X-ray photoelectron spectroscopy (XPS) Cr 2p spectra of CTNF catalyst 1 h post-BOR measurement.

2.2.4.5. Mechanistic studies:

In-situ Raman analysis was done in a self-made Teflon cell to understand the role of various contributing sites. Raman data were recorded during the chronoamperometry at different potentials starting from the open circuit potential (OCP) in a three-electrode arrangement. During the in-situ Raman analysis **(*Figure 2.2.29.a*)** of CTNF shows the bands corresponding to NiOOH species (at 473 cm^{-1} and 553 cm^{-1}) 1.35 V due to oxidation of Ni^{2+} species in alkaline conditions under positive biasing (oxidation).(*36*, *38*, *39*) The intensity of NiOOH peak is very high for CTNF as compared to NF-U **(*Figure 2.2.30.a*)**,(*40*) supporting the findings observed in CV analysis (area under the Ni oxidation peak).

As the electrical potential was removed (in CTNF), the intensity of peaks corresponding to NiOOH species diminished to zero within a few seconds (20-30 seconds). Also, in the absence of BA **(*Figure 2.2.29.b*)** in the electrolyte (just OER), these NiOOH peaks remain even after removing electric potential from the electrochemical system. In contrast, the Ni^{2+} species reversibly convert to NiOOH in presence of benzyl alcohol (BA) and converting into PhCOOH by chemical oxidation **(*Figure 2.2.31.*)**.

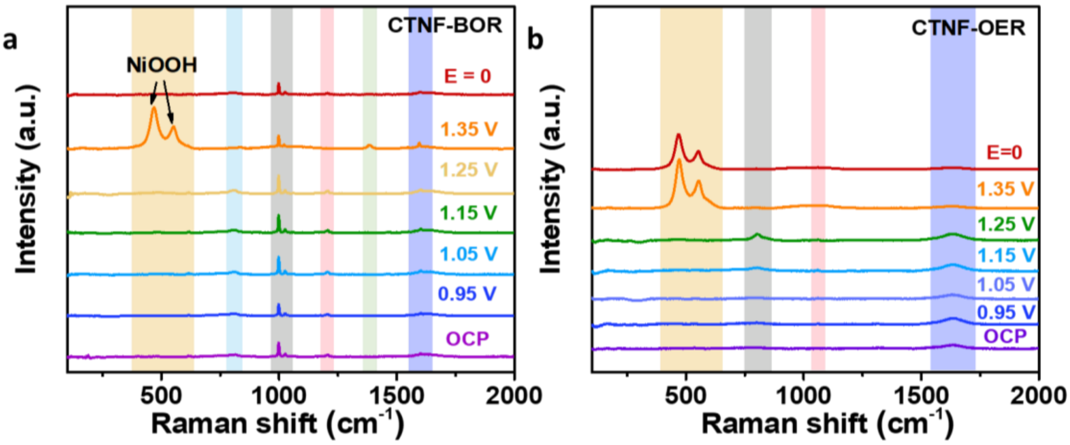

Figure 2.2. 29. In-situ Raman analysis of CTNF catalyst towards (a) BOR, and (b) OER analysis.

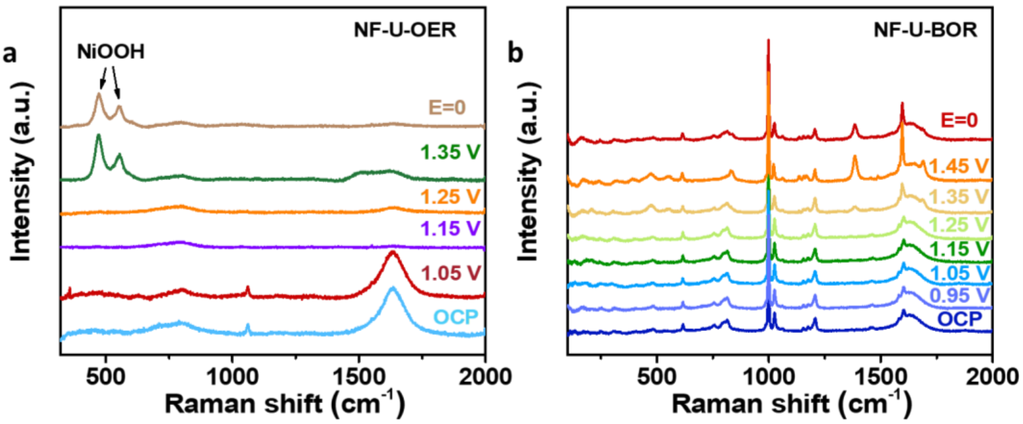

Figure 2.2. 30. In-situ Raman analysis of NF-U catalyst towards (a) OER, and (b) BOR analyses.

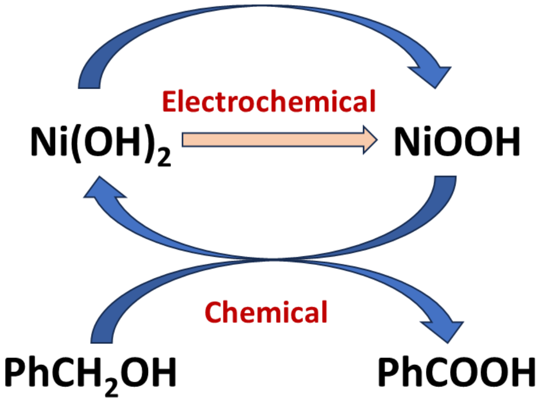

Figure 2.2. 31. Schematics of the probable mechanism of BOR at the active Ni sites.

2.2.5. Conclusions:

In conclusion, chromium oxide incorporated Ni foam shows a great performance towards benzyl alcohol oxidation reaction (BOR). It attained high current density of 1.4 A cm^{-2} at 1.45 V which is one of the highest values reported so far for BOR. The introduction of chromium enhances the intrinsic performance with formation of new active sites. The in-situ analyses reveal the positive impact of chromium addition to the catalyst with Ni as the active sites for benzyl alcohol oxidation. The full cell assembly with MoNi as the cathode shows high current density of 750 mA cm^{-2} at 2.33 V. This opens new ways for commercial-level hybrid electrolysis.

2.2.6. References:

1. A. Raveendran, M. Chandran, R. Dhanusuraman, A comprehensive review on the electrochemical parameters and recent material development of electrochemical water splitting electrocatalysts. *RSC Adv* **13**, 3843-3876 (2023).
2. R. Li, K. Xiang, Z. Peng, Y. Zou, S. Wang, Recent Advances on Electrolysis for Simultaneous Generation of Valuable Chemicals at both Anode and Cathode. *Advanced Energy Materials* **11**, (2021).
3. Y. Xu, B. Zhang, Recent Advances in Electrochemical Hydrogen Production from Water Assisted by Alternative Oxidation Reactions. *ChemElectroChem* **6**, 3214-3226 (2019).
4. C. A. Martínez-Huitle, M. A. Rodrigo, I. Sirés, O. Scialdone, A critical review on latest innovations and future challenges of electrochemical technology for the abatement of organics in water. *Applied Catalysis B: Environmental* **328**, (2023).
5. C. M. Pichler, Coupled Electrochemical Processes as Versatile Route for Converting Waste Substrates into Value Added Chemical Products. *ChemCatChem* **15**, (2023).
6. T. Wang *et al.*, Combined anodic and cathodic hydrogen production from aldehyde oxidation and hydrogen evolution reaction. *Nature Catalysis* **5**, 66-73 (2021).
7. L. Chen, J. Shi, Chemical-assisted hydrogen electrocatalytic evolution reaction (CAHER). *Journal of Materials Chemistry A* **6**, 13538-13548 (2018).
8. F. Arshad, T. u. Haq, I. Hussain, F. Sher, Recent Advances in Electrocatalysts toward Alcohol-Assisted, Energy-Saving Hydrogen Production. *ACS Applied Energy Materials* **4**, 8685-8701 (2021).
9. B. You, X. Liu, X. Liu, Y. Sun, Efficient H2 Evolution Coupled with Oxidative Refining of Alcohols via A Hierarchically Porous Nickel Bifunctional Electrocatalyst. *ACS Catalysis* **7**, 4564-4570 (2017).
10. J. Zhong, Y. Shen, P. Zhu, S. Yao, C. An, Size-effect on Ni electrocatalyst: The case of electrochemical benzyl alcohol oxidation. *Nano Research* **16**, 202-208 (2022).

11. H. Li *et al.*, Selective oxidation of benzyl alcohols to benzoic acid catalyzed by eco-friendly cobalt thioporphyrazine catalyst supported on silica-coated magnetic nanospheres. *J Environ Sci (China)* **60**, 84-90 (2017).
12. Y. Wei, W. Zhang, Potential Cycling Effects on Activities of Nickel-Mediated Benzyl Alcohol and Glycine Electrooxidation in Alkaline Solutions. *Catalysts* **10**, (2020).
13. B. You, Z. Cheng, Y. Tian, S. Wang, B. Wang, Highly Efficient and Selective Oxidation of Benzyl Alcohol by WO42− Catalyst Immobilized by a Phosphonium-Containing Porous Aromatic Framework. *Catalysts* **13**, (2023).
14. J. Yi, J. Lu, D. Song, M. Li, Z. Shen, Electrochemical Oxidation of Benzyl Alcohol on Platinum Electrode with TEMPO in CH3CN/H2O. *Asian Journal of Chemistry* **27**, 3197-3200 (2015).
15. H. Huang *et al.*, Ni, Co hydroxide triggers electrocatalytic production of high-purity benzoic acid over 400 mA cm−2. *Energy & Environmental Science* **13**, 4990-4999 (2020).
16. M. Xu, J. Geng, H. Xu, S. Zhang, H. Zhang, In situ construction of NiCo2O4 nanosheets on nickel foam for efficient electrocatalytic oxidation of benzyl alcohol. *Inorganic Chemistry Frontiers* **10**, 2053-2059 (2023).
17. J. Zheng *et al.*, Hierarchical Porous NC@CuCo Nitride Nanosheet Networks: Highly Efficient Bifunctional Electrocatalyst for Overall Water Splitting and Selective Electrooxidation of Benzyl Alcohol. *Advanced Functional Materials* **27**, (2017).
18. B. You, X. Liu, N. Jiang, Y. Sun, A General Strategy for Decoupled Hydrogen Production from Water Splitting by Integrating Oxidative Biomass Valorization. *J Am Chem Soc* **138**, 13639-13646 (2016).
19. R. Li, P. Kuang, L. Wang, H. Tang, J. Yu, Engineering 2D NiO/Ni3S2 heterointerface electrocatalyst for highly efficient hydrogen production coupled with benzyl alcohol oxidation. *Chemical Engineering Journal* **431**, (2022).
20. G. Liu *et al.*, Electrocatalytic oxidation of benzyl alcohol for simultaneously promoting H2 evolution by a Co0.83Ni0.17/activated carbon electrocatalyst. *New Journal of Chemistry* **42**, 6381-6388 (2018).
21. J.-K. Li *et al.*, Construction of 2D C,N-co-doped ZnO/Co3O4over Ni(OH)2mesoporous ultrathin nanosheets on Ni foam as high-performance

electrocatalysts for benzyl-alcohol oxidation and accelerating hydrogen evolution. *New Journal of Chemistry* **47**, 5970-5976 (2023).

22. M. Zhang *et al.*, Anchoring hydroxyl intermediate on NiCo(OOH)x nanosheets to enable highly efficient electrooxidation of benzyl alcohols. *AIChE Journal* **69**, (2023).
23. Z. Li *et al.*, Alcohols electrooxidation coupled with H(2) production at high current densities promoted by a cooperative catalyst. *Nat Commun* **13**, 147 (2022).
24. M. T. Bender, Y. C. Lam, S. Hammes-Schiffer, K. S. Choi, Unraveling Two Pathways for Electrochemical Alcohol and Aldehyde Oxidation on NiOOH. *J Am Chem Soc* **142**, 21538-21547 (2020).
25. D. Xu *et al.*, The role of Cr doping in Ni Fe oxide/(oxy)hydroxide electrocatalysts for oxygen evolution. *Electrochimica Acta* **265**, 10-18 (2018).
26. C.-C. Lin, C. C. L. McCrory, Effect of Chromium Doping on Electrochemical Water Oxidation Activity by Co3–xCrxO4Spinel Catalysts. *ACS Catalysis* **7**, 443-451 (2016).
27. X. Liu, J. Wu, Coupling interface constructions of NiO–Cr2O3 heterostructures for efficient electrocatalytic oxygen evolution. *Electrochimica Acta* **320**, (2019).
28. J. Chen *et al.*, Co–Fe–Cr (oxy)Hydroxides as Efficient Oxygen Evolution Reaction Catalysts. *Advanced Energy Materials* **11**, (2021).
29. W. J. Liu *et al.*, Efficient electrochemical production of glucaric acid and H(2) via glucose electrolysis. *Nat Commun* **11**, 265 (2020).
30. J. Zhang *et al.*, Efficient hydrogen production on MoNi(4) electrocatalysts with fast water dissociation kinetics. *Nat Commun* **8**, 15437 (2017).
31. W.-X. Zhang *et al.*, Morphological effects of ordered Cr2O3 nanorods and Cr2O3 nanoparticles on fluorination of 2-chloro1,1,1-trifluoroethane. *J Mater Sci* **51**, 6488-6496 (2016).
32. A. S. O. Gomes, N. Yaghini, A. Martinelli, E. Ahlberg, A micro-Raman spectroscopic study of Cr(OH)3 and Cr2O3 nanoparticles obtained by the hydrothermal method. *Journal of Raman Spectroscopy* **48**, 1256-1263 (2017).

33. Wang, Zhang, Lv, Removal Efficiency and Mechanism of Cr(VI) from Aqueous Solution by Maize Straw Biochars Derived at Different Pyrolysis Temperatures. *Water* **11**, (2019).
34. L. Q. Guo, S. X. Qin, B. J. Yang, D. Liang, L. J. Qiao, Effect of hydrogen on semiconductive properties of passive film on ferrite and austenite phases in a duplex stainless steel. *Sci Rep* **7**, 3317 (2017).
35. M. Aronniemi, J. Sainio, J. Lahtinen, Chemical state quantification of iron and chromium oxides using XPS: the effect of the background subtraction method. *Surface Science* **578**, 108-123 (2005).
36. M. Aghazadeh, H. F. Rad, In situ growth of Ni(OH)2-porous nitrogen-doped graphene composite onto Ni foam support as advanced electrochemical supercapacitors materials. *Journal of Materials Science: Materials in Electronics* **33**, 11038-11054 (2022).
37. X. Yang *et al.*, A doping element improving the properties of catalysis: in situ Raman spectroscopy insights into Mn-doped NiMn layered double hydroxide for the urea oxidation reaction. *Catalysis Science & Technology* **12**, 4471-4485 (2022).
38. C. Guillén, J. Herrero, Structural Changes Induced by Heating in Sputtered NiO and Cr2O3 Thin Films as p-Type Transparent Conductive Electrodes. *Electronic Materials* **2**, 49-59 (2021).
39. B. S. Yeo, A. T. Bell, In Situ Raman Study of Nickel Oxide and Gold-Supported Nickel Oxide Catalysts for the Electrochemical Evolution of Oxygen. *The Journal of Physical Chemistry C* **116**, 8394-8400 (2012).
40. H. Radinger *et al.*, Importance of Nickel Oxide Lattice Defects for Efficient Oxygen Evolution Reaction. *Chemistry of Materials* **33**, 8259-8266 (2021).

Chapter- 2.3 Specular CuO nanostructures for glucose oxidation and sensing

Summary:

Specular CuO microcubes on Ni foam support showed a current density of 1.4 A cm^{-2} at a potential of 1.45 V towards the electrooxidation of readily available glucose biomass. The catalyst used for glucose sensing application showed promising results with a very high sensitivity of 4 *10^{9} μA mM^{-1} cm^{-2} with a response time of 0.5 s and LOD of 5 nM. The two-electrode arrangement of the electrocatalyst also showed promising results for using this catalyst in electrolyzers. The in-situ Raman analysis indicates the NiO as the active site with the chemical conversion of alcohol groups of glucose to the carbonyl.

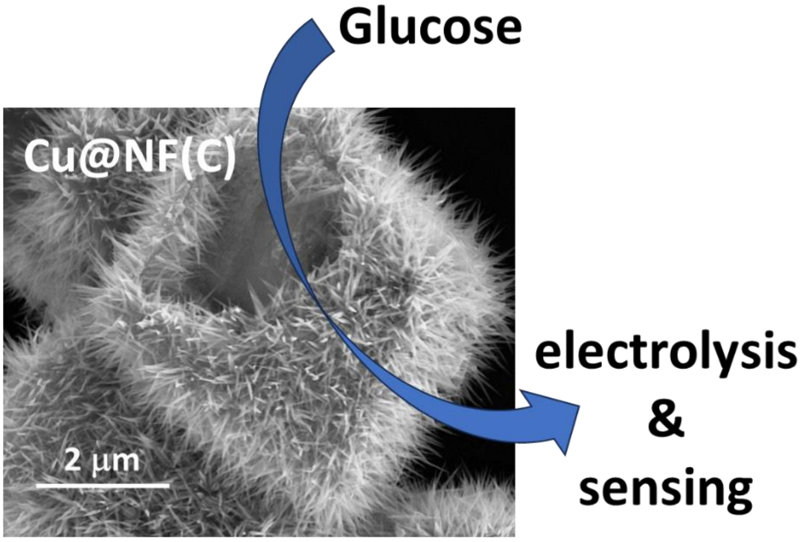

(A manuscript based on this work is under preparation)

2.3.1. Introduction:

Fuel cell technologies are gaining global recognition as highly efficient methods amidst the escalating energy demand with rapidly growing population. Not only meeting the high demands, but these technologies also mitigate carbon emissions, conserving our finite reserves of petroleum-based energy sources. Glucose, a readily available and abundant monosaccharide, presents distinctive advantages as a fuel. Its unique properties as a cost-effective fuel, renewable, and eco-friendly nature makes it compelling source for energy generation. Furthermore, its non-toxicity enhances its appeal as a renewable energy source. During the complete oxidation of glucose (equation 1) in direct glucose fuel cells (DGFCs), 24 electrons (ca. 2870 kJ mol^{-1}) are liberated. This remains theoretical because even the 1st stage of the formation of gluconic acid is uncertain.(*1*)

Overall reaction: $C_6H_{12}O_6 + 6\ O_2 \rightarrow 6\ CO_2 + 6H_2O$…………………………………… (1)

The partial oxidation of glucose (GOR) to valuable products like gluconic acid (GNA), glucaric acid (GRA), formic acid (FA), etc has been investigated for more than 50 years.(*2*) Energy-efficient and environment-friendly methods have been searched to replace the chemical routes relying on strong oxidants like HNO_3. The well-known thermocatalytic process of oxidation was limited by highly expensive noble metal catalysts and O_2/air at high pressure and temperature of 50-120 ^{o}C.(*3*) The electrochemical route was considered as an effective alternative to working under mild conditions, at room temperature using H_2O as the green solvent and renewable energy as the power source. Moreover, electrooxidation of biomass can be coupled with H_2 generation to drive the reaction potentials to a lower value compared to conventional water splitting process to produce oxygen as the anodic product via oxygen evolution reaction (OER).(*4-11*)

Over the past few decades, the scientific community revisited the glucose oxidation field which used to be the center of attraction 100 years back considering the great potential of glucose oxidation in various areas. Numerous efforts have been employed to efficiently replace the batteries used in the electronic implants with self-supportive alternatives like fuel cells. In this regard, glucose can be considered as all-time accessible fuel in biomedical implantable devices which can not only empower the source but can also independently operate for prolonged periods. Direct glucose fuel cells (DGFCs) can be broadly classified into three major categories, viz. enzymatic, microbial, and non-enzymatic (abiotically catalysed) fuel cells.(*8*) Enzymatic FCs employ bio-compatible enzymes as the catalyst while microbial involves microbes. The enzyme and microbial based systems have major limitations with their low shelf life, denaturation, low output power, temperature sensitivity, and infective nature.(*12, 13*) In non-enzymatic FCs, various noble metals (Pt, Au, Ag and their alloys) supported on carbon or metal oxides were used as the catalysts. Among the noble metals, Pt was mainly used for its high performance towards GOR. The poisoning effect of carbohydrate oxidation intermediate, CO, in addition to the high cost, poor stability and durability of Pt drives researchers to look for non-noble metal-based catalysts.(*1, 2, 8, 14-16*)

Among the non-noble metal catalysts ***(Table 2.3.1.)***,(*17-21*) nanostructured Ni catalysts have been widely explored for GOR due to their high stability and high dispersion of hydrophilic sites in alkaline conditions.(*2, 22-26*) The electrochemical glucose oxidation reactions mainly carried out in alkaline conditions due to favorable charge transfer kinetics and existence of hydrous species on the metal surface.(*27-29*) As reported in various studies, two steps are involved in the mechanistic analysis of GOR on Ni oxide and hydroxide systems. The first step in GOR over Ni-based catalysts involve electrochemical oxidation of Ni^{2+} ($NiO/Ni(OH)_2$) to Ni^{3+} (NiOOH) species. These NiOOH species further chemically oxidize glucose while converting back to Ni^{2+}. The extent of chemical oxidation depends on the electrochemically generated NiOOH species.(*30*) Porous Ni foam for its high dispersion of active sites, and facile diffusion of analyte has been used as a self-supported catalyst for GOR.(*31-33*) However, the Ni catalysts oxidise glucose at higher potentials thereby reducing the performance. Adding a second metal to Ni can improve its intrinsic characteristics by modifying its electronic structure. Several reports emphasize on the use of binary metals, with a notable focus on Ni-Cu combination, as they demonstrate a synergistic effect, particularly in glucose oxidation and sensing applications.(*20, 34-37*) Oxides of Ni and Cu and their combinations have been studied as the best-performing non-noble metal-based catalysts for GOR.(*38*)

Table 2.3. 1. Reported catalysts for electrochemical glucose oxidation reaction.

Catalyst	Glucose conc. (M)	j_{max} at onset OER (mA cm^{-2})	Stability	Ref.
PbHfCd/C-HAp	0.5	4.73	1000 s	*Journal of Solid State Electrochemistry*, 2023, 27, 3425
Cu-doped@MiL88B/NF	0.1	350	50 h	*Dalton Trans.*, 2023, 52, 10933
$NiCoSe_x$/NF	0.1	500	50 h	*Inorg. Chem.*, 2023, 62, 10513
PdIn/CNT	0.5	1	1000 s	*Materials Chemistry and Physics*, 2020, 254, 123318
4A-F	1	2	1000 s	*Journal of Electronic Materials*, 2022, 51, 1653
PdRh/C	0.5	5	30 days	*Applied Catalysis B: Environmental*, 2014, 147, 481
CuNi@Cu foil	0.001	20	1200 s	*Chem. Mater.*, 2007, 19, 4174
NiCu@VC-72	0.004	3	350 s	*Synthetic Metals*, 2020, 269, 116578
GC/NiCu	0.005	10	-	*J Solid state Electrochem*, 2009, 13, 1171
$Ni_{10}Cu_{90}$	0.005	2	-	*Journal of electroanalytical chemistry*, 2001, 495, 110
CuNi-NGr/GCE	0.006	12	-	*Electrochimica Acta*, 2017, 224, 295
NiCu/TiO2-GCE	0.003	7	-	*J. Serb. Chem. Soc.*, 2018, 83, 733
NiCu/GC	0.05	-	3600 s	*Int. J. Electrochem. Sci.*, 2020, 15, 2449
NiCu	0.001	2	-	*Jpn. J. Appl. Phys.*, 2020, 59
CuNi@Cu foil	0.001	20	1200 s	*Chem. Mater.*, 2007, 19, 4174

C-Hap= C-doped hydroxyapatite, CNT= carbon nanotubes, 4A-F= 3-iodo-2-(aryl/alkyl)benzo[b]thiophene,

For practical applications, there is still room for improvement in attaining high current densities (more than 500 mA cm^{-2}) at lower potentials with improved long term stabilities.(*25*, *33*, *39*, *40*)

2.3.2. Scope of the present investigation:

In this work, utilizing Ni foam containing specular morphology of mixed copper oxide nanostructures, we were able to significantly improve the performance of Ni-Cu catalyst for GOR. Specular morphology helps in providing huge surface area thus high accessibility to the active sites.

During electrochemical GOR, we observed a remarkable current density of 1.4 A cm^{-2} towards glucose electrooxidation at 1.45 V utilizing specular mixed copper oxide nanostructures supported on Ni foam. The catalyst showed 93% conversion of glucose with a mixture of products in 1 h in alkaline conditions. The catalyst also showed good conversion and stability for 15 cycles. Further, this catalyst was explored for glucose sensing applications. A high sensitivity of $4*10^9$ µA mM^{-1} cm^{-2} with a low detection limit of 5 nM and rapid response time of 0.5 s were observed in the very low range of 10 fM-100 nM concentrations of glucose. The in-situ Raman analysis reveals the NiO as the active site, which electrochemically getting oxidized to NiOOH species. These NiOOH species chemically oxidises glucose while getting itself reduced to NiO. This study can enlighten the utilization of high performing catalysts in the field of direct glucose fuel cells (DGFCs) and sensing applications.

2.3.3. Materials and methods:

2.3.3.1. Materials required:

The materials required for the synthesis of various catalysts and their application in electrochemical analysis were purchased from different sources. Copper chloride dihydrate ($CuCl_2$. $2H_2O$), glucose, glucaric acid, and gluconic acid were purchased from Sigma-Aldrich, nickel chloride hexahydrate ($NiCl_2$. 6 H_2O) from Loba Chemie, and urea from S D Fine Chemicals. All chemicals were used as received without any further purification. Milli Q water (18.2 S cm) is used for all the synthesis and electrochemical analyses. Ni foam (1.2 mm thick) used as the support for electrochemical studies was purchased from MTI, USA.

2.3.3.2. Synthesis of the catalysts:

Ni foam (NF) was cleaned with acetone and 3 M HCl solution and dried. Specular CuO microcubes supported on Ni foam were synthesized **(*Figure 2.3.1.*)** via hydrothermal process followed by calcination.(*40*) In the first step, 370 mg of 12.5 mL aqueous solution of $CuCl_2$. $2H_2O$ salt (2 mmol of Cu) was taken in a Teflon-lined autoclave (50 mL), followed by the addition of 900 mg of urea (15 mmol). To this solution, 12.5 mL absolute ethanol was added with a piece (2x2 cm) of cleaned Ni foam. The tightened autoclave was heated at 160 °C in the oven for 7 h. After that, the autoclave was allowed to cool in ambient conditions, and the recovered Cu@NF catalyst was washed with water and ethanol and dried. In the second step, the Cu@NF was calcined at 300 °C for 3 h in the air in a tubular furnace to attain the final Cu@NF(C) catalyst. Urea-treated NF (NF-U) was also synthesized with a similar procedure without adding Cu salt and further calcined to get NF-U(C) catalyst.

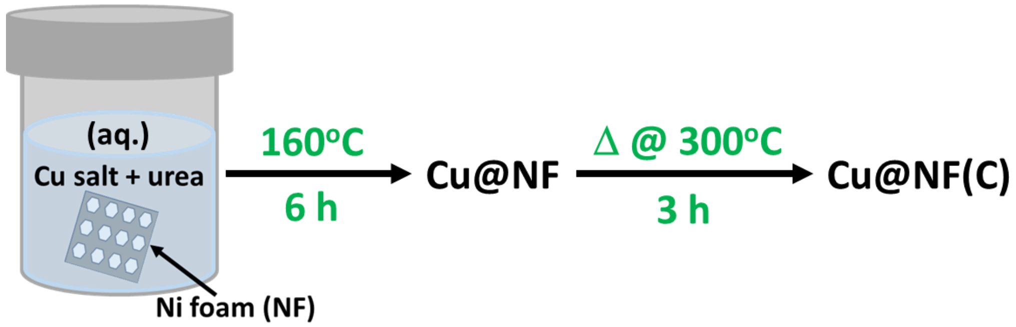

Figure 2.3. 1. Schematics of synthesis of Cu@NF(C).

MoNi-based catalyst for hydrogen evolution reaction (HER) analysis was synthesized with a modified procedure reported in the literature.(*41*) In a typical synthesis, (0.01 M) $(NH_4)_6Mo_7O_{24}.4H_2O$, (0.04 M) $Ni(NO_3)_2.6H_2O$, and a piece of Ni foam (2x2 cm) in 15 mL DI water were taken in a Teflon-lined autoclave and heated at 150 ℃ for 6 h. The obtained sample was dried at 60 ℃ for two days and then treated under an H_2 environment at 500 ℃ for 2 h. The as-synthesized catalyst supported on NF was treated with NaH_2PO_2 at 300 ℃ in air to obtain MoNiP sample.

2.3.3.3. Characterization details:

The instrumentation techniques (PXRD, FESEM, TEM, Raman, XPS, etc) used to characterize the samples are described in detail in the appendix at the end of this thesis.

2.3.3.4. Electrochemical studies:

Electrochemical measurements were carried out using an electrochemical workstation EC-Lab, Biologic Science Instruments VSP for evaluating the electrochemical activities of catalysts towards oxygen evolution reaction (OER), hydrogen evolution reaction (HER) in the presence and absence of glucose, sensing studies, and other electrochemical analyses. All the primary electrochemical measurements were carried out in a small cell (10.0 mL solution) with a standard three-electrode arrangement while full cell studies were done in a two-electrode arrangement. NF-U(C), Cu@NF, and Cu@NF(C) considered as the working electrodes, a high surface area graphite rod was taken as a counter electrode, and a mercury-mercuric oxide (Hg/HgO) electrode as a reference electrode in alkaline (1 M NaOH) conditions. All the polarization curves were recorded at 20 mV s^{-1} with 85% iR compensation (wherever mentioned if iR uncompensated) arising due to the ohmic resistance of the cell. All the measured potentials are reported with respect to reversible hydrogen electrode (RHE). The specific activities were reported with geometrical surface area normalized current densities. At the same time, intrinsic performance was shown with current densities normalized to electrochemically active surface areas calculated from cyclic voltammetry studies. During HER analysis, the dispersion of standard 20 wt. % Pt/C catalyst (2.0 mg) was prepared in (1.0 mL) IPA and (20 μL) Nafion. The ink (loading of 95 μg cm^{-2}) was drop casted on NF while MoNi catalyst supported on NF was used as such as the working electrode.

2.3.3.5. Product analysis (NMR):

Proton-nuclear magnetic resonance (^{1}H-NMR) spectrometer (Bruker 400) was used to analyze the products at 400 MHz frequency with solvent suppression (to supress the water peak (δ4.8 ppm)). ^{1}H-NMR studies of different concentration of standard samples (glucose, glucaric acid, gluconic acid, and sodium formate) were done using 50 μL of D_2O as the solvent and 20 μL of DMSO as the internal standard. The area under the signals corresponding to the existence of glucose (δ 8.02 ppm) and formate species (δ 8.3 ppm) in the ^{1}H-NMR spectra were quantified with respect to the area under DMSO peak (δ 2.71 ppm). The peak area under the DMSO peak was calibrated and set as 6 **(*Figure 2.3.2.*)**. The calibration plot **(*Figure 2.3.3.*)** using peak integrals of standard samples was plotted.

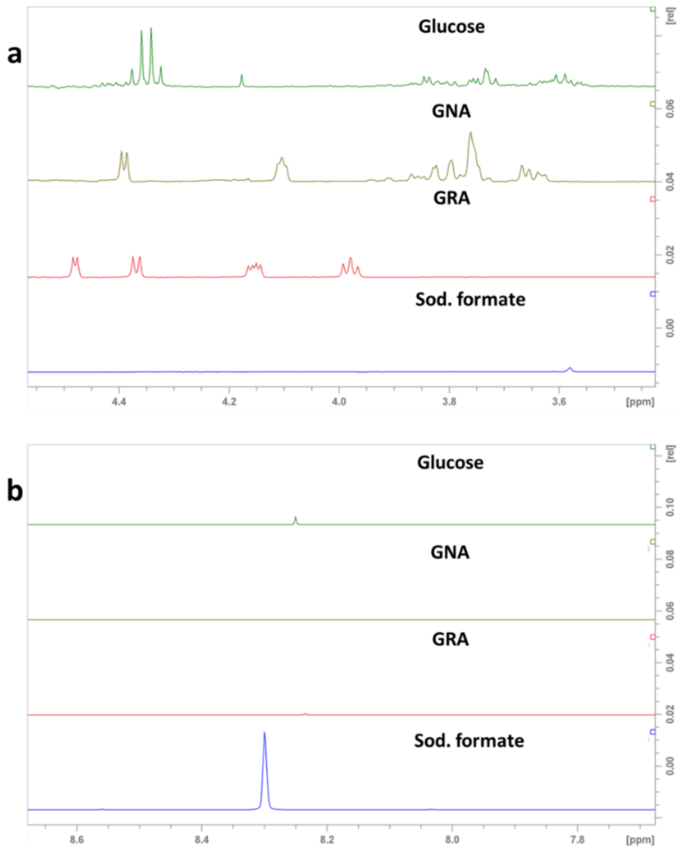

Figure 2.3. 2. Proton nuclear magnetic resonance (^{1}H-NMR) peak positions of standard glucose, gluconic acid (GNA), glucaric acid (GRA), and sodium formate (sod. formate) samples.

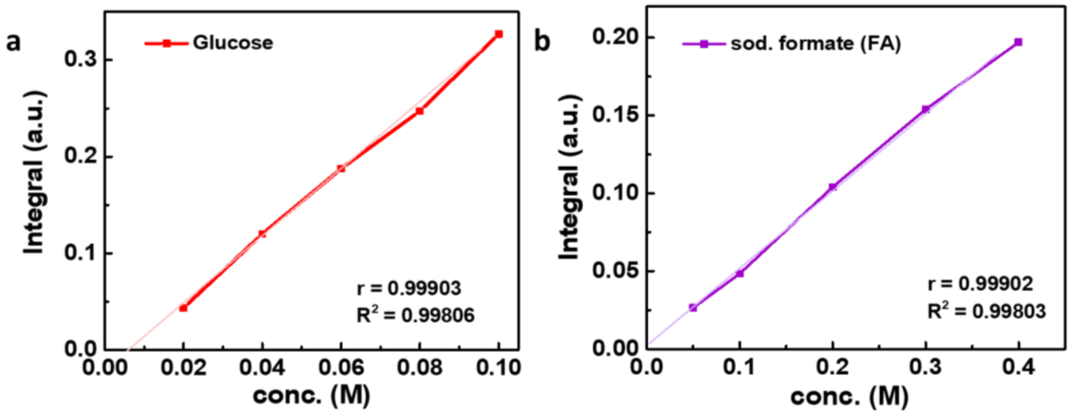

Figure 2.3. 3. Calibration plots of (a) glucose and (b) sodium formate analysed through proton nuclear magnetic resonance (^{1}H-NMR) spectroscopy.

Chronoamperometric analysis was done on different catalysts and the products are collected from the electrolyte. 0.2-micron filters were used to filter the samples collected from electroanalysis. 200 µL of electrolyte was collected from the reaction chamber and neutralized with 500 µL of H_2SO_4. 20 µL of DMSO (internal standard) and 50 µL of D_2O (solvent) were added to 700 µL of the above-neutralized sample. The sample was transferred to NMR tube for ^1H NMR analysis. The quantitative analysis of various species in the collected sample was determined from the calibration plot of normalized area versus concentration.

2.3.3.6. Product analysis (HPLC):

The calibration plots **(*Figure 2.3.4.*)** were obtained using different concentration of standard solutions of glucose (G), gluconic acid (GNA), glucaric acid (GRA), and formic acid (FA). 0.5 mM H_2SO_4 was taken as the mobile phase and Hiplex-H column at 60 ^{0}C was used as the stationary phase. The analysis was done using UV detector at wavelength of 210 nm with flow rate of 0.5 mL min^{-1}. 400 µL of the electrolytes containing the products were first filtered with 0.2-micron filters and then neutralized with 0.2 M H_2SO_4 solution. The samples were taken in 1.5 mL HPLC vials, sonicated and were loaded in HPLC sampler chamber. For all the samples, major peak area corresponds to the presence of formate in the system was observed.

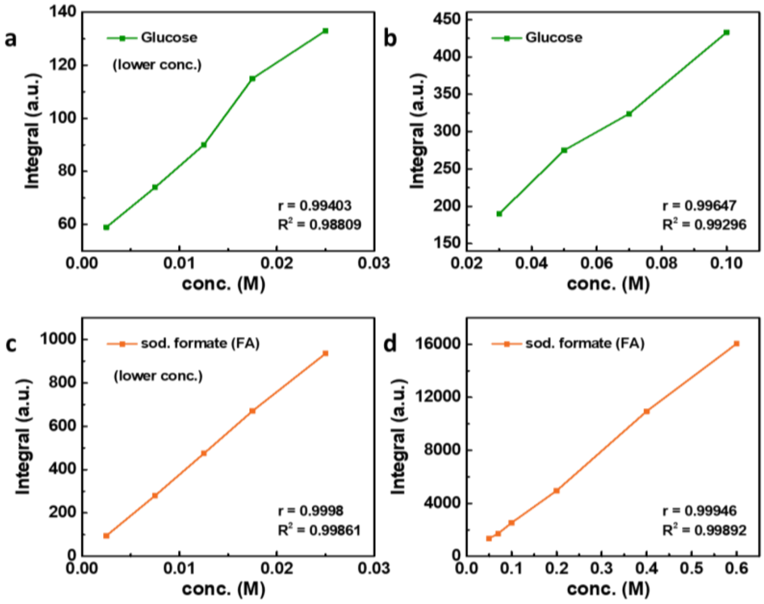

Figure 2.3. 4. Calibration plots of (a, b) glucose and (c, d) sodium formate analysed through high performance liquid chromatography (HPLC) technique.

2.3.4. Results and discussion:

2.3.4.1. Characterization of Cu@NF(C) catalyst:

A powder X-ray diffraction (PXRD) study (***Figure 2.3.5.***) was done on the as-synthesized Cu@NF, Cu@NF(C), and NF-U(C) catalysts to analyze the nature and existence of the phases of Cu and Ni species. In comparison, sharp peaks at 44.8°, 52°, and 76.5° can be assigned to (110), (200), and (220) planes of Ni from Ni foam. Major peaks in Cu@NF can be assigned to $Cu(OH)_2$ species.(*20*, *31*, *34*, *42*) However on calcination, $Cu(OH)_2$ peaks disappear and copper oxide peaks (CuO and Cu_2O) were observed along with NiO peaks.

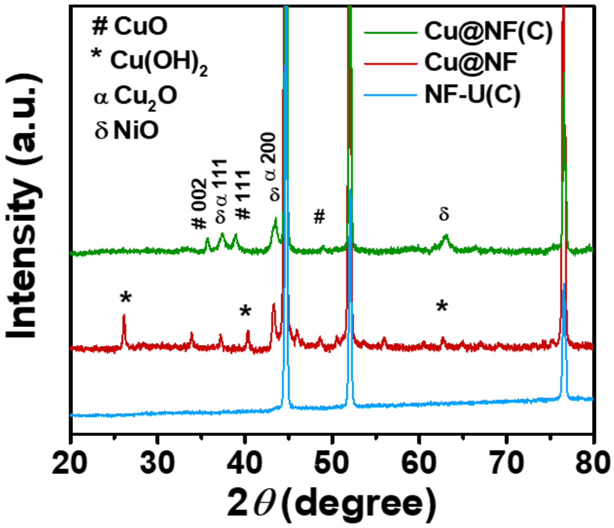

Figure 2.3. 5. Powder X-ray diffraction (PXRD) pattern of Cu@NF(C) catalyst.

Field emission scanning electron microscopy (FESEM) images (***Figure 2.3.6.***) of NF-U(C) shows flat surface.

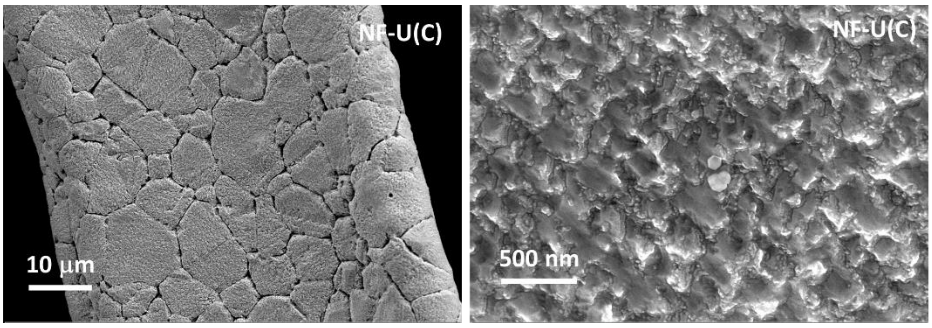

Figure 2.3. 6. Field emission scanning electron microscopy (FESEM) images of NF-U(C) catalyst.

The FESEM images of Cu@NF (***Figure 2.3.7.***) shows the framework of Ni foam decorated with completely covered specular nanostructures.

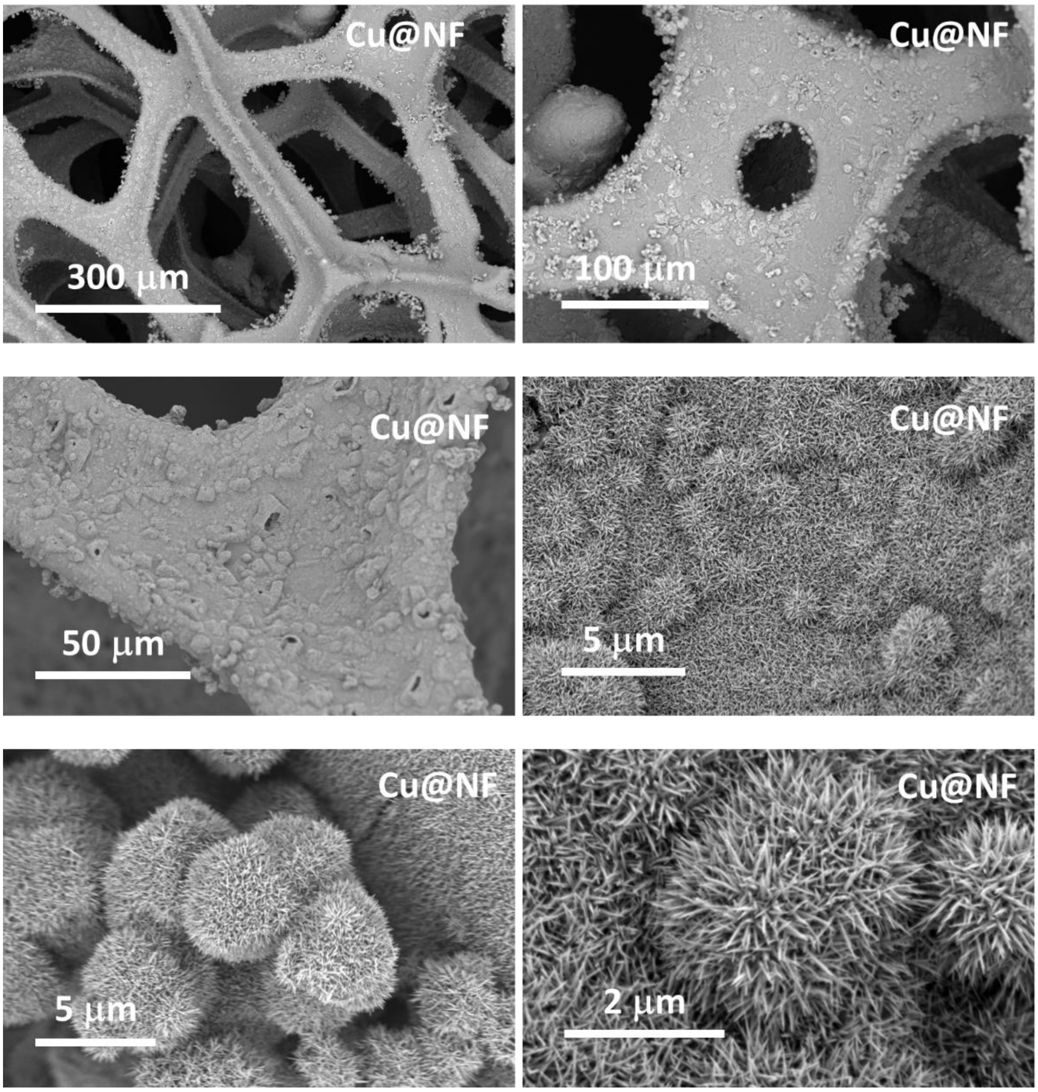

Figure 2.3. 7. Field emission scanning electron microscopy (FESEM) images of Cu@NF catalyst.

The Cu@NF(C) catalyst showed (***Figure 2.3.8***) occasionally disrupted specular morphology with opened up microcubes due to the shrinkage of microstructures on heat treatment. The size of microcubes vary between 4 µm and 5 µm. The thickness of spikes falls within the range of 30-50 nm and length in 400-500 nm.

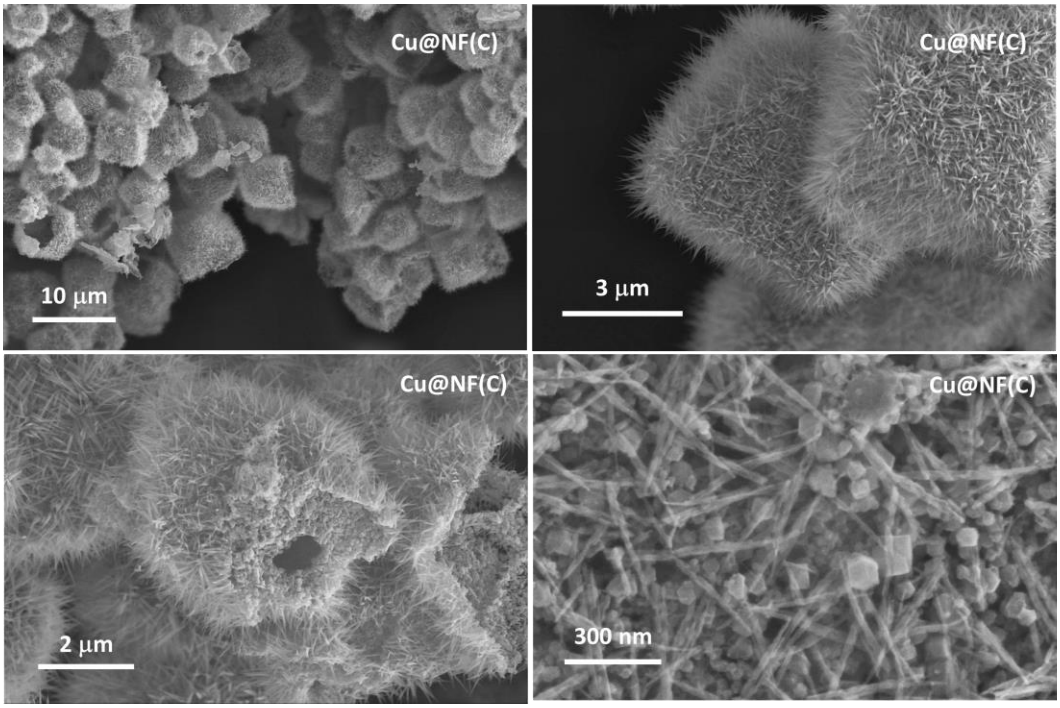

Figure 2.3. 8. Field emission scanning electron microscopy (FESEM) images of Cu@NF(C) catalyst.

Energy dispersive X-ray (EDS) analysis of Cu@NF(C) catalyst shows the presence of Cu, O, and Ni (***Figure 2.3.9.***). The distribution of Cu is non-uniform, and it varies from 3-15 % in different regions (***Figure 2.3.10.***).

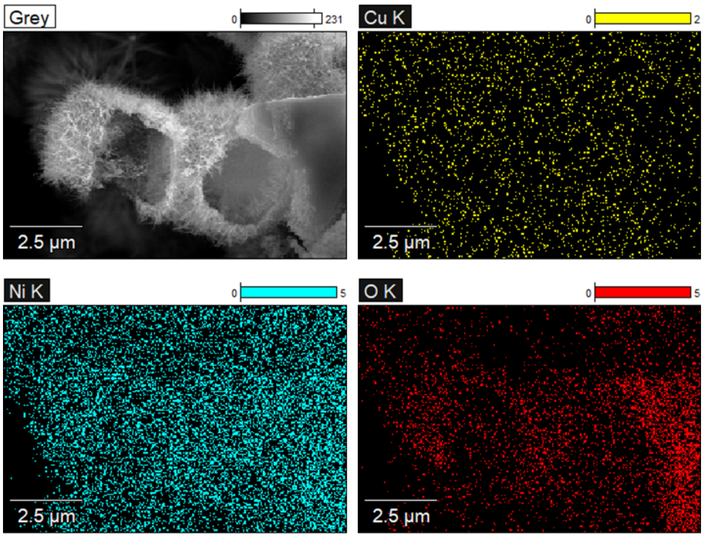

Figure 2.3. 9. Energy dispersive X-ray spectroscopy (EDS) mapping images of Cu@NF(C) catalyst.

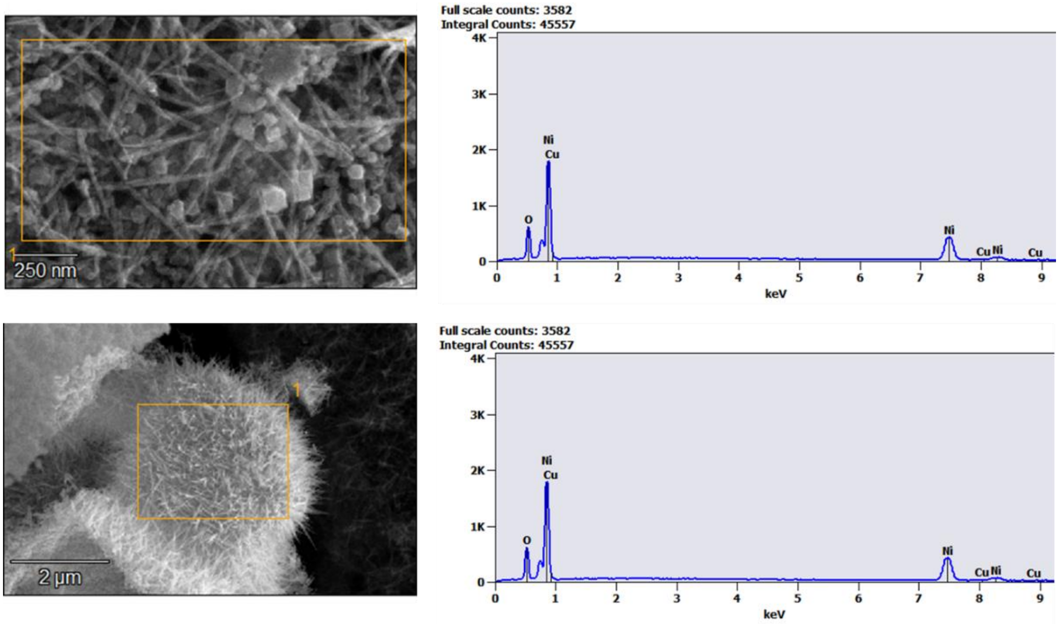

Catalyst	% Weight		
	Cu	Ni	O
CuO-thick	17.0	76.0	7.0
CuO-thin	1.1	87.2	11.7

Figure 2.3. 10. Energy dispersive X-ray spectroscopy (EDS) analysis of CuO@NF(C) catalyst.

Further, the TEM (***Figure 2.3.11.a, b***) of calcined sample (Cu@NF(C)) shows porous nanostructure of CuO nanoparticles of size 2-4 nm which could improve the diffusion kinetics of reactants to the active surface. Various lattice fringes of 0.21 nm, and 0.245 nm shows presence of both Cu_2O and CuO nanoparticles in the high-resolution transmission electron microscopy (HRTEM) images (***Figure 2.3.11.c***). Further, planes corresponding to CuO, Cu_2O and NiO species were also observed in the selected area electron diffraction (SAED) pattern (***Figure 2.3.11.d***).

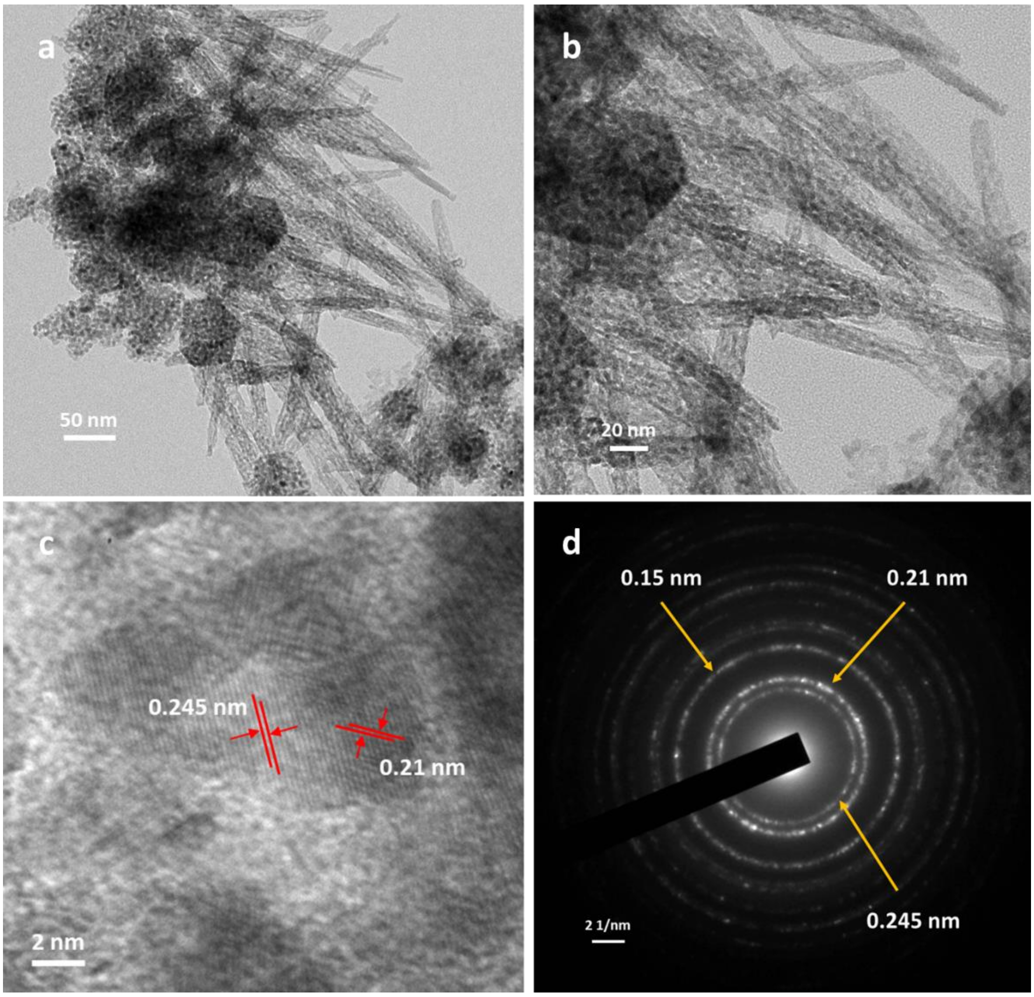

Figure 2.3. 11. (a, b) Transmission electron microscopy images, (c) high-resolution transmission electron microscopy images (HRTEM) image, and (d) selected area electron diffraction pattern image of Cu@NF(C) catalyst.

The chemical nature of elements in Cu@NF and Cu@NF(C) catalysts were determined by X-ray photoelectron spectroscopy (XPS) analysis. The high-resolution Cu 2p spectra of Cu@NF catalyst (***Figure 2.3.12.c***) shows peaks at 932.1 eV and 952.0 eV corresponding to Cu_2O species while peaks at 934.2 eV and 954.7 eV can be assigned to $Cu(OH)_2$ as there are no features for CuO seen from PXRD analysis. The ratio of Cu^+ to Cu^{2+} oxides observed to be 0.4. Cu@NF(C) catalyst (***Figure 2.3.12.a***) shows peaks at 934.1 eV and 954.9 eV, corresponding to Cu (II) species coming from CuO.(*43*) Peaks corresponding to Cu_2O were also seen at 932.3 eV and 952.35 eV. Further, in Ni 2p high-resolution spectra (***Figure 2.3.12.b***),(*44*) the peaks at 853.7 eV and 871.7 eV can be assigned to NiO species, and the peaks at 856.0 eV and 873.4 eV are assigned to $Ni(OH)_2$ species. The satellite peaks for Ni^{2+} species were observed at 860.5 eV, 863.2 eV, 878.7

eV, and 880.7 eV. The calcined sample shows increase in intensity of peaks for Cu^{2+} species with Cu^{+}/Cu^{2+} ratio of 1.6.

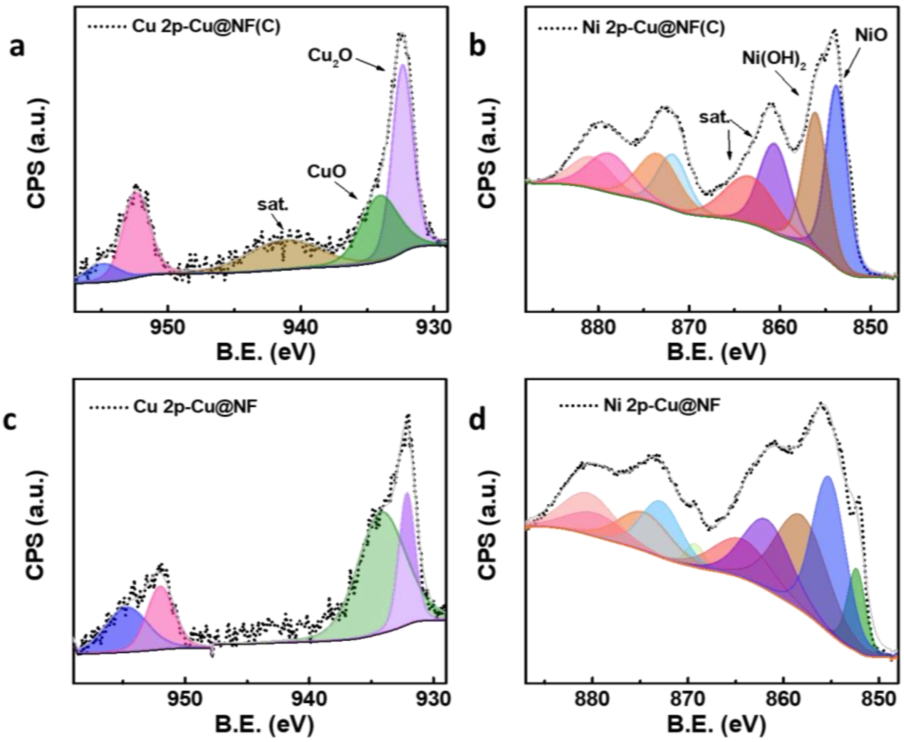

Figure 2.3. 12. High-resolution X-ray photoelectron spectroscopy (XPS) analysis of (a, b) Cu@NF(C), and (c, d) Cu@NF catalysts.

2.3.4.2. Electrochemical measurements:

The electrochemical OER studies carried out in 1.0 M NaOH in the absence of glucose show an onset potential (***Figure 2.3.13.a***) of 1.45 V for Cu@NF(C) electrode. The onset potential (***Figure 2.3.13.b***) of glucose oxidation reaction (GOR) appeared at 1.0 V. The Cu@NF(C) attained a current density of 100 mA cm^{-2} at a potential of 1.17 V for GOR. Further, a high current density of 1.4 A cm^{-2} was achieved over Cu@NF(C) at a very low potential of 1.45 V vs. RHE for GOR before the onset for OER starts. This is the highest current density observed at a very low potential for GOR as compared to the literature reports (***Table 2.3.1***). NF-U(C) and Cu@NF, on the other hand show a current density below 400 mA cm^{-2} at 1.45 V. The high current observed for Cu@NF(C) compared to Cu@NF could be due to improved conductivity which may have arisen shifting from insulating $Cu(OH)_2$ species at the surface to semiconducting cuprous and cupric oxides and also improved porosity.

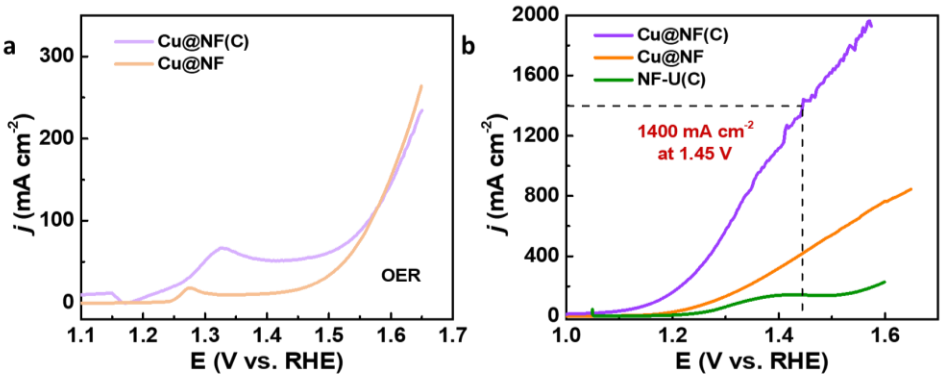

Figure 2.3. 13. Linear sweep voltammograms (LSVs) of different catalysts towards (a) OER and (b) glucose oxidation reaction (GOR) in 0.1 M glucose and 1.0 M NaOH.

The percentage of glucose conversion (***Figure 2.3.14.***) was determined by collecting the electrolyte at different intervals during the chronoamperometry study. The sample was analyzed for the remaining glucose with ^{1}H-NMR and HPLC studies. Cu@NF(C) catalyst shows 93 % conversion in 60 min.

The performance of Cu@NF(C) for glucose oxidation was stable for 15 cycles (***Figure 2.3.15.a***) tested using a single electrode with changing electrolyte. The Cu@NF(C) catalyst retained 93 % conversion ***(Figure 2.3.15.b,*** and ***Table 2.3.2.)*** during continuous 15 cycles. The reproducibility of GOR results over Cu@NF(C) was confirmed by conducting the reaction across various synthesized batches (***Figure 2.3.15.c***) of Cu@NF(C).

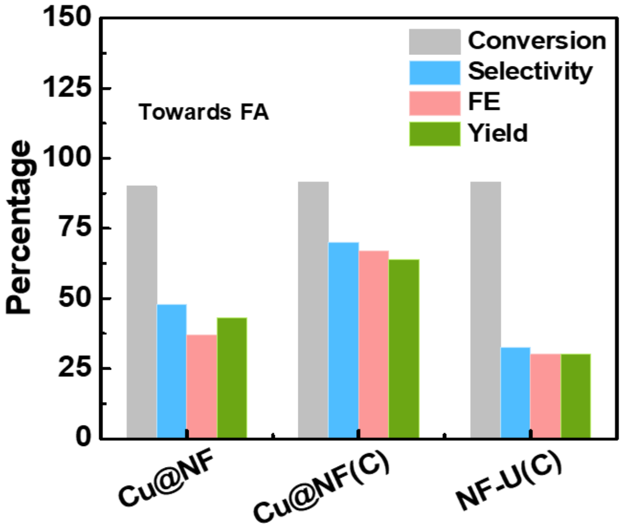

Figure 2.3. 14. Conversion, yield, selectivity, and faradaic efficiency towards the formation of formic acid by different catalysts.

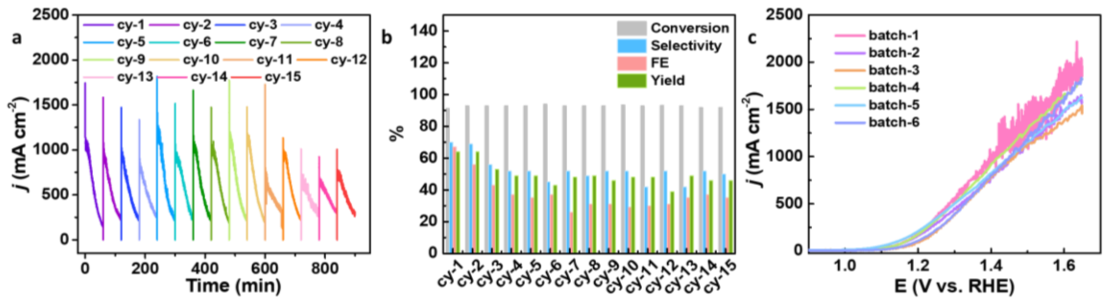

Figure 2.3. 15. (a) Chronoamperometry analysis, (b) performance matrices towards the production of formic acid in 15 cycles using Cu@NF(C) catalyst, and (c) retained performance of different batches of synthesized Cu@NF(C) catalysts.

Table 2.3. 2. Percentage conversion of glucose analysed after different time and in various cycles during GOR using Cu@NF(C) catalyst.

Sample	Conversion of glucose (%)	Sample	Conversion of glucose (%)
15 m	94	**cy-7**	93
30 m	93	**cy-8**	93
45 m	93	**cy-9**	93
60 m	93	**cy-10**	93.5
cy-1	93	**cy-11**	93
cy-2	93	**cy-12**	93.3
cy-3	93	**cy-13**	93
cy-4	93	**cy-14**	92
cy-5	93	**cy-15**	92
cy-6	94		

Breakup stability test conducted at an interval of 30 days also shows (***Figure 2.3.16.***) retained performance for more than 3 months. Ni surface may have been blocked by completely covered $Cu(OH)_2$ nanostructures in Cu@NF while in Cu@NF(C), the creation of disrupted structure allows the improved accessibility of glucose at the active sites. Further, these were confirmed by C_{dl} and impedance analysis.

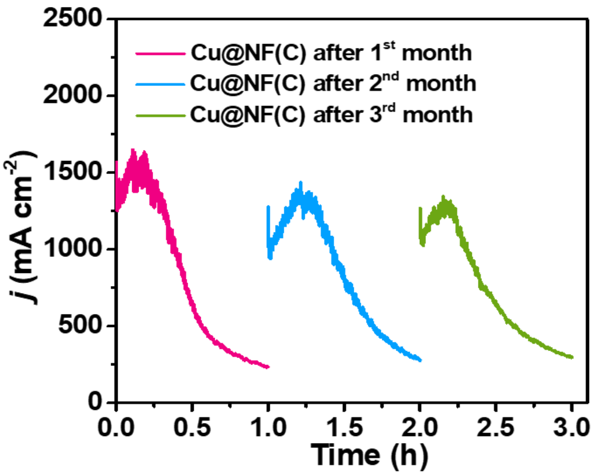

Figure 2.3. 16. Chronoamperometry analysis of Cu@NF(C) catalyst for 3 months in an interval of 30 days towards GOR.

To understand the contributions from intrinsic activity, electrochemically active surface area (ECSA) studies were done. A higher double-layer capacitance value **(*Figure 2.3.17.*)** of 161.5 mF cm^{-2} was observed for Cu@NF(C) in comparison to Cu@NF (2.3 mF cm^{-2}) and NF-U(C) (1.3 mF cm^{-2}) catalysts. Similarly, higher electrochemically active surface area (ECSA) was observed for Cu@NF(C) towards GOR. This could be due to increased porosity of the surface as observed from TEM analysis. Electrochemical impedance spectroscopy (EIS) studies were done to understand the mechanism at the interfaces. The Nyquist plot **(*Figure 2.3.17.d*)** shows low charge transfer resistance (R_{ct}) of 2.5 Ω for Cu@NF(C) catalyst with respect to NF-U(C) (4.3 Ω) and Cu@NF (5 Ω) hence a lower hindrance to the flow of charges in case of Cu@NF(C). This could have arisen from the low barrier to charge transfer offered by the nanospecular morphology of Cu@NF(C) catalyst.

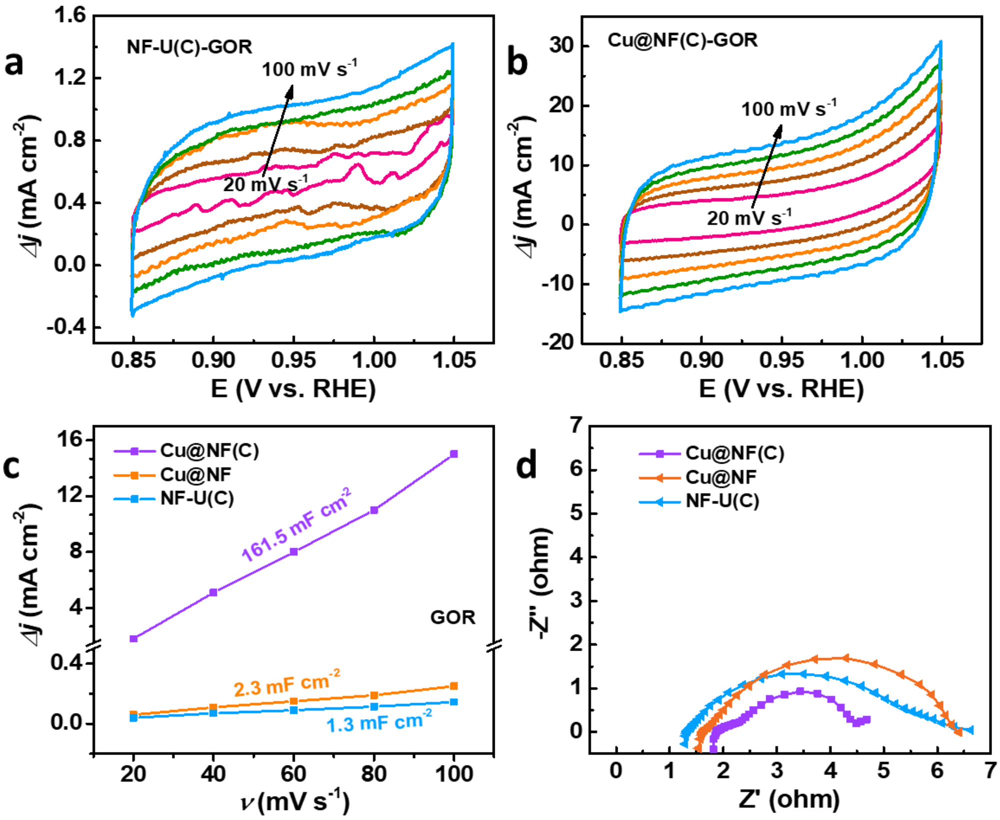

Figure 2.3. 17. Cyclic voltammetry analyses in non-Faradaic region with varying scan rate of (a) NF-U(C), and (b) Cu@NF(C) catalysts, (c) double layer capacitance (C_{dl}) plot, and (b) Nyquist plot showing impedance analysis of Cu@NF(C) catalyst towards GOR.

To fabricate the catalysts in full cell arrangement, HER analysis was first carried out in 1.0 M NaOH. The HER studies carried over Cu@NF showed (***Figure 2.3.18.***) an overpotential of 315 mV for attaining a current density of 100 mA cm^{-2}, while the state-of-the-art 20 wt %-Pt/C catalyst showed a low overpotential of 150 mV. As MoNi-based catalysts are known as effective alternatives to the noble Pt-based catalyst, we synthesized the MoNi catalyst with modified procedure reported in the literature. The as-prepared MoNi catalyst showed a current density of 100 mA cm^{-2} at an overpotential of 135 mV and the highest current density of 1.8 A cm^{-2} at 465 mV overpotential.

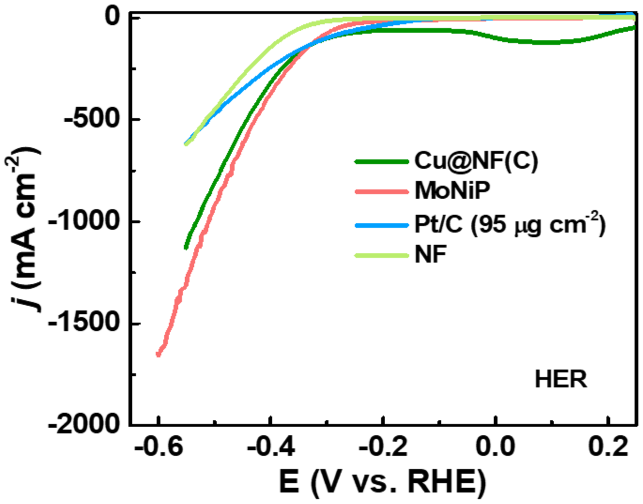

Figure 2.3. 18. Electrochemical hydrogen evolution reaction (HER) measurement of various catalysts in 1.0 M NaOH.

2.3.4.3. Full cell studies in two-electrode arrangement:

The performance of the Cu@NF(C) catalyst, NF-U(C), and MoNi catalysts were checked in full cell (two-electrode) arrangement (***Figure 2.3.19.a***) to mimic the commercial electrolyzers with H_2 evolving at the cathode and oxidation of glucose occurring at the anode side. The Cu@NF(C) coupled with MoNi showed the best performance with a cell potential of 1.64 V required to achieve a current density of 100 mA cm^{-2}. Also, a very high current density of 1.9 A cm^{-2} was obtained at 2.3 V. The performance of the catalyst for 3 cycles of different time period was analyzed by chronoamperometry. The first cycle was for 400 h and other two cycles were for 200 h each. The catalyst showed 20 % decrease only during first cycle and it remains constant for next two cycles. (***Figure 2.3.19.b***).

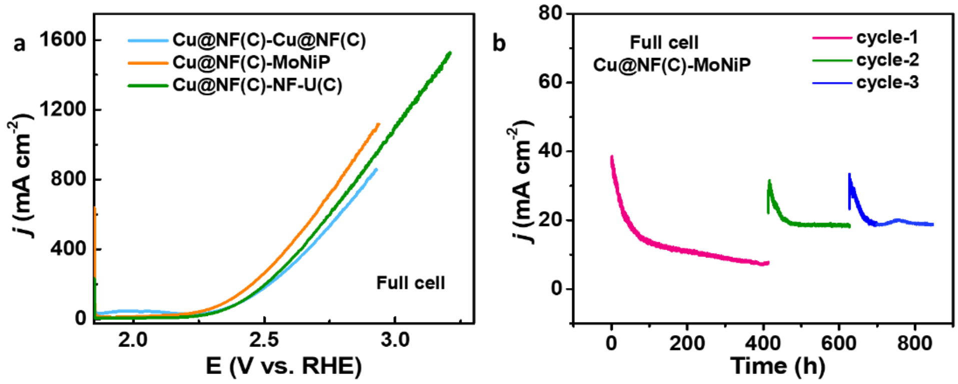

Figure 2.3. 19. Full cell (a) performance of different catalysts, and (b) cycle stabilities of Cu@NF(C)-MoNiP couple towards glucose-assisted HER.

2.3.4.4. Post-reaction analysis:

Post-reaction (GOR) PXRD analysis of Cu@NF(C) catalyst showed showed retained peaks corresponding to oxides of Cu, and Ni (***Figure 2.3.20.a***). The TEM, HRTEM analysis and SAED analysis also showed the porous morphology with lattice fringes corresponding to oxides of Cu and Ni (***Figure 2.3.20.b-d***).

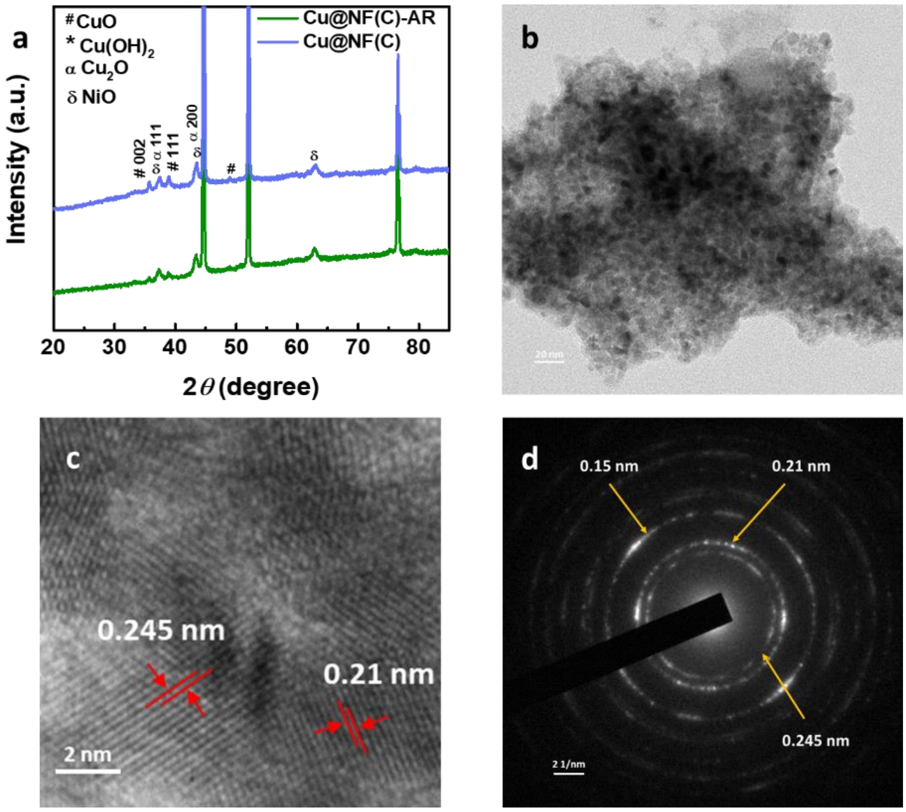

Figure 2.3. 20. (a) Powder X-ray diffraction (PXRD), (b) transmission electron microscopy (TEM), (c) High-resolution transmission electron microscopy (HRTEM), and (d) selected area electron diffraction analysis of Cu@NF(C)-AR catalyst post GOR measurement.

After 1h reaction FESEM analysis showed the creation of nano cubes on the surface of larger cubes (***Figure 2.3.21.*)**. After 15 cycles, the catalyst showed agglomerated morphology (***Figure 2.3.22.***) has been observed after 15 cycles. This will account for the decrease in activity over 15 cycles.

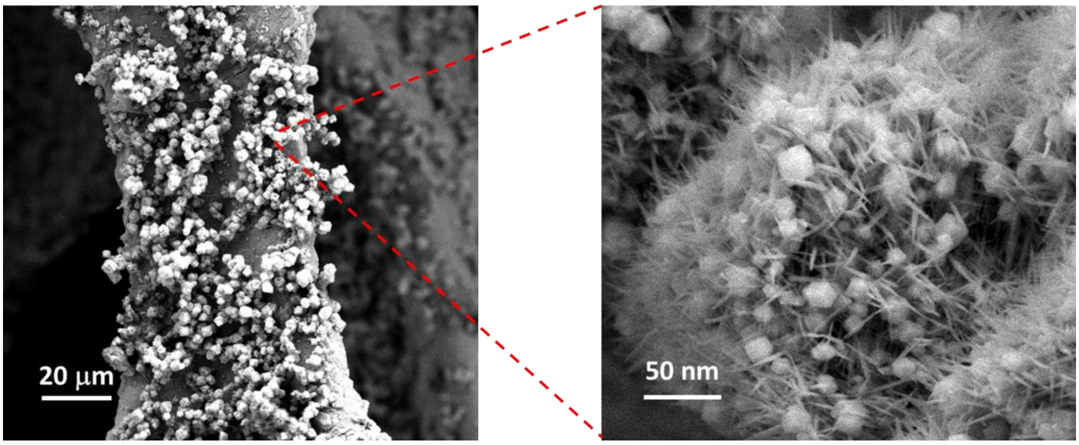

Figure 2.3. 21. Field emission scanning electron microscopy (FESEM) analysis of Cu@NF(C)-AR catalyst post-GOR. (AR means after reaction)

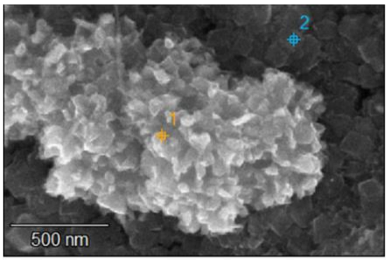

Catalyst	% Weight		
	Cu	Ni	O
Cu@NF(C)-AR-#1	17.0	76.0	7.0
Cu@NF(C)-AR-#2	1.1	87.2	11.7

Figure 2.3. 22. Energy dispersive X-ray spectroscopy (EDS) analysis of Cu@NF(C)-AR catalyst post-GOR. (AR means after reaction)

The EDS analysis of Cu@NF(C) showed uniform dispersion of Cu, Ni, and O all over the matrix with increase in O content after 15 cycles **(*Figure 2.3.22,*** and ***2.3.23.*)**.

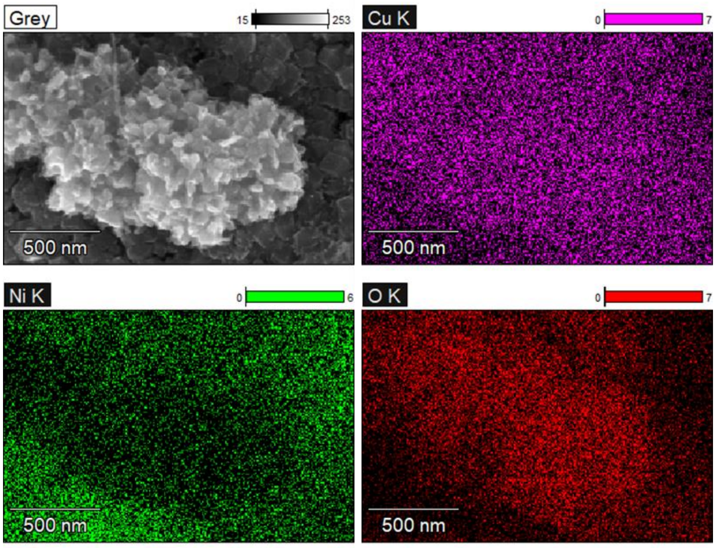

Figure 2.3. 23. EDS elemental mapping analysis of Cu@NF(C)-AR catalyst 15 cycles post-GOR. (AR means after reaction)

The high-resolution XPS analysis **(*Figure 2.3.24.*)** showed presence of oxides of Cu (CuO, and Cu_2O) and NiO along with metallic Ni and hydroxides of Ni.

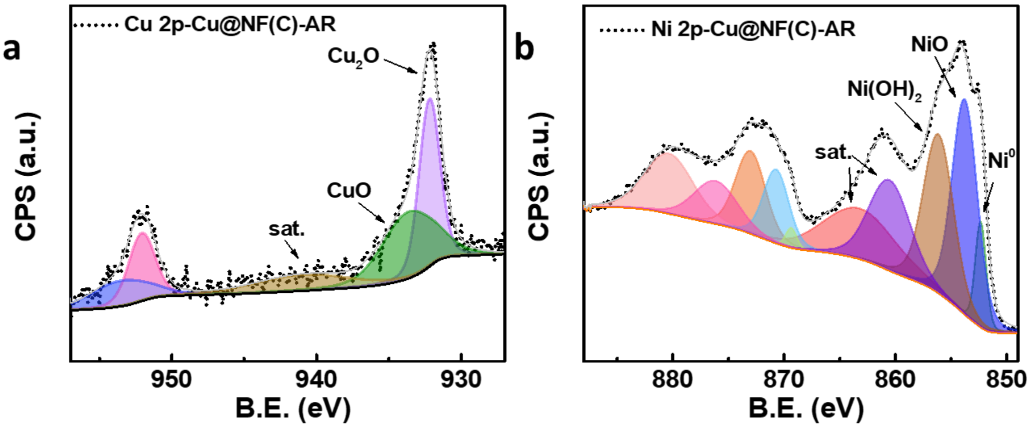

Figure 2.3. 24. X-ray photoelectron spectroscopy (XPS) analysis: (a) Cu 2p, and (b) Ni 2p of Cu@NF(C)-AR catalyst. (AR means after reaction)

2.3.4.5. Mechanistic studies:

In-situ Raman analysis was done in a self-made Teflon cell to understand the role of various contributing sites. Raman data were recorded during the chronoamperometry at different potentials starting from the open circuit potential (OCP) in a three-electrode arrangement. During the in-situ Raman analysis **(*Figure 2.3.25.a*)**, the broad peak appears at 500 cm^{-1} corresponds to NiO species. New peaks for NiOOH species were seen at 470 cm^{-1} and 550 cm^{-1} during OER (in the absence of glucose) when the potential reaches 1.35 V (Ni^{2+} to Ni^{3+} conversion). However, the NiO peak at 500 cm^{-1} disappeared (***Figure 2.3.25.b***) at 1.35 V during GOR (presence of glucose in the system) indicating the immediate chemical oxidation of glucose by the NiOOH thus getting itself reduced to NiO. On removal of electrical potential after reaching 1.35V, no NiOOH peak appears and only NiO peak teappers cin glucosontaining e solution. In-situ Raman analysis of NF-U(C) catalyst (***Figure 2.3.26.a***) also showed appearance of NiOOH peaks during OER, and their disappearance in GOR (***Figure 2.3.26.b***).

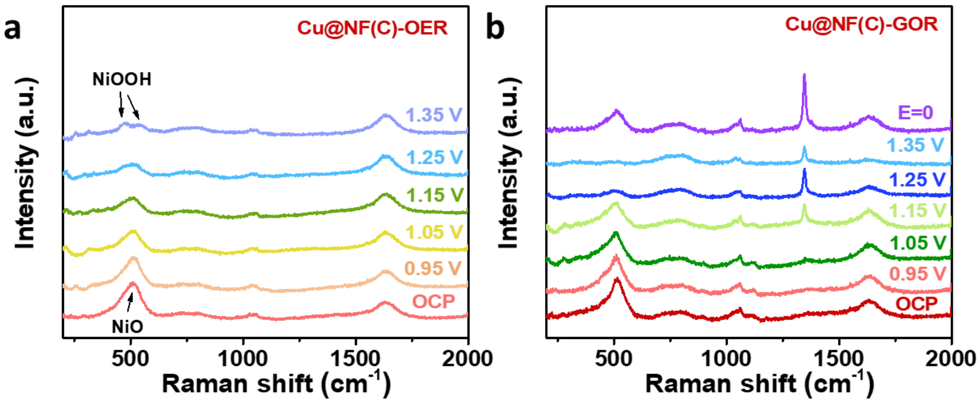

Figure 2.3. 25. In-situ Raman analysis of Cu@NF(C) catalyst towards (a) OER and (b) GOR.

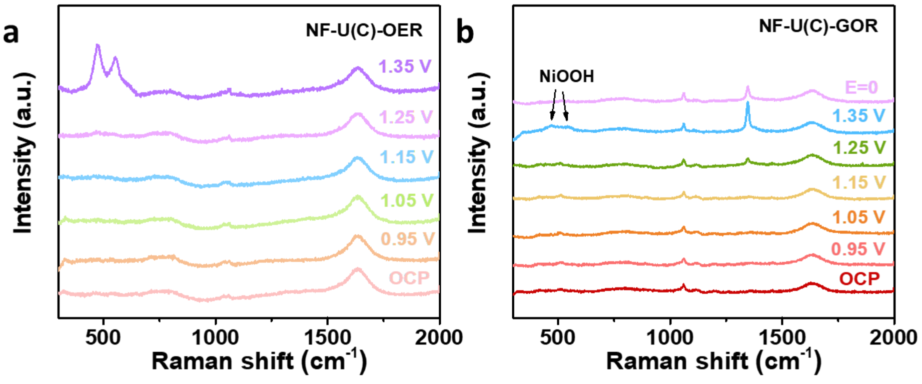

Figure 2.3. 26. In-situ Raman analysis of NF-U(C) catalyst towards (a) OER and (b) GOR.

As observed from the in-situ Raman analysis the appearance and disappearance of NiO peaks it can be assumed that Ni is the active site for glucose oxidation (***Figure 2.3.27.***). It is believed that Cu oxide in close proximity with NiOOH may affect the intermediate adsorption improving the glucose conversion.

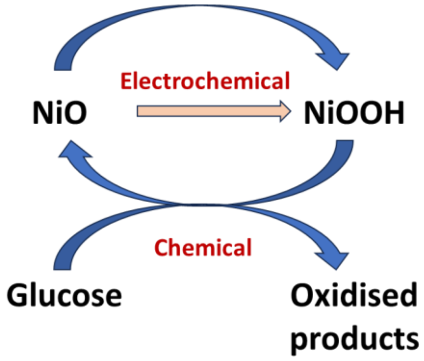

Figure 2.3. 27. Schematics showing the mechanistic view of Ni^{2+} sites as the active GOR sites.

2.3.4.6. Glucose sensing applications:

The expansion of this field of glucose oxidation to sensing applications has been known from decades. Considering chronic diabetic conditions and improving the regular diagnosis of blood glucose levels, the studies on cost-effective, non-enzymatic glucose sensors has been gradually increasing.(*45-47*) Moving on from the simplest 1st generation glucose sensors to the commercialization of 3rd generation sensors still lags with various limitations to use of enzymes.(*13*) The low stability, shelf life, high cost, and denaturation of the enzymes used lead to exploration of non-enzymatic systems. Non-enzymatic glucose sensors also have significance in other fields like food and ecological monitoring and development. The sensing capability of non-enzymatic systems ***(Table 2.3.3.)*** can be analysed in terms of amperometric response of the sensor towards varying concentration of glucose. Highly sensitive sensors (current response per unit glucose concentration) are required for early detection of imbalances in the glucose levels. Lower detection limits are favored during biomedical studies procuring impact of glucose on cancer cells and other deadly diseases. Complete exploration involves other important figures like response time, rate constant, and linear range of detection.(*12, 27, 28, 48-55*)

Table 2.3. 3. Reported catalysts for electrochemical glucose sensing.

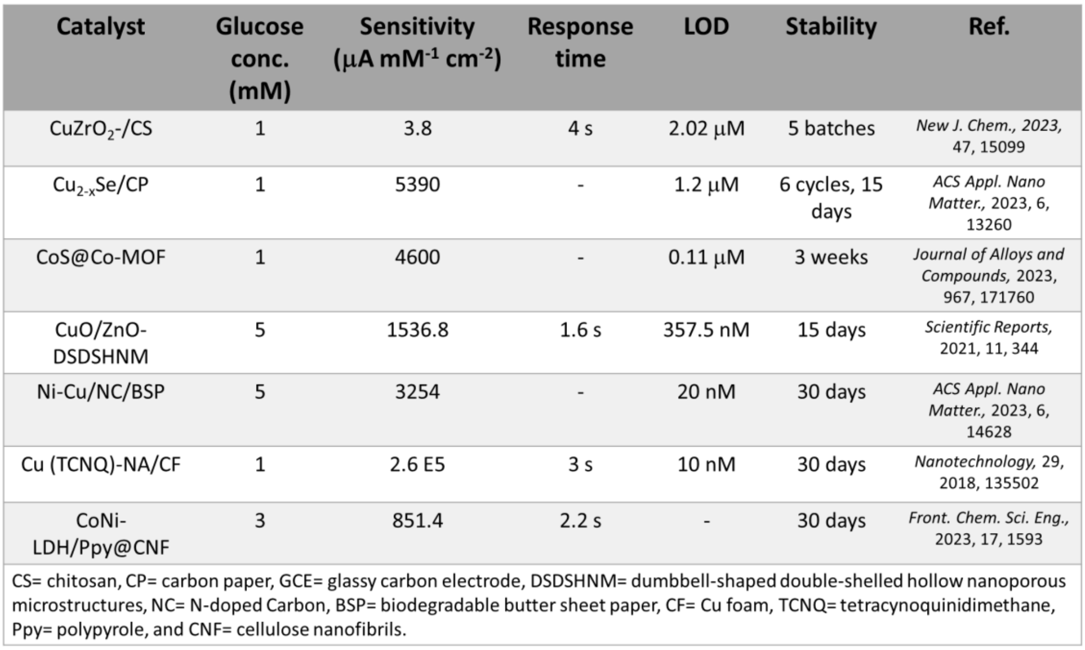

Catalyst	Glucose conc. (mM)	Sensitivity (μA mM^{-1} cm^{-2})	Response time	LOD	Stability	Ref.
$CuZrO_2$-/CS	1	3.8	4 s	2.02 μM	5 batches	*New J. Chem., 2023,* 47, 15099
$Cu_{2-x}Se$/CP	1	5390	-	1.2 μM	6 cycles, 15 days	*ACS Appl. Nano Matter.,* 2023, 6, 13260
CoS@Co-MOF	1	4600	-	0.11 μM	3 weeks	*Journal of Alloys and Compounds,* 2023, 967, 171760
CuO/ZnO-DSDSHNM	5	1536.8	1.6 s	357.5 nM	15 days	*Scientific Reports,* 2021, 11, 344
Ni-Cu/NC/BSP	5	3254	-	20 nM	30 days	*ACS Appl. Nano Matter.,* 2023, 6, 14628
Cu (TCNQ)-NA/CF	1	2.6 E5	3 s	10 nM	30 days	*Nanotechnology,* 29, 2018, 135502
CoNi-LDH/Ppy@CNF	3	851.4	2.2 s	-	30 days	*Front. Chem. Sci. Eng.,* 2023, 17, 1593

CS= chitosan, CP= carbon paper, GCE= glassy carbon electrode, DSDSHNM= dumbbell-shaped double-shelled hollow nanoporous microstructures, NC= N-doped Carbon, BSP= biodegradable butter sheet paper, CF= Cu foam, TCNQ= tetracynoquinidimethane, Ppy= polypyrole, and CNF= cellulose nanofibrils.

Co-detection methods have also been employed to detect more than one biological component with single catalysts. For example, the co-existence of dopamine and glucose is beneficial to be determined in a person with Parkinson's disease. Similarly, uric acid and glucose should be determined for a hyperuricemia patient. Likewise, the effect of various interfering species, such as ascorbic acid, glycine, sucrose, etc., must be studied.(*56*)

The Cu@NF(C) catalyst was also studied towards glucose sensing applications. Cyclic voltammetry (CV) analysis of different Cu@NF(C) electrodes was done in known concentrations of glucose varying from 10 fM to 100 mM in 0.1 M NaOH and 1.0 M NaOH electrolyte. The calibration plot showed four different linear regions **(*Figure 2.3.28.*)** in both 0.1 M NaOH and 1.0 M NaOH solutions.

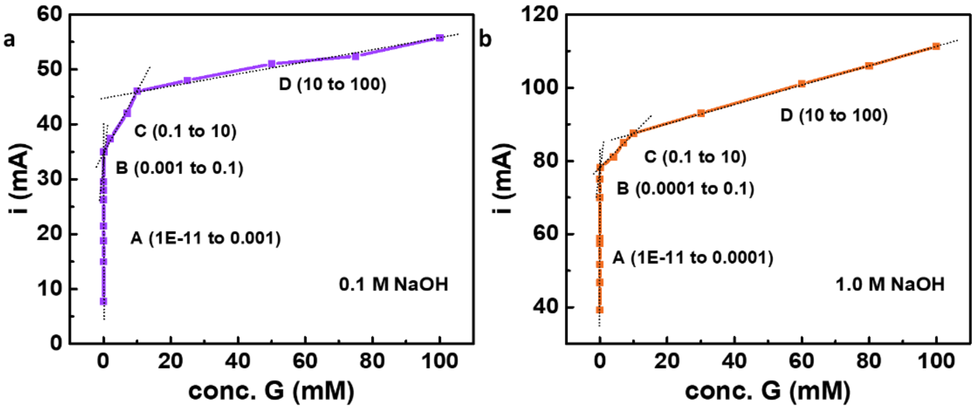

Figure 2.3. 28. Calibration plots for standard glucose samples for sensing application in (a) 0.1 M NaOH, and (b) 1.0 M NaOH.

The sensitivity of the sensor was calculated to be very high as tabulated in ***Table 2.3.4.*** in four different linear regions.

For calculating the limits of detection in these linear regions, standard deviations were evaluated from the consecutive cyclic voltammetry (CV) analysis of blank electrolyte. The LOD values are calculated using the relation:

LOD = 3.3 σ/s, wherein 'σ' is the standard deviation of peak current observed from the consecutive CV analysis of blank electrolyte **(*Figure 2.3.29.*)**, and 's' is the slope of the calibration plot.

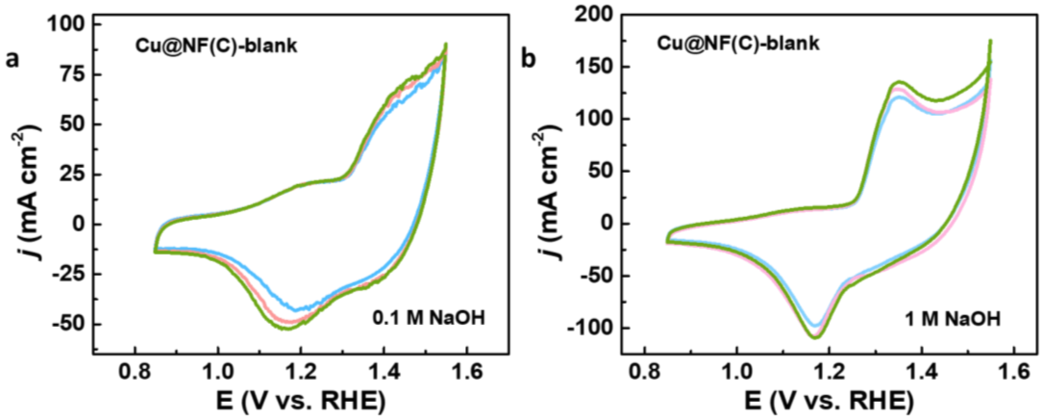

Figure 2.3. 29. Cyclic voltammograms of Cu@NF(C) samples in blank electrolyte (a) 0.1 M NaOH, and (b) 1.0 M NaOH.

The sensor made with Cu@NF(C) showed very high sensitivity of 4*E9 and a low limit of detection of 5 nM with linear range lying as low as 10 fM to 100 nM. The fittings of linear regions in different concentrations can be written in the form of y = mx + c.

In 0.1 M NaOH:

Region (A): $i\ (\mathrm{mA}) = (113017.6 \pm 74107)\ c\ (\mathrm{mM}) + (17.47 \pm 3.04)$

Region (B): $i\ (\mathrm{mA}) = (66.5 \pm 7.7)\ c\ (\mathrm{mM}) + (28.4 \pm 3.04)$

Region (C): $i\ (\mathrm{mA}) = (1.1 \pm 0.72)\ c\ (\mathrm{mM}) + (34.9 \pm 36.06)$

Region (D): $i\ (\mathrm{mA}) = (0.11 \pm 0.00)\ c\ (\mathrm{mM}) + (44.92 \pm 0.24)$

In 1.0 M NaOH:

Region (A): $i\ (\mathrm{mA}) = (1007690 \pm 86355)\ c\ (\mathrm{mM}) + (48.76 \pm 3.86)$

Region (B): $i\ (\mathrm{mA}) = (64.16 \pm 39.8)\ c\ (\mathrm{mM}) + (72.06 \pm 2.31)$

Region (C): $i\ (\mathrm{mA}) = (0.97 \pm 0.09)\ c\ (\mathrm{mM}) + (77.85 \pm 0.54)$

Region (D): $i\ (\mathrm{mA}) = (0.26 \pm 0.00)\ c\ (\mathrm{mM}) + (85.00 \pm 0.14)$

Table 2.3. 4. Parameters observed from sensing studies of Cu@NF(C) sensor in 0.1 M NaOH and 1.0 M NaOH electrolytes.

NaOH conc. (M)	Linear range	Sensitivity (μA mM^{-1} cm^{-2})	Limit of detection (LOD)
0.1	10 fM-1 μM	4.52 E8	26.0 nM
0.1	1 μM-100 μM	2.66 E5	44.0 μM
0.1	100 μM-10 mM	4400	2.6 mM
0.1	10 mM-100 mM	440	26.6 mM
1.0	10 fM-100 nM	4.03 E9	5.0 nM
1.0	100 nM-1 μM	2.57 E5	78.4 μM
1.0	1 μM-10 mM	3860	5.2 mM
1.0	10 mM-100 mM	1052	19.1 mM

Further, the response time for the sensor was evaluated by a chronoamperometry study ***(Figure 2.3.30.)*** with the addition of glucose every 100 s. The Cu@NF(C) sensor took just 0.5 s to respond to a particular glucose concentration.

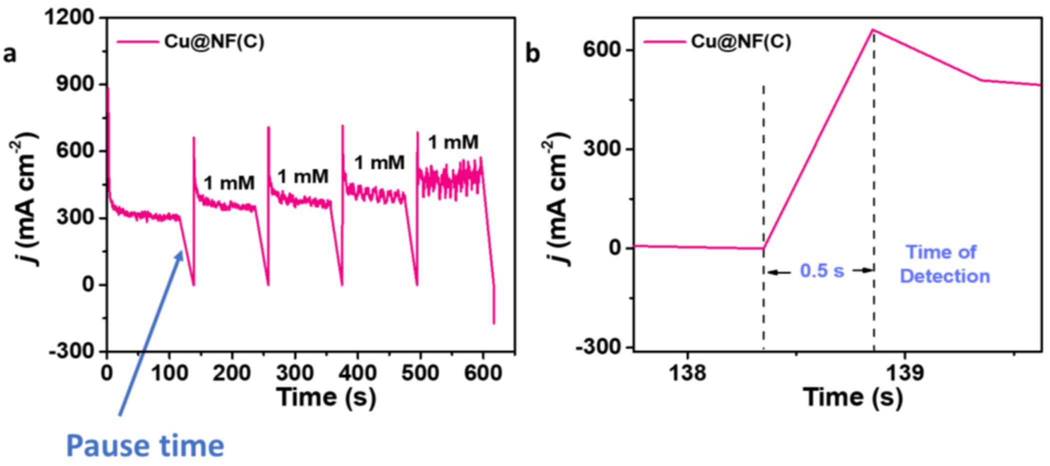

Figure 2.3. 30. Chronoamperometry studies for determination of response time for Cu@NF(C) sensor.

2.3.4.7. Kinetic rate constant studies:

The reaction of electrochemical conversion of glucose can be considered as a decay process wherein reactants are consumed with time. The system follows Cotrell's equation as the reaction (charge transfer) rate and diffusion kinetics behave differently. Thus, the catalytic current proportionally depends on the square root of the rate constant and time as given in the relation:

$I_C / I_L = (k\, c_0\, t)^{1/2}$, where I_C and I_L are the catalytic and limiting peak current densities, c_0 is the initial concentration of glucose, k is the rate constant, and t is time.

The I_C and I_L were determined from the chronoamperometry studies (***Figure 2.3.31.***) of Cu@NF(C) catalyst in presence and absence of glucose for three consecutive cycles.

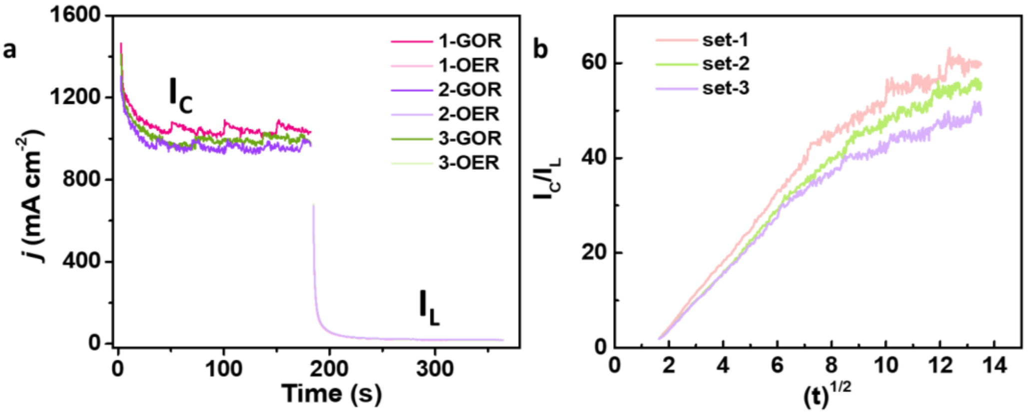

Figure 2.3. 31. Rate constant studies of Cu@NF(C) sensor: (a) double-step chronoamperometry, and (b) rate plot. I_C is catalytic current density and I_L is limiting current density.

The rate constant of 13.5 E4 $cm^3\ mol^{-1}\ s^{-1}$ was calculated from the slope of the linear plot of I_C/I_L vs. $(t)^{1/2}$.

2.3.4.8. Interference studies:

During chronoamperometry analysis, the interference studies (***Figure 2.3.32.***) were conducted via the stepwise addition of dopamine, ascorbic acid, sucrose, and glycine to a glucose-containing solution.

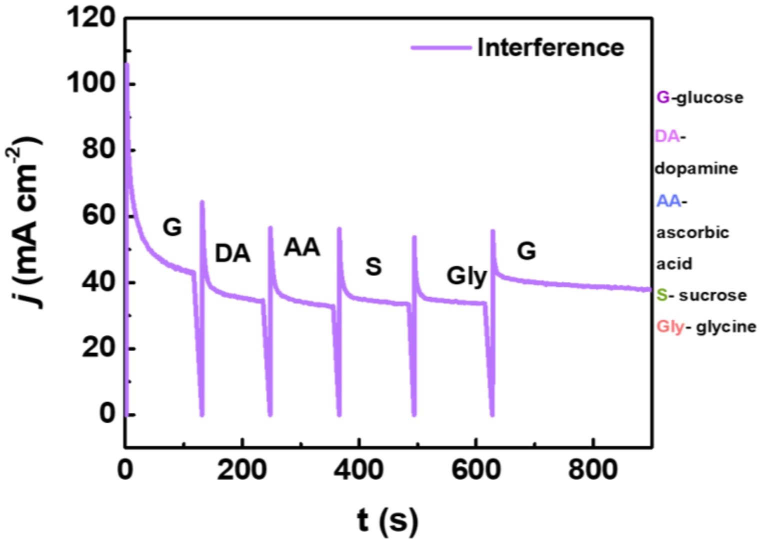

Figure 2.3. 32. Interference study of the Cu@NF(C) sensor.

No interference was seen, and the sensor showed retained performance with further addition of glucose at the last step.

2.3.5. Conclusions:

This work projected the utilization of Cu oxide decorated Ni foam support for effective glucose oxidation and sensing. The copper hydroxide decorated NF, Cu@NF on calcination in air produces porous Cu oxide nanostructures which shows good conductivity and demonstrated very high performance towards GOR and sensing in varying glucose concentrations. High current density of 1.4 A cm^{-2} was achieved at low potential (1.45 V) with 93 % conversion of glucose in alkaline conditions. For sensing applications, remarkably high sensitivity is observed with detection limit of 5 nM. The in-situ Raman studies confirmed NiO as the active sites for chemical oxidation of glucose.

2.3.6. References:

1. O. F. Er, A. Caglar, H. Kivrak, Enhanced electrochemical glucose oxidation in alkaline solution over indium decorated carbon supported palladium nanoparticles. *Materials Chemistry and Physics* **254**, (2020).
2. M. Zhiani, A. Abedini, S. Majidi, Comparison of Electro-Catalytic Activity of Fe-Ni-Co/C and Pd/C Nanoparticles for Glucose Electro-Oxidation in Alkaline Half-Cell and Direct Glucose Fuel Cell. *Electrocatalysis* **9**, 735-743 (2018).
3. T. N. Smith *et al.*, Modifications in the nitric acid oxidation of D-glucose. *Carbohydr Res* **350**, 6-13 (2012).
4. Y. Holade *et al.*, Recent advances in the electrooxidation of biomass-based organic molecules for energy, chemicals and hydrogen production. *Catalysis Science & Technology* **10**, 3071-3112 (2020).
5. Y. Xu, B. Zhang, Recent Advances in Electrochemical Hydrogen Production from Water Assisted by Alternative Oxidation Reactions. *ChemElectroChem* **6**, 3214-3226 (2019).
6. H. Luo *et al.*, Progress and Perspectives in Photo- and Electrochemical-Oxidation of Biomass for Sustainable Chemicals and Hydrogen Production. *Advanced Energy Materials* **11**, (2021).
7. W. Liu, C. Liu, P. Gogoi, Y. Deng, Overview of Biomass Conversion to Electricity and Hydrogen and Recent Developments in Low-Temperature Electrochemical Approaches. *Engineering* **6**, 1351-1363 (2020).
8. A. Brouzgou, P. Tsiakaras, Electrocatalysts for Glucose Electrooxidation Reaction: A Review. *Topics in Catalysis* **58**, 1311-1327 (2015).
9. T. Wang *et al.*, Combined anodic and cathodic hydrogen production from aldehyde oxidation and hydrogen evolution reaction. *Nature Catalysis* **5**, 66-73 (2021).
10. L. Chen, J. Shi, Co-electrolysis toward value-added chemicals. *Science China Materials* **65**, 1-9 (2021).
11. L. Chen, J. Shi, Chemical-assisted hydrogen electrocatalytic evolution reaction (CAHER). *Journal of Materials Chemistry A* **6**, 13538-13548 (2018).
12. S. Radhakrishnan *et al.*, Recent Developments and Future Perspective on Electrochemical Glucose Sensors Based on 2D Materials. *Biosensors (Basel)* **12**, (2022).

13. E. H. Yoo, S. Y. Lee, Glucose biosensors: an overview of use in clinical practice. *Sensors (Basel)* **10**, 4558-4576 (2010).
14. A. Brouzgou, L. L. Yan, S. Q. Song, P. Tsiakaras, Glucose electrooxidation over PdxRh/C electrocatalysts in alkaline medium. *Applied Catalysis B: Environmental* **147**, 481-489 (2014).
15. G. Dong *et al.*, Electrocatalytic Glucose Oxidation at Coral-Like Pd/C3N4-C Nanocomposites in Alkaline Media. *Catalysts* **10**, (2020).
16. J. Chen *et al.*, An alkaline direct oxidation glucose fuel cell using three-dimensional structural Au/Ni-foam as catalytic electrodes. *RSC Advances* **7**, 3035-3042 (2017).
17. H. Huu Do, S. Y. Kim, Q. V. Le, Development of non-precious metal oxide-based electrodes for enzyme-free glucose detection: A review. *Microchemical Journal* **193**, (2023).
18. N. Sattarahmady, H. Heli, A non-enzymatic amperometric sensor for glucose based on cobalt oxide nanoparticles. *Journal of Experimental Nanoscience* **7**, 529-546 (2012).
19. P. Du, J. Zhang, Y. Liu, M. Huang, Hydrogen generation from catalytic glucose oxidation by Fe-based electrocatalysts. *Electrochemistry Communications* **83**, 11-15 (2017).
20. J. Wang, L. Zhu, L. Ji, Z. Chen, Preparation of nanostructured $Cu(OH)_2$ and CuO electrocatalysts for water oxidation by electrophoresis deposition. *Journal of Materials Research* **33**, 581-589 (2017).
21. N. K. Shrestha, S. A. Patil, A. S. Salunke, A. I. Inamdar, H. Im, Accelerating glucose electrolysis on Cu-doped MIL-88B for an energy efficient anodic reaction in water splitting. *Dalton Trans* **52**, 10933-10941 (2023).
22. J. Yang, M. Cho, Y. Lee, Synthesis of hierarchical NiCo2O4 hollow nanorods via sacrificial-template accelerate hydrolysis for electrochemical glucose oxidation. *Biosens Bioelectron* **75**, 15-22 (2016).
23. A. Salimi, M. Roushani, S. Soltanian, R. Hallaj, Picomolar Detection of Insulin at Renewable Nickel Powder-Doped Carbon Composite Electrode. *Anal. Chem.* **79**, 7431-7438 (2007).
24. P. Yang *et al.*, NiO/SiC nanocomposite prepared by atomic layer deposition used as a novel electrocatalyst for nonenzymatic glucose sensing. *ACS Appl Mater Interfaces* **7**, 4772-4777 (2015).

25. X. Lin, H. Zhong, W. Hu, J. Du, Nickel-Cobalt Selenide Electrocatalytic Electrode toward Glucose Oxidation Coupling with Alkaline Hydrogen Production. *Inorg Chem* **62**, 10513-10521 (2023).
26. G. A. El-Nagar, C. Roth, Enhanced electrooxidation of glucose at nano-chitosan-NiOOH modified GC electrode: fuel blends and hydrocarbon impurities. *Phys Chem Chem Phys* **19**, 2537-2548 (2017).
27. G. A. Naikoo *et al.*, Recent Advances in Non-Enzymatic Glucose Sensors Based on Metal and Metal Oxide Nanostructures for Diabetes Management- A Review. *Front Chem* **9**, 748957 (2021).
28. N. Mohamad Nor, N. S. Ridhuan, K. Abdul Razak, Progress of Enzymatic and Non-Enzymatic Electrochemical Glucose Biosensor Based on Nanomaterial-Modified Electrode. *Biosensors (Basel)* **12**, (2022).
29. M. Janyasupab *et al.*, A comparative study of non-enzymatic glucose detection in artificial human urine and human urine specimens by using mesoporous bimetallic cobalt-iron supported N-doped graphene biosensor based on differential pulse voltammetry. *Sensors and Actuators B: Chemical* **286**, 550-563 (2019).
30. Y. Wei, W. Zhang, Potential Cycling Effects on Activities of Nickel-Mediated Benzyl Alcohol and Glycine Electrooxidation in Alkaline Solutions. *Catalysts* **10**, (2020).
31. M. Aghazadeh, H. F. Rad, In situ growth of Ni(OH)2-porous nitrogen-doped graphene composite onto Ni foam support as advanced electrochemical supercapacitors materials. *Journal of Materials Science: Materials in Electronics* **33**, 11038-11054 (2022).
32. X. Niu, M. Lan, H. Zhao, C. Chen, Highly sensitive and selective nonenzymatic detection of glucose using three-dimensional porous nickel nanostructures. *Anal Chem* **85**, 3561-3569 (2013).
33. G. Sanghez de Luna *et al.*, Electrification of glucose valorization over NiO/Ni foam. *Sustainable Energy & Fuels* **7**, 4474-4485 (2023).
34. V. Sudha, G. Murugadoss, R. Thangamuthu, Structural and morphological tuning of Cu-based metal oxide nanoparticles by a facile chemical method and highly electrochemical sensing of sulphite. *Sci Rep* **11**, 3413 (2021).

35. K. Yamagiwa, N. Suzuki, T. Wakatabe, D. Satou, Self-formed nanocatalyst layers on Ni–Cu alloy substrates and their characteristics for electrochemical glucose oxidation. *Japanese Journal of Applied Physics* **59**, (2020).
36. L. Goodnight, D. Butler, T. Xia, A. Ebrahimi, Non-Enzymatic Detection of Glucose in Neutral Solution Using PBS-Treated Electrodeposited Copper-Nickel Electrodes. *Biosensors (Basel)* **11**, (2021).
37. M. M. Abuzaied, Y. M. Asal, A. M. Mohammad, I. M. Al-Akraa, Enhanced Glucose Electrooxidation at Ni-Cu Binary Oxide Nanocatalyst. *International Journal of Electrochemical Science* **15**, 2449-2457 (2020).
38. A. Maizelis, Multilayer Nickel–Copper Anode for Direct Glucose Fuel Cell. *Journal of Electrochemical Energy Conversion and Storage* **16**, (2019).
39. X. Wu, W. Lu, High-performance electrochemical glucose sensing enabled by Cu(TCNQ) nanorod array. *Nanotechnology* **29**, 135502 (2018).
40. W. J. Liu *et al.*, Efficient electrochemical production of glucaric acid and H(2) via glucose electrolysis. *Nat Commun* **11**, 265 (2020).
41. J. Zhang *et al.*, Efficient hydrogen production on MoNi(4) electrocatalysts with fast water dissociation kinetics. *Nat Commun* **8**, 15437 (2017).
42. X. Yang *et al.*, A doping element improving the properties of catalysis: in situ Raman spectroscopy insights into Mn-doped NiMn layered double hydroxide for the urea oxidation reaction. *Catalysis Science & Technology* **12**, 4471-4485 (2022).
43. Z. Dan, Y. Yang, F. Qin, H. Wang, H. Chang, Facile Fabrication of Cu(2)O Nanobelts in Ethanol on Nanoporous Cu and their Photodegradation of Methyl Orange. *Materials (Basel)* **11**, (2018).
44. N. Weidler *et al.*, X-ray Photoelectron Spectroscopic Investigation of Plasma-Enhanced Chemical Vapor Deposited NiOx, NiOx(OH)y, and CoNiOx(OH)y: Influence of the Chemical Composition on the Catalytic Activity for the Oxygen Evolution Reaction. *The Journal of Physical Chemistry C* **121**, 6455-6463 (2017).
45. M. A. Khaleque *et al.*, Nanostructured wearable electrochemical and biosensor towards healthcare management: a review. *RSC Adv* **13**, 22973-22997 (2023).
46. H. Teymourian, A. Barfidokht, J. Wang, Electrochemical glucose sensors in diabetes management: an updated review (2010-2020). *Chem Soc Rev* **49**, 7671-7709 (2020).

47. A. Heller, B. Feldman, Electrochemical Glucose Sensors and Their Applications in Diabetes Management. *Chem. Rev.* **108**, 2482-2505 (2008).
48. L. E. Rebolledo-Perales, P. Hernández, G. A. Álvarez-Romero, D. Hernández-Ramírez, Trends on the Development of Non-Enzymatic Electrochemical Sensors Modified with Metal-Organic Frameworks for the Quantification of Glucose. *Journal of The Electrochemical Society* **170**, (2023).
49. A. Mohammadpour-Haratbar, S. Mohammadpour-Haratbar, Y. Zare, K. Y. Rhee, S. J. Park, A Review on Non-Enzymatic Electrochemical Biosensors of Glucose Using Carbon Nanofiber Nanocomposites. *Biosensors (Basel)* **12**, (2022).
50. K. Tian, M. Prestgard, A. Tiwari, A review of recent advances in nonenzymatic glucose sensors. *Mater Sci Eng C Mater Biol Appl* **41**, 100-118 (2014).
51. Z. Haghparas, Z. Kordrostami, M. Sorouri, M. Rajabzadeh, R. Khalifeh, Highly sensitive non-enzymatic electrochemical glucose sensor based on dumbbell-shaped double-shelled hollow nanoporous CuO/ZnO microstructures. *Sci Rep* **11**, 344 (2021).
52. N. Miya, L. F. E. Machogo-Phao, B. Ntsendwana, Exploring Copper Oxide and Copper Sulfide for Non-Enzymatic Glucose Sensors: Current Progress and Future Directions. *Micromachines (Basel)* **14**, (2023).
53. K. Dhara, D. R. Mahapatra, Electrochemical nonenzymatic sensing of glucose using advanced nanomaterials. *Mikrochim Acta* **185**, 49 (2017).
54. V. B. Juska, M. E. Pemble, A Critical Review of Electrochemical Glucose Sensing: Evolution of Biosensor Platforms Based on Advanced Nanosystems. *Sensors (Basel)* **20**, (2020).
55. D. AnnieCanisius *et al.*, Analysing the bifunctional ability of CuO/BiOBr/rGO as an electrode for non-enzymatic glucose sensor and supercapacitor. *Materials Letters* **346**, (2023).
56. D. A. Gough, F. L. Anderson, J. Giner, C. K. Colton, J. S. Soeldner, Effect of Coreactants on Electrochemical Glucose Oxidation. *ANALYTICAL CHEMISTRY* **50**, 941-944 (1978).

Appendix. Characterization techniques and instrumentation

Various characterization techniques utilized in this work are described herewith.

1. PXRD analysis:

Powder X-ray diffraction (PXRD) patterns were recorded using Rigaku diffractometer using Cu Kα radiation, (λ=1.54 Å, step size: 0.02, current: 30 mA and voltage: 40 kV). The crystallite size observed from PXRD is determined using Scherrer equation given as:

$$\tau=(k\lambda)/(\beta\cos\theta),$$

where τ, k, λ, β, and θ are crystallite size, shape factor (=1), wavelength of source (0.154 nm), full width half maxima (FWHM), and Bragg's angle respectively.

2. FESEM, EDS, and TEM analyses:

Field-emission scanning electron microscopy (FESEM) images and energy-dispersive X-ray spectroscopy (EDS) were obtained by using FEI (Thermofischer, Apreo 2S) equipment, and FEI (Nova-Nano SEM-600 Netherlands). The powdered samples were dispersed in absolute ethanol, drop-casted on Si wafer and dried in ambient conditions. The samples supported on Ni foam are directly used in the microscopy column without any further treatment. Transmission electron microscope (TEM) imaging was done using JEOL (JEM 2100 Plus) electron microscope and TALOS F200 S G2 electron microscope operating at an accelerating voltage of 200 kV. The samples were prepared by drop casting a very dilute dispersion of the powdered sample (in absolute ethanol) on a TEM grid (carbon polymer, 300 mesh). The hydrothermally synthesized samples on Ni foam support are sonicated and the material was drop casted on Cu grid.

3. ICP-OES analysis:

Further, to determine the composition of Fe and Ni in the samples, inductive coupled plasma-optical emission spectroscopy (ICP-OES) was carried out using a Perkin−Elmer Optima 7000 DV instrument. The samples were digested overnight in aqua regia and filtered using 0.2-micron filters. The calibration plot was generated by analysing the different concentrations of standard samples. The concentration of unknown samples was determined from the calibration plot.

4. XPS analysis:

X-ray photoelectron spectroscopy (XPS) has been performed using Omicron EA 125 spectrometer with Al K_α (1486.6 eV) source, and Thermofischer (K-Alpha) spectrometer with Al K_α (100-4000 eV) source. The depth profiles are studied with EX06 Ion Source in 1 mm area at 1000 eV for 30 s per scan. The powdered samples were cold pressed into pellets while the hydrothermally synthesized NF supported samples were used without further treatment.

5. Raman analysis:

A Raman micro-spectroscopy system (LabRam HR Evolution, Horiba) with an open electrode CCD air-cooled to -60 °C was used to obtain the Raman spectra. The Raman spectra were collected by mapping random areas of the powdered sample placed on a glass slide, using a 50x objective to focus the laser beam to an approximate diameter of 1 μm. The Raman scattering generated with about 3mW of 633 nm radiation in the spectral range of 50-2000 cm^{-1} was collected for 300 s per window of the spectrum using an 1800 grooves/mm diffraction grating, using the LabSpec software to analyse the metal phosphide samples. The other samples and in-situ analyses were done using (Renishaw, inVia Raman Microscope) system with an open electrode CCD air-cooled to -60 °C. The in-situ analysis was done using Teflon-made cell in three-electrode arrangement. The Raman spectra were collected using 50x objective to focus the laser beam (572 nm) on the sample.

6. Magnetic analysis:

A magnetic properties measurement system (MPMS–SQUID, Quantum Design) coupled with a vibrating sample magnetometer (VSM) was used for magnetic property measurements. Prior to the measurement, the instrument was demagnetized by oscillating the magnetic field. Zero-field cooled (ZFC) and field cooled (FC) magnetic measurements were performed by cooling the sample under zero and certain magnetic fields, respectively. For magnetic field-dependent magnetic moment measurements, the magnetic field was swept between −80 and 80 kOe at a specific temperature (2 K, and 300 K). The samples were cold pressed into pellets and inserted in the magnetometer for analysis.

7. XAS analysis:

All XAFS measurements were carried out at High-flux XAFS-beamline P64 at PETRA III, Deutsches Elektronen-Synchrotron DESY in Hamburg, Germany. The powdered samples were cold pressed with cellulose and fixed on scotch tape for the measurements. X-ray energy was calibrated to 7112 eV for the Fe K-edge. The data were processed with *Athena* software showing the Fourier transform in position (R) space for better representation of bond lengths involved in the system. To further analyse the data, *Artemis* software was utilized. The data analysis involves modelling using theoretical standards (obtained from ICSD and Materials Project database). FEFF6 can be built within a cluster size, which fit all the experimental data with the theoretical standards. IFEFFIT generates the list of all possible arrangements of all the atoms in the lattice (in the provided cluster size) and then the possible interactions can be computed.

8. NMR analysis:

The products were analyzed by hydrogen-nuclear magnetic resonance (^{1}H-NMR) studies at 400 MHz frequency in Bruker 400. 0.2-micron filters were used to filter the samples collected from electroanalysis. 200 mL of electrolyte was collected from the reaction chamber and neutralized with 500 uL of H_2SO_4. 20 μL of DMSO (internal standard) and 50 μL of D_2O (solvent) were added to 700 μL of the above-neutralized sample. The sample was transferred to NMR tube for ^{1}H NMR analysis. The area under the signals corresponding to the existence of benzyl alcohol (δ 8.02 ppm), benzoic acid (δ 7.41 ppm), glucose (δ 8.02 ppm) and formate species (δ 8.3 ppm) in the ^{1}H-NMR spectra were quantified with respect to the area under DMSO peak (δ 2.71 ppm). The peak area under the DMSO peak was calibrated and set as 6. The quantitative analysis of various species in the collected sample was determined from the calibration plot of normalized area versus concentration.

9. HPLC analysis:

The calibration plots were obtained using various standard solutions of glucose (G), gluconic acid (GNA), glucaric acid (GRA), and formic acid (FA). 0.5 mM H_2SO_4 was taken as the mobile phase and Hiplex-H column at 60 ℃ was used as the stationary phase. The analysis was done using UV detector at wavelength of 210 nm with flow rate of 0.5 mL min^{-1}. 400 uL of the electrolytes containing the products were first filtered with 0.2-micron filters and then neutralized with 0.2 M H_2SO_4 solution. The samples were taken in 1.5 mL HPLC vials, sonicated and were loaded in HPLC sampler chamber. For all the samples, major peak area corresponds to the presence of formate in the system.

Conclusions, challenges and future outlook

Conclusions

In the world of material science, nanomaterials have a huge demand and application in the field of electrocatalysis. These materials play a major role as electrocatalysts in water splitting. Despite advancements in the field, anodic oxygen evolution reaction (OER) is still a major hurdle to its commercialization. This is mainly because of the large thermodynamic potential (1.23 V vs. RHE) and sluggish kinetics (four-electron process), which increases the overall potential requirement. By coupling thermodynamically more favorable oxidation reactions at the anode in place of energy-intensive OER, the overpotential required for water electrolysis can be reduced with the generation of value-added products (VAPs). Non-noble metal-based catalysts have been utilized as alternatives to highly expensive and scarce noble metal-based electrocatalysts. Research in this direction is rapidly evolving to find better substitutes. This thesis focuses on the application of non-noble metal-based nanostructured materials for oxygen evolution, hydrogen evolution, benzyl alcohol and glucose oxidation (as alternatives to OER), and glucose sensing. We have thoroughly investigated and explored these effective electrocatalysts and their reactions using various techniques.

The structure-activity correlations hugely impact the electrocatalysis field using nanostructured materials. There is still an immense need to explore the actual catalytic sites and the catalyst applicability at the commercial level. We utilized various characterization techniques to understand the structure-activity correlations and performed electrochemical controls. In the first part of the thesis (chapters 1.2 and 1.3), we have explored metal phosphides and metal oxides, which are highly stable even at high current densities. The generation of heterointerfaces through a simple way of physical mixing FeP and CoP and the dynamic formation of active sites ($NiFe_2O_4$ formation via catalyst-support interactions) has been studied as high-performing catalysts towards OER. The one-time activation of magnetic electrocatalysts with the influence of magnetic fields on electrocatalysis is a fascinating area to explore in order to mitigate the energy requirements during OER. The as-employed catalysts showed remarkably high current densities at ultra-low potentials with immense stability in harsh conditions.

The next part of the thesis (chapters 2.2 and 2.3) explores the hybrid water electrolysis utilizing benzyl alcohol and glucose for oxidation and sensing reactions at the anode side of the cell. Metal oxide or hydroxide supported on NF were utilized as the electrocatalysts for BOR and GOR studies in alkaline conditions. High conversion, yield, and selectivity were observed by using a Cr-oxide-treated Ni foam (CTNF) catalyst for PhCOOH production and specular CuO supported on NF for glucose oxidation and sensing applications. The catalysts showed high cyclability and stability. The in-situ studies revealed the active sites responsible for the oxidation of chemicals.

Challenges and Future Perspectives

Though various reports showed good electrochemical performance of non-noble metal-based electrocatalysts towards oxidation reactions, there is an issue with the leaching of the catalytically active material from the electrode surface. Self-standing electrodes and chemically treated metal supports are being used to overcome this issue. Further, the use of metal supports in the form of a porous matrix facilitates diffusion kinetics and conductivity. Although high current densities (> 1 A cm^{-2}) at low potentials (< 2 V) have been reported using these strategies, the poor stability in the long run is a major impediment to large-scale commercialization. Several reports highlight the degradation of the electrocatalyst during the stability test performed at commercial-level current densities.

Another important challenging aspect is to study any system on an industrial scale with consideration of activity and merits visualized in lab-scale studies. During lab-scale studies, we usually work with very small electrodes with areas as low as 0.07068 cm^2 for glassy carbon electrodes and 0.25 cm^2 for Ni foam electrodes and with small quantities (in μg or mg) of samples. Scaling up these specific activities (mA cm^{-2}) and mass activities (A g^{-1}) for large-scale device fabrication is still a challenging task. Several reports still try to design electrocatalysts with low amounts of noble metals and show remarkable results on lab-scale testing. Taking these materials will not be feasible for sustainable energy production. Furthermore, the field of chemical-assisted hydrogen generation still lags in attaining commercial-level current densities at lower potentials (<1.5 V) with 100 % charge utilization.

The potential application of the materials studied in this thesis can be extended in various ways. These high-performing and stable catalysts can be utilized further for energy applications in the fuel cells and electrolyzers for efficient and sustainable energy production. Low-cost Fe-based materials (similar to Fe@NF(M)) can be explored for applications in high-power-consuming devices with lower energy input. Large-sized electrodes can be fabricated and utilized for industrial energy storage and conversion applications. The effective electro-synthesis of benzoic acid can further be explored for large-scale production. Sensors obtained with copper-based catalysts can be utilized for cost-effective glucose sensing device fabrication in biomedical. With proper optimizations, these findings can be transformed from lab scale to commercial usage.

List of publications

List of publications based on thesis:

1. ***Divya Bhutani***, Sisir Maity, Shashank Chaturvedi, Divya Chalapathi, Umesh V. Waghmare, Chandrabhas Narayana, Vinod C. Prabhakaran, M. Eswaramoorthy, Heterostructure from heteromixture: Unusual OER activity of FeP and CoP nanostructures on physical mixing, *J. Mater. Chem. A*, 2022,10, 22354-22362.
2. ***Divya Bhutani,*** Abhishek Garg, Debendra Prasad Panda, Saptarshi Chakraborty, Pooja Ghakad, A. Sundaresan, Ranjani Viswanatha, Abhishek Kumar Singh, M. Eswaramoorthy, One-time magnetic activation with room temperature magnetic spinel phase generation for electrochemical water splitting. (Patent submitted and Manuscript under preparation)
3. ***Divya Bhutani,*** Abhishek Garg, Supriti Dutta, Swapan K. Pati, M. Eswaramoorthy, C N R Rao, High current density response of Cr-treated Ni foam towards electrosynthesis of benzoic acid from benzyl alcohol oxidation. (Manuscript under preparation)
4. ***Divya Bhutani,*** Aditi Prabhu, M. Eswaramoorthy, Highly effective glucose electrooxidation and sensing enabled by specular metal nanostructures. (Manuscript under preparation)

List of miscellaneous publications:

1. Sisir Maity, Dheeraj Kumar Singh, **Divya Bhutani**, Suchitra Prasad, Umesh. V. Waghmare, Srinivasan Sampath, Muthusamy Eswaramoorthy, High surface area NiCoP nanostructure as efficient water splitting electrocatalyst for the oxygen evolution reaction, *Mater. Res. Bull*, 2021, **140**, 111312.